Middle infrared beam-steering using liquid crystals for spatial light modulation

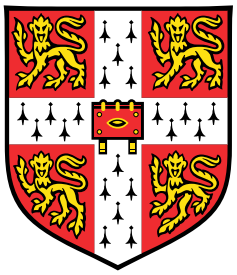

Fabian Micallef

Department of Engineering
University of Cambridge

This dissertation is submitted for the degree of
Doctor of Philosophy

Churchill College

September 2018

I dedicate this thesis to all that I left behind me to embark on this experience. I dedicate it to my mother who always listened. I dedicate it to my father who broke his back to provide for me. I dedicate it to my sisters who always propped me up. I dedicate it to Malta where I was born and raised. I dedicate it to its seas. I dedicate it to its sounds and fragrances. I dedicate it to its culture and its values. I dedicate it to my roots. Most of all, however, I dedicate this thesis to Lucia, whom I am honoured to call mine, and to our daughter Evelyn, whose curiosity and inquisitiveness puts all of ours to shame, and gives me hope for the future of this grand experiment we call mankind.

Declaration

This dissertation is the result of my own work and includes nothing which is the outcome of work done in collaboration except as declared in the Preface and specified in the text. It is not substantially the same as any that I have submitted, or, is being concurrently submitted for a degree or diploma or other qualification at the University of Cambridge or any other University or similar institution except as declared in the Preface and specified in the text. I further state that no substantial part of my dissertation has already been submitted, or, is being concurrently submitted for any such degree, diploma or other qualification at the University of Cambridge or any other University or similar institution except as declared in the Preface and specified in the text, This dissertation contains fewer than 65,000 words including appendices, bibliography, footnotes, tables and equations and has fewer than 150 figures.

Fabian Micallef
September 2018

Acknowledgements

I would like to acknowledge first and foremost the guidance of my supervisor Professor Daping Chu throughout this work. I would like to also acknowledge the support of my advisor Dr.Misha Pivnenko. The help of Dr.Ken McEwan from the defence science and technology laboratory(DSTL) was crucial in framing the problem within the demands of the defence sector. Little would have been possible without the technical input of Dr. Pawan Shrestha, Kasia Surowiecka and other colleagues at the centre for photonic devices and sensors(CPDS). Special thanks go to Dr. Felice Torrisi and Tian Carey from the Cambridge graphene centre(CGC) for providing expertise and materials crucial to the employment of CVD graphene in this work. Particular thanks go to the engineering and physical sciences research council(EPSRC) and again to DSTL for funding this project.

My gratitude also goes out to the dedicated individuals at Churchill College, particularly to Rebecca Sawalmeh, the tutor for advanced students, and Professor Alex Webb, my tutor. I would also like to thank the porters and everyone who supported me in my moments of greatest need.

Abstract

Middle infrared beam-steering is attractive for a number of applications, particularly in the defence sector, where infrared countermeasures are a cornerstone in protecting lives and assets from infrared seeking weapons. Liquid crystal based alternatives to the current opto-mechanical state of the art are investigated, in particular electrically addressed optical phased arrays. Material and design challenges are addressed. CVD graphene is found to be an appropriate transparent conductor, with a sheet resistance $< 1\text{k}\Omega/\square$ and an optical transmission $> 97\%$ in the frequency band of interest. Liquid crystal BL-037 was found to have a birefringence of 0.23 in the middle infrared, where absorption bands exist between 3.3μm and 3.6μm, and at 4.5μm. When incorporated into a single-pixel anti-parallel aligned cell subject to an electric field, the response time for the liquid crystal layer was found to be slower than expected for typical thicknesses required for middle infrared operation (7.5μm - 30μm). This was due to high angle reorientation which is typically absent in visible operation. The effects of various considerations, such as aperture size and shape, illumination, pixelation, dead-space and fringing effects, on the performance of a spatial light modulator were investigated. Liquid crystal on silicon implementation was simulated. For $\lambda = 2.3\mu$m an efficiency $> 10\%$ was attained for angles up to 7°. For longer wavelengths this was attained for angles up to 11°. Multi-interaction and non-diffractive devices were investigated as alternatives for increasing the viewing range while preserving resolution.

Table of contents

List of figures

List of tables

Chapter 1

Introduction

1.1 The middle infrared as a frequency range for atmospheric applications

1.1.1 Comparison of the middle infrared to lower frequency bands for atmospheric applications

The harnessing of electro-magnetic radiation to obtain information regarding our surroundings is as old as the eye itself. As the electro-magnetic spectrum was increasingly better described by the likes of Maxwell and Hertz [109] the possibility of using a wider range of frequencies for sensing and communication became an attractive possibility.

It is critical to select the correct frequency of operation for the job at hand. From a physical perspective the interaction processes of electro-magnetic radiation with its surroundings, such as reflection, transmission, absorption and diffraction, vary highly with frequency. On the other hand, from an engineering perspective, sources, modulators, antennas and sensors with appropriate performance parameters are required to realise a viable system. Systems which transmit and/or collect electro-magnetic radiation outside of the visible spectrum can be used for ranging, such as in radar systems, imaging, such as synthetic aperture radar [109], and communications, such as radio transmissions [137]. Depending on the application these devices can either be passive, like our eyes, which depend on the radiation from the sun, or active, where the radiation targeted for detection is also emitted by the device.

For such applications knowledge of the transmissive properties of the atmosphere is key. The attenuation per kilometre arising from oxygen and water vapour is given in Figure1.1 for the GHz range. Note that this is the highest frequency range which is employed on a large scale in environments where interactions with humans occur. This is because at higher

frequencies potential health hazards start to arise [56]. The attenuation can be seen to tend to increase as the frequency increases, such that a trade-off between range and frequency exists. Spikes of high absorption, which should be avoided, are also more abundant as the frequency increases.

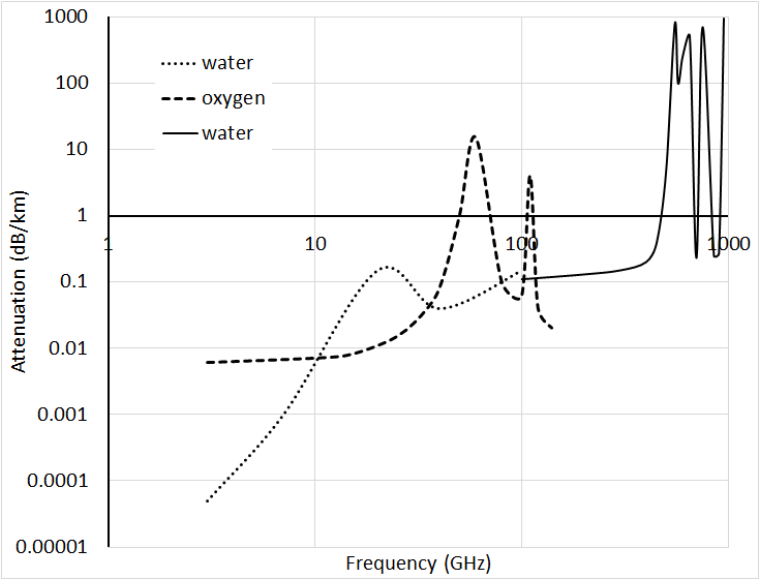

Fig. 1.1 Attenuation in decibels per km of water vapour and oxygen in the GHz range [109] [56].

Apart from the atmosphere itself, radiation will interact with object and surfaces in its path. For radio waves having low frequency the reflection off of the ground, sea, clouds and even the ionosphere [119] need all be taken into account in the development of long-range radar systems. Diffraction occurs most acutely when the relevant aperture and wavelength are of approximately the same size, this can be detrimental but can also be harnessed in MHz frequency radar systems to collect data about objects lying beyond the horizon [109]. Reflection and diffraction are also used to maximise the coverage of radio transmissions as the frequencies employed are often of the same order of magnitude as everyday apertures, such as windows and doorways [137].

Low frequency systems are therefore ideal for long range applications, such as meteorology, astronomy and satellite-mounted remote sensing and communications [109]. What high frequency systems lack in range they make up for in resolution, for ranging and imaging, and bit rate, for communications [78]. Millimetre wave systems, having a frequency of a few hundred GHz, result in highly directional beams, which are used in short range automotive anti-collision systems, where directionality is paramount.

THz systems are a natural progression towards smaller frequency bands. In this region an optical approach to device design becomes viable, such that fully electrical and optical systems, but also hybrid systems, can be realised [56]. Modulation is necessary in communications to encode information. This has been achieved by both semiconductor heterostructures and liquid crystal layers, even though the latter is unable to attain the bit rate required for communications. The path forward towards infrared based devices seems to be mapped out as a progression of the above. Having said that, issues of thermal noise, diffuse reflections and eye-health hazards complicate the problem and demand careful consideration.

1.1.2 Atmospheric middle infrared applications

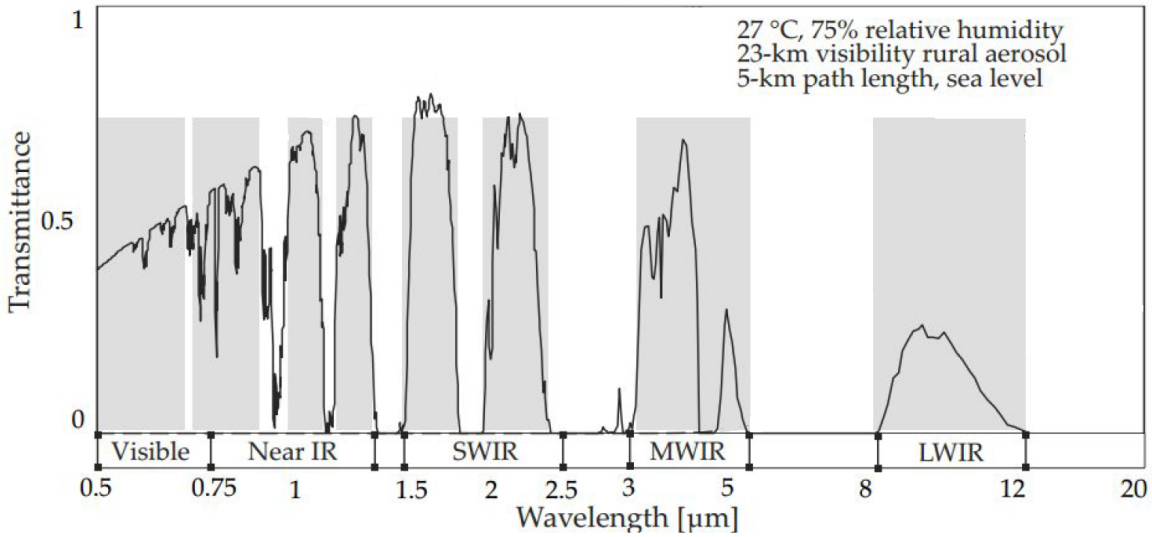

Fig. 1.2 Atmospheric transmission spectrum of the visible and infrared range [58].

As outlined, atmospheric transmission bands restrict the frequencies we can use in our devices. This also has a knock on effect by influencing the applications we can investigate for a particular frequency range. Atmospheric transmission in the infrared is confined to a few bands, as can be seen in Figure1.2. Communication in the infrared is often limited to indoor, low-power systems which allow for very high bit rate communication [49]. Low power operation is necessary for eye-safety, while directionality allows for higher intensities and the minimisation of cross-talk. Noise is further increased from indoor illumination sources. Particularly in the near infrared we have mature source, modulation and detector technologies. Note that, unlike lower frequency technologies, intensity modulation is the most commonly used way of encoding information in the transmitted radiation. Outside of

local area networks infrared radiation can be used for satellite communications, where health hazard considerations are moot and the increased directionality can be fully exploited [133].

Infrared passive satellite-based devices are used for meteorology and temperature mapping, often where operation in the visible spectrum is impossible. The 8-12 μm band is the most commonly used for such applications [112]. Short range mapping/locating of infrared sensitive materials of geological, biological or environmental importance is also possible [111] [42] [29].

The defence sector is a strong driver in the development of middle infrared atmospheric devices. Seeker devices identify the infrared signature of enemy hardware passively so as to be able to lock-on and take appropriate action [58]. Infrared countermeasures attempt to fool seeker systems. This leads to a race between infrared countermeasures and infrared counter-countermeasures. Active countermeasures require fast and accurate beam-steering to deliver false target information to the seeking system [73].

1.2 The current state of the art of optical beam-steering for atmospheric applications

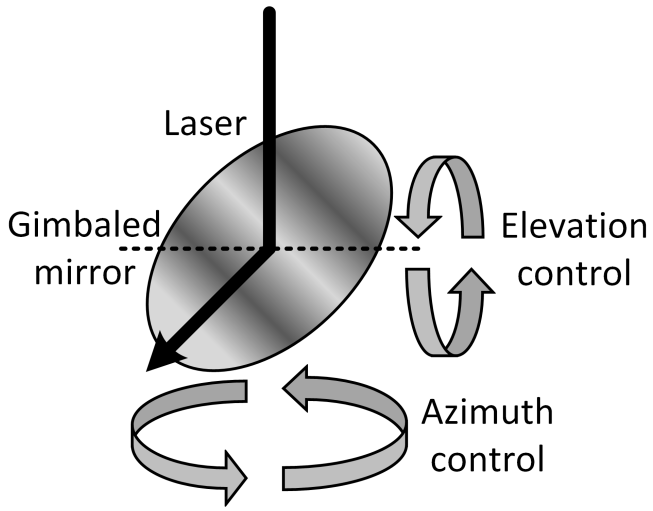

Fig. 1.3 Simple schematic of a gimbaled mirror system for opto-mechanical beam-steering [83].

Given the usefulness of the mid-IR , as outlined in the previous section, it is unsurprising that development of beam-steering/forming/modulating devices for this frequency range has been of interest. Optical wavelengths allow for good directionality of transmitted beams. Barring interactions between fixed positions this imposes some requirement for dynamic

steering. The most prevalent beam steering technologies used presently are opto-mechanical. These systems typically make use of gimbaled mirrors as the key steering component, such as seen in Figure1.3. They feature a large field of view but have considerable drawbacks. Tracking requires multiple independent axes, more so if the system is imaging and must therefore account for roll as well. Mechanical moving parts make the system difficult to operate accurately due to inertia considerations. These are not negligible, especially for wide, fast sweeps which must end quickly and accurately. These devices are therefore not random access, which results in a greatly limited speed of operation. Due to the strain of such demanding operation maintenance is a constant issue. Additionally, the power necessary to operate such devices is prohibitive for small platforms. Many of these systems are financially prohibitive if any sort of accuracy is expected [83], limiting their wide-scale use.

Miniaturisation of opto-mechanical systems can reduce inertial effects and costs. A millimetre-scale mirror mounted on a gimbal can be actuated by applying a potential difference between intersecting comb electrodes, where one set is fixed and the other is mounted on the gimbal arm. This results in a fast, chip sized steering system [86]. The voltage applied controls the steering magnitude, with the maximum steering angle of a few degrees occurring for some resonant frequency. Steering range is restricted by manufacturing limitations and the constraints set by the intersecting comb electrode actuating interaction.

Direct steering is therefore restricted by the limitations in manipulating the singular steering element. Optical phased arrays, on the other hand, are formed of many elements which operate on the phase and/or intensity of the incident radiation in a pattern such that the superposition of this field results in steering. In this case the steering range is determined by the size of the smallest steering element involved. Opto-mechanical phased array systems made up of micro-mirror arrays are used to attain both one and two dimensional beam-steering [129] [77]. The electrically actuated micro-mirrors move up and down, creating a phase pattern in the incident light due to varying path lengths. These systems are often restricted to binary patterns such that the maximum efficiency attainable is limited. Their performance is also intimately related to the level of miniaturisation that can be attained for a steering element which has to be actuated vertically with an accuracy and range that are crucial to the final operation of the device. Note finally that such devices can have added functionalities, such as lensing, fanning out and in and aberration compensation [13].

Arrays of thermo-optic or electro-optic phase shifters offer a true non-mechanical approach to beam-steering. The integration of these into photonic circuits realised through lithography, along with some in/out-coupling structures, yields promising chip-sized steering devices [43]. The required phase delay occurs by varying the effective optical path length within the phase shifter. This can occur electrically, by varying the amount of free carriers,

or by harnessing the thermo-optic effect. Where the application allows, wavelength dependent steering is also possible. These devices can have high speed and can even attain two dimensional steering by employing carefully designed coupling structures so as to be able to illuminate a grid of independent shifters using only a single source. The maximum power allowable is often the limiting factor in such systems, as heating can degrade performance heavily. Metasurfaces with sub-wavelength metallic or semiconducting features have been shown to provide polarisation selective steering in two or more directions [27].

It is often impossible for these non-mechanical devices to attain the large steering range required for field applications in ranging, targeting and countermeasures. Where steering range is crucial, polarisation gratings (PGs) [52] and non-diffractive devices based on patterned active cladding waveguides [24] are the non-mechanical devices at the forefront of the sector. Unfortunately, this is only the case for wavelengths up to 1.55μm, where research in the necessary optical materials is mature.

Polarisation gratings are based on photo-imprinted steering elements which are polarisation selective. PGs can be passive or active. Active elements can be erased by applying an electric field. Photo-imprinting occurs by UV laser irradiation. The pattern is created by interference. The steering angle of the device, which is fixed, is determined by the spacing between interference fringes. This process is very challenging and expensive. Additionally, large steering requires many stacked PGs, particularly if 2-D steering is desired, which effectively doubles the required elements. This not only makes device cost a concern, but also presents considerable optical challenges in terms of the materials chosen and the device assembly.

Steer-enabled optical waveguides can attain very large steering. A patterned active cladding is used to generate a series of boundaries at which radiation is steered according to Snell's law. The steering magnitude is determined by the controllable refractive index change across the boundary. The large steering angle is attained by the large number of boundaries involved. Such devices can yield high efficiency steering at satisfactory speeds. Unfortunately, such a device offers intrinsically 1-D steering. Integration into a 2-D system is not trivial. Along with optical phased arrays, the possibility of such a non-diffractive device for the mid-IR has been investigated in this work.

1.3 Phase holography as a key tool in developing novel devices for the middle infrared

Given the intrinsic maintenance and durability problems effecting opto-mechanical systems, non-mechanical devices are an attractive alternative. Materials that have non-linear optical properties are pivotal in developing these alternative devices. Materials which exhibit these non-linear optical properties such as the Kerr and Pockels effect [101] undergo a change in their optical properties when subject to an electric field which corresponds to a change in the optical path length. For such a material sandwiched between a controllable pixelated electrode structure we have a phase-only optical phased array. The change induced in the refractive index via the Kerr and Pockels effect is smaller than 10^{-4}. It is therefore difficult to obtain a steering device, which requires at least π phase shift in the case of binary devices, using these materials.

Liquid crystals offer a highly non-linear alternative to crystalline materials which exhibit the Pockels or Kerr effect, with an electrically controllable birefringence in the order of 10^{-1}. Liquid crystal spatial light modulators(LC-SLMs) have a broad range of applications from displays [102] to aberration control and beam-steering [113]. The optical non-linearity of liquid crystals extends into the infrared spectrum, however, absorption peaks in this band can limit their use [92]. Their flexibility of implementation has also enabled their use for many applications [51]. For example, the liquid crystal display(LCD) industry has accelerated material and device research greatly and driven down the cost of production considerably [29].

As such, LC-SLM devices have great potential in being a cost effective, compact and reliable alternative to the current state-of-the-art. In addition to being completely non-mechanical, LC devices are random access with negligible inertia considerations [76]. For a fully addressable pixel structure, multiple functionalities can be implemented without any additional cost or device complexity [128].

A basic LC-SLM device is formed of five essential components as shown in Figure 1.4. Firstly, there is the liquid crystal layer which provides the variable retardation necessary to set up the phase pattern. This layer is enclosed between two substrates where either one or both, for reflective or transmissive devices respectively, must be transmissive in the operational frequency. Patterned electrodes on these substrates set up the electric field necessary to reorient the LC molecules. They are also reflective or transmissive depending on the set-up. Alignment layers in contact with the LC-layer lock the orientation of the liquid crystal molecules at the boundaries and therefore determine the behaviour of the LC-SLM in the off-state. LC-SLM operation depends on the polarisation of the incident light. Therefore,

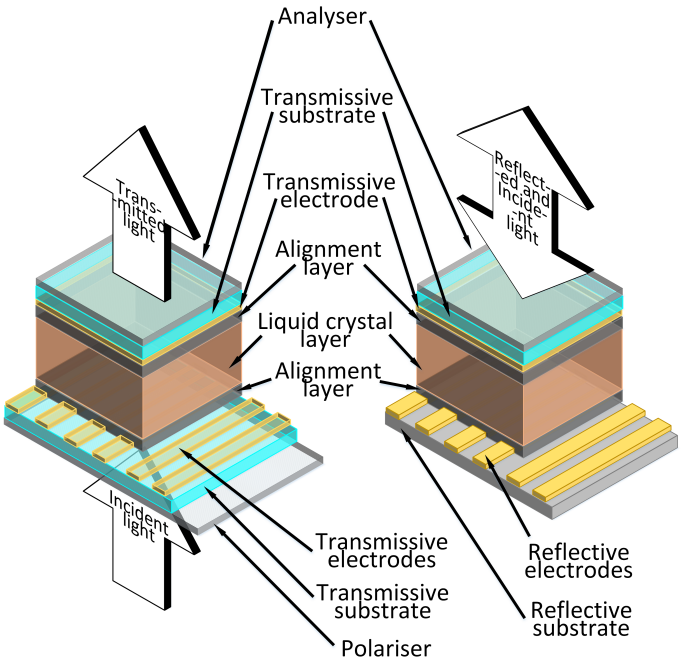

Fig. 1.4 Cross-section of an amplitude modulating basic transmissive and reflective LC SLM respectively [50].

unless the source light is already polarised a polariser is used. An analysing polariser on top of the device is used to obtain light and dark states for amplitude modulating devices and as a way to visualise phase changes in the development of phase modulating devices [50].

Key defence agencies outline demanding parameters to be matched regarding future liquid crystal beam steering devices: A high element density (64×64 elements) device with a 90° field of view (-45° to $+45^\circ$). Such a device must also be capable of sub-millisecond steering agility with a 30dB sidelobe suppression. Beam forming capabilities are expected [23]. Attaining this performance presents both design and material challenges [29]. On top of this, middle infrared operation adds a number of material challenges as most commercially available materials are developed for the display industry and are therefore designed for use with visible radiation [65]. The hurdles are substantial but the reward is attractive: Fast, efficient and aberration-compensated sensing, targeting, navigation and countermeasure devices which are sure to revolutionise wireless communication, surveying and security both in civilian and military contexts [125] [23].

This work is divided into three primary chapters, excluding the introduction and conclusion. Chapter 2 tackles the problem of finding appropriate transparent conducting materials for the mid-IR. CVD graphene is suggested as the material of choice. Chapter 3 investigates the properties of liquid crystal BL-037 for operation in the mid-IR. It is found to be suitably

transparent with an acceptable optical birefringence. Information gathered in these two chapters is brought together in Chapter 4 to outline the operating principles and simulate the performance of multiple potential solutions. Liquid crystal on silicon (LCOS) devices and non-diffractive devices are investigated, and a novel multiple-interaction LCOS-based device is outlined.

Chapter 2

Transparent conductors for the middle infrared

2.1 Material properties and geometries for transparent conductors

2.1.1 The relationship between transparency and conduction

Finding materials which are optically transmissive at operational frequencies and electrically conductive at driving signal frequencies is pivotal in the fabrication of LC-SLMs. An ideal transparent conductor is a perfect conductor at electrical frequencies and a lossless dielectric at optical ones [101].

Conductivity requires a drift of free carriers under the influence of an electric field. It is therefore determined both by the amount of free carriers and their ability to drift with ease within the material. Materials are considered as insulators, conductors or semiconductors depending on the availability of free carriers [132]. The availability of free carriers depends primarily on the band structure of the material and the band gap energy E_g, which are determined by the constituent atoms forming the material, the structure they are assembled in and the presence of impurities, whether accidental or intentional. In conductors the conduction band is partially filled or the valence band and the conduction band overlap such that the band gap is absent and therefore electrons readily populate the conduction band without applying any energy. Note that a conduction band is simply an energy band which is only partially filled with electrons. This implies that the free carriers are easily allowed to gain energy, such as the energy gained by free carriers which are experiencing drift. In an insulator we have a full valence band and an empty conduction band, but E_g is large enough

such that electrons in the valence band do not have the required thermal energy to enable transitions up to the conduction band. In a semiconductor E_g is small enough such that some electrons have the required thermal energy to transition up to the conduction band. This leaves vacancies in the valence band such that electrons can drift in the valence band as well. It is however easier to refer to carriers within the valence band in terms of the vacancies themselves, which are referred to as holes. Holes drift opposite to the free electrons, but since they are oppositely charged they still aid in conduction. These thermally generated electron-hole pairs are refereed to as intrinsic carriers and their amount depends on the thermal energy of the system. The amount and type of free carriers in a semiconductor can be further tailored using dopants. Dopants either donate a free electron or accept a valence electron, thus generating a hole. Assuming that there is enough thermal energy for the dopant to be ionised, the free carrier density of a doped semiconductor is given by its intrinsic part added to the dopant density in the material.

An electron being accelerated in vacuum under the influence of an electric field is referred to as a ballistic electron. This is not the case in a solid [38] where we have the interplay of a drifting electron with multiple internal electric fields and scattering sources. Ionised impurities, acoustic and optical phonon scattering, lattice dislocations and granular structures all hinder free carrier acceleration. These factors are typically dependent to varying degrees on the temperature, the dopant/impurity density and the crystalline quality of the material.

The force experienced by an electron in an electric field is eE, where e is the electronic charge and E is the electric field strength. This results in a net change of momentum, which when averaged over the number of free electrons gives:

$$neE = \frac{dp}{dt} \tag{2.1}$$

where n, p and t are the electron density, momentum and time respectively. As discussed, this acceleration is hindered by scattering phenomena. Assuming a constant probability for the scattering of electrons, the rate of scattering with time is proportional to the free carrier density, such that $-dn/dt = n/\tau$, where τ is a proportionality constant giving the mean free time between scattering episodes. The probability of a scattering interaction occurring in time dt is dt/τ, such that the change of momentum in time dt is $dp = -pdt/\tau$. Rearranging and combining with Equation2.1 for steady state drift yields:

$$-\frac{p}{\tau} - neE = 0 \tag{2.2}$$

The average momentum of drifting electrons is given by $\bar{p} = p/n$. Therefore $\bar{p} = -e\tau E = m_e^* v_d$, where v_d is the drift velocity and m_e^* is the effective mass of the drifting electron. The

effective mass varies from the rest mass of an electron due to its interactions with other electrons and with the periodic potential of atoms distributed in a lattice. It is therefore strongly related to the band structure.

The current density J is therefore given by $J = \sigma E = -nev_d$, where σ is the conductivity. Conductivity is therefore given by:

$$\sigma = \frac{ne^2\tau}{m_e^*} = ne\mu_e \tag{2.3}$$

where $\mu_e = e\tau/m_e^*$ is the electron mobility. The mobility involves both the effective mass and the mean free time, and it can therefore be defined as the ease of drift of the charge carrier in the material.

Note that for a material where both electrons and holes are present conductivity is given by $\sigma = ne\mu_e + pe\mu_p$, where p is the hole density and μ_p is the hole mobility. Note that $\mu_p < \mu_e$. An electron in the conduction band has a higher mobility than a hole since it is further away from the positively charged nucleus, and therefore less tightly bound, than the valence electrons, which are required to drift so as to enable the hole drift. Note that intrinsic semiconductors typically have higher mobilities than metals due to lower electron effective mass. Note finally that for each scattering or interaction source a mobility μ_i can be extracted with a dependency on τ and m^* according to the particular physical phenomenon. The total mobility is then given by $(1/\mu) = \sum_i (1/\mu_i)$.

Maximisation of conductivity is therefore achieved by a combination of high carrier concentration and high mobility. Metals have high conductivity due to much higher carrier concentrations which make up for the lower mobilities. Mobility in metals decreases with increase in temperature due to the decrease in τ arising from increased interactions with ions. In a semiconductor the conductivity can be more accurately tailored by varying the dopant concentration. Note however that increasing dopant density has a degrading effect on the mobility due to increased impurity scattering. For example, mobility drops for Si:P from approximately 1400 $\mathrm{cm}^2/\mathrm{Vs}$ to approximately 100 $\mathrm{cm}^2/\mathrm{Vs}$ as dopant density increases from 10^{15} to 10^{19} [38].

For alternating currents a time dependent electric field is being applied. In this case Equation2.2 is given by:

$$m^* \frac{d\mathbf{v}}{dt} = -e\mathbf{E} - m^* \frac{\mathbf{v}}{\tau} \tag{2.4}$$

Additionally, given the relationship $\sigma\mathbf{E} = ne\mathbf{v}$, the complex conductivity is given by:

$$\sigma = ne\mu \left(\frac{1}{1+\omega^2\tau^2} + i\frac{\omega\tau}{1+\omega^2\tau^2} \right) \tag{2.5}$$

Which is valid for a harmonic electric field of the form $\mathbf{E} \propto \exp(-i\omega t)$. For metals $\tau \approx 10^{-14}$ [32] and for semiconductors $\tau \approx 10^{-12}$ [38]. Additionally, the frequency of driving signals for liquid crystal applications rarely exceeds 1MHz, even for high frequency operation strategies [102]. Therefore, $\omega\tau$ is typically much smaller than 1. In this case Equation2.5 reduces to Equation2.3, applicable for constant driving electric fields.

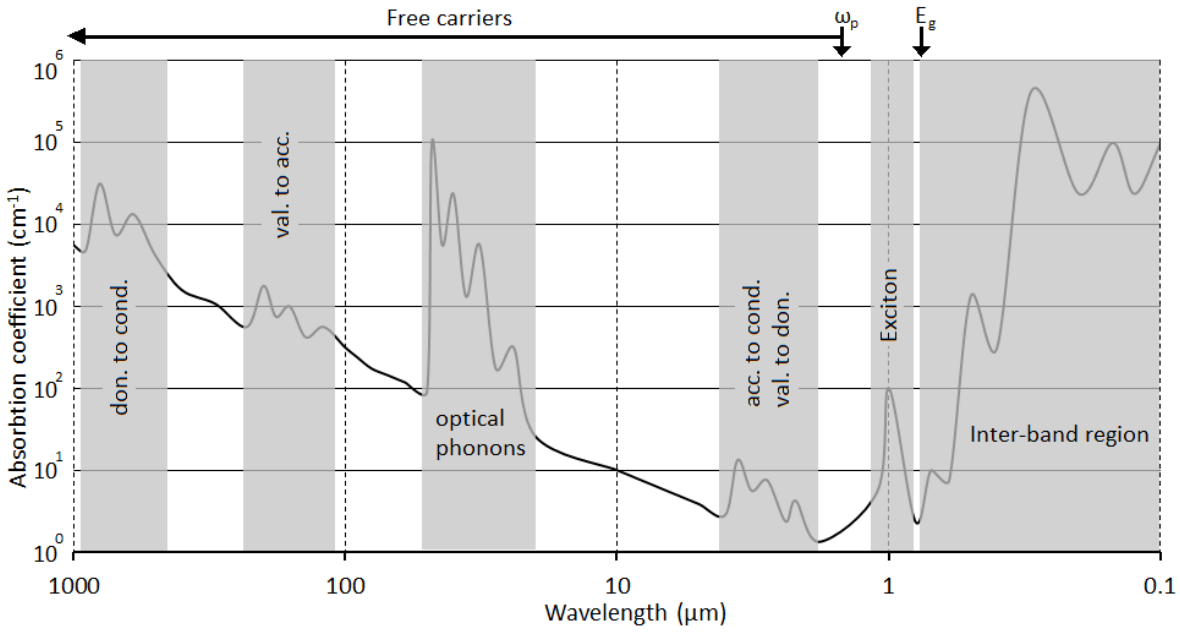

Fig. 2.1 Representative photon absorption spectrum for a typical semiconductor showing the primary physical phenomena involved [38].

Figure2.1 outlines the primary absorption phenomena of a typical semiconductor. Two primary regions of interest are evident when discussing photon absorption in and around the infrared range. In the high wavelength range free carrier absorption dominates. The effective lower wavelength limit of this effect is the plasma frequency ω_p. In the smaller wavelength range absorption is dominated by inter-band transitions, and is limited at higher wavelengths by the band gap energy E_g. Note that in metals there is no band gap. However, transitions between energy bands still occur [32]. These are more of note in the near infrared and visible ranges, explaining the variety of colours metals exhibit. In the middle infrared transition metals have inter-band absorption peaks, but these only vary the optical properties negligibly when superimposed on the effect of free carrier absorption.

Choosing a semiconductor which has a band gap energy greater than that corresponding to a mid-IR wavelength is critical in preventing direct photon absorption due to an electron excitation from the valence band to the conduction band. Indirect photon absorption aided by an additional acoustic or optical phonon absorption enables absorption of photons with an

energy lower than the band gap. Note that absorption can occur involving multiple phonons, this extends this phenomenon further into lower photonic energies. Having said that, indirect absorptions only extend the range where absorption occurs by about 0.1eV [38]. Note that absorption due to indirect transitions is typically three orders of magnitude smaller than that due to direct transitions. Note finally that such a process requires phonons to be present, but this condition is amply fulfilled at room temperature operation.

Other phenomena which give rise to absorption in the region close to, but smaller than, E_g are two-photon absorptions, excitons and the Urbach tail. In two-photon absorption two less energetic photons are required to excite an electron to the conduction band. Such interactions have a much lesser absorption contribution than others at the same photon energy and are therefore often disregarded. Excitons arise when an electron in the conduction band and a hole in the valence band are attracted by a Coulomb force and together behave similarly to a hydrogen atom. The effect of excitons is only detectable at low temperatures and for highly homogeneous samples. The Urbach tail is a modification of the absorption characteristics around E_g which is experimentally observed. It results in an initial exponential increase of absorption before and at E_g, where it then gives way to the typical square root dependency of absorption with photon energy. This is attributed to band tail transitions. Band tails exist below band levels and arise due to disorder, impurities and vibrational effects. The width of the Urbach tail depends on sample temperature, but at room temperature it is still < 0.1eV.

Absorption due to electron transitions involving donor or acceptor levels occur at photon energies dependant on the impurity's physical characteristics. Donor and acceptor levels occur between the top of the valence band, given by E_v, and the bottom of the conduction band, given by E_c. Transitions from the donor level to the conduction band or from the valence band to the acceptor level result in absorption phenomena in the far infrared. Transitions from the valence band to the donor level or from the acceptor level to the conduction band are more energetic and can occur in the middle infrared. It has been assumed that impurities do not interact with each other. However, for high impurity concentrations the corresponding levels broaden into a band. This results in a broadening of the corresponding absorption peaks. For a suitably large dopant density the dopant band overlaps the conduction band, thus changing the behaviour of the material from semiconducting to metallic. The dopant density at which this transition occurs for a given semiconductor and dopant is called the critical doping concentration. Note that in this case the band gap still exists. However, due to the large carrier concentration in the conduction band, electron transitions from the valence band to the conduction band require an energy $> E_g$ since the levels closest to the bottom of the conduction band are full. This pushes the effective band gap to higher energies and is referred to as the Burnstein-Moss shift.

While many absorption sources arise from the band structure of a semiconductor, choosing a material with a sufficiently high E_g can mitigate absorption in a target frequency range. On the other hand, keeping in mind that conductivity is required in addition to transparency, free carrier absorption is the key trade-off parameter. The wave equation for an electric field in a material containing free carriers is given by:

$$\nabla^2\mathbf{E} = \varepsilon_r\varepsilon_0\mu_0\frac{d^2\mathbf{E}}{dt^2} + \sigma\mu_0\frac{d\mathbf{E}}{dt} \tag{2.6}$$

where ε_r is a high frequency relative permittivity and σ is the complex conductivity as seen in Equation2.5. For a plane wave equation, which has a form $\propto \exp[i(\mathbf{k}.\mathbf{r} - \omega t)]$, the resultant dispersion relation is of the form:

$$-k^{*2} + i\omega\mu_0\sigma + \omega^2\mu_0\varepsilon_r\varepsilon_0 = 0 \tag{2.7}$$

where k^* is the complex wavevector. Given that $\mu_0\varepsilon_0 = 1/c^2$ we obtain, after rearranging:

$$\frac{k^*c}{\omega} = \sqrt{\varepsilon_r + i\frac{\sigma}{\varepsilon_0\omega}} = n^* \tag{2.8}$$

where $n^* = n_r + in_i$ is the complex refractive index. Note that n_i is typically referred to as the extinction coefficient. Squaring and separating Equation2.8 into real and imaginary parts, with the inclusion of Equation2.5 for σ, yields:

$$n_r^2 - n_i^2 = \varepsilon_r - \frac{ne\mu\tau}{\varepsilon_0(1+\omega^2\tau^2)}$$

$$2n_rn_i = \frac{ne\mu}{\varepsilon_0\omega(1+\omega^2\tau^2)} \tag{2.9}$$

From this the absorption coefficient $\alpha = 2(\omega/c)n_i$ is given by:

$$\alpha = \frac{ne\mu}{cn_r\varepsilon_0(1+\omega^2\tau^2)} \tag{2.10}$$

Simplifying approximations relate to the condition $\omega\tau \gg 1$. For the mid-IR range $\omega = 3.8$ to 9.4×10^{14}, with the optical range about an order of magnitude larger. As already stated, for metals $\tau \approx 10^{-14}$ and for semiconductors $\tau \approx 10^{-12}$. For semiconductors the condition is easily fulfilled, but this is not necessarily the case for metals, even though $\omega\tau > 1$ is typically true. Assuming $\omega\tau \gg 1$, the refractive index n_r is given by:

$$n_r^2 = \varepsilon_r\left(1 - \left(\frac{\omega_p}{\omega}\right)^2\right) \quad \text{where} \quad \omega_p = \sqrt{\frac{ne^2}{\varepsilon_r\varepsilon_0m^*}} \tag{2.11}$$

ω_p is referred to as the plasma frequency. This is the frequency above which free carrier interactions cannot effectively occur.

The absorption coefficient α is proportional to the free carrier density and the mobility. It is also approximately inversely proportional to ω^2. Unfortunately, reducing n and μ has a proportional effect on the conductivity. Absorption from free carriers is limited above the plasma frequency. Reducing the plasma frequency below the target spectrum for transmission is ideal for achieving a transparent material. However, given the dependency of ω_p on n this is very difficult to achieve. For metals the plasma frequency is typically in the ultraviolet range [38]. For intrinsic semiconductors it is typically in the middle to far infrared [38] due to low values of n, but the corresponding conductivity is therefore low. Doping enables some control on the trade-off between the absorption coefficient and conductivity. However, other factors such as the dependency of μ on n and the effects of high doping on the band structure, which have already been discussed, make this exercise a non-trivial one.

Indium tin oxide(ITO) is the industry standard transparent conductor for use in the visible spectrum. It is formed of highly tin-doped indium oxide. Indium oxide is a high band-gap semiconductor with $E_g \approx 3$eV, which places this absorption edge at the lower wavelength end of the visible spectrum. Tin doping is above the critical limit, creating a material which behaves as a metal. The critical doping for indium oxide is approximately $5 \times 10^{18}\text{cm}^{-3}$ [7]. Finally the Burnstein-Moss shift pushes E_g to higher energies, enabling more transmission in the visible spectrum.

An indium tin oxide layer designed for mid-IR operation would require the dopant level to be adjusted so as to yield a plasma frequency corresponding to the edge of the desired transmissive range. This is given at approximately 5μm, resulting in a target $\omega_p \approx 3.8 \times 10^{14}$. From Equation2.11, given that for ITO $m^* = 0.4m_0$ [7], $n_{mid-IR} \approx 1.82 \times 10^{19}\text{cm}^{-3}$. This is greater than the critical doping and metallic behaviour would therefore still occur. Unfortunately, we would expect the conductivity to be approximately two orders of magnitude smaller than for layers tailored to the visible spectrum.

Doping of indium oxide with molybdenum[79] or tungsten [65] can increase mobility considerably. Replacement of indium ions with tungsten or molybdenum ions provides more free carriers than replacement with tin ions. These extra free carriers reduce the scattering effect due to interstitial oxygen, resulting in an increase of mobility. Both materials are suggested as alternatives to tin doping for near infrared transparent conducting oxides.

Unfortunately it is very difficult to deposit transparent conducting oxide samples with good crystalline characteristics and predictable properties. This is highly challenging not only because of the large number of variables involved and the high sensitivity of the resultant films to them, but also because many are heavily equipment and material dependent, meaning

that the reproducibility of recipes found in the literature is typically poor. This, in conjunction with the limitations of the available equipment, restricted the possibility of pursuing the development of a mid-IR transparent conducting oxide as part of this work. Furthermore, commercially available high quality ITO coated glass is tailored for operation in the visible range and therefore performs poorly in the infrared [140].

A further constraint on the electrical properties of a prospective transparent conducting material is the capacitative effect within the completed cell as well as the voltage drop along the electrode. A liquid crystal cell can be thought of as a parallel plate capacitor with some capacitance C. This capacitor is assumed to have a leak resistance in parallel R_{cap} and electrode resistances R_1 and R_2 in series, along with an alternating current supply V_{source} as seen in Figure2.2 along with its equivalent Thevenin's circuit.

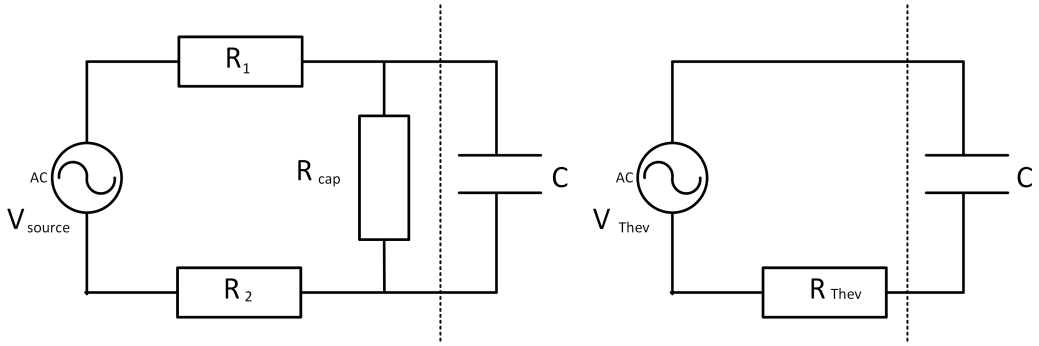

Fig. 2.2 Representative circuit for a parallel plate LC cell and its corresponding Thevenin's circuit.

A full treatment of this circuit requires a complex analysis to account for phase behaviour. The complex impedance of this circuit is given by [68]:

$$\begin{aligned} Z_{tot} &= Z_{cap} + R_1 + R_2 \\ Z_{cap} &= \frac{-iR_{cap}\chi_{cap}}{R_{cap} - i\chi_{cap}} \end{aligned} \tag{2.12}$$

Where Z_{cap} is the capacitor's complex impedance and $\chi_{cap} = 1/(\omega C)$. Using Ohm's law with complex valued quantities, $I = V_{source}/Z_{tot}$, the loss of voltage across any of the two electrode resistances R_1 or R_2 is given, say for R_1, by $V_{drop-R_1} = IR_1 = (V_{source}/Z_{tot})R_1$. This means that the voltage drop will be in phase with the current and typically out of phase with the voltage signal applied.

The charging and discharging times of a capacitor cause a high frequency filtering effect in series resistor - capacitor circuits. This is because the capacitor cannot charge and discharge fast enough to keep up with the applied voltage signal. If a step function between V_{min} and V_{max}, or vice-versa, is applied, then the equation for charging and discharging is:

$$V_c(t) = V_{end} + (V_{start} - V_{end}) \exp(\frac{-t}{RC}) \tag{2.13}$$

with V_{min} and V_{max} plugged in accordingly and where RC is a time constant which denotes the time taken for V_c to be a fraction $1/e$ away from V_{end} and is usually set as a cut-off point for the filtering effect. It is therefore preferable that the driving frequency $f < 1/(2\pi RC)$.

Establishing the RC constant is therefore critical in determining the actual voltage set up across the cell. Using Thevenin's method the three resistances can be combined into one resistance R_{th} in series with the capacitor [68]:

$$R_{th} = \frac{(R_1 + R_2)(R_{cap})}{R_{cap} + R_1 + R_2} \tag{2.14}$$

yielding RC constant $R_{th}C$. Note however that this treatment requires the replacement of V_{source} with V_{th} obtained as the voltage across the open-circuit caused by removing the capacitance in the Thevenin conversion. In this case the voltage across R_{cap} is:

$$V_{th} = IR_{cap} = V_{source} \frac{R_{cap}}{R_{cap} + R_1 + R_2} \tag{2.15}$$

The above treatment allows the determination of the voltage drop along electrodes and that due to high frequency sources. Minimising these losses sets geometrical, material and electrical constrains. Driving frequency is limited by both resistance and capacitance. Capacitance is given by $C = (\varepsilon_0 \varepsilon_r A)/D$, with overlapping plate, or electrode, area A, separated by a cell thickness D and filled with a liquid crystal mixture of relative permittivity ε_r. Note that the dielectric anisotropy of the LC material complicates the determination of ε_r. Reducing the overlap area reduces the active area of the device, and increasing the distance affects operational speed. Electrode resistance is given by $R = \rho(l/wd)$, where ρ is the resistivity and l, w and d are the length, width and thickness of the electrode respectively. For transparent conductors, conductivity and thickness are typically fixed. The electrode aspect ratio is therefore the most easily controllable way of minimizing voltage drop, with wider electrodes being preferable. In direct-address or passive-address [50] devices this is a limitation on the minimum pixel size attainable.

2.1.2 Electrode design for improved trade-off between transparency and conduction

As seen in the previous subsection, controlling the amount and nature of dopant in a semiconductor does give some control over the trade-off between conduction and transmission. However, it is often difficult or impossible to obtain desirable bulk material properties. Geo-

metric considerations have the potential to allow materials to have a satisfactory performance in spite of their bulk properties.

Sub-wavelength perforations in metallic films hold promise in this regard [28]. For an array of cylindrical holes in a film of thickness t, as seen in Figure2.3, the shift from bulk properties is primarily dependent on the diameter d and period a of the perforation array. The location of frequency transmission peaks is related to the periodicity a and is independent of metal used.

The width of these peaks is determined by t/d with greater peak definition for larger values of this ratio. If rectangular apertures are used the performance depends highly on the relation between incident polarisation and aperture aspect ratio [33]. It is of particular interest that the fraction of light transmitted at the maxima exceeds the fraction of area exposed by the holes. The transmission spectrum at non-normal incidence suggests that the interaction of incident light with surface plasmons gives rise to this anomalous transmission.

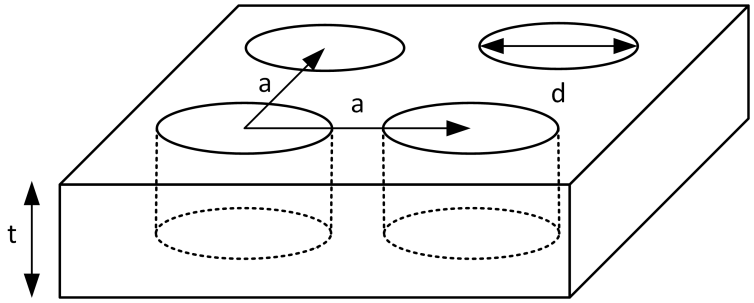

Fig. 2.3 Array of period a of cylindrical perforations of diameter d in a metallic film of thickness t.

The transmission characteristics of such patterned films depend highly on the quality of the lithographic process used [33]. For our frequency band of interest, while not as stringent as for visible light, sub-micron resolution would still be necessary. This is challenging to achieve cost-effectively. Furthermore, note that any electrode pattern would be superimposed on this transmission-enabling pattern. These two patterns would differ in minimum feature size by an order of magnitude at best. This is likely to cause not only structural problems, such as points of very small electrode cross-section, but also heavy degradation of the transmission characteristics as a small number of holes in the array are isolated electrically from their neighbours [33]. Finally, the phase characteristics of the transmitted radiation is altered due to interaction with the array [33]. For a phase-only spatial light modulator this problem is critical and non-trivial.

A cost and time effective alternative is the use of metal nanowire [62] or even carbon nanotube [135] meshes obtained from solution. These conductive transparent films are

obtained by spreading the solution on the desired substrate surface followed by an annealing bake to remove any solvent. For metal nanowire meshes the properties of the mesh depend on the nanowire length, width and material, but also on the density of nanowires along with the annealing parameters. These nanowires are typically micron-scale in length and nanometre scale in diameter. Annealing time and temperature must be enough to allow for solvent removal and nanowire contact and fusion to occur, which optimises the electrical properties. Note that over-baking causes the nanowires to melt. This causes isolated metallic islands to form, resulting in a prompt degradation of electrical properties. Films with a transmission of $\approx 80\%$ in the visible range and a sheet resistance of $\approx 20\Omega/\square$ are attainable. For the mesh to be conductive a minimum density is required [57]. This percolation threshold density is given as approximately one nanowire in the area enclosed by its length. While lithography quality issues do not apply here, the other issues in sub-wavelength perforation arrays still apply. These are further compounded by the randomness in size and shape of the holes in a nanowire mesh.

A diametrically opposite approach to perforated, but relatively thick, metal films is to maximise the transmission by minimising the film thickness of the metallic conductive film. For these few-nanometre thick ultra thin metallic films(UTMFs) bulk properties have to be modified to account for morphological properties, such as granularity and voids, which typically depend on the deposition parameters. These phenomena are more critical than for transparent conducting oxide layers, which are typically a few hundred nanometres thick. A combination of the Fuch's theory (FS-model) [75] and the model by Mayadas and Shatzkes (MS-model) [75] can be employed. The FS-model explains the increase in resistivity from the bulk resistivity value ρ_{bulk} for thin films by introducing a parameter p taking value from 0 to 1 with 0 and 1 implying complete diffuse and specular electron reflection from the film boundaries respectively. The MS-model considers the grain reflection coefficient R, again taking values between 0 and 1, to model the electron reflection that occurs at the boundaries between grains [75].

The FS-model is appropriate for thicker films but starts to underestimate the resistivity for smaller thicknesses, with 30 nm for Ni being the typical deviation point between the empirical data and the FS-model [3]. For UTMFs, the effect of both models on ρ_{bulk} can be summated according to Mattheiessen's rule as higher order interactions between the two only come into play at temperatures far lower than the operational temperatures [3]. Therefore, for a resultant resistivity ρ we have:

$$\rho = \rho_{bulk} + \Delta\rho_{FS} + \Delta\rho_{MS} \tag{2.16}$$

$$\text{where} \quad \Delta\rho_{FS} = \rho_{FS} - \rho_{bulk} \quad \text{and} \quad \Delta\rho_{MS} = \rho_{MS} - \rho_{bulk}$$

where ρ_{FS} and ρ_{MS} are the resistivities found by applying the FS and MS models respectively, which are given by [75]:

$$\rho_{FS} = \rho_{bulk}\left[1 - \left(\frac{3}{2K}\right)(1-p)\int_1^{\inf}\left(\frac{1}{t^3} - \frac{1}{t^5}\right)\frac{1-e^{-Kt}}{1-pe^{-Kt}}dt\right]^{-1} \tag{2.17}$$

$$\rho_{MS} = \rho_{bulk}\left[1 - \frac{3\alpha}{2} + 3\alpha^2 - 3\alpha^3 ln\left(1 + \frac{1}{\alpha}\right)\right]^{-1} \tag{2.18}$$

where $K = t_f/l$, where l is the electron mean free path and t_f is the film thickness, and $\alpha = (l/g)(R/(1-R))$, where g is the grain-size.

A further complication arises from voids which typically form a non-negligible fraction of the volume of UTMFs. This means that the value of ρ_{bulk} found from data-sheets cannot be used. The Bruggeman model can be used to obtain a corrected value for ρ_{bulk} [90]. This model assumes that inclusions, in this case voids, exist within a uniform matrix, in this case the metal, and that these inclusions do not interact. The behaviour of the model depends on two parameters: λ, the ratio of the conductivity of the inclusions with the conductivity of the matrix, and ϕ, the fraction by volume of inclusions, which takes a value between 0 and 1. For UTMFs, where λ approaches 0, we have an expression for the corrected bulk resistivity, ρ'_{bulk} given by [90]:

$$\rho'_{bulk} = \frac{\rho_{bulk}}{1-\phi^{3/2}} \tag{2.19}$$

This change in the bulk resistivity creates a corresponding change in the electron mean free path l since the two are related by [75]:

$$\rho'_{bulk} l' = \frac{12\pi^3\hbar}{e^2 S_f} \tag{2.20}$$

where S_f is the free area of the Fermi surface, e is the charge of an electron and $\hbar$ is the reduced Planck constant. S_f is introduced by a simplification, for polycrystalline films, of the general expression for the conductivity tensor [11], which involves an integral over the Fermi surface. The Fermi surface is known to change as the composition of the film changes [118]. We can therefore expect S_f to change too.

As for bulk materials, determining the optical properties of UTMFs requires a description of the dielectric constant as a function of the frequency of the impinging radiation. Accounting for voids requires the application of the Maxwell-Garnett formula [22]:

$$\frac{\varepsilon(\omega)-\varepsilon_i(\omega)}{\varepsilon(\omega)+2\varepsilon_i(\omega)} = (1-x)\frac{\varepsilon_m(\omega)-\varepsilon_i(\omega)}{\varepsilon_m(\omega)+2\varepsilon_i(\omega)} \tag{2.21}$$

This describes the effective complex dielectric constant $\varepsilon(\omega)$ of a mixed medium with metallic spherical particles having complex dielectric constant $\varepsilon_m(\omega)$ in another insulating medium having complex dielectric constant $\varepsilon_i(\omega)$. x gives the volume fraction of insulator. Furthermore, a shape factor L_m is introduced to account for the possibility of non-spherical particles:

$$\frac{\varepsilon(\omega)-\varepsilon_i(\omega)}{L_m\varepsilon(\omega)+(1-L_m)\varepsilon_i(\omega)} = (1-x)\frac{\varepsilon_m(\omega)-\varepsilon_i(\omega)}{L_m\varepsilon_m(\omega)+(1-L_m)\varepsilon_i(\omega)} \tag{2.22}$$

L_m takes a minimum value of 0 for flat discs in the plane of the thin film, a maximum value of 1 for flat discs perpendicular to the plane of the film and $1/3$ for spherical particles. Values in between represent oblate spheroids with circular cross-section parallel ($0 < L_m < 1/3$) and perpendicular ($1/3 < L_m < 1$) to the film. Considering the large proportion of metal which we expect in our films, if they are to be conductive, the model has to be modified to represent insulating particles within a metallic medium. This results in $\varepsilon_i(\omega)$ and $\varepsilon_m(\omega)$ to switch positions, $(1-x)$ to become x and L_m to become L_i, the shape factor for the insulating inclusions. A significant simplification occurs for wavelengths larger than the near-infrared ($\lambda > 1\mu$m) since in this wavelength range $|\varepsilon_m(\omega)| \gg |\varepsilon_i(\omega)|$ so that the expression used reduces to [22]:

$$\varepsilon(\omega) = \varepsilon_m(\omega)\left(\frac{(1-x)(1-L_i)}{1-L_i(1-x)}\right) \tag{2.23}$$

Note that this expression is not dependant on $\varepsilon_i(\omega)$.

The values of $\varepsilon_m(\omega)$ used in the above equation cannot however be those for the bulk material due to the granular structure of the films. $\varepsilon_m(\omega)$ can be decomposed, as outlined earlier, into a free carrier component and an inter-band component. The inter-band component is assumed to remain constant. The free carrier component is given in Equation2.9. The plasma frequency ω_p is kept unchanged from the bulk value, while the relaxation time τ is known to decrease for highly granular films [22].

The logical progression from UTMFs is the use of 2-D materials where the thickness is minimised to the mono-atomic scale [41]. This results in a very low absorption, which for mono-layer CVD graphene in the visible spectrum is about 2.3%. The mobility of CVD graphene is very high, approximately $2.3\times10^5\text{cm}^2/\text{Vs}$ for suspended films. Note however that the properties of 2-D materials are highly susceptible to any other materials in contact. Accounting for these effects is pivotal in determining the suitability of a 2-D material for a

specific application. Good electrical conduction is ensured if the material has a high quality crystalline structure due to an increased carrier mobility [9]. Achieving high quality 2-D materials is difficult and expensive at the large-scale due to the delicate nature of the material [16]. Maintaining integrity through every processing step is a challenge.

In conclusion, investigating UTMFs and 2-D materials allows us to move forward given the equipment restrictions we have to developing recipes for high quality semiconductor deposition and doping. Note further that sub-wavelength structured layers are promptly excluded due to their degrading effect on the spatial coherency of any impinging light.

2.1.3 Anti-reflection techniques

Minimisation of absorption must go hand-in-hand with minimisation of reflection for maximum transmission to be attained. This holds true not only for electrodes but for all other layers in the LC SLM which interface with each other or with the surrounding air.

A theoretically straightforward approach is to make the transition between a material with refractive index n_1 and another with refractive index $n_2 = n_1 + \Delta n\,(\Delta n > 0)$ gradual. For dielectric films with such properties and a normal light incidence the reflectance R is given by [10]:

$$R = |\frac{\Delta n}{2n_1 + \Delta n}|^2 \tag{2.24}$$

Substituting this single interface for N ones such that the refractive index varies as $n_1\,,\, n_1 + (\Delta n/N)\,,\, n_1 + (2\Delta n/N) \ldots n_1 + ((N-1)\Delta n/N)\,,\, n_1 + \Delta n$ in the $N+1$ layers gives a total R, ignoring internal reflections, of:

$$R = \sum_{k=1}^{N} |\frac{\Delta n}{2Nn_1 + \Delta n + 2(k-1)\Delta n}|^2 \tag{2.25}$$

Note that since internal reflections back to the transmission direction would reduce the total reflectance this is always an overestimation. Without the last term in the denominator the summation would always yield Equation2.24 for any value of N. Since the denominator is strictly greater than one the last term implies division by a greater number than if it were not present, thus always yielding a smaller amount to the total R value. An analogous approach can be applied for transmission from a high refractive index to a lower refractive index material by setting $n_1 = n_2 + \Delta n\,(\Delta n > 0)$. For a continuous shift in the refractive index, such that $N = \infty$, every term in the summation is equal to zero and therefore $R = 0$.

Realising a continuous gradient is challenging for devices which are assembled and not grown in-situ, even though the use of glues and coatings with appropriate optical properties

can approximate this. It is also possible to approximate a continuous refractive index gradient by using a "moth-eye" structure [21]. This is typically composed of corrugations in one or two dimensions of period l and height d. The performance of such structures depends on the dimensions l and d with respect to the incident wavelength λ. To prevent diffraction effects l should be smaller than λ. If the height $d \ll \lambda$ there is no effect since the corrugations are negligibly small. For $d \gg \lambda$ R does indeed fall to 0 but such structures are difficult to create and highly fragile due to their aspect ratio. The decrease in R is not monotonic, and a minimum exists for $(d/\lambda) \approx 0.4$.

Realising such structures can be challenging depending on the desired dimensions. Additionally, while useful for a material-air interface, they are difficult to incorporate within a device. A homogeneous anti-reflection layer is both easier to produce and implement within a larger assembly. It is however prohibitive to have a large number of intermediate layers. However, by restricting design frequencies, it is possible to obtain good anti-reflection coatings with few, or even one, intermediate layers.

Expanding on Equation2.25 for one intermediate layer, and accounting for internal reflections and optical path lengths within the intermediate layer, the reflectance R is given by [10]:

$$R = \frac{r_{12}^2 + r_{23}^2 + r_{12}r_{23}\cos(2\beta)}{1 + r_{12}^2 r_{23}^2 + r_{12}r_{23}\cos(2\beta)} \tag{2.26}$$

where:

$$r_{12} = \frac{n_1 - n_2}{n_1 + n_2} \quad \text{and} \quad \beta = \frac{2\pi}{\lambda_0} n_2 h$$

where r_{23} is analogous to r_{12}, n_1, n_2 and n_3 are the refractive indices of the first, intermediate and second layer respectively, λ_0 is the vacuum wavelength of the incident radiation and h is the intermediate layer thickness. Note that $n_2 h = H$ is the optical path length. Differentiating with respect to H allows localisation of extrema at particular values of both n_2 and h. Ignoring the results for which the intermediate layer has no bearing on R, extrema occur for $H = ((2k-1)\lambda_0)/4$ for $k \varepsilon \mathbb{N}$ where the reflectance is given by:

$$R = \left(\frac{n_1 n_3 - n_2^2}{n_1 n_3 + n_2^2}\right)^2 \tag{2.27}$$

This value of R is a minimum if n_2 is between n_1 and n_3. $R = 0$ is obtained for $n_2 = \sqrt{n_1 n_3}$, but finding a material having this exact optical property is often challenging. Note that for off-normal incidence the process must be modified accordingly, most importantly for the extremum condition and the corresponding expression for R. However, in a neighbourhood

around the normal the anti-reflection coating performs well and in the worst case scenario it has no bearing at all on the reflection. Obtaining an anti-reflection coating for a wider range of frequencies and/or incidence angles requires the use of multiple layers [108]. Such a system is often difficult to optimise analytically and therefore convenient material stacks are chosen with their thickness being the optimising variable. Stacks with alternating high and low refractive index materials are typical.

2.2 Deposition, characterisation and patterning of electrodes

Well established techniques exist for the deposition and characterisation of thin film layers. Once deposited, standard techniques for lithography are also available. These deposition, characterisation and patterning techniques are outlined in this section. Note that in some cases a technique is described for completeness but was actually not available for use in this work.

2.2.1 Deposition techniques

Liquid crystal spatial light modulators start off as two separate substrates. These must be coated with an electrically conductive layer having optical properties depending on the type of cell to be constructed. Note that the substrates need to be thoroughly cleaned to remove dust, lint, bacteria and any residue before any deposition process can be commenced [74].

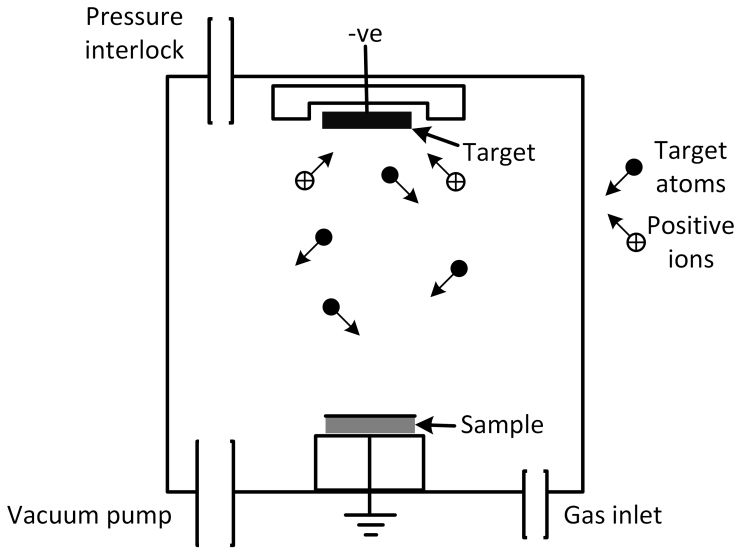

Fig. 2.4 Schematic of a typical sputtering deposition system, where positive ions, typically argon, dislodge target atoms which deposit on the substrate.

The two primary techniques for coating substrates with nanometre and micron scale films are sputter deposition and chemical vapour deposition. Sputter deposition involves the ion-bombardment of a very pure target of the material to be deposited. This dislodges atoms from the target, which deposit themselves on the substrate to be coated, as seen in Figure2.4. Deposition rate and uniformity is based on a large number of factors. In terms of set-up, it is vital to have a target larger than the substrate to ensure uniformity. Purity of the target is paramount. The energy of the bombarding ions, usually argon ions, is tailored so as to dislodge target atoms but prevent embedding of the argon ion. The angle of incidence of these ions is also set to maximise performance. High pressure is required to maximise the deposition rate but this is limited by the fact that dislodged atoms must have a mean free path which at least matches the distance between target and substrate. Magnetron sputtering locks electrons around the target, ionising more argon atoms and thus speeding up the coating process without increasing the pressure [105].

These parameters influence dramatically the optical and electrical properties of the deposited films [48]. The grain-size in deposited aluminium films influences the optical properties, with the optimal grain size varying depending on the operational wavelength [98]. Doped semiconducting oxides are deposited either using a ceramic oxide target or via reactive sputtering. The process is identical but the chamber is filled with a reactive gas, O_2 to create oxides, which interacts with the sputtered atoms before deposition. Doping of the deposited layer can also occur via co-sputtering where two separate targets are used [105][5].

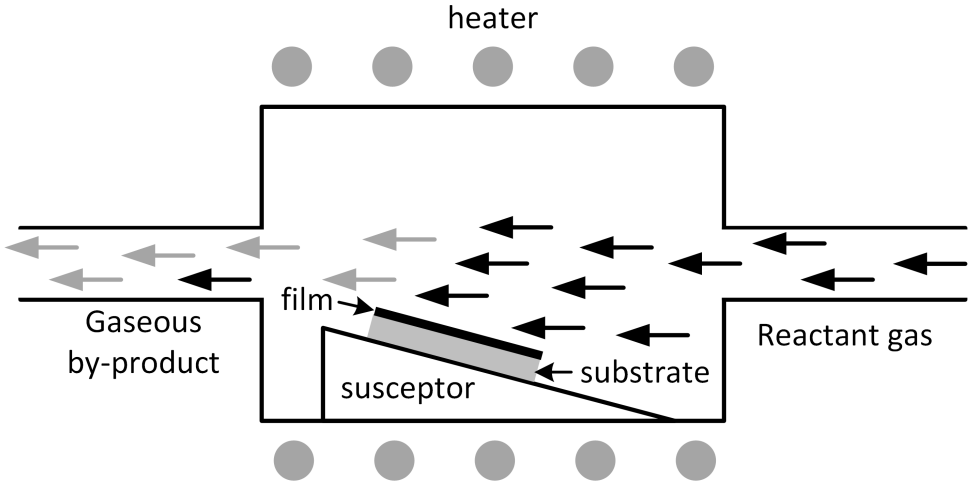

Fig. 2.5 Schematic of a typical chemical vapour deposition system, where a gaseous precursor reacts at the substrate, depositing the required compound. The gaseous by-product is pumped out of the system for neutralisation [19].

Chemical vapour deposition (CVD) operates by depositing solid material from a gaseous precursor onto a heated substrate as it flows through the system. The deposition leaves a gaseous by-product which is often hazardous, and is therefore pumped away for neutralisation. The neutralisation process might be simply absorption of the gas, or its combustion. Recycling is also possible in some cases [19]. A diagram of such a system can be seen in Figure2.5. Deposition rate and uniformity depends on the reactivity of the reactant gas, but also on the flow dynamics within the deposition chamber. The type of deposition also hinges on these properties, especially for deposition of crystalline materials on crystalline substrates [93]. The two main types of reaction chambers are hot-wall and cold-wall. In hot-wall chambers everything is heated so that temperature can be easily controlled, thus ensuring that the uniformity of the deposited layer is maintained. In a cold-wall chamber attaining very good uniformity is a challenge. The drawback of a hot-wall chamber is that all the chamber gets coated and as such cleaning is a big concern due to the hazardous nature of the substances involved [19].

A comparison between sputtering deposition and CVD hinges on the particular job requirements. The material to be deposited, the properties of the substrate, the thickness and uniformity needed and the budget available are all factors which must be weighed carefully. Generally speaking, cost is dependant on the material to be deposited. Sputtering requires a high purity target which might make the process prohibitive for expensive materials. On the other hand, creating an ad-hoc precursor gas to deposit an unusual material via CVD might be financially prohibitive and time consuming. In all cases apart from cold-wall, CVD material will be wasted. The quality of the coating is more dependant on the specific machine, techniques and parameters used. CVD is however more suited to coating non-planar substrates evenly and effectively [19]. In terms of safety, sputtering deposition is certainly safer as it creates no hazardous waste which has to be dealt with, nor does it operate at the high temperatures, up to 900°C, required for CVD [93].

2.2.2 Material characterisation by four-point probing, FTIR, spectroscopic ellipsometry and AFM

The characteristics of deposited films depend on a variety of deposition factors, understanding these relationships requires accurate characterisation data. Testing of potential transparent conductors for our application must include the collection of electrical and optical information. This can be attained by four-point probing, which yields sheet resistance($R_{\square}$) data, and fourier transform infrared (FTIR) spectroscopy, which yields transmittance(%) data, respectively. However, as discussed in Section2.1, understanding why different materials have different

electrical and optical properties requires knowledge of the film structure and granularity. Spectroscopic ellipsometry can be used to identify the structure of multi-layered media, even if they contain inclusions and voids, while atomic force microscopy (AFM) helps with the identification of granular or crystalline structures in thin films and surfaces. AFM can also be used to describe the topography of patterned films.

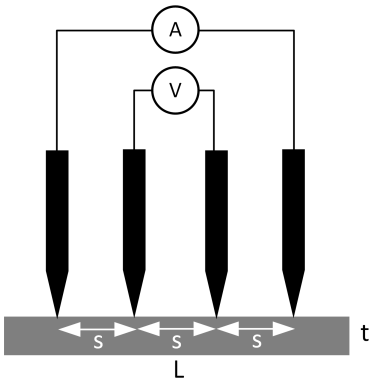

Fig. 2.6 Schematic of a typical four-point probe setup.

A four-point probe is required to isolate the sheet resistance of a thin film from the contact resistance present due to the probes themselves [81]. A typical setup has four in-line probes, with the inner pair detecting voltage and the outer pair detecting current, as seen in Figure2.6. For an infinite, homogeneous isotropic film of negligible thickness $R_{\square}$ is obtained by removing a geometric term purely dependent on the probe spacing. The ratio between sample size and probe spacing and that between sample thickness and probe spacing determines the deviation from the ideal for samples having finite dimensions and non-negligible thickness respectively. The probe spacing of the equipment used was approximately 1 mm and as such for our nanometre-scale thin films a two dimensional system can be assumed. An overestimation of no more than 7% in the $R_{\square}$ values recorded can be expected for our centimetre-scale samples in relation to the probe spacing. A generalised description also accounts for anisotropy, inhomogeneities and probe tips of finite diameter. Anisotropy requires a tensor treatment but for our thin sputtered films we do not expect this to be relevant. While it is true that sputtering is typically non-uniform between the centre of the sputtering area and the edges, by centring the samples this effect is minimised. Inhomogeneities are only critical at the probe spacing scale, while much smaller features, such as those we expect in our granular films, are averaged out. A rough estimation of the error introduced due to contact size is given by the square of the ratio between contact diameter and sample size, which we expect to be negligible for our setup.

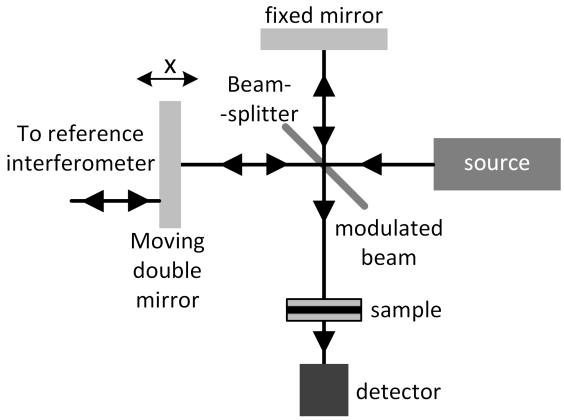

Fig. 2.7 Typical Michelson interferometer-based FTIR system.

FTIR is a non-destructive way of establishing the transmissive properties of a material [115]. IR is absorbed by materials not only due to the rotational and vibrational modes of their molecules, but also from overtones of a particular mode or combinations of multiple modes, thus FTIR is often used for the identification of molecules. A basic FTIR setup is based on the Michelson interferometer, as seen in Figure2.7. Spatially coherent light is split using a beamsplitter and re-combined after one of the beams has been subjected to a variable path length by using a moving mirror. The two beams interact destructively or constructively depending on the path difference. This combined beam passes through the test sample and is recorded as an interferogram. The interferogram is a function of path difference and is intuitively a cosine function for a single frequency source and some superposition of cosine curves for the typical broadband IR sources used in FTIR systems, such as globar light sources. The spectrum of these interferograms, as obtained by Fourier transform, is therefore the intensity of the light as a function of frequency. This is a single datum for monochromatic light but a full spectrum for typical sources. The ratio of the spectrum obtained from the interferogram transmitted through the test sample to a reference interferogram spectrum yields the fractional transmittance of the test sample.

Alignment of samples in the FTIR system is pivotal since extracting the absorption coefficient requires accurate determination of the thickness of the material exposed. Furthermore, using too thick samples will result in non-detectable levels of light being transmitted, particularly for strong absorption peaks, which makes accurate determination of absorption coefficients impossible. On the other hand, samples which are too thin will result in non-detectable weak absorptions, making identification more difficult. For a test material enclosed by two substrates, much like the transmitting liquid crystal cells tested, internal reflections create destructive and constructive fringes for different frequencies, depending on the path difference. Eliminating this factor from the data is challenging, particularly since the

refractive index is frequency dependent for both the substrate material and the liquid crystal. The absorption peaks which we expect in the mid-IR are for O-H, C-H and N-H stretching (4000-2500 cm^{-1}), but also X-H stretching for heavier atoms and the triple bonds C≡C and C≡N (2500-2000 cm^{-1}).

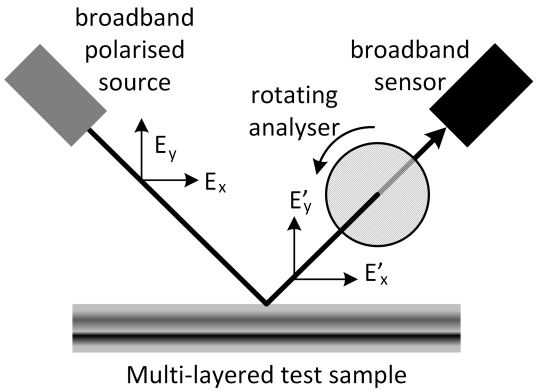

Fig. 2.8 Typical automated ellipsometry setup with rotating analyser. Manual ellipsometers are monochromatic and require adjustment of the incidence angle to extract sample information.

Spectroscopic ellipsometry is a non-invasive, non-destructive way of determining the structure of layered media by analysing the properties of polarised light reflected off of the test sample [36]. A typical system is shown schematically in Figure2.8. Polarised light, which can be decomposed into a parallel and perpendicular component to the plane of incidence, impinges on the sample. The reflected light goes through an analyser which rotates at a specific frequency, this creates a time dependent intensity function. Fourier transform is used to obtain the spectrum. Fresnel's equations are then used to extract the frequency dependent refractive index and extinction coefficient of the test sample, or, if the material is known, to extract the layer thickness. Note that the test layer can be composed of a mixture, or even a gradient, of materials. In fact, granular films and film surface roughness are aptly represented by material/void layers. The Bruggeman model is typically used for such layers. For multi-layered media the equations are a more complex generalised version of those given in Section2.1. A model is typically defined based on the expected composition of the multi-layered film, the software can then fit values of thickness and fractional composition of layers to best approximate the empirical data collected.

Atomic force microscopy enables mapping of the topography of a surface. This is achieved by scanning a nanometre scale tip at the end of a cantilever over the test surface and recording changes to the tip elevation as the cantilever is bent [138]. A typical system can be seen in Figure2.9. This bending is detected as a piezo-electric effect or as a deviation of a

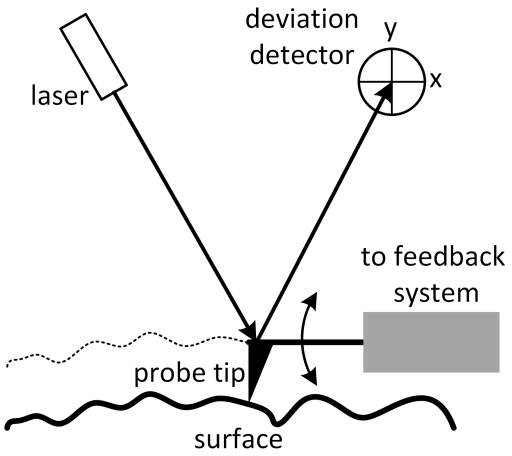

Fig. 2.9 Typical topographic contact scanning AFM setup. Extracting more information regarding the test sample requires further elements in the system.

laser beam which is reflected off of the top of the probe tip. This information is then used to adjust the tip elevation back to a given setpoint. This setpoint can be the force of contact or the amplitude or frequency of the bending cantilever, depending on the scanning method chosen. A contact scanning method, where the tip touches the sample continuously, gives accurate results but has heavy wear and tear on the probe tip. A tapping method is therefore typically used to minimise this effect. The interplay between tip quality, actuation accuracy and feedback system determines the quality of the AFM system. Note that by using different tip materials and configurations it is possible to use the basic AFM principles to detect a large array of properties of the surface studied. These include piezoelectricity, conductivity and nano-spectroscopy.

Interpreting data collected by AFM involves the use of dedicated image processing software which allows corrections to be made to the data and also statistical information collection [55]. Depending on the feature scale to be investigated, low spatial frequency terms, such as tilting of the whole sample and undulations of the substrate are typically removable. Roughness can also be smoothed out. Artefacts, both real, due to occasional inhomogeneities of the test sample, and virtual, due to the data collection process are also typically removed or discounted for statistical information collection. Information can be collected for whole, or part, of the area. Specific to our aim is the use of processing to highlight and analyse the grains in the sample thin films. To achieve this the watershed method is used, as seen in Figure2.10 for a nickel thin film. First the dataset is flipped, such that grains are now local depressions. "Rain" is then simulated using user-defined parameters, such as droplet separation, droplet volume and rain repetition. The droplets pool according

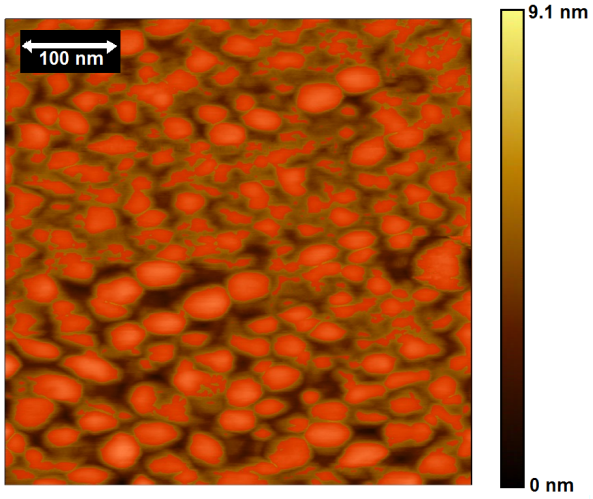

Fig. 2.10 0.5μm $\times$ 0.5μm AFM topographic image of an ultra thin nickel film with grain data obtained via the watershed method and highlighted in red.

to the maximal gradient they are subjected to. Once the grains are defined statistical data on the granularity can be collected.

2.2.3 Patterning techniques

While some deposited layers are required to remain whole, etching of a pattern within a deposited layer is required for many applications. For LC SLMs etching is required to create the pixel structure within the electrode material layer. For photolithography and e-beam lithography patterning starts off as a layer of photoresist spread on top of the layer to be etched. A photoresist material polymerises or degrades when illuminated. The photoresist is spin coated, as seen in Figure2.11. A dispenser supplies the viscous photoresist which is spread over the whole area with a thickness and uniformity dependant on the viscosity of the photoresist, rotational velocity of the spin-coater and the time-dependent volatility of the solvent used in the photoresist mixture [80]. A soft bake sets the photoresist in preparation for subsequent processes.

For optical exposure, whether by UV radiation, deep UV radiation from excimer lasers or X-rays the set-up is similar, seen in Figure2.12. A sufficiently intense source of radiation, something challenging in its own right if X-rays are used, irradiates the photoresist. A mask is inserted between the two to set the pattern which must be exposed. Such masks are typically manufactured out of chrome on fused silica for UV exposure systems, but the materials differ for larger frequencies. In an e-beam system exposure is conducted directly via the beam and as such no mask is required [60].

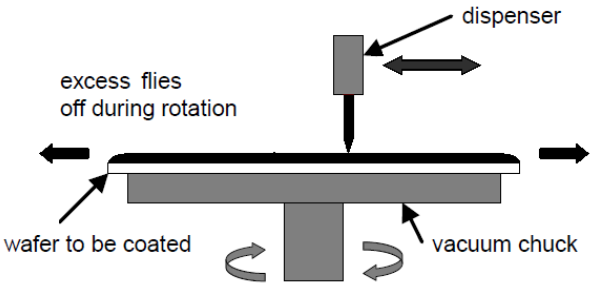

Fig. 2.11 Set-up for spin-coating of photoresist. The same technique is used to dispense alignment material.

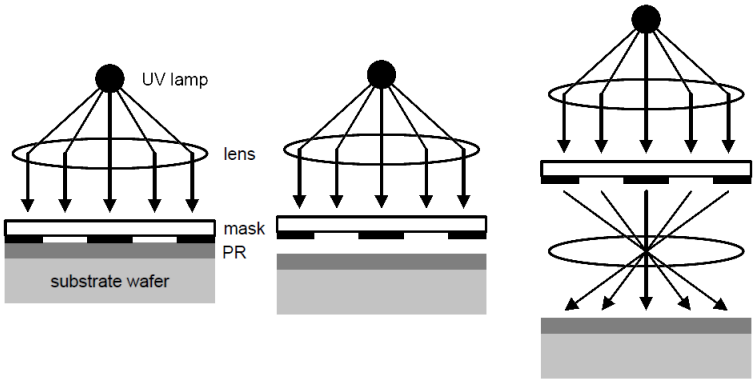

Fig. 2.12 Schematic of different mask aligner types: Contact, proximity and projection aligner respectively [131].

The difference between these techniques lies in the resolution of the transferred pattern to the photoresist when compared to that of the mask. Shorter wavelength systems are more challenging to produce but yield better results [60]. External techniques to improve the resolution are seen in Figure2.12. Proximity systems are the most commonly used. Contact systems offer greater results but the mask undergoes much more wear and tear due to contact with the photoresist [131]. Projection exposure systems use an optical system to diminish the mask pattern down to the desired dimensions, this enables the use of a larger more accurate mask. Unfortunately this introduces errors due to possible aberrations in the optics [99]. Projection lithography allows for novel ways to improve performance, such as water-immersion lithography and contrast-enhancing illumination patterns. Note that even though optical diffraction effects are not present for e-beam systems, aberrations in the electron-beam deflection system and proximity effects due to electron backscattering, as seen in Figure2.13, still degrade the result. When designing a pattern, optical proximity correction elements can be introduced so as to minimise errors[131]. An example is adding small squares, the size of which depends on the resolution of the system and the interaction between illumination and resist, to vertices of angle $\leq 90^\circ$ in the pattern, as seen in Figure2.13. The best results are obtained by e-beam systems, which can achieve sub-micron feature sizes. The drawback is the cost and time necessary to expose equivalent areas when compared to optical systems. As it stands, e-beam can only used effectively for small research applications.

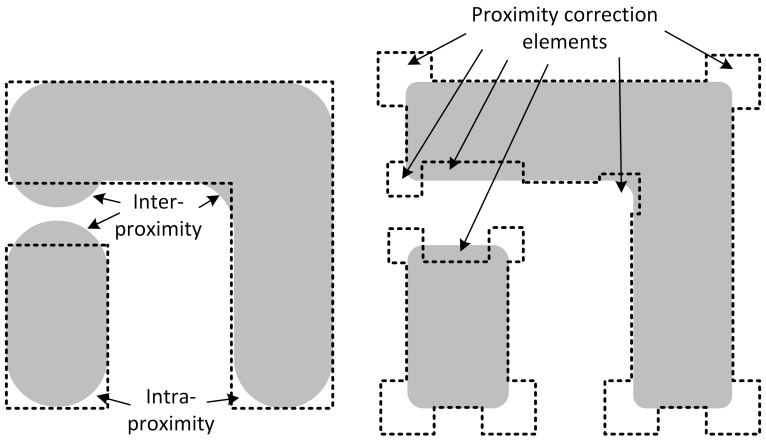

Fig. 2.13 Example of inter-proximity, occurring when exposed features are too close causing overexposure, and intra-proximity, occurring when there is underexposure [60]. Proximity correction elements improve the result.

Whether the exposed pattern is retained or removed after exposure depends on the type of resist used. For a negative photoresist exposure polymerises the material, making it resistant to the development process. For a positive resist we have the opposite effect, where exposure

decomposes the photoresist so that it is removed when the pattern is developed. Note that for a given mask these two processes will result in developed layers which are the inverse of each other. At this stage a further bake is conducted to clear off any developer residue and to further harden the photoresist layer in preparation for etching.

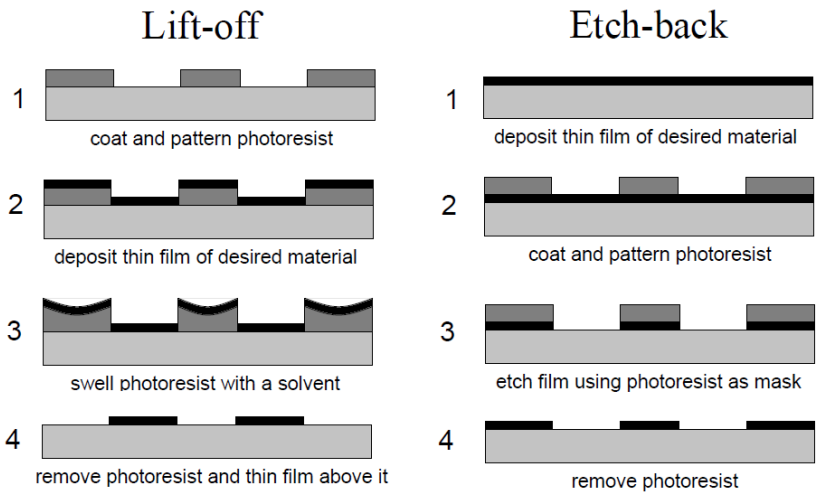

Fig. 2.14 Step-by-step guide and comparison between lift-off and etch-back film patterning [110].

Before delving further into the etching process, note that another technique called lift-off can also be used to attain a patterned film. The two can be seen in Figure2.14. Lift-off involves laying, exposing and developing the photoresist before the material to be patterned is deposited. After the deposition process the resist is removed along with the material deposited on top of it. Note that the two processes result in inverse patterns. Depending on the material and thickness to be patterned lift-off might be more appropriate. It is of interest that in lift-off, there can be no residue of the patterned material in the spaces as it never touches the substrate. Conversely, there can never be photoresist residue when etching as it never touches the substrate [110]. Note however that in lift-off the deposited material might be effected by photoresist residue between itself and the substrate, as such it is important to thoroughly clean these areas without damaging the photoresist pattern.

Fig. 2.15 Comparison between isotropic, anisotropic and directional etching respectively [31].

Etching is further divided into wet and dry etching. In both cases the quality of the etch is described by two parameters; the selectivity of the etching process between photoresist, coating and substrate and the isotropy, or lack thereof, of the etch. The former is described by two ratios comparing the etching rate of the material to be etched with the etching rate of the photoresist and the substrate respectively. For high values of these ratios the quality of the etch is better [31]. The latter is described as the ratio between the horizontal and vertical etching rate of the coating. The possible cases are seen in Figure2.15. Isotropic etching, which is characteristic of most wet etching techniques results in undercutting, or etching of the material below the photoresist. If undercutting is not properly accounted for the pattern will be ruined, especially if it contains small features. However, undercutting is useful if free standing structures like cantilevers are required. In come cases, such as for silicon wet etched with KOH, anisotropic etching rates occur since the rate varies depending on the crystal plane being etched.

Wet etching is a cheaper alternative to dry etching as it most commonly involves simple immersion in a bath of corrosive liquid to etch the exposed layer. By comparison, reactive-ion etching involves the creation of a plasma from an introduced gas which results in chemically reactive ions. These ions attack the layer both chemically, resulting in a gaseous by-product, and physically, resulting in knocked off atoms. Note that the chemical etching has good selectivity but is not perfectly directional while physical ionic bombardment has greater directionality but lower selectivity. The process results in a gaseous by-product which is vacuum pumped away. Wet etching is therefore easy to implement cheaply and on a large scale. However, for high-quality etching dry etch techniques are necessary, particularly for sub-micron features which would be ruined by the isotropy of a wet-etch [31].

Laser ablation can achieve micron scale etching enabled by highly directional laser illumination with controllable beamsize and pulse length [84]. At the micron scale the energy delivery needs to be accurately controlled so as to prevent damaging the surrounding material, something that can be disregarded at larger scales. Beam intensity, wavelength and pulse repetition need to be tailored depending on the material to be etched, since different physical mechanisms are involved for different materials, from metals to polymers.

Molding and stamp printing can be used to cheaply and effectively reproduce a master [34]. The mold or stamp must however itself be made using another lithography technique and therefore the attainable resolutions are bound to those of other techniques. It is challenging to preserve the resolution of the mold or stamp in the product. For molding, the mold material, the material to be molded, and curing and release techniques need to be accurately designed to minimize mold damage and maximise product fidelity and desirable properties. For printing, the relationship between stamp, ink and substrate must be carefully designed to maximise the

ink coverage of the stamp, but also transferability of the ink to the substrate. In both cases wear and tear is inevitable. Inkjet printing is attractive for low resolution applications as it offers a fast customisable prototyping tool [121]. In all of the above cases the challenge is to create molding materials or inks which fulfil all the necessary properties for the required processing and yet are also both conductive and transparent.

2.3 Test sample choice, preparation and experimental set-up

As already outlined, heavily doped and degenerate semiconductors were excluded due to the poor repeatability of recipes in literature and the inability to work towards an *ad hoc* transparent conducting oxide for the mid-IR due to equipment limitations. UTMFs offer an alternative for which samples can be deposited straightforwardly.

The sputtering system used disallowed modification of the sputtering power and the substrate temperature. As such granularity could not be controlled for a given material. The characterisation techniques discussed in the previous section are therefore primarily employed in comparing the properties of UTMFs of different thicknesses and materials, and not for optimisation within a given material.

Copper was chosen due to its high conductivity. It is also a standard material for use with sputtering systems. Nickel is a less conductive alternative but is also less subject to oxidation. High Cu content Cu_xO are known to be transmissive in the visible spectrum [20]. Using thicker films is an attempt at mitigating the degrading effect of its lower mobility while reducing the influence of voids. The 2-D material CVD graphene was shown to have attractive electrical properties. It also has very weak absorption, due to free carriers, in the visible spectrum. Any absorption increase for larger wavelengths, particularly given its thinness, is an interesting avenue of investigation.

Cu, Ni and Cu_xO film samples were prepared in a DC magnetron sputtering system (Metallifier Sputter Coater, Precision Atomics, Cambridge, UK). The sputtering targets used were high purity (99.9% purity) 4 inch diameter by 3mm thick targets. Sputtering power was fixed at 100 W and the process pressure was set to 3.5×10^{-3} mbar. Graphene was grown by chemical vapour deposition (CVD) (Graphenea) on a copper foil at 1000°C. A PMMA layer was spin-coated onto the graphene surface as a sacrificial layer. Graphene was detached from the Cu foil by wet etching of the Cu foil using a solution of $FeCl_3$, and subsequent cleaning steps were done in de-ionized water. Next, the graphene layer with the PMMA was transferred onto the final substrate and dried on a hot plate to remove the excess of water.

Last, the PMMA layer was removed with acetone. Samples were deposited on soda lime glass (1.1 mm) for investigating sheet resistance and the effects of heating and ageing on the samples. Sapphire substrates (0.5 mm) were used for optical tests, due to its superior transmittance up to 5 μm, and etching tests.

An EVG620 Automated Mask Alignment System was used for photolithography in the patterning process. Due to the nm scale thicknesses involved a lift-off process with Microposit S1818 was used. Pre-baking and baking steps were conducted in an oven instead of a hotplate due to the thermally insulating nature of the substrates used. Baking time was slightly increased to account for heat loss in opening and closing of the oven. After the conducting material was sputtered upon the patterned photo-resist, lift-off was conducted using acetone in an ultrasonic bath.

Sheet resistance $R_{\square}$ was measured using a Jandel probe head in a 4-point in-line probe configuration. Transmittance data was collected for the wavelength range 1.6-6.5 μm using a Cary 600 Series FTIR spectrometer. Film thickness and composition was probed using both spectroscopic ellipsometry (Horiba Jobin Yvon UVISEL Spectroscopic Ellipsometer) and atomic force microscopy (AFM) (Agilent 5420 AFM/SPM).

For ageing, samples were stored in a sealed container at atmospheric pressure in a room-temperature, low-humidity environment and $R_{\square}$ values were collected at intervals. For baking, samples were heated on a hotplate at atmospheric pressure, in a room-temperature, low-humidity environment so that $R_{\square}$ data could be collected efficiently.

Single pixel LC cells were assembled using both Ni UTMF and graphene mono-layer on sapphire substrates. Ni UTMF samples were spin coated with nylon in formic acid (2:998) at 3000 rpm for 30 s. They were then baked at 200 °C for 120 min. All samples were rubbed using a rubbing machine for the LC alignment. These rubbed layers were glued in an anti-parallel configuration facing each other with 15 μm spacers in between to form the cell. The cell gap of the empty cell was measured to be 15 $\pm$ 0.7 μm across the device using spectral interference fringes. The cell was then filled with the nematic liquid crystal mixture BL037 at 110 °C using capillary effect followed by slowly cooling down to room temperature. The filling hole of the cell was sealed and wires were bonded using silver epoxy to form an electrical connection. Multiple working LC SLMs were fabricated to confirm the reproducibility of the process.

The LC SLMs' electro-optic response was observed between crossed polarisers at λ =2.3 μm using a Cr^{2+}:ZnS/Se Laser (IPG Photonics) as a laser light source. An InGaAs Detector (Thorlabs) was used for data collection.

2.4 Middle infrared transparent conductor development

2.4.1 Morphology of films investigated

Typical thickness and composition values for freshly deposited samples collected by reflective ellipsometry are given in Table 2.1. The empirical model used in the spectroscopic ellipsometer to obtain the above is formed by four layers for UTMFs in the order: air, oxide, metal/void, substrate. This agrees with literature for a copper or nickel granular film that is exposed to air since a layer of Cu_2O or NiO respectively forms at the air/metal interface [94, 63]. All layers are assumed to be homogeneous and isotropic, with a Bruggeman effective medium model [90] as seen in Equation2.19, used to explain the metal/void layer. For Ni and Cu UTMFs the data shows good fitting with the model. For Cu_xO TFs this model is not appropriate since we do not expect the oxide layer to be separate from the metal/void layer. In this case the Bruggeman effective medium model combined Cu, Cu_2O and voids even though a higher concentration of Cu_2O is still expected at the air/film interface. Due to the large oxidation in air the same treatment as Cu_xO TFs was used for 4 nm Cu films. As the Cu_xO films tested were deposited with a low oxygen to argon flow ratio of 3:28, this resulted in films that were a particulate composite of primarily metallic Cu with Cu_2O and voids, as seen in literature [45].

Table 2.1 Thickness and composition data obtained from measured reflective ellipsometry data. t_{est} is the estimated thickness from standard sputtering recipes, t_m is the thickness of the metal/void effective medium layer, $\%m$ is the percentage of metal in the metal/void effective medium layer, t_{ox} is the thickness of oxide at the air/film interface, t_{tot} is the total thickness if an effective medium model having metal/oxide/void is used, $\%ox$ is the percentage of oxide if an effective medium model having metal/oxide/void is used and χ^2 is a measure of the goodness of the fit.

	t_{est} (nm)	t_m (nm)	$\%m$	t_{ox} (nm)	χ^2
Ni UTMF	6	11.2±1.2	81.0±5.2	0.02±0.0	1.30
	3	6.0±1.5	58.7±5.2	0.1±0.1	0.80
Cu UTMF	9	13.8±2.2	78.9±5.3	0.7±0.2	0.16
	6	8.8±1.5	68.0±4.9	1.8±0.1	0.35
		t_{tot}(nm)		$\%ox$	
	4	3.20±0.7	12.7±4.5	70.5±5.4	3.46
Cu_xO TF	10	18.2±0.4	55.1±1.6	24.3±3.3	0.84
	5	11.0±1.2	45.5±1.6	1.2±14.5	0.08

The estimated sputter thickness, t_{est}, in Table 2.1 was obtained by assuming proportionality between sputtering time and film thickness so that standard lab recipes, which are designed for micron-scale films, could be used. From the model fit to the ellipsometry data for UTMFs t_m is the metal/void thickness, $\%_m$ is percentage of metal in the metal/void layer and t_{ox} is the oxide thickness. For Cu_xO thin films (TFs) t_{tot} is the total thickness while $\%_m$ and $\%_{ox}$ are the percentage of Cu and Cu_2O in the layer respectively.

Properties of nm-scale films depend highly on the granularity of the deposited material. Granularity is given by the size and shape of the grains that form the film. For a crystalline material a grain is a crystallite in a polycrystalline film. In general, a grain is a volume of the film which is separate from the rest by a boundary [75]. The size and shape of granules depends on the material deposited but also on the sputtering parameters, primarily oxygen partial pressure, if any, and sputtering power [45, 97]. Figure 2.16 shows the grains in 0.5 μm $\times$ 0.5 μm topographic AFM images for Ni UTMFs 3 nm and 6 nm, Cu UTMFs 6 nm and 9 nm and Cu_xO TFs 5 nm.

Table 2.2 Granularity data obtained from the AFM images in Figure 2.16 using the watershed method in Gwyddion software. t_{est} is the estimated thickness from standard sputtering recipes, h_{gr} is the mean grain height with respect to the surrounding local minimum, r_{gr-eq} is the equivalent grain radius for a circular grain of the same area and $r_{gr-insc}$ is the radius of the largest inscribed circle in the grain.

	t_{est}(nm)	h_{gr}(nm)	r_{gr-eq}(nm)	$r_{gr-insc}$(nm)
Ni UTMF	3	1.33±0.53	8.71±3.57	5.22±2.15
	6	0.48±0.38	6.89±4.94	3.13±1.65
Cu UTMF	6	0.42±0.13	5.00±1.94	2.69±0.99
	9	0.63±0.14	10.93±4.89	4.17±1.01
Cu_xO TF	5	1.10±0.52	5.44±2.23	2.79±1.11

Granule property data was obtained using the watershed method as previously described in Section2.2 and implemented in Gwyddion software [55]. Results are summarised in Table 2.2, where t_{est} is the estimated sputter thickness, h_{gr} is the mean grain height with respect to the surrounding local minimum, obtained by subtracting the grain base height from the grain peak height, r_{gr-eq} is the equivalent grain radius for a perfectly circular grain of the same area as the detected grain while $r_{gr-insc}$ is the radius of the largest circle which can be inscribed in the detected grain. Comparing the latter two parameters gives an estimate of the circularity of the grains, since an inscribed circle only has the same area as the equivalent circle if the grain is circular. Note also that h_{gr} is not a measure of the thickness of the film, but is effectively a 'roughness' measurement localised to each grain. It can be seen that Ni UTMFs tend to form

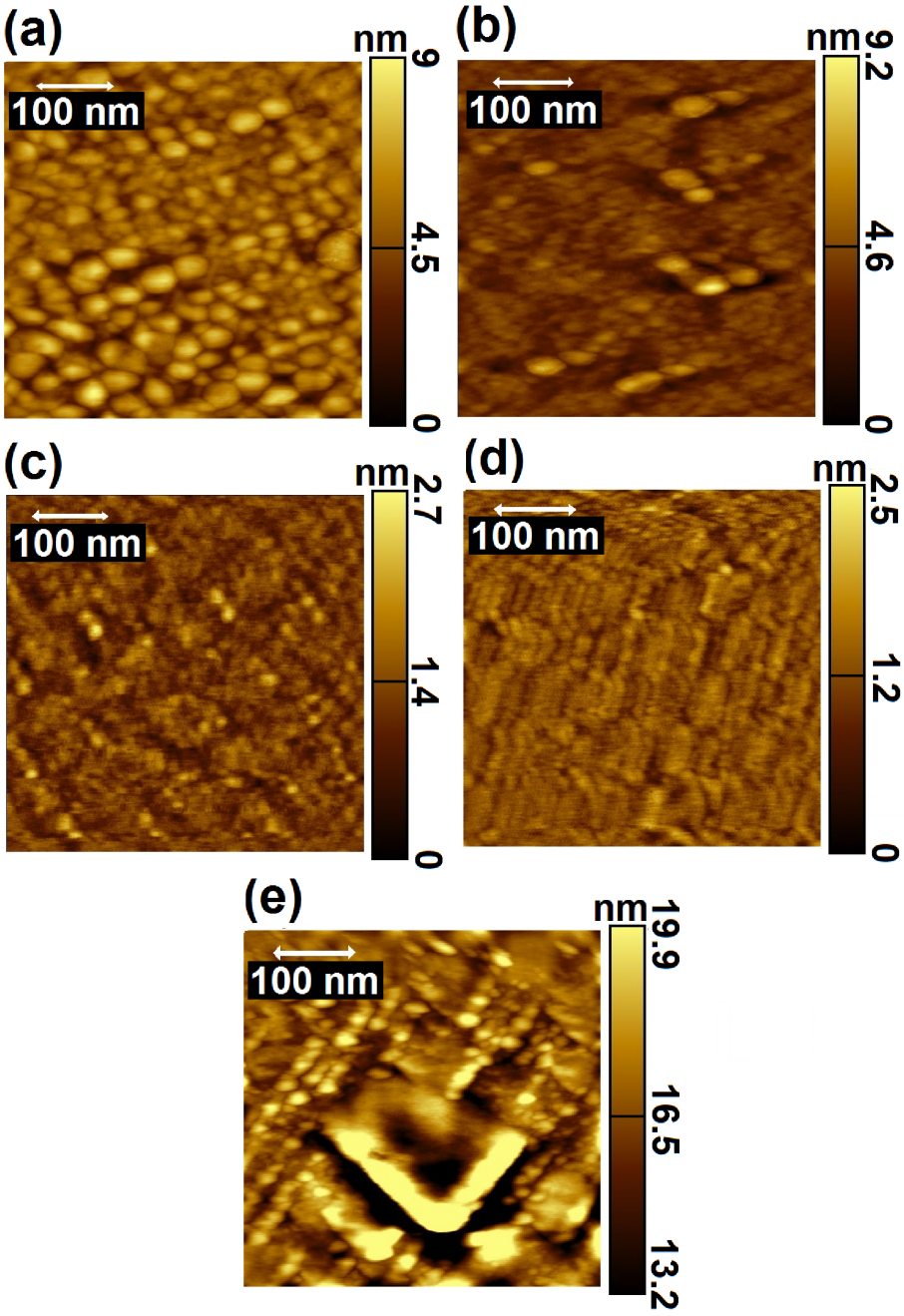

Fig. 2.16 0.5 μm $\times$ 0.5 μm topographic AFM images for deposited films: Ni UTMFs (a) 3 nm and (b) 6 nm, Cu UTMFs (c) 6 nm and (d) 9 nm and Cu_xO TFs (e) 5 nm.

the largest granules for a given thickness, but at 6 nm the topography is considerably more even since h_{gr} is less than half that of 3 nm films , with a few large granules still dominating. This suggests that the spaces between the granules are being filled up. For films deposited using the same deposition parameters grain-size is known to be linearly proportional to t_{est}^{β} for some factor β [12], and therefore the reduction in r_{gr-eq} and $r_{gr-insc}$ for increasing Ni UTMF thickness does not indicate that there is a reduction in grain-size. From Figure 2.16 particularly large granules do not appear for Cu and there is an increase in grain-size which obeys the proportionality we expect. It is important to note that for Cu_xO TFs the central 'V' shaped artefact that can be seen in Figure 2.16 has been excluded from the analysis.

To successfully model the electrical and optical properties of our samples it is necessary to estimate the thickness and grain-size of the thin films accurately. The estimated thickness values were obtained by dividing the sputtering time required to deposit known thicknesses, typically of a few μm. However our data shows that this proportionality does not hold. The model $t \propto t_{est}$, while appropriate for larger thicknesses, was changed to $t = A \times t_{est}^{\alpha}$, where A and α are proportionality constants, for our small thickness range [12]. Note that the oxide layer was not modelled as it has a negligible effect on the conductivity of the films due to its very high resistivity and its thickness does not have bearing on the transmissive properties at the wavelengths investigated due to the very low value of the extinction coefficient k [96, 82]. Due to the proportionality relationship between thickness and grainsize [12], the same model was used for grain-size with B and β as proportionality constants. For Ni UTMFs and CuxO TFs the lack of AFM data for multiple thickness values meant that the β constant was the same as that for the thickness model α. This is justified by the fact that AFM data for Cu yields very close values of α for thickness and β for grain-size. The void fraction ϕ, which comes into play for both the electrical and optical properties, was modelled using a model $\phi = Ce^{-\gamma\, t_{est}}$, where C and γ are proportionality constants, based on the ellipsometry data collected. These constants are given in Table 2.3. Note that in all cases the model parameters were extracted based on three data points. As such there is no additional information extracted by quantifying the error in the fitting technique or by displaying the fit graphically.

Table 2.3 Model constants for thickness, grain-size and void fraction. Thickness$= A \times t_{est}^{\alpha}$, grain-size$= B \times t_{est}^{\beta}$ and void-fraction$= Ce^{-\gamma\, t_{est}}$.

	Thickness		Grain-size		Void fraction	
	A	α	B	β	C	γ
Ni UTMF	2.15	0.92	3.81	0.92	0.90	0.26
Cu UTMF	1.26	1.09	0.78	1.08	4.07	0.39
Cu_xO TF	3.41	0.73	1.67	0.73	0.66	0.04

Raman spectroscopy was used to assess the quality of the CVD graphene used and the success of the transfer process. A Raman spectrum for a typical CVD graphene layer as transferred can be seen in Figure2.17. The small height of the D peak when compared to the G peak shows high purity. The characteristics of the 2D peak change according to the number of graphene layers invovled. The single Lorentzian peak as seen in Figure2.17 shows monolayer graphene that has transferred well without folds or discontinuities [89].

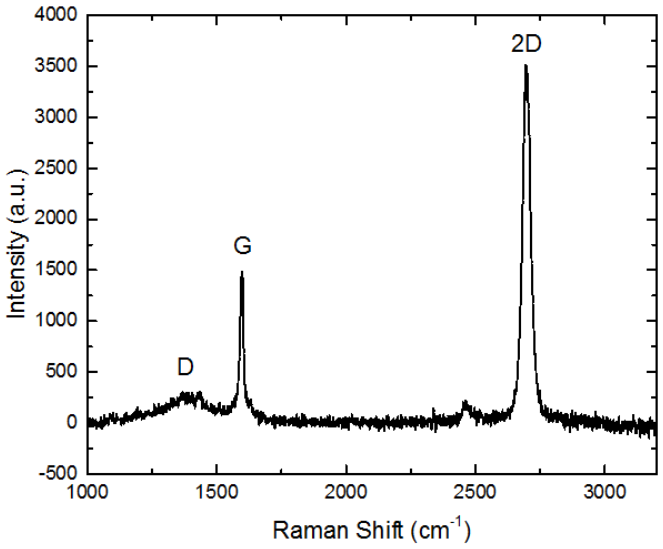

Fig. 2.17 Raman spectrum for typical as deposited CVD graphene layer used.

2.4.2 Electrical properties

Measured and modelled $R_{\square}$ data for Cu, Ni and Cu_xO samples are illustrated in Figure 2.18. Cu_xO TFs were found to have a sheet resistance up to 8 times larger than Ni and Cu UTMFs for equal thicknesses. It can also be observed that the sheet resistance for Cu UTMFs becomes larger than Ni UTMFs for thicknesses smaller than $\approx$10 nm, with the $R_{\square}$ value for Cu UTMFs becoming more than twice as large as that for Ni UTMFs around 5 nm. CVD mono-layer graphene was found to have a sheet resistance of $360\pm34\ \Omega/\square$ by taking readings from three different samples. This is comparable to Ni and Cu UTMFs between 7 nm and 9 nm thick. Note that for graphene, doping might occur during further processing stages, primarily due to the polyimide coating necessary for LC-SLM construction. This can potentially decrease the sheet resistance of the graphene layer considerably [8].

It is evident from literature that the R parameter increases dramatically for thicknesses less than 20nm for a range of metals [12]. It is also clear that the p parameter becomes progressively less important as thickness drops to this range [12] where it can be set to 0

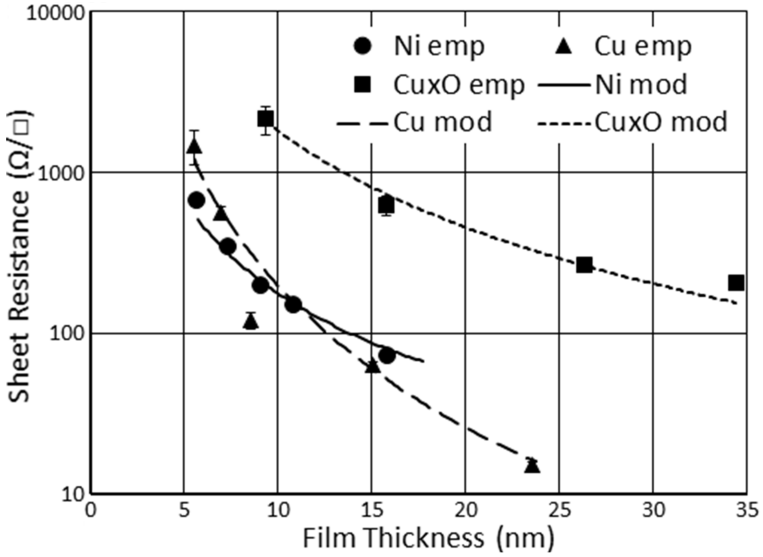

Fig. 2.18 Comparison of $R_{\square}$ empirical data along with model fit for Ni and Cu UTMFs and Cu_xO TFs against film thickness.

with confidence [75]. In this case, the R values fit to the data were $R = 0.981$ for Ni UTMFs, $R = 1 - 0.0105t_{est}$ for Cu UTMFs, giving $R = 0.97$ and $R = 0.84$ at t_{est} 4nm and 15nm respectively and $R = 0.99$ for all Cu_xO TFs.

Using the FS-MS model, as outlined in Equations2.17 and 2.18, the relationship between the ρ values for Ni and Cu UTMFs and Cu_xO TFs can be interpreted in terms of the interplay between grain-size g and corrected bulk resistivity ρ'_{bulk}. Note that the values of ρ_{bulk} taken for Ni and Cu were 69.9 Ωnm and 16.8 Ωnm respectively and those for the electron mean free path length l were 5.87 nm and 39.9 nm respectively [32]. Values of grain-size g and corrected bulk resistivity ρ'_{bulk} for our samples are shown in Figure 2.19. ρ'_{bulk} for Cu starts to increase dramatically as thickness decreases below 10 nm, while the grain-size for Ni is larger throughout. Over 10 nm and throughout Cu_xO has dramatically larger ρ'_{bulk} than Cu, as expected.

2.4.3 Optical properties

Figure 2.20 shows the transmittance(%) vs. $\lambda(\mu\text{m})$ for samples with selected values of t_{est}(nm). Samples tested are Ni and Cu UTMFs, Cu_xO TFs and CVD graphene mono-layer. In all cases the results include the effect of the sapphire substrate since this is integral when moving forward towards device design, and comparisons between the different materials can still be drawn with confidence as identical sapphire substrates were used for all tests. Graphene can be seen to have transmissive properties far better than any of the other samples,

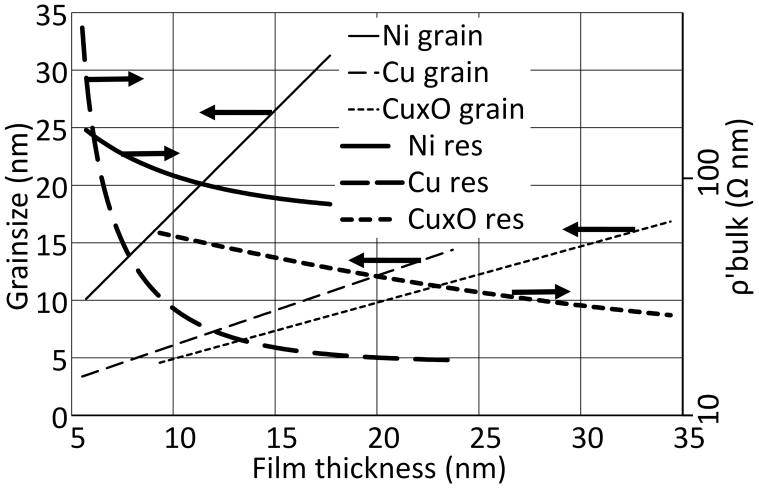

Fig. 2.19 Comparison of ρ'_{bulk} and grain-size for Ni and Cu UTMFs and Cu_xO TFs against film thickness. Arrows point to the vertical axis used for each plot.

with a transmittance better than 97% across the whole range investigated once substrate effects are subtracted. In all other cases the performance is seen to decrease with increasing wavelength, even when accounting for the effects of the sapphire substrate, which only drops in transmittance sharply after 5 μm. Cu UTMFs have the largest transmittance, particularly for smaller values of t_{est}. Ni UTMFs follow, differing by approximately 15% at small values of λ for small, comparable values of t_{est}. Cu_xO TFs are observed to have a transmittance comparable to Ni UTMFs for similar t_{est} values and small wavelengths, with the performance for Cu_xO TFs being poorer at larger wavelengths.

Table 2.4 collects the manually fit constants required by the model outlined in Equations2.23 and 2.9 to be able to obtain the results seen in Figure 2.20. Note that attaining this requires implementation of the modelled data into a stack which includes the sapphire and air layers, which results in multiple interfaces that have to be treated using Fresnel Equations, as outlined in Equation2.26.

Note furthermore that the role of the oxide layer on top of the metal/void partition layer cannot now be disregarded as in the case of the electrical model. Due to the highly granular structure of the film, the oxide/metal interface was disregarded, assuming that the transition from the oxide layer to the metal/void layer is gradual. Due to the grain structure it was also assumed that the oxide cover would not be complete nor uniform. As such a weighing factor w was introduced such that when $w = 0$ the reflection at the film/air interface is purely dependant on the metal/void layer and when $w = 1$ it depends entirely on the oxide layer on top. Note that the film thicknesses t_m and the insulator volume fractions x used were those

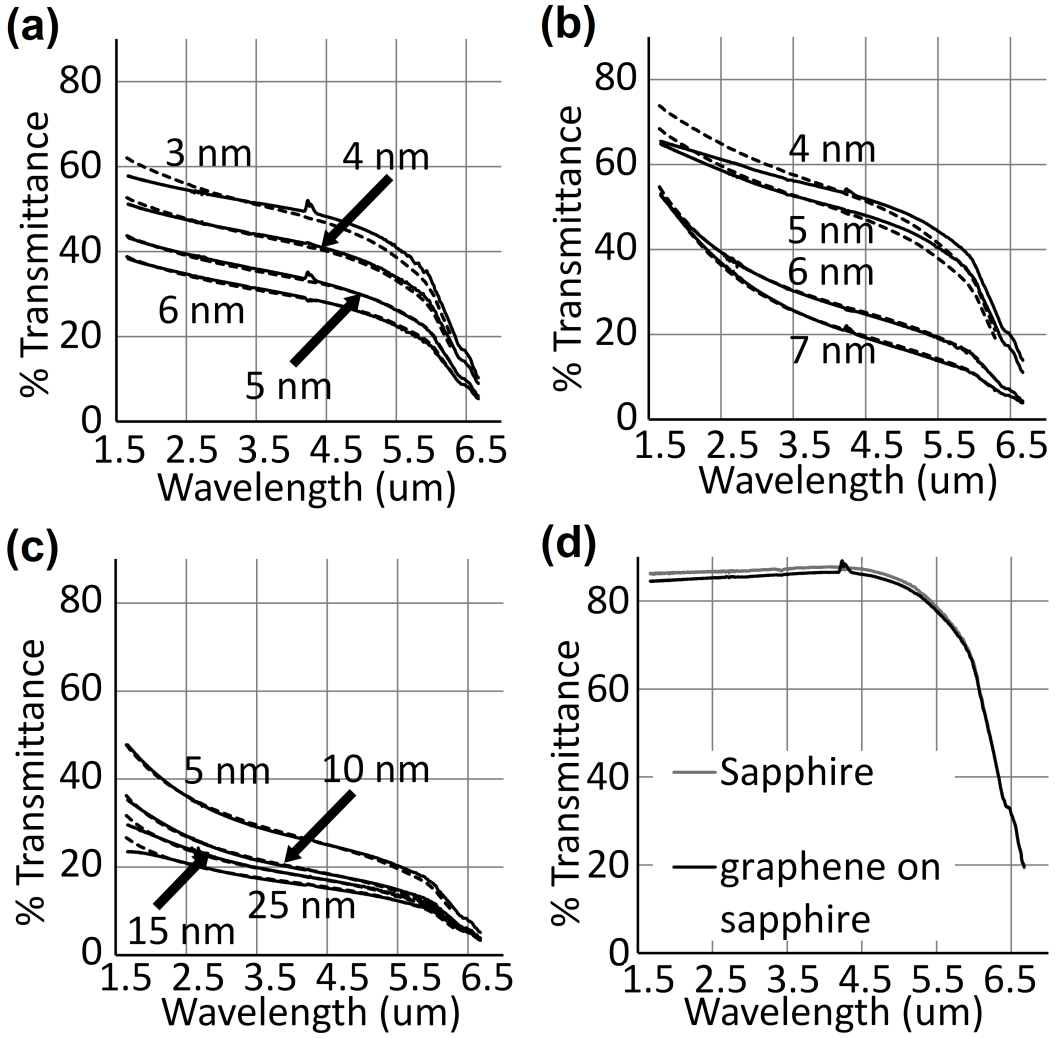

Fig. 2.20 transmittance(%) vs. $\lambda(\mu\text{m})$ for selected values of t_{est}(nm) for sapphire substrate with (a) Ni and (b) Cu UTMFs, (c) Cu_xO TFs and (d) CVD graphene mono-layer. Note that in (a), (b) and (c) solid lines represent experimental data while dashed lines represent modelled data.

Table 2.4 Optical model constants of films having estimated thickness t_{est}; insulating inclusion shape factor L_i, conduction electron relaxation time reduction factor τ_o and oxide/metal reflection weighing factor w.

	t_{est} (nm)	L_i	τ_o	w
Ni UTMFs	3	1.7/3	5×10^{-6}	1
	4	1.5/3	10×10^{-6}	1
	5	2.1/3	40×10^{-6}	0.75
	6	2.35/3	50×10^{-6}	0.60
Cu UTMFs	4	0.1/3	0.0065	1
	5	2.32/3	0.0065	1
	6	2.55/3	0.023	1
	7	2.7/3	0.04	0.95
Cu_xO TFs	5	2.2/3	0.01	0.55
	10	2.42/3	0.01	0.4
	15	2.6/3	0.01	0.4
	25	2.8/3	0.01	0.4

obtained by ellipsometry and given in Tables 2.1 and 2.3. Refractive index values for NiO, Cu_2O and sapphire were collected from various sources [106, 130].

Comparing these results with the ones in Table 2.1 for ellipsometry it is observed that variations in w largely follow what is expected as there is a decrease of the oxide effect on reflection for thicker films, with the biggest variation seen for Ni UTMFs. This is similar to what we see from the ellipsometry data. L_i is seen to increase for all samples, with most values larger than 1/3, suggesting that most insulator inclusions were perpendicular to the plane of the film. This is also justified by literature [75], where the MS-model hinges on the fact that inclusions tend to become more vertical in aspect ratio as the thickness of the film increases, thus assumptions required by the model regarding the vertical nature of grain boundaries can be made with confidence. Values of τ_o for Cu UTMFs and Cu_xO TFs were found to be typically more than 2 orders of magnitude larger than for Ni UTMFs. Increase of τ_o with increased metal proportion is expected [22] and indeed observed for Cu UTMFs and Ni UTMFs but not for Cu_xO TFs, where it was constant.

Figure2.21 illustrates the relationship between the key optical property and key electrical property for TC use in LC-SLMs. Note that ITO is not presented in the figure for comparison with the studied films. Commercial ITO products typically have a sheet resistance smaller than the range presented, and have therefore a correspondingly small transmittance in the mid-IR. This arises since many will have a plasma frequency in the near infrared and therefore performance deteriorates dramatically at larger wavelengths. Additionally, the substrates

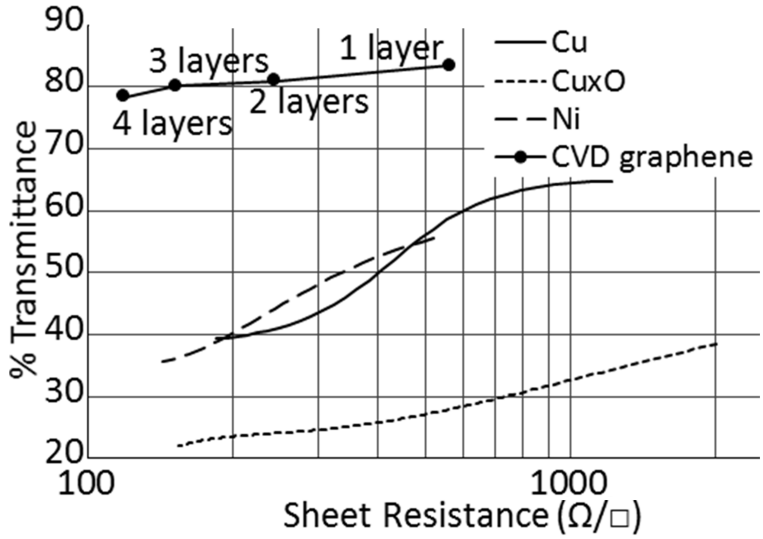

Fig. 2.21 transmittance(%) for on sapphire samples at $\lambda = 2.3$ μm vs. $R_{\square}$ ($\Omega/\square$) for mono-layer to quad-layer CVD graphene, Ni and Cu UTMFs and Cu_xO TFs.

used for such commercial products is also targeted at the visible spectrum. This is typically soda lime glass, which performs poorly at wavelengths above approximately 2.7μm. There is also no inclusion of experimental ITO layers due to the lack of repeatability from literature and impossibility of independent development due to equipment limitations, as previously discussed.

Note from Figure2.21 that for mono-layer to quad-layer CVD graphene the transmittance data was collected at 550 nm for samples on polyethylene-naphthalate (PEN). Due to the similarity of the results obtained to that collected for 2.3 μm for mono-layer graphene a direct comparison is made in Figure 2.21 by multiplying the transmittance for graphene extracted from the on PEN samples with the empirical result we obtained for bare sapphire samples at 2.3 μm; T = 86.6 %. Cu_xO TFs have the poorest performance. Having a larger fraction of oxygen sputter flow rate produces more transmissive films, but the resistance would also increase. Cu_xO TFs are therefore henceforth disregarded in this work. Ni UTMFs are seen to perform better than Cu UTMFs for $R_{\square}$ up to ≈ 500 $\Omega/\square$, while Cu UTMFs take over at larger values of $R_{\square}$, corresponding to thinner films. Graphene performs considerably better than all the other materials tested, with mono-layer on sapphire samples having transmittance of 85.1% and a sheet resistance of 360 ± 34 $\Omega/\square$. Manipulated on PEN results suggest that multi-layer graphene can be used if smaller $R_{\square}$ values are required, which is particularly useful for applications where the electrode geometry makes voltage drop along the electrode a primary concern. This since adding more layers results in only a marginally smaller

transmittance: For quad-layer samples the transmittance is 78%, which is still better than that of all other films tested irrespective of their $R_{\square}$ value.

2.4.4 Stability under further processing

Moving from a TC coated substrate to a final product involves a number of process steps, with the alignment layer coating and baking being the most pivotal since the polyimide layer is directly in contact with the TC and the required imidisation bake is the highest temperature to which the TC is subjected to; 200 ^{o}C for 120 min [66] according to our standard lab procedures. Degradation due to ageing is also a concern both for obtaining repeatable information at the experimental stage but also out in the field for finalised products.

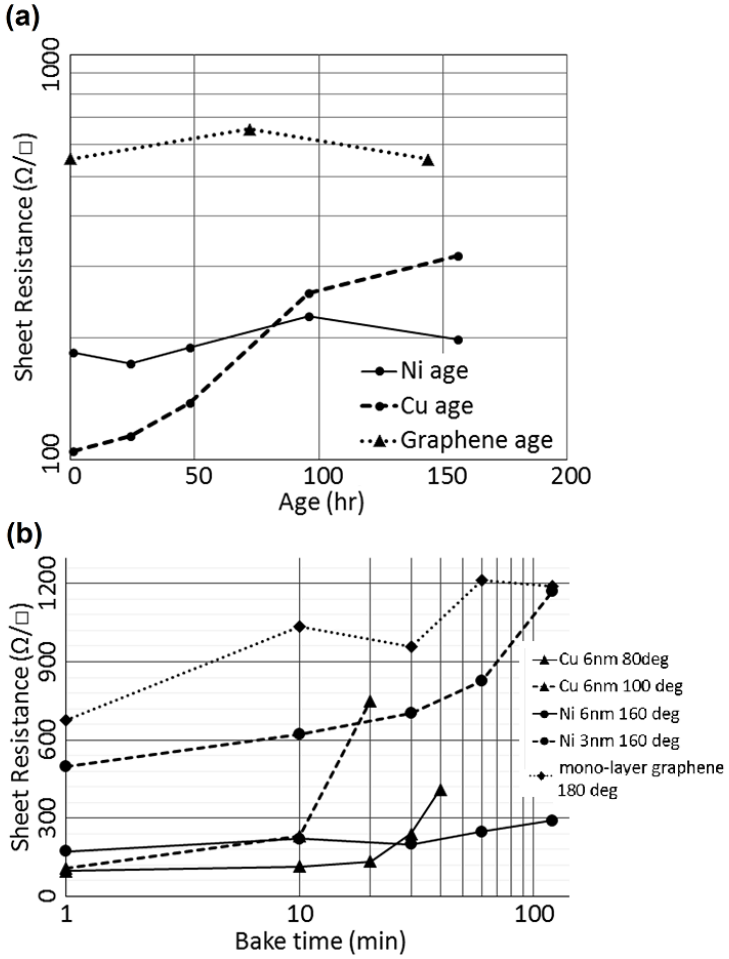

Fig. 2.22 $R_{\square}(\Omega/\square)$ vs. (a) age (hr) and (b) baketime (min) respectively for mono-layer CVD graphene and Ni and Cu UTMFs.

Oxidation in air is the primary concern regarding stability at the pre-assembly stage for Ni and Cu UTMFs. Figure 2.22 shows the increase in $R_\square$ due to oxidation for Ni and Cu UTMFs of various t_{est} values under both the effect of ageing and of baking at different temperatures. It can be seen that Ni UTMFs oxidise at a much slower rate than Cu, with change in $R_\square$ for Ni UTMFs being minimal over a 156 hr ageing period, while $R_\square$ for Cu UTMFs increased three-fold in the same period of time. Baking at 160 °C for 120 min approximately doubles the $R_\square$ value of Ni UTMFs for both 3 nm and 6 nm films but for 6 nm Cu UTMFs $R_\square$ increases to > 9 M$\Omega/\square$ in 5 min for a 120 °C bake and in 30 min for a 100 °C bake. These results largely agree with similar findings in literature [94, 63]. Such increase in sheet resistance value was also observed during the imidisation bake, and as such the covering of the TC by the polyimide precursor did not slow the oxidation process enough to make Cu UTMFs viable. Baking in an atmosphere without oxygen could be a solution pending data on the post-bake oxidation rate of UTMFs when covered with a polyimide layer.

Graphene is thermally stable in air in our temperature range [88], as confirmed in Figure 2.22(a). However, contaminants like water, oxygen and carbon dioxide act as dopants, reducing the sheet resistance of the CVD graphene [6]. These dopants can be removed by annealing. The baking process conducted at 180 °C for graphene acts as an annealing process, reducing dopant level and doubling the sheet resistance in about an hour, as we can see in Figure 2.22(b). Another advantage of graphene over UTMFs is that metallic films are known to cause degradation of the LC-layer and lowering of the breakdown voltage of devices as ions from the film diffuse into the LC-layer. This is mitigated by driving the device using alternating currents. Graphene does not have this drawback at all, potentially adding to the lifetime of the system [8, 134].

2.4.5 Patternability

The ability to pattern TC materials is vital in creating addressable structures able to set up the controllable phase profiles desired across the LC-device. Figure 2.23 shows the AFM topography for an 80 μm $\times$ 80 μm area that has a repeating pattern made up of 3 μm wide, $t_{est} = 3$ nm, Ni UTMF electrodes and 12μm spacing on sapphire, along with an averaged surface profile for the grating. Patterning was done by lift-off as described in Section2.2.

In Figure 2.23(b) the surface profile height is seen to spike at the edges of the electrodes. In a lift-off process this occurs when the metallic film deposited is continuous, as seen in Figure 2.24. When the resist is stripped this results in the spikes we observed [26]. Since a large electric field tends to occur at spikes these are undesirable. A solution is to use an undercut resist layer which ensures that the metallic film is not continuous [61].

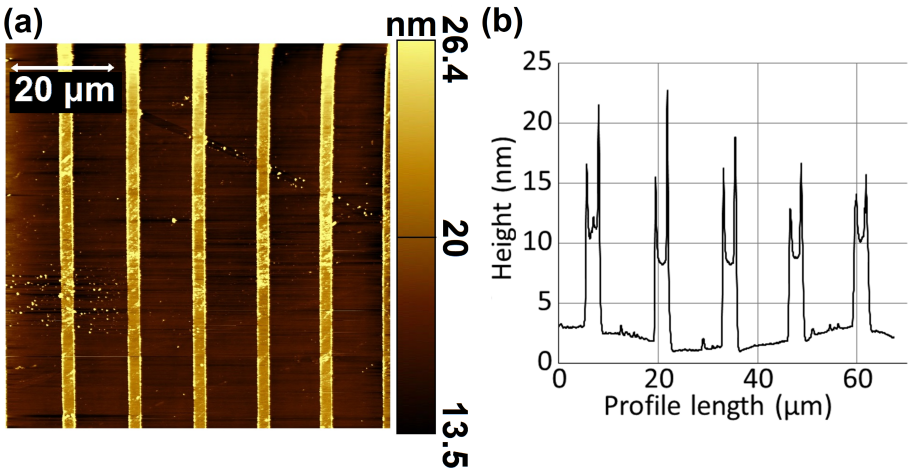

Fig. 2.23 (a) AFM 80 μm $\times$ 80 μm topography image and (b) surface profile for a grating profile made up of 3 μm wide Ni UTMF of $t_{est} = 3$ nm electrode and 12 μm spacing on sapphire.

Typical geometry measured from the profile for this grating is as follows: electrode height 7.3 ± 0.3nm, electrode width $2.76 \pm 0.02\mu$m, electrode spacing $10.74 \pm 0.14\mu$m, grating period $13.50 \pm 0.14\mu$m and spacing to electrode width ratio 0.257 ± 0.005. The electrode height measured is within a standard deviation of the t_m value found by ellipsometry in Table 2.1. This is a verification that the ellipsometric model applied is indeed appropriate. The electrode width and electrode spacing are both underestimated, but since the grating period is also underestimated this suggests that the mask itself might not have been entirely faithful to the design, or that the mask copying process from the master shrunk the design slightly. Irrespective of this, given that we have a spacing to electrode width ratio larger than 0.25, slight over-exposure or over-development might have occurred.

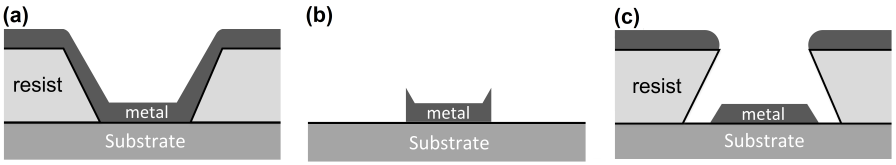

Fig. 2.24 Lift-off for a tapered resist layer (a) before and (b) after stripping, showing formation of spikes at the edges of the electrode. Lift-off for an (c) undercut resist layer with spikes absent.

For the required resolution of a few microns graphene can be patterned by laser ablation [100], e-beam lithography [69] or photolithography [107]. Laser ablation and e-beam lithography are both slow and expensive compared to photolithography but can achieve sub-micron structures. Resist residue after stripping dopes the graphene and causes loss

of carrier mobility and reduction in sheet resistance [53]. If required, this residue can be removed by various processes such as chemical cleaning using an ethyl- 2-pyrrolidone based remover [107] or via an annealing bake in Ar for PMMA [30]. For e-beam lithography and photolithography graphene can be etched with oxygen plasma [69, 2].

2.4.6 Electro-optic response for selected transparent conductors

The electro-optic(EO) response for the LC material used given the thickness of the LC layer, its alignment and the TC used is crucial. Figure 2.25 gives the EO response at $\lambda = 2.3$ μm for the single pixel cells assembled. Note that for each extremum in the curves we have a π phase shift and that the curves have a long tail with 0π phase shift attained for an infinite voltage applied [117]. For both Ni UTMF cells and mono-layer graphene cells a maximum phase delay (δ_{max}) of $\approx 3\pi$ can be attained. This equality suggests equal thickness but also a comparable out of plane performance of the alignment layer.

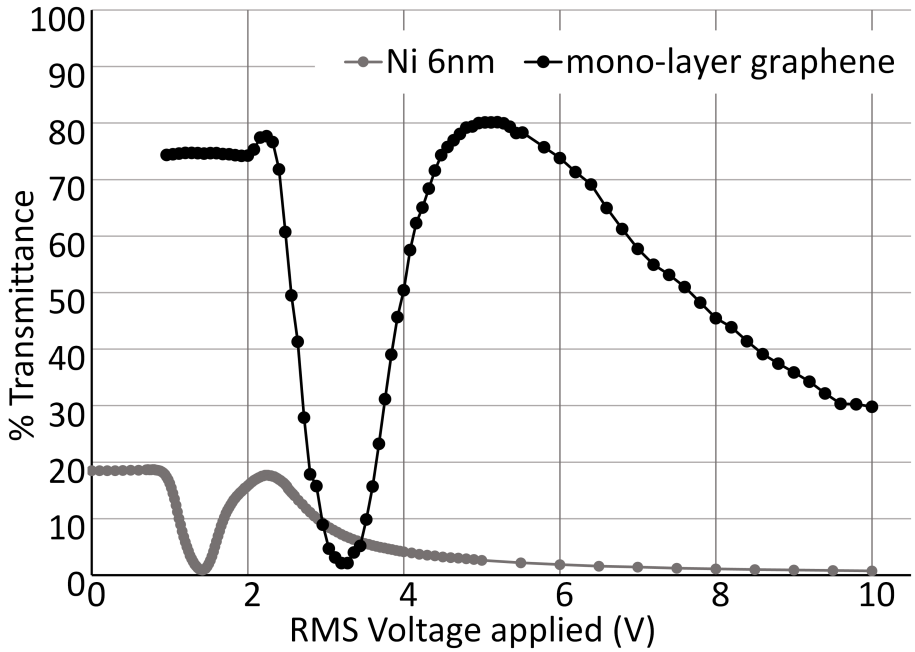

Fig. 2.25 transmittance(%) at $\lambda = 2.3$ μm vs. Applied root mean square(RMS) voltage (V), or electro-optic (EO) response, for BL037 filled, anti-parallel aligned, 15 μm thick LC cells having t_{est}=6 nm Ni UTMF or mono-layer graphene electrodes on sapphire respectively.

From Table 2.5 the transmittance of the mono-layer graphene cell is more than four times better than that of the t_{est}=6 nm Ni UTMF cell. A t_{est}=3 nm Ni UTMF cell would have yielded better transmittance results and assembly of such a cell was attempted but the alignment layer precursor was found to destroy the TC samples, likely due to the formic acid.

Table 2.5 Results extracted from EO response curves in Figure 2.25 comparing Ni UTMF and graphene cells. δ_{max} is the maximum phase delay, T (%) is the transmittance percentage and CR is the contrast ratio between minima and maxima in the curve.

TC	t_{est}=6 nm Ni UTMF	mono-layer graphene
δ_{max}	$\approx 3\pi$	$\approx 3\pi$
T (%)	18.7	81.1
CR	25.0	50.7

Preliminary tests conducted suggest that an alignment precursor which contains solvents such as NMP instead of acids would enable realisation of cells with thinner Ni UTMFs. Note that any alignment coating attempted on mono-layer graphene also resulted in a damaged layer and therefore alignment rubbing was done directly on the mono-layer graphene for the working cells.

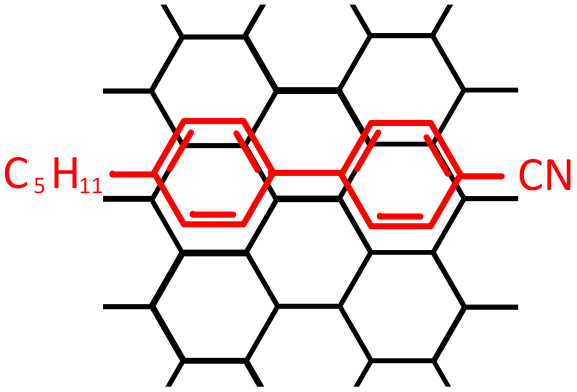

Fig. 2.26 Alignment of the benzene rings of liquid crystal molecule 5CB with the hexagonal structure of graphene.

The contrast ratio (CR) between driven light and dark states was also better for the graphene cell than for the Ni UTMF cell, even though there was no dedicated alignment layer in the former. Alignment in this case was either due to rubbing of residual PMMA from the transfer process, alignment of the LC benzene rings to the hexagonal graphene structure [4], as seen in Figure2.26 for LC 5CB, or a combination of the two. Note that for the benzene ring alignment three orientations are possible, but the PMMA effect described, along with filling direction alignment could have been enough to cause a global preferential alignment direction throughout the cell.

Comparing the transmittance data for TC on sapphire samples in Figure 2.20 to the transmittance data for the assembled cells on sapphire in Figure 2.25 we have a 3.4% and a 17.4% drop in transmittance, for Ni UTMF and mono-layer graphene TCs respectively.

For Ni UTMFs this is a 49.0% drop, which indicates that the absorption of the LC BL037 is negligible at $\lambda = 2.3$ μm for the thicknesses typically used in LC SLMs. For mono-layer graphene the drop is 4.0%, suggesting that there is a high degree of refractive index matching between the sapphire, graphene and LC.

In Figure 2.25 it can be observed that the EO curve for the graphene cell is shifted towards larger voltages when compared to the Ni UTMF cell. This suggests either an increased contact resistance between the wires connecting the device to the driver and the graphene layer or else an increased voltage drop along the TC electrode itself, which is dependant on the $R_{\square}$ value of the TC.

In conclusion, we have established CVD graphene as the transparent conductor of choice in the middle infrared. This is particularly true when patterning is not necessarily required. Having said that, it would still be interesting to investigate the possibility of developing an *ad hoc* transparent conducting oxide for the mid-IR. This is due to the fact that such TCO layers can typically have a thickness up to a few hundred nanometres, resulting in much more durable layers when compared to the extremely thin CVD graphene layer.

Chapter 3

Liquid crystals for variable and controllable phase retardation in the middle infrared

In the previous chapter we have established CVD graphene as the transparent conductor of choice for the middle infrared. The nest step is to identify a liquid crystal(LC) eutectic mixture which can perform in the same spectrum. Such an investigation requires careful consideration of the transmissive properties of the LC layer and the optical birefringence in the selected band. Operation in the middle infrared is likely to require an LC layer thickness greater than that required for operation in the visible spectrum. This adds complexity to the response dynamics of the LC layer to an applied electric field. This complexity arises from the interplay between various elastic and viscous phenomena. This is further compounded by the pre-orientation of the layer in the off-state set by the applied alignment layers. Equations found in literature are typically first approximations only applicable to thin layers. A more detailed analysis is required to move towards more optimal driving strategies.

3.1 Key liquid crystal optical, electrical and material properties

3.1.1 Structure and phases

Liquid crystal(LC) molecules are thus named because they present optical anisotropies, like crystalline materials, but can also flow and rotate, like liquids. Such molecules are typically rod-like(calamitic) or disc-like(discotic). Mesophases of these materials between

the crystalline, at low-temperatures, and isotropic, at high temperatures, are allowed due to the particular structure of these molecules and the dipole interactions between them. They are formed of a stiff core and a flexible tail. Note that discotic LCs have multiple tails [136]. A number of mesophases exist with varying degrees of orientational and positional order and an LC will exhibit multiple phases as the temperature changes. Note however that not all LCs will exhibit the full range of mesophases possible. Transitions occur at specific temperatures, with the nematic-isotropic transition occurring at a temperature referred to as the clearing temperature(T_c).

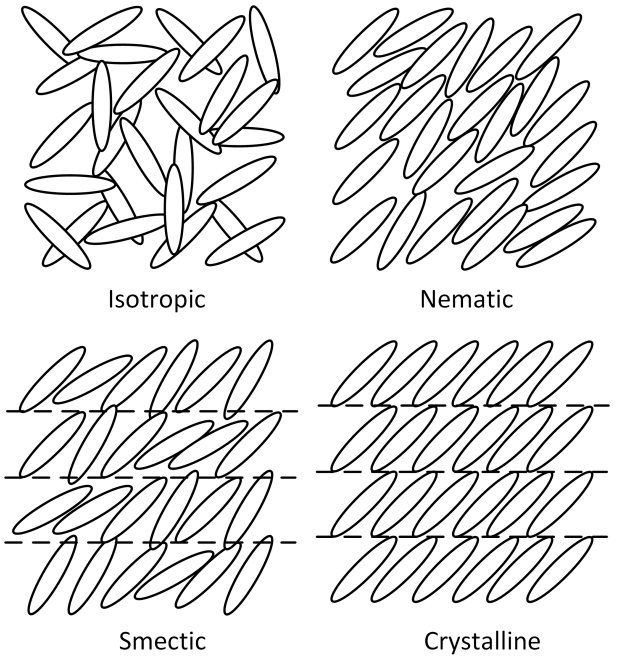

Fig. 3.1 Mesophases going from the isotropic to the crystalline phase for calamitic liquid crystal molecules[136].

Mesophases can be broadly divided into nematic and smectic, as seen in Figure3.1. Nematic LCs have orientational but no positional order, while smectics have both orientational and positional order. The quality of this order, given by a parameter $S = \langle \frac{1}{2}(\cos^2\theta - 1)\rangle$, is quantified as the deviation from an average over the molecules in the LC layer, and will vary as temperature changes within the same mesophase. $S = 0$ for an isotropic material and $S = 1$ for a mesophase where all molecules point in the direction of the director axis $\hat{\mathbf{n}}$. Modelling S with respect to temperature is a non-trivial exercise involving a number of constants that can be obtained empirically [136]. For molecules that are symmetric under reflection, known as non-chiral, orientation is approximately the same in space, at least within the bulk of the layer. For smectic LCs, the same holds across different layers of LC molecules in the bulk.

On the contrary, for chiral molecules a helical pattern emerges since the azimuthal orientation varies gradually around the normal to the layer with a pitch determined by the properties of the molecule.

In practice, it is difficult to realise an LC molecule which fits perfectly the application at hand. Eutectic mixtures of different LC molecules are therefore used to fit the properties required. Due to interactions between the two, or more, types of molecule it is often not straightforward to predict the mixture performance from that of its components [59].

3.1.2 Optical and electrical birefringence

The liquid crystal optical birefringence enables the phase retardation and the electrical birefringence allows it to be controllable via some driving voltage. Optical birefringence $\Delta n = n_e - n_o$ is the difference between the refractive index in the director axis direction, n_e, and that in the plane perpendicular to it, n_0. For a nematic LC layer of thickness t with extraordinary axis x , for incident light having, in x and y, components E_{xo} and E_{yo}, the output electric field components E_x and E_y are given in Jones notation by:

$$\begin{pmatrix} E_x \\ E_y \end{pmatrix} = e^{\frac{-i\pi(n_e+n_o)t}{\lambda}} \begin{pmatrix} e^{\frac{-i\delta}{2}} & 0 \\ 0 & e^{\frac{i\delta}{2}} \end{pmatrix} \begin{pmatrix} E_{xo} \\ E_{yo} \end{pmatrix} \tag{3.1}$$

Where the first exponent is the absolute phase, required for thickness correction in potentially non-uniform devices [117] and the phase retardation δ is given by:

$$\delta = \frac{2\pi\Delta nt}{\lambda} \tag{3.2}$$

where λ is the operational wavelength [50]. The retardation is modified by varying Δn. This occurs because the applied electric field reorients the LC molecules so that there is now an angle θ between the direction of propagation of the laser radiation $\mathbf{k}$ and the n_0 plane. The variable $n_e(\theta)$ is then given by:

$$n_e(\theta) = \left(\frac{n_0^2 \quad n_e^2}{n_0^2 \sin\theta + n_e^2 \cos\theta} \right)^{\frac{1}{2}} \tag{3.3}$$

So that the variable birefringence is now $\Delta n(\theta) = n_e(\theta) - n_0$[51]. Note that in general n_e and n_o are complex refractive indices and that therefore can be separated into a real refractive index and an extinction coefficient. LC absorption is therefore also typically anisotropic [14]. Note that due to the anchoring effect of the cell alignment layer, which allows for an

extraordinary axis to be established, θ, and therefore $n_e(\theta)$, changes across the LC layer. A fuller treatment therefore requires the decomposition of the LC layer into multiple layers of different t and θ which in Equation3.1 would be applied sequentially as multiple Jones matrices [136].

Furthermore Δn depends also on the wavelength used and on the temperature of the liquid crystal material. The refractive index decreases with increased wavelength. It also decreases with increasing temperature until a sharp drop occurs at the clearing temperature T_c when the nematic phase changes into the isotropic phase. This relationship is given approximately by $\Delta n(T) = \Delta n_0(1-(T/T_c))^{\beta}$ where β is a material dependent constant and Δn_0 is the birefringence for the solid crystalline phase [136]. This is seen for a sample LC material in Figure3.2.

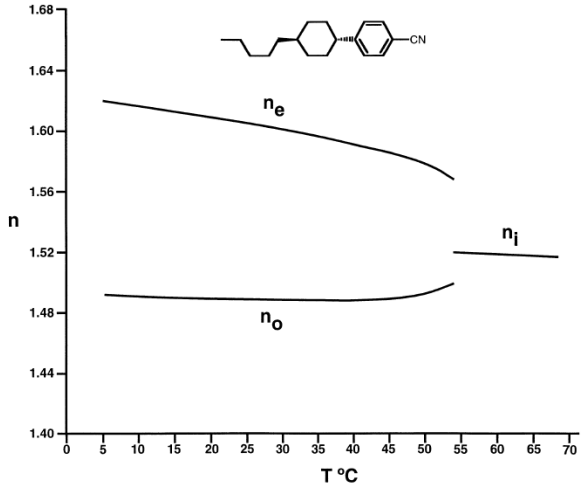

Fig. 3.2 Plot of n_e, n_0 and n_i against T for a typical LC material [50].

The dielectric permittivity in the director axis direction $\varepsilon_{\parallel}$ and that in the perpendicular axis direction $\varepsilon_{\perp}$ are important parameters for modelling the reorientation behaviour of LC molecules inside an electric field, behaviour upon which $\Delta n(\theta)$ hinges, as seen in Equation3.3. The dielectric anisotropy is given by $\Delta\varepsilon = \varepsilon_{\parallel} - \varepsilon_{\perp}$. $\Delta\varepsilon$ varies with temperature in a similar way to the optical birefringence. $\varepsilon_{\parallel}$ and $\varepsilon_{\perp}$ are determined from the parallel and perpendicular polarisability of the molecule, including any permanent dipole moments, along with the molecular density and the order parameter S [136]. Molecular polarisability is dependent on the frequency of the electric field. At typical driving frequencies, less than a few hundred kHz, only the dipole rotation polarisability is of interest.

This rotation polarisability is anisotropic since rotation around the long axis is readily allowed while rotation along a short axis is hampered [102]. The corresponding dielectric

permittivity $\varepsilon_\perp$ is therefore constant in the typical driving frequency range since the corresponding rotation is allowed but $\varepsilon_\parallel$ often exhibits a drop as the driving frequency is increased and the corresponding rotation is now allowed. The frequency at which this occurs depends on the molecular structure and typically increases with increasing temperature of the LC layer. For carefully designed eutectic mixtures this change in $\varepsilon_\parallel$ leads to a change in the sign of $\Delta\varepsilon$ as $\varepsilon_\parallel$ becomes smaller than $\varepsilon_\perp$ above some crossover frequency, as seen in Figure3.3. This enables the LC molecule to be driven in both directions, as opposed to relying on relaxation, which is slower, for one direction [25].

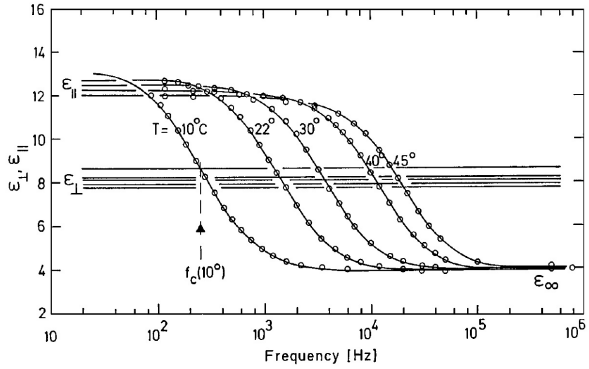

Fig. 3.3 Dependency of $\varepsilon_\parallel$ and $\varepsilon_\perp$ on temperature and frequency showing point of transition from positive to negative $\Delta\varepsilon$ [102].

3.1.3 Alignment of liquid crystal layers

The LC layer in a spatial light modulator must be pre-oriented by fixing the molecule orientation at the boundary so that the director axis in the off state can be predicted. To achieve this pre-orientation an alignment layer is applied on both surfaces enclosing the LC material. For horizontal, or homogeneous alignment, alignment direction is typically established via mechanical rubbing using a roller coated in soft velvet [116] or polarized UV irradiation. Note that mechanical rubbing creates a preferential alignment direction even without a dedicated alignment layer material. This is due to the mechanical micron-scale scratches caused on the substrate from the roller. However, having a polyimide layer enhances this alignment effect greatly since the rubbing causes a preferential alignment in the polymer chains, which interact with the LC molecules.

The alignment layer is dispensed using a spin coater. Since polyimide does not flow easily, it is dispensed in solution with an organic solvent. A soft bake eliminates the solvent and hard curing of the coated substrates yields a polyimide layer [114]. A typical assembly can be seen in Figure3.4. Spherical Mylar spacers of the desired cell thickness are mixed into

UV-curing glue. This is then dispensed around the border of the rubbed substrates, leaving either one or two openings, depending on the subsequent LC filling technique. Note that the amount of glue dispensed depends on the cell thickness, since too little glue will leave holes and too much will most likely close the required openings and spread over the active area. Delicate pressure is applied to make sure that the spacers touch both substrates ensuring a correct cell thickness. In practice, undulations of the substrates will always result in thickness variations within the cell. LC cell glue must have favourable thermal and chemical properties. It must be able to withstand the operational temperature of the device and it must not be reactive with any of the materials in the device. The adhesive must also be able to bond different substrates.

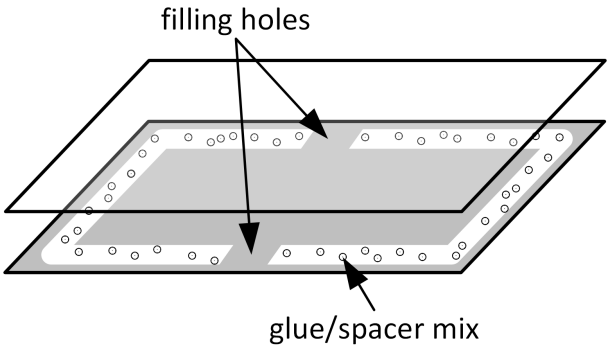

Fig. 3.4 Unassembled cell with spacers spread and glue dispensed.

Before filling the cell, the liquid crystal material is heated up to its clearing temperature to ensure better flow. The heating temperature is chosen with care to prevent evaporation of the LC, this is particularly challenging in eutectic mixtures made up of a number of LC molecules. For fast prototyping filling occurs on a hotplate at the clearing temperature. When the empty cell is thus heated a drop of LC is placed at one of the holes in the glue line and the cell is filled by capillary effect. This technique requires two filling holes.

For liquid crystal on silicon(LCOS) devices filling is conducted under vacuum, which also helps to remove any air bubbles in the LC. This process can be seen in Figure3.5. The empty cell is attached to a vertical heating plate with its single filling hole facing downwards. A small receptacle filled with liquid crystal is brought into contact with the filling hole. As soon as air is again let into the chamber LC floods in the empty cell, helped along by the capillary effect. In all cases once the cell is full of LC, epoxy is used to seal any filling holes.

For vertical, or homeotropic, alignment, the alignment molecule typically has a "branch" which is perpendicular to the main "trunk" of the molecule and therefore perpendicular to the cell substrate. This interacts with the LC molecules, causing vertical alignment [136].

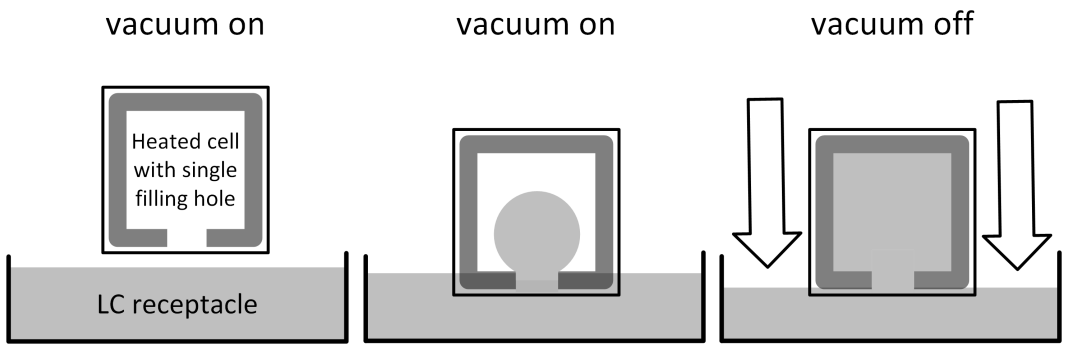

Fig. 3.5 Method for vacuum filling of liquid crystal devices.

Photoalignment is attractive as it is a non-contact alignment technique and is therefore ideal for large-scale, repeatable manufacture. It can be however expensive at the experimental stage due to the UV lasers and the high quality optical systems required, particularly if some interference pattern is to be written on the photosensitive layer [37]. Exposure changes the properties of the alignment layer, either permanently, in which case it is a viable alternative to mechanical rubbing, or temporarily, in which case it can be used for both alignment and addressing[103].

The alignment direction and type depends on the cell type desired, with twisted nematic cells having the plates rubbed in perpendicular directions, and parallel aligned cells having them rubbed in the same direction. In twisted nematic LC cells the polarisation of incident light is rotated as it goes through. The LC layer is effectively used as a wave-guide. Thickness is carefully designed with respect to the LC material properties to allow for this desired change in polarisation to occur. Parallel aligned cells are however better suited for phase-only devices [46]. Vertical alignment has been investigated as a possibility for SLM performance improvement as it can provide higher contrast ratio and switching speed, especially for intensity modulating devices[70]. Note that a vertically aligned cell requires an LC material with a negative $\Delta\varepsilon$ such that molecule rotation perpendicular to the applied field can occur.

The out-of-plane performance for an alignment layer is gauged by the pre-tilt angle it induces in the LC layer, with ideal values being close to 0° for parallel aligned or twisted nematic designs and approximately 90° for vertically aligned cells. Note that a pre-tilt angle of 0° would cause an uncertainty in the helical handedness adopted by cholesteric and twisted nematic LC layers, thus jeopardising their circular polarization capabilities[114]. In parallel or vertically aligned cells this can lead to domains where the molecules reorient clockwise or anti-clockwise. While this creates no issues within the domain itself, areas at the boundaries of domains would exhibit disturbed reorientation, effecting the performance of the device [136].

Note that a full treatment, including the deviation of the LC molecules from the desired direction in-plane, requires a more complex analysis involving tensor parameters[114]. Such an analysis involves, apart from pre-tilt, the order parameter S and considerations for a non-infinite anchoring strength between the LC and alignment molecules. The latter comes into play when modelling how an electric field effects the LC molecules close to the alignment layer [136]. However, a first representation of the in-plane order coefficient $S_{\parallel}$ can be given by [139]:

$$S_{\parallel} = \frac{A_{\parallel} - A_{\perp}}{A_{\parallel} + 2A_{\perp}} \tag{3.4}$$

where $A_{\perp}$ and $A_{\parallel}$ are the absorbances perpendicular and parallel to the expected alignment direction for some absorption band which only comes into play for the expected alignment orientation.

3.1.4 Elasticity, viscosity and response times of liquid crystal layers

The viscous and elastic properties of the LC layer are also essential in modelling its behaviour. This is particularly true of the dynamic response of the LC layer when an electric field is applied. The elastic energy can be described using an orthogonal set of three parameters, k_{11}, k_{22} and k_{33}, commonly referred to as splay, twist and bend respectively [50]. A pictorial representation of the these can be seen in Figure 3.6. These are proportional to S^2 where S is the order parameter. It is also of note that typically $k_{33} > k_{11} > k_{22}$. In the off-state the LC layer relaxes so as to minimise this energy. For calamitic achiral molecules this means parallel alignment. However, minimising this elastic energy must also account for the interaction energy with the alignment layers, which is why a twisted nematic cell relaxes in its characteristic twisted state [136].

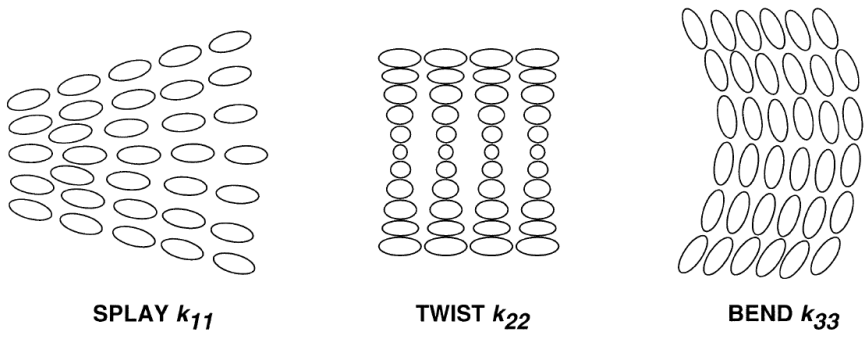

Fig. 3.6 The orthogonal elastic parameters of an LC material[50].

The relative importance of these elastic constants in LC cell operation depends on the way the LC molecules tend to re-orient when subjected to an electric field. When an electric field is present the potential energy of the LC layer is better described by its free energy f, which has both an elastic and an electric component. Therefore, the energy minimisation exercise involves also decreasing the electrical component due to the driving electric field. This causes reorientation of the LC molecules with respect to the electric field. However, this can only occur if the decrease in electrical energy is greater than the increase in elastic energy, which requires an electric field strength E greater than some threshold value E_{th} [136]. E_{th} is inversely proportional to the cell thickness such that the threshold voltage V_{th} is independent of thickness and given by:

$$V_{th} = \pi \left(\frac{k_{11}}{\Delta \varepsilon} \right)^{\frac{1}{2}} \tag{3.5}$$

for a parallel aligned cell. k_{11} is replaced by k_{33} for operation at high frequencies in dual-frequency driving [25] and for a homeotropic cell. It is replaced by $k_{11} + ((k_{33} - 2k_{22})/4)$ for a twisted nematic cell [50]. κ is typically used as a general place-holder for this structure-dependent compound elastic coefficient. This treatment assumes negligible pre-tilt and very strong anchoring to the alignment layer which should be considered for a more complete model.

The flow viscosity η is also fully described using three orthogonal parameters, but while translational effects may be present [136], effectively only the rotational viscosity γ is used. This parameter depends on the temperature of the LC layer proportionally as $\exp(E/kT)$, where k is the Boltzmann constant, and is pivotal in determining the rise and decay time of the LC molecules from one state to the next. The decay time τ_d and the voltage-driven rise time τ_r of a nematic LC layer are given by [76]:

$$\tau_d = \frac{t^2 \gamma}{\kappa \pi^2} \tag{3.6}$$

$$\tau_r = \frac{\tau_d}{\left(\frac{V}{V_{th}} \right)^2 - 1} \tag{3.7}$$

where V is the operational voltage, usually larger than $\sqrt{2}V_{th}$ [76]. This expression, like that for V_{th} assumes negligible pre-tilt and very strong anchoring to the alignment layer[136]. Note that Equations3.6 and 3.7 are only analytically correct for a cell which is subject exclusively to twist deformation, where translational effects are completely absent. The decay and rise times depend on the rate of change of liquid crystal free energy with liquid

crystal director variation across the LC layer and in time [136]. The director variation is given by some function $\theta(z,\tau)$, where z is distance across the LC layer and τ is time. Decay time is based solely on the elastic component of the free energy, where the governing differential equation, arising from the relationship between free energy and director angle, is given by:

$$\gamma\frac{\partial\theta(z,\tau)}{\partial\tau} = k_{22}\frac{\partial^2\theta(z,\tau)}{\partial z^2} \tag{3.8}$$

In the case of twist geometry. As a first approximation, $\theta(z,\tau)$ for twist geometry is given by [136]:

$$\theta(z,\tau) = A\sin\left(\frac{\pi z}{t}\right)e^{\frac{-\tau}{\tau_d}} \tag{3.9}$$

Where A is a voltage dependent constant. Substituting Equation3.9 in Equation3.8 yields the decay time expression we expect, which has a square dependency on LC layer thickness.

For an anti-parallel aligned cell there is a translational 'backflow' effect. This increases τ_d for decay from large steering angles, corresponding to large driving voltages [136]. In practice, however, Equations3.6 and 3.7 can be used for other alignment types since they yield results in the same order of magnitude and having the same thickness dependency.

3.2 BL-037 as a middle infrared nematic liquid crystal material

In this section the theoretical principles outlined in section 3.1 are used to describe the optical properties of BL-037 in the mid-IR. Furthermore, its performance when implemented in a relatively thick layer is investigated. A thicker layer is required to obtain the necessary phase retardation at infrared wavelengths, which are longer than visible ones. In conclusion, the response times for such an LC layer are observed and explained in light of viscous and elastic effects.

3.2.1 Test sample preparation and experimental set-up

A Cary 600 Series FTIR spectrometer was used to obtain the electro-optic response in the 1.6-6.5 μm wavelength range by observing the transmission spectra of our test cells between parallel polarisers to detect absorption anisotropy, and crossed polarisers to detect refractive index anisotropy, subject to increasing driving voltages.

Data for rise and decay times for single pixel LC cells of different LC layer thickness was collected by capturing oscilloscope display information using a large enough display time period so as to capture the rise-decay cycle in one frame. Data was collected for the sensor response and driving RMS voltage. The start of both rise and decay cycles could be pinpointed by taking the time value where the driving voltage changed from, and to, zero volts respectively. The end times for both rise and decay cycles was set as the point when the sensor response was constant and equal to the expected value, whether it was at 0 volts or at some other V_{RMS}, and as such the electro-optic response was an important prerequisite in extracting dynamics data. Note that depending on the section of the electro-optic response scanned by the shift it was harder to obtain an accurate result, particularly close to the extrema.

3.2.2 Absorption bands of BL-037 in the middle infrared

FTIR data was collected for parallel-aligned thin and thick single pixel cells having UTMF Ni electrodes. Liquid crystal BL-037 was used with layer thickness $t = 15\mu$m and 31μm respectively. Data collection between parallel polarisers enabled the ordinary and extraordinary properties to be separated as well as the in-plane alignment quality allowed. Transmission data for the extraordinary axis against the band of wavelengths investigated is seen in Figure3.7. This figure also shows the spectra with the internal reflection component removed. This was attained by the removal of a term of the form:

$$f(\lambda)\left(\sin\left(\frac{4\pi t}{n\lambda}+\phi\right)\right) \tag{3.10}$$

where ϕ is some phase shift, n is the ordinary or extraordinary refractive index of BL-037, depending on set-up, and $f(\lambda)$ is some oscillation amplitude function which is dependent on the reflection and transmission properties at the LC-electrode interfaces of the cell being investigated. This was approximated by a linear variation for simplicity. Note that while this model does not account for the dependency of n_e and n_o with λ it is a useful first approximation, giving $n_e = 1.783 \pm 0.025$ and $n_o = 1.547 \pm 0.019$ and therefore $\Delta n = 0.236 \pm 0.044$.

Figure3.8 shows all the spectra collected with the internal reflection component removed and highlights the absorption bands that emerge. The band from 3.3μm to 3.6μm and around 4.5μm show the greatest absorption. These are coherent with C-H stretching and C≡N triple bond stretching respectively [115]. This is very similar to the absorption spectrum of the liquid crystal molecule 5CB [17]. Note further that, unlike the C-H stretching band, the absorption band at 4.5μm is far more prominent for extraordinary polarisation. If this

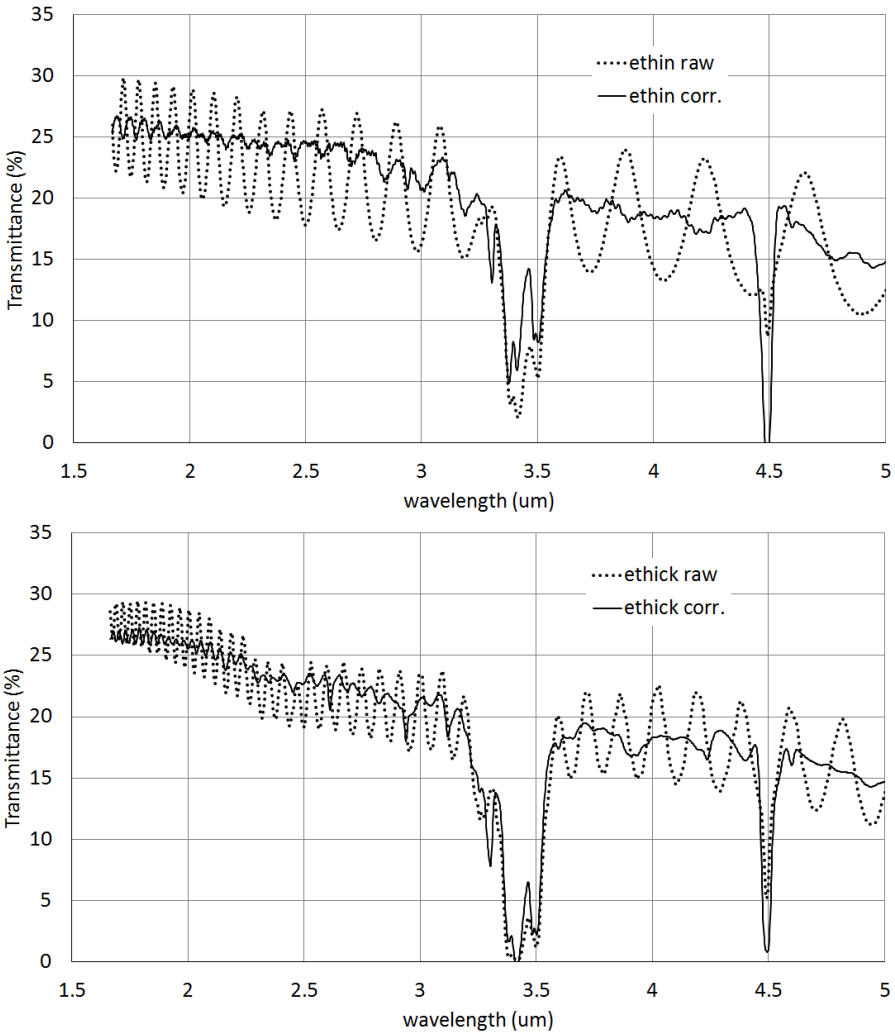

Fig. 3.7 Raw FTIR spectra for thin(15μm) and thick(31μm) cells between parallel polarisers aligned to the extraordinary axis along with the same spectra corrected for internal reflections.

absorption band should only be present for extraordinary polarisation, then the presence of a small peak for ordinary polarisation implies either inaccuracy in the alignment of the system or else disorder in the in-plane alignment of the cell itself. The in-plane order coefficient $S_{||}$ can be extracted by applying Equation3.4 on the depth of the absorption peaks yielding $S_{||thick} = 0.17$ and $S_{||thin} = 0.48$ implying that the thin LC cell is better aligned.

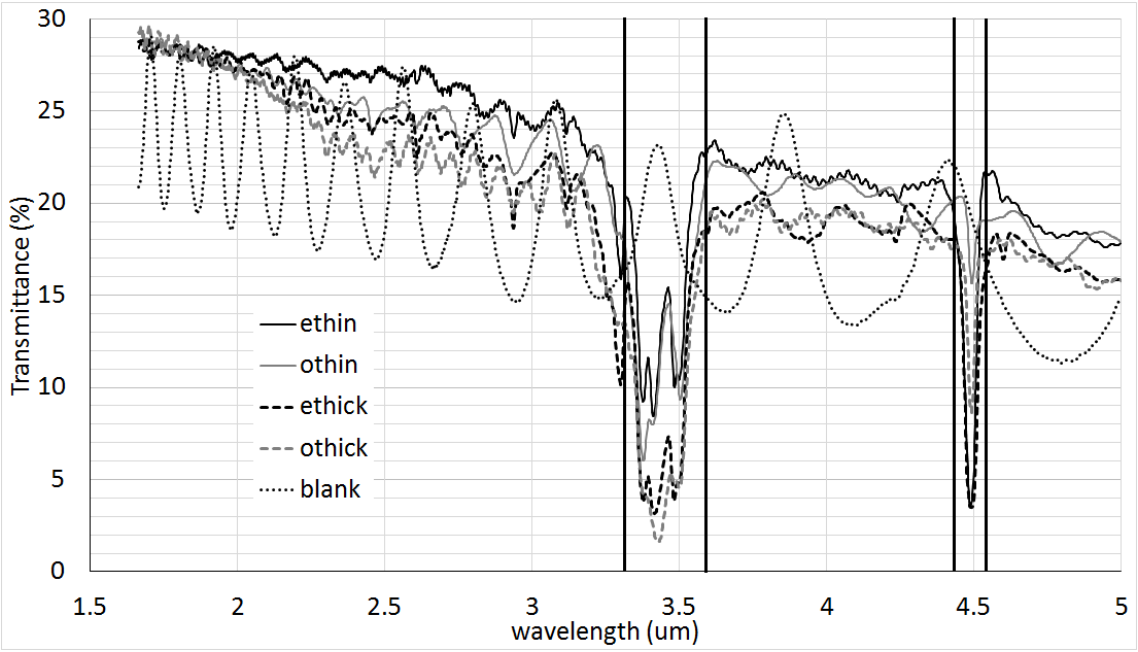

Fig. 3.8 Internal reflection corrected FTIR spectra for thin(15μm) and thick(31μm) cells between parallel polarisers aligned to the extraordinary or ordinary axis along with highlighting of the observed absorption bands.

3.2.3 Middle infrared optical birefringence

Obtaining an expression for the birefringence Δn as a function of wavelength requires analysis of the electro-optic response. FTIR data collected for some range of driving RMS voltages between crossed polarisers results in an array of transmission information with two independent axes, λ and V_{RMS}. Internal reflection effects were removed using Expression3.10 with the data considered with respect to λ. The resultant transmission information is then expressed as an electro-optic response for each individual wavelength in the spectrum. An accurate value of the phase delay attainable for each λ was obtained by considering the extrema in the EO response, with π phase delay added for each extremum as $V_{RMS} \to 0$, as can be seen in Figure3.9. Note that the fraction of π phase between the last extremum and the threshold voltage V_{th} is given as the ratio of the height between these two points

and that between the last two extrema approaching zero, or between the last extremum and 0 in the case where only one extremum exists. The phase retardation expression given by Equation3.2 was then used to extract $\Delta n(\lambda)$ which is given in Figure3.10.

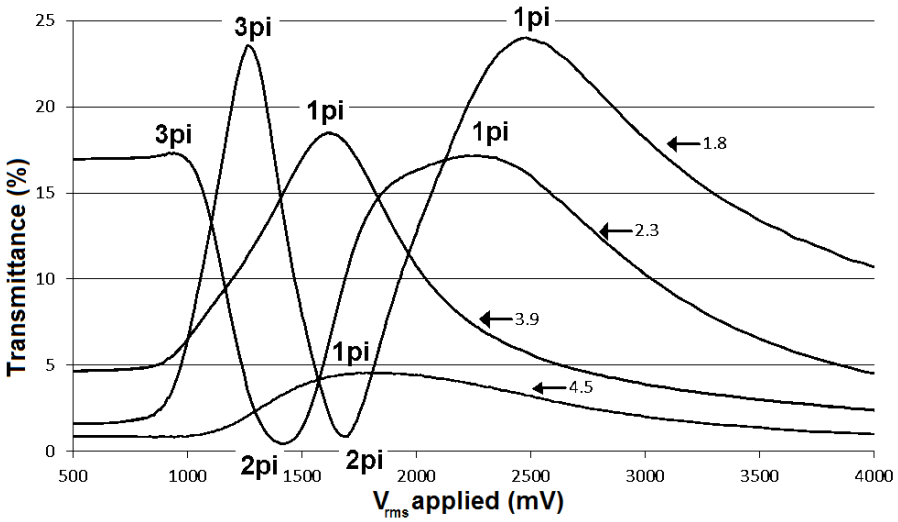

Fig. 3.9 Electro-optic response for selected values of λ in microns with extrema highlighted.

This result validates the approximation obtained from internal reflection and the downward trend agrees with known values of Δn for BL-037, which for the visible spectrum is 0.28 and in the terahertz region is 0.18 [126]. Note that the discontinuities in the data are due to the code used to pinpoint the extrema.

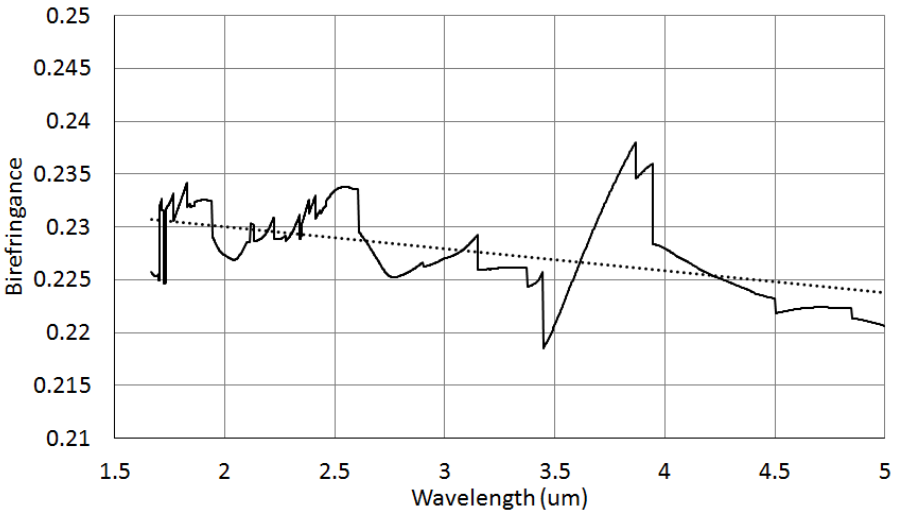

Fig. 3.10 Wavelength dependent birefringence for LC BL-037 from 1.6μm to 5μm.

3.2.4 Response times

Response time data between 0V and V_{RMS}V is presented in Figure3.11 for single pixel LC cells having LC layer thickness 7.5μm, 15μm and 31μm. It is immediately evident that the decay time τ_d is not constant with ΔV as predicted by Equation3.6. It is also of note that, even for low values of ΔV, values of τ_d obtained empirically are greater than the theoretically calculated values by approximately an order of magnitude. Theoretical elasticity and viscosity values for BL-037 where obtained from literature [91] with $k_{11} = 21.8$ pN, $k_{33} = 42.3$ pN, $\gamma = 81$ msPa and $\Delta\varepsilon = +16.9$.

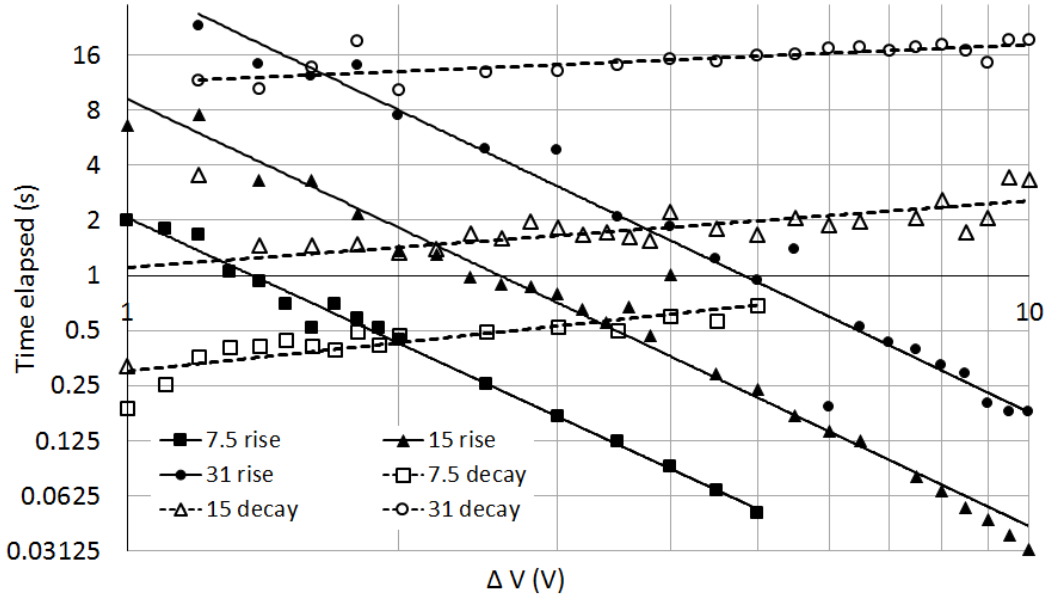

Fig. 3.11 Rise and decay times from 0 V to V_{RMS} V for single pixel cells having LC layer thickness 7.5μm, 15μm and 31μm.

Extracting an empirical threshold voltage V_{th} for the three thicknesses by considering the ratio τ_r/τ_d and rearranging yields $V_{th-7.5} = 1.29 \pm 0.17$ V, $V_{th-15} = 1.55 \pm 0.44$ V and $V_{th-31} = 1.14 \pm 0.20$ V which compare well with the theoretically expected value of 1.12 V.

Values of κ were extracted using Equation3.5 from V_{th}. It is clear from Figure3.12 that the κ factor is a function of both thickness and ΔV, while theoretically we expect $\kappa = k_{11}$ in all cases. As V increases above V_{th} the tilt angle of the LC molecules also increases, with the maximum tilt angle being equal to 90° for $V > 4V_{th}$, so that small angle assumptions can no longer be used and the k_{33} component in the elastic energy becomes relevant [136]. While pre-tilt and anchoring strength effects cannot be disregarded outright, these would cause a corresponding change in V_{th}, which is not observed. κ is therefore likely to involve k_{11} and k_{33}. A more detailed description would require data to be collected for a larger range

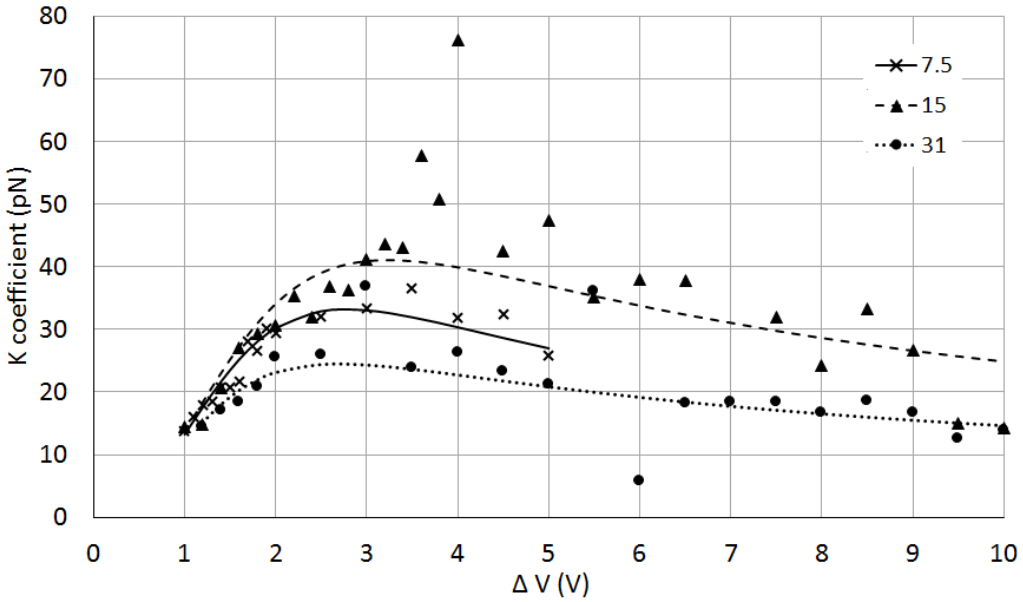

Fig. 3.12 Elastic constant κ extracted from rise and decay times for single pixel cells having LC layer thickness 7.5μm, 15μm and 31μm.

of thicknesses, so as to be able to model the functions $f_{k_{11}}(t,\Delta V)$ and $f_{k_{33}}(t,\Delta V)$ giving $\kappa(t,\Delta V) = f_{k_{11}}k_{11} + f_{k_{33}}k_{33}$.

Values of γ were obtained by rearranging Equation3.6 and using data for τ_d and κ. For all cells investigated γ increases quickly and peaks between $\Delta V = 3$ to 4 V while it decreases marginally for larger values of ΔV. Note that this increase does not arise from a change in the rotational viscosity γ, which is a material constant, but can be attributed to a translational backflow effect in the plane of the LC layer, which is induced by the rotational motion [136]. This effect slows down τ_d since the translational motion effectively becomes a rotational effect in the opposite direction to that desired for decay. Note that as V increases above $\approx 4V_{th}$ not only the molecules at the centre of the LC layer attain the maximum tilt angle of 90°, but also those in a thickness neighbourhood around the LC layer centre which increases with increasing V. From Figure3.13 γ is also seen to diminish slightly above this $\approx 4V_{th}$ threshold, suggesting some interplay between backflow and the tilt angle distribution along the LC cell thickness which merits further investigation.

Depending on the addressing strategy for a liquid crystal based device it might be relevant to acquire knowledge of the response times of the LC layer for switching between some constant maximum voltage V_{max} and some variable voltage $V < V_{max}$. Such data is presented for a 15 μm single pixel device for $V_{max} = 4$ V and 10 V in Figure3.14. The decay times are very similar in both cases, suggesting that there is very little difference in the molecular re-orientation between the cell at 4 V and at 10 V. However, from Figure2.25 the electro-optic

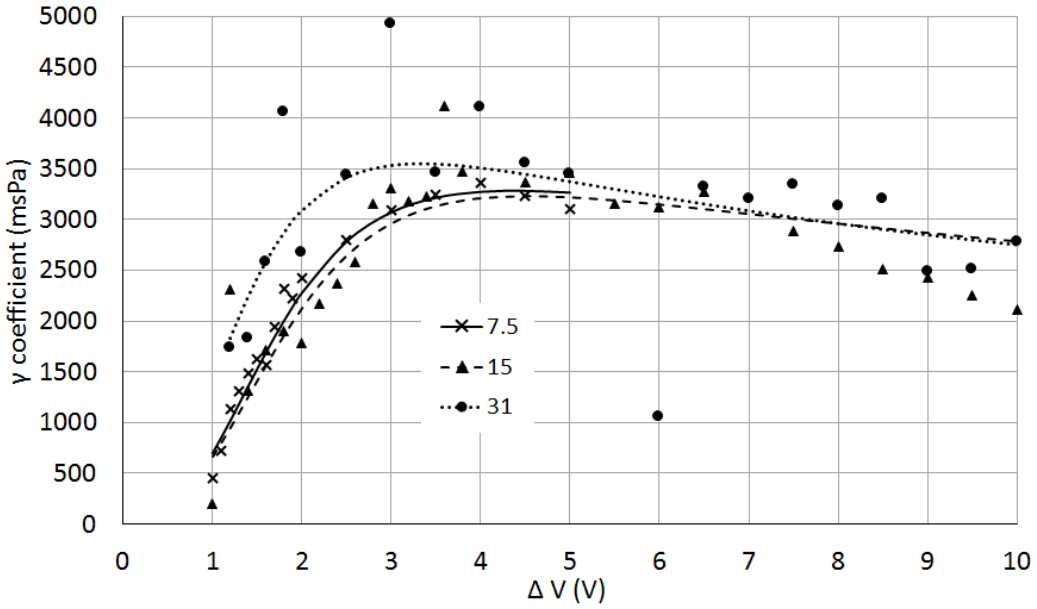

Fig. 3.13 Rotational viscosity constant γ extracted from decay times for single pixel cells having LC layer thickness 7.5μm, 15μm and 31μm.

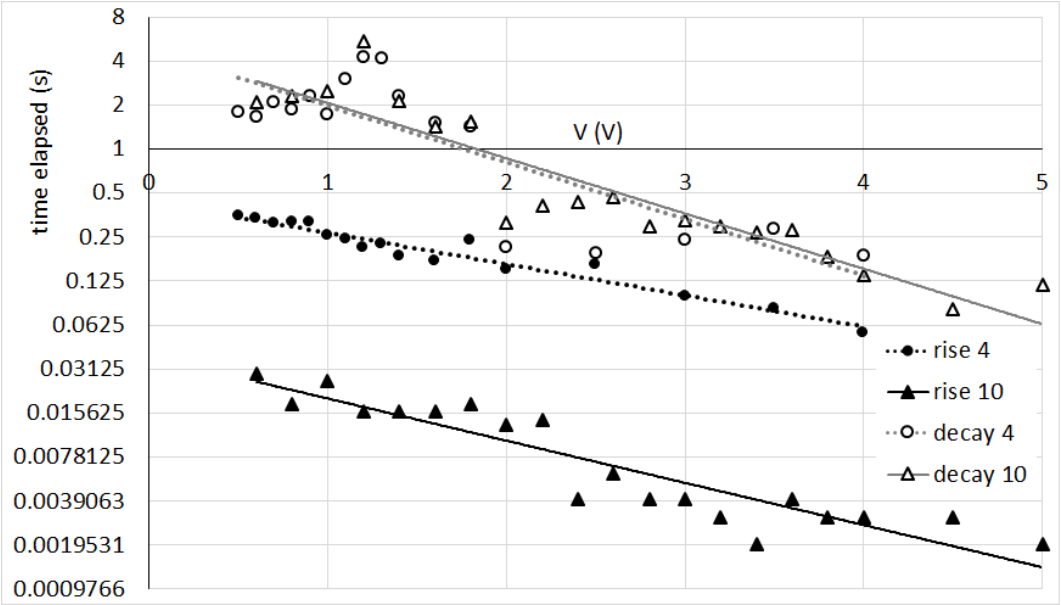

Fig. 3.14 Rise and decay times between some voltage V and 4 V or 10 V, such that $V < 4$ V or 10 V respectively, for a 15 μm thick Ni UTMF single pixel cell.

response for the Ni UTMF cell shows that a phase difference of $\approx \pi/5$ exists between the 4 V and the 10 V state of the same cell for $\lambda = 2.3\mu$m. This is not negligible. Furthermore, from Figure3.14, decaying from 10 V to 4 V does not take a negligible amount of time. As such the reorientation is not negligible. What we can therefore conclude is that for a sufficiently large ΔV down from 10 V, such that the end voltage is smaller than 4 V, the fractional time of that process going from 10 V to 4 V is negligible, meaning that it occurs at very high speed. Note also that a peak in the decay time, again comparable between the two, exists at the threshold voltage.

Rise times to 4 V are approximately 16 times slower than those to 10 V for an equal starting voltage. In fact, rising from 2 V to 4 V takes effectively the same amount of time as rising from 2 V to 10 V and subsequently decaying to 4 V. This reorientation time is a factor of 15 better than that attained, by referring to Figure3.11, by decaying from 2 V to 0 V and then rising from 0 V to 4 V. Staying above the threshold voltage is therefore useful in minimising the switching time between two orientation states.

In conclusion, BL-037 is found to have absorption bands in the mid-IR which are well contained and easily avoidable. They are also congruent with those of well established LC molecules such as 5CB. The optical birefringence is found to be satisfactory. It is also located in the expected range given that the birefringence in the visible spectrum and for THz radiation is known. The LC layer was found to not follow the typical rise and decay time expressions that are standard for operation in the visible range. This was due to the increased thickness required for 2π phase retardation in the middle infrared. This introduced a more complex relationship with the elastic coefficients and a transitional "back-flow" effect. With this material knowledge, along with the work in Chapter 2, structures for beam-steering based on electrically addressable liquid crystal layers can be investigated with confidence.

Chapter 4

Middle infrared, phase only, nematic LC-based spatial light modulation

The results from Chapter 2, regarding transparent conductors, and those from Chapter 3, regarding LC materials, are used in here to move towards a non-mechanical beam-steering device. Before progressing to real devices the theoretical basis is investigated. Diffraction patterns at different distance regimes away from the modulating element are investigated. Particular attention was given to the far-field pattern. The modulating patterns corresponding to key beam-forming functionalities are given. Issues of finite aperture and illumination are explored. The effects of pixelation are pivotal and are therefore also investigated. Issues of dead-space and fringing fields are particular to real optical phased arrays and a model is developed to account for these phenomena in our simulations.

Having developed the theoretical basis, the investigation progressed towards the simulation of real devices. Addressing structures are discussed along with their implementation in LC optical phased arrays. Non-diffractive devices are investigated as a high-efficiency and high-speed alternative to optical phased arrays. Both are based on active cladding optical waveguides. The combination of a controllable patterned top cladding and an Ulrich out-coupler enables 2-D steering. Unfortunately, fabrication of such a device is exceedingly complicated.

Liquid crystal on silicon(LCOS) devices enable fully addressable optical phased arrays. Performance is limited by the thickness of the LC layer required, which results in a fringing field effect comparable to the pixel size. A multiple interaction device is proposed as an attempt to increase the steering range attainable. Unfortunately, the effects of the LC layer thickness are a bottleneck in developing faster, more efficient devices.

4.1 Principles of spatial light modulation

4.1.1 Basics of amplitude and phase spatial light modulation

A spatial light modulator varies the amplitude or phase of incident radiation across its plane. The modulating elements exist within an aperture outside of which the incident radiation is assumed to be completely blocked. The transmitted electromagnetic field at a general point in the replay field is determined by a superposition of all the infinitesimally small modulating elements and their distance from the arbitrary point. A schematic outlining the system is given in Figure4.1.

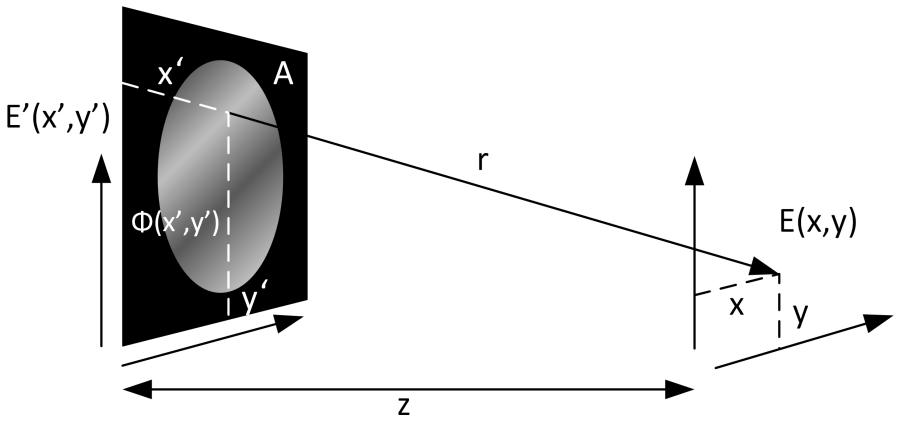

Fig. 4.1 General diffraction system for electric field E', having aperture A and some modulating pattern Φ, yielding a diffracted electric field E a distance z away.

The electric field at a general point $E(x,y)$ on an image plane a distance z away from an SLM with aperture A, modulation $\Phi(x',y')$ and incident electric field $E'(x',y')$ is given by the Fresnel-Kirchoff formula [10] [101]:

$$E(x,y) = \frac{1}{i\lambda}\int_A E'(x',y')\Phi(x',y')\frac{\exp(ikr)}{r}dx'dy' \tag{4.1}$$

where $r = \sqrt{(x-x')^2+(y-y')^2+z^2}$ and $k = 2\pi/\lambda$. Note that the inverse r proportionality accounts for the loss of amplitude at a distance r, such that the intensity $I(x,y) = |E(x,y)|^2$ is inversely proportional to r^2 as expected. $\Phi(x',y')$ is in general complex valued, with the real part determining the amplitude modulation and the imaginary part determining the phase modulation.

Obtaining analytical solutions for the above formula is typically impossible, however solutions can be obtained through approximations for simple systems. Considering Equation4.1 in 2-D for simplicity, letting $\Delta x = x - x'$ and using the binomial expansion:

$$r = \sqrt{(\Delta x)^2 + z^2} = z\sqrt{\frac{\Delta x^2}{z^2} + 1} = z\left(1 + \frac{\Delta x^2}{2z^2} - \frac{\Delta x^4}{8z^4} + \dots\right) = z + \frac{\Delta x^2}{2z} - \frac{\Delta x^4}{8z^3} + \dots \quad (4.2)$$

In the region where the third term of r is much smaller than λ it can be ignored along with higher order terms, which are even smaller. This is the Fresnel approximation, which occurs for $z \gg \sqrt[3]{(\Delta x^4)/(8\lambda)}$. Equation4.1 reduces to:

$$E(x) = \frac{1}{i\lambda z}\exp\left(ik\left(z + \frac{x^2}{2z}\right)\right)\int_A E'(x')\Phi(x')\exp\left(ik\frac{x'^2}{2z}\right)\exp\left(-ik\frac{xx'}{z}\right)dx' \quad (4.3)$$

Where $r \approx z$ for the term in the denominator. In the far-field a further approximation can be applied. The Fraunhofer Equation is obtained by setting the phase contribution of the second order exponent in Equation4.3 to be negligible. This can be applied if $z \gg x'^2/\lambda$ and gives;

$$E(x) = \frac{1}{i\lambda z}\exp\left(ik\left(z + \frac{x^2}{2z}\right)\right)\int_A E'(x')\Phi(x')\exp\left(-ik\frac{xx'}{z}\right)dx' \quad (4.4)$$

Note that this implies that $E(x)$ is obtained by applying a Fourier transform on $E'(x')\Phi(x')$, for which we have well established analytical techniques. For our purposes this far-field approximation is often the most appropriate.

4.1.2 Steering and other functionalities

For a desired replay field $E(x,y)$ in Equations4.1-4.4, $\Phi(x',y')$ needs to be chosen carefully. It is typically impossible to find an analytical expression for this and therefore computer generated holograms are commonly used to generate patterns which when implemented in Equation4.1 yield results approaching the desired replay field [122]. Using the Huygens-Fresnel principle allows $\Phi(x',y')$ to be constructed for very simple cases. This principle states that each wavefront can be treated as a collection of point sources from which circular waves are emitted, the next wavefront is then constructed as an interference between all the point source wavelets. For phase-only devices the problem of obtaining a desired wavefront in the replay field then reduces to creating a modulation pattern which delays the wavelets such that the reconstructed wavefront has the desired properties. Considering a 2-D system for simplicity, steering a plane wave by an angle θ is given by:

$$\Phi(x') = \exp(-ik\lambda x' \sin\theta) = \exp\left(-ik\left(\left[\frac{x'\lambda}{d}\right] \bmod \lambda\right)\right) \tag{4.5}$$

For a convex lensing effect with focal length f the aim is to convert a plane wavefront into a circular wavefront with centre at a distance f. This is given by:

$$\Phi(x') = \exp\left(-ik\left(\lambda - \left[\sqrt{x'^2 + f^2} - f\right] \bmod \lambda\right)\right) \tag{4.6}$$

On the other hand, for a concave lensing effect:

$$\Phi(x') = \exp\left(-ik\left(\left[\sqrt{x'^2 + f^2} - f\right] \bmod \lambda\right)\right) \tag{4.7}$$

All of these expressions are obtained by construction and assume a spatially coherent plane incident light source. The modulo operation is used in real devices to account for the 2π periodicity of a complex exponent.

Aberration effects in a system can also be mitigated by applying a suitable ad-hoc phase pattern to compensate for those effects which degrade the desired result. These effects can arise from the optics forming the system [39] or from geometric inaccuracies in the modulating components [117]. Optical aberrations can be minimised by iteratively applying polynomial compensation patterns to move towards the required pattern. A basic such pattern space given by:

$$\Phi(x', y') = \exp(-ik\lambda([A(x'^2 + y'^2)^2 + By'(x'^2 + y'^2) +$$

$$C(x'^2 + 3y'^2) + D(x'^2 + y'^2) + Ey' + Fx' + G] \bmod 1)) \tag{4.8}$$

Where A is the spherical coefficient, B is the coma coefficient, C is the astigmatism coefficient, D is the focus coefficient, E and F are the tilt coefficients and G is the constant coefficient. Modulator inaccuracies can be treated similarly depending on their nature.

4.1.3 Considerations for Gaussian illumination and of a pixelated structure

An infinitely large grating with an equally infinite coherent and uniformly intense light source is not realisable, though in practice assuming this allows some conclusions about the replay field to be obtained analytically or else enables the use of numerical processes which reduce computational times considerably. The periodicity of the steering phase pattern, unlike for the other functionalities described, allows such an approach. The diffraction equation

$\sin\theta_q = \sin\theta_i + m(\lambda/d)$ where $m\,\varepsilon\,\mathbb{Z}$ [101] gives the angular direction of all orders created by an infinite grating of period d but gives no information regarding the efficiency of each order.

Rigorous coupled wave analysis(RCWA) allows for the approximation of order efficiencies based on an eigenvector decomposition of the system being investigated [85]. The incident, transmitted and reflected fields are decomposed into orders based on the grating equation with the respective unknown reflection and transmission coefficients applied. The electric permittivity of the grating structure is also decomposed into orders.

Fourier decomposition and Maxwell equations allow a coupled electric-magnetic system of differential equations to be obtained for the electric and magnetic amplitudes within the grating. This linear system can be written in matrix notation and eigenvectors extracted. A harmonic representation of the electric and magnetic fields within the grating can thus be obtained. All constants involved can then be obtained from boundary conditions relating the field outside and inside the grating. The number of Fourier harmonics determines the accuracy of the model, with more harmonics required to obtain a stable result for thicker grating structures.

While such techniques can offer useful approximations, they fall short for more general cases and offer no information on the beam width and divergence of the diffracted orders. A more general approach requires considerations of aperture, illuminating radiation properties, and pattern pixelation to be incorporated.

Aperture shape and size are critical in determining the replay field. For a 2-D square aperture the far-field pattern is based on the sinc function while for a circular aperture it is based on the Bessel function of order one [101]. For a one dimensional aperture having width d and a phase modulation pattern yielding a far field intensity $I(x) = |E(x)|^2$, repeating this pattern M times about the origin, thus obtaining a total aperture width of Md, yields:

$$I_M(x) = \left(\frac{\sin\left(\frac{Mkxd}{2z}\right)}{M\sin\left(\frac{kxd}{2z}\right)} \right)^2 I(x) \tag{4.9}$$

The effect of increasing M on efficiency and beam-width can be demonstrated by setting $d = 1$ and $\lambda = 1/z$ and can be seen in Figure4.2. This has a minimal effect on the efficiency which decreases to a constant value due to the diffraction effect at the aperture edges. This is a constant independent of the aperture width. For RCWA this constant effect does not exist because edges do not exist and therefore the efficiency can rise up to unity. On the other hand this has a large effect on the beamwidth of the desired order. Note that the typical $1/e$ threshold is used for determining the cut-off points. For $M = 10$ and 100 the beamwidth

is approximately 10% and 1% that for $M = 1$ respectively. Techniques such as RCWA can therefore be used to extract efficiency information accurately for periodic structures repeated for only a handful of times. On the other hand, beamwidth information still requires a more direct implementation of the Fraunhofer diffraction equation to obtain, but the effect of increased M drops dramatically depending on the system.

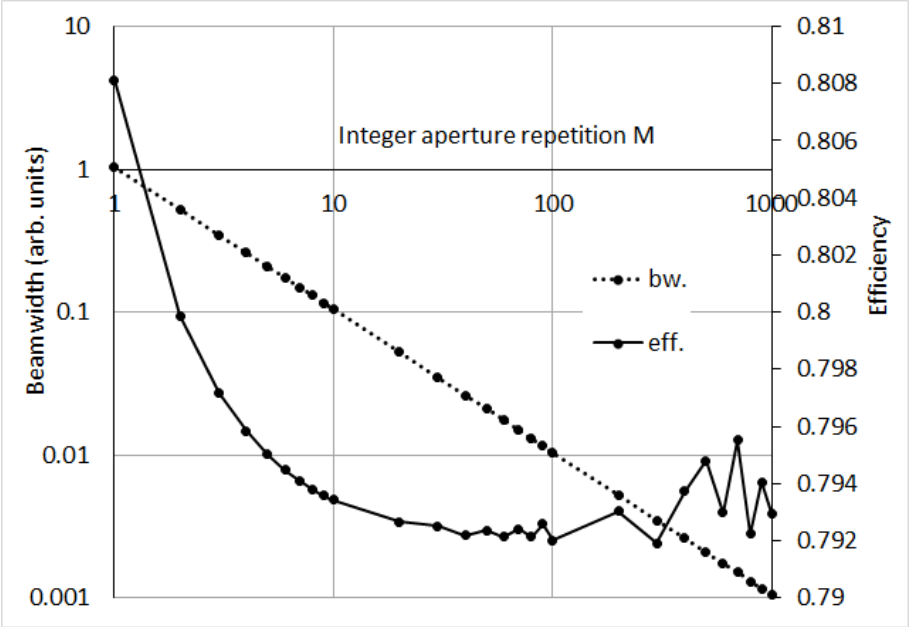

Fig. 4.2 Efficiency and beamwidth variation with increased aperture repetition.

Uniform and coherent plane illumination cannot always be assumed. In practice laser illumination, which can be more accurately described as a Gaussian beam, is most often utilised. The Gaussian beam can be fully described by [44]:

$$E_G(x',z') = \frac{E_{G0}}{\sqrt{1+i\dfrac{z'\lambda}{\pi w_0^2}}} \exp\left(\frac{-x'^2}{w(z')^2} + ikz' + i\frac{kx'^2}{2R(z')}\right) \tag{4.10}$$

where $w(z')$ and $R(z')$ are the half-width, determined in terms of $1/e$ remaining intensity, and the radius of curvature, respectively, of the beam at a distance z' away from the beam source. For a typical system, z' can be considered constant and very large, such that the radius of curvature is also extremely large, yielding the much simplified normalised expression:

$$E_G(x') = \exp\left(\frac{-x'^2}{w^2}\right) \tag{4.11}$$

Note that while the Fraunhofer diffraction expression given by Equation4.4, for no modulating function and uniform illumination, does not give a result when integrating between $-\infty$ and $+\infty$ due to non-convergence, allowing for Gaussian illumination does, yielding:

$$E(x) = \frac{1}{i\lambda z}\exp\left(ik\left(z+\frac{x^2}{2z}\right)\right)\int_{-\infty}^{+\infty}\exp\left(-\left[\frac{x'^2}{w^2}+ik\frac{xx'}{z}\right]\right)dx'$$

$$E(x) = \frac{1}{i\lambda z}\exp\left(ik\left(z+\frac{x^2}{2z}\right)\right)w\sqrt{\pi}\exp\left(-\left(\frac{wkx}{2z}\right)^2\right) \tag{4.12}$$

This expression is of particular use when the beamwidth of the incident Gaussian beam is considerably smaller than any modulating element that might be introduced. The above yields normalised intensity pattern:

$$I(x) = \left(\exp\left(-\left(\frac{wkx}{2z}\right)^2\right)\right)^2 = \exp\left(-\frac{1}{2}\left(\frac{wkx}{z}\right)^2\right) \tag{4.13}$$

In most cases the Gaussian beam will be clipped by some aperture of width d. In this case the terms involving the error function do not conveniently tend to ± 1 as x' tends to $\pm\infty$ such that the intensity is now given by;

$$I(x) = \left[\exp\left(-\frac{1}{2}\left(\frac{wkx}{z}\right)^2\right)\right]\left|\operatorname{erf}\left(\frac{d+\frac{ikxw^2}{z}}{2w}\right)+\operatorname{erf}\left(\frac{d-\frac{ikxw^2}{z}}{2w}\right)\right|^2 \tag{4.14}$$

Applying $w = 1$ and $\lambda = 1/z$ enables investigation of the target order properties for varying d, effectively varying the size of the aperture superimposed on the incident Gaussian beam. The beamwidth decreases as d increases, while efficiency increases, as seen in Figure4.3. Note that the efficiency values calculated do account for the fraction of the beam that is truncated at the object plane. The efficiency is 90% that for $d = \infty$ at $d \approx 2.25$ and 99% for $d \approx 3.25$. The beamwidth at these points is $\approx 25\%$ and $\approx 6\%$ respectively more than the beamwidth for an infinite aperture.

It is also useful to compare the replay field for Gaussian illumination over an infinite aperture, or for $(d/w) > 3.25$, with that for a constant illumination such that $2w = Md$. Figure4.4 shows that Gaussian illumination is $\approx 6\%$ more efficient but has 20% increased beamwidth, with variation of only $\pm 3\%$ for the whole range of M investigated. The increase in efficiency can be attributed to a lower intensity at the aperture edges, which mitigates the

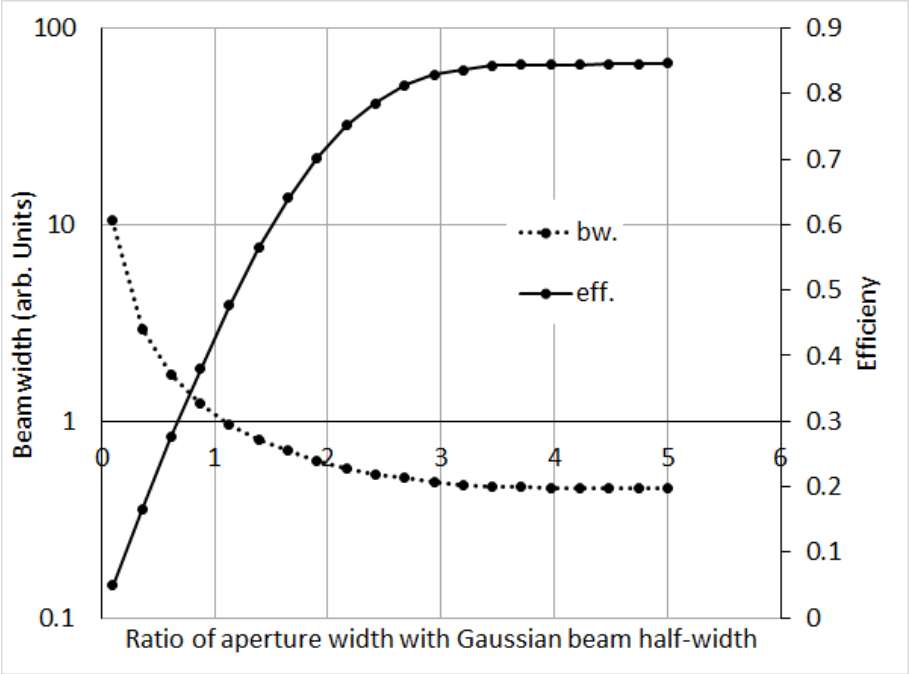

Fig. 4.3 Efficiency and beamwidth variation as the width d of an aperture increases with respect to an incident Gaussian beam of unit half-width.

edge diffraction effects that set an upper efficiency limit for a uniform illumination aperture as discussed.

A further complication arises due to pixelation. While it is possible to use continually varying elements to achieve a continuous modulation function in simple systems, typically by using wedged or curved elements [87], making a device with variable and controllable phase pattern is more desirable for beam steering and forming applications. This implies that the desired phase pattern has to be approximated by a pattern with pixel-size resolution such that it can be displayed on the pixelated surface. For a system having a steering modulation pattern as described in Equation4.5, having aperture d and made up of N pixels the Fraunhofer diffraction expression for normalised intensity is given by:

$$I_N(x) = |\int_{-d/2}^{d/2} \exp\left(\frac{-i2\pi}{d}\left(x' - [x']\bmod\frac{d}{N}\right)\right)\exp\left(-ik\frac{xx'}{z}\right)dx'|^2 \tag{4.15}$$

Note that the integral cannot be found analytically for a general N, and therefore numerical methods have to be used. As N increases it is expected that the replay field approaches that for a continuous phase pattern $I_{+\infty}(x)$, which is given,when normalised, by:

$$I_{+\infty}(x) = \left(\mathrm{sinc}\left(\frac{\pi d}{\lambda z}\left(x + \frac{\lambda z}{d}\right)\right)\right)^2 \tag{4.16}$$

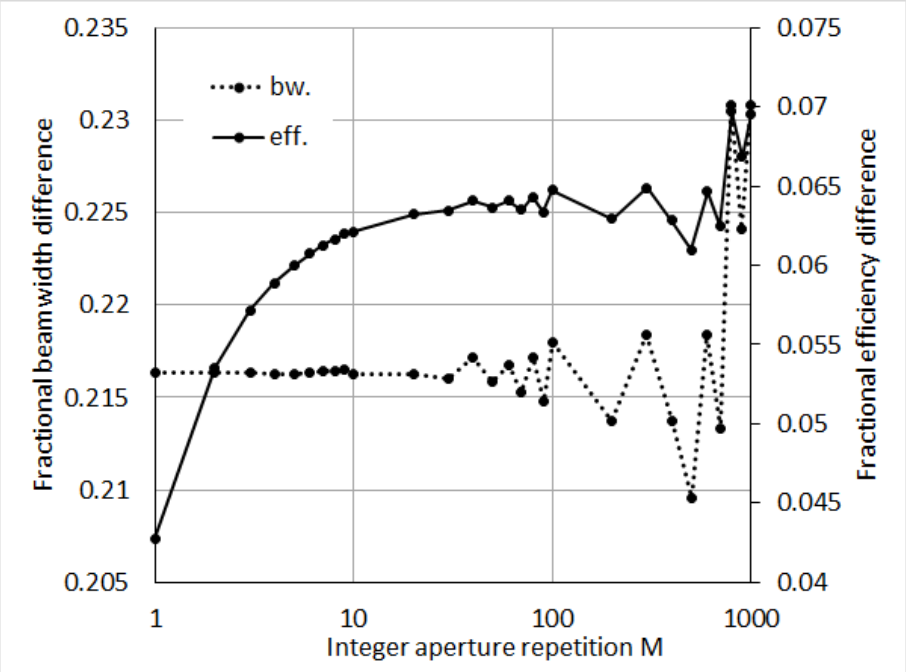

Fig. 4.4 Difference in efficiency and beamwidth between the replay fields of a Gaussian beam having half-width w and an aperture of width d repeated M times such that $2w = Md$.

Where $\mathrm{sinc}(x) = \sin(x)/x$. Replacing for demonstration $d = 1$ and $\lambda = 1/z$, the variation in beamwidth, accuracy and efficiency of Equation4.15 as N increases when compared to those of Equation4.16 can be seen in Figure4.5. 90% and 99% of the $N = +\infty$ values for efficiency are obtained at $N \geq 5$ and ≥ 11 respectively. For beamwidth they are obtained at $N \geq 2$ and ≥ 4 respectively. Note that this approximation also leads to inaccuracy in the steering direction, with a 25% inaccuracy for $N = 2$. This goes down to 10% and 1% at $N \geq 3$ and ≥ 8 respectively.

In a real pixelated spatial light modulator it is not typical for the whole pixel area to have modulating properties. This leads to 'dead-space' between the pixels where the phase delay is typically constant. To represent this the modulated phase pattern given in Equation4.15 needs to be multiplied by some function $D_f(x')$ given by:

$$D_f(x') = 1 \quad \text{for} \quad [x'] \bmod \frac{d}{N} < \frac{fd}{N} \quad \text{and} \quad D_f(x') = 0 \quad \text{otherwise} \tag{4.17}$$

where f is some fill factor between 0 and 1. Taking $N = 4$ and 16 for demonstration, efficiency, beamwidth and accuracy are given in Figure4.6 for $f > 0.5$. 90% accuracy in all three parameters is obtained for $f > 0.87$ and 0.79 for $N = 4$ and 16 respectively. Accuracy above 99% occurs for high values of f, with $f > 0.97$ in all cases.

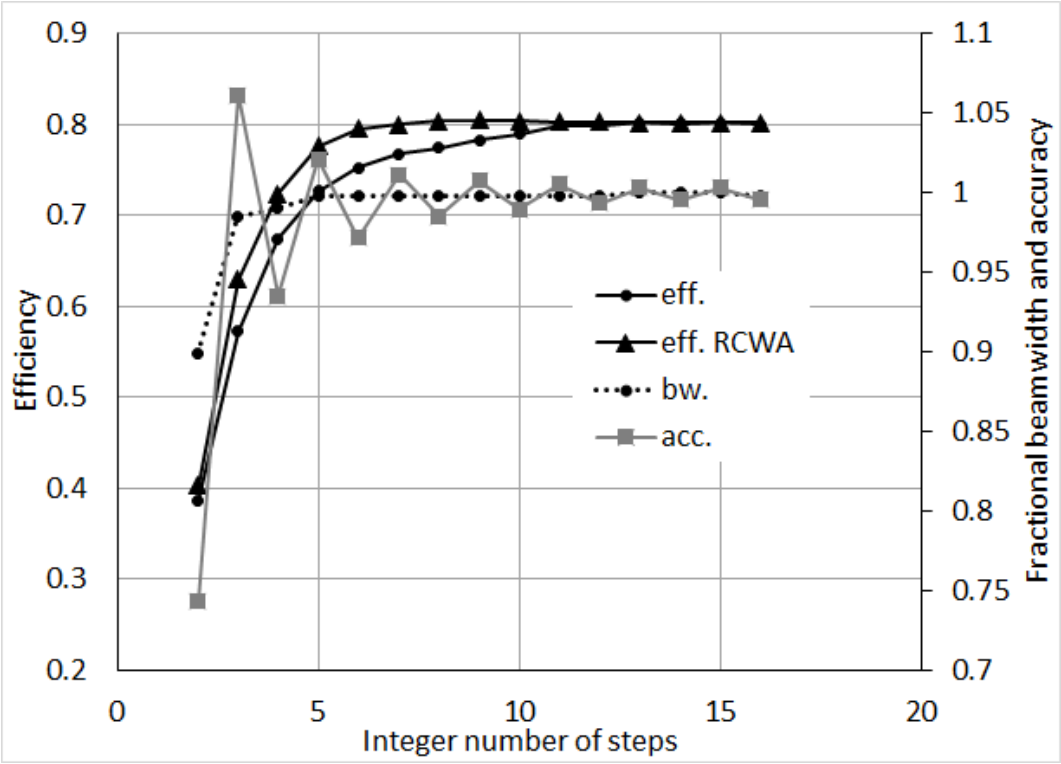

Fig. 4.5 Variation of key replay field properties for pixelation of an otherwise linear phase pattern. Accuracy is given as a ratio between numerically integrated and RCWA results.

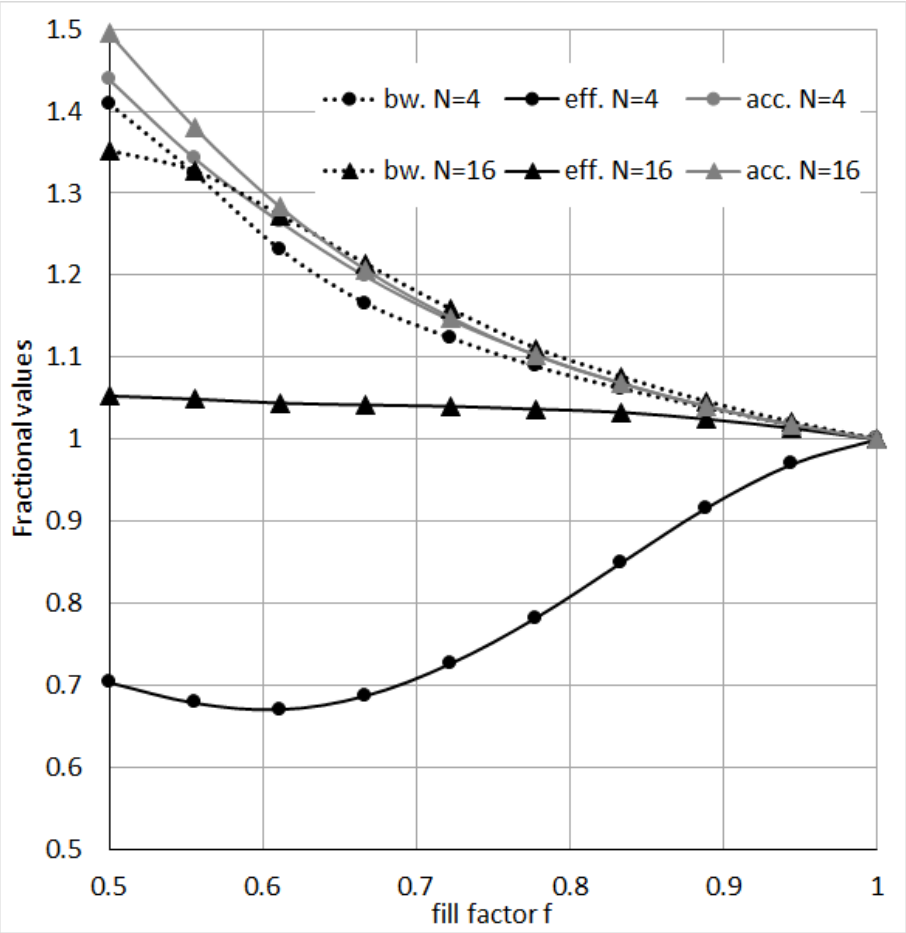

Fig. 4.6 Beamwidth, efficiency and accuracy as a function of fill factor. Values are expressed as a fraction of the same for maximum fill.

For practical devices, implementation of the equations detailed in this section requires further considerations. Fresnel equations need to be incorporated and grating thickness effects taken into account. A fuller model is provided by the Reticolo software [47] which applies an RCWA analysis to a user defined infinitely repeating grating stack. Pixelation efficiency data was obtained using Reticolo and compared to that obtained by implementing Equation4.15. Parameters where maintained constant, with $\lambda = 1/z = 0.1$. The phase pattern was realised by a slab of thickness $t = 1$ with a refractive index gradient in N steps from 1 to 1.1 such that from the function for phase retardation given in Equation3.2 this yields a 2π phase shift over the distance d. Figure4.5 compares efficiency results for both techniques. There is some difference for $N < 10$ with maximum error $\approx 7\%$. Note that target order direction was identical to that expected and recall that no beamwidth information can be extracted by RCWA. However, for a practical Gaussian beam illumination, if the aperture is large enough, a tentative value for beamwidth can be extracting by considering its equivalent M value and the corresponding beamwidth corrected for Gaussian illumination, as discussed.

4.1.4 The nematic liquid crystal, phase-only, spatial light modulator

Combining considerations for liquid crystal layers, transparent conductors and spatial light modulators is required to be able to realise devices and predict their performance. Of particular interest is the fringing field effect which has the potential to degenerate the addressed phase pattern dramatically. Attaining the required maximum phase shift δ_{max} in a liquid crystal layer, based on the phase retardation expression in Equation3.2, requires a minimum thickness t_{min};

$$t_{min} = \frac{\delta_{max}\lambda}{2\pi\Delta n_{max}} \tag{4.18}$$

where $\delta_{max} = 2\pi$. Note that for a binary grating $\delta_{max} = \pi$ such that the LC layer can be half as thick. This makes a device, according to the LC reorientation decay time expression in Equation3.6, four times as fast. For a reflective device incident radiation undertakes two passes in the LC layer such that this can also be half as thick. Note that in practice, due to the various alignment and ordering effects, LC layer thickness is typically slightly larger than this t_{min}.

The electrode structure allows a user-defined voltage to be applied to the liquid crystal layer. Note, from the electro-optic response, as seen in Figure2.25, that the relationship between voltage and phase is typically not linear and needs to be extracted for a specific device by calibration. Furthermore, fringing electric fields from the electrodes, in addition to the elastic properties of the LC material, result in a phase pattern that does not follow the

voltage pattern accurately. This effect is most pronounced for stepped voltage patterns. A typical case can be seen in Figure4.7. For a step phase change of δ going from phase ϕ_1 to ϕ_2 occurring at $x = 0$ this effect is implemented by replacing the stepped transition with [72]:

$$\phi(x) = \frac{\delta}{2}\left(\text{erf}\left[\frac{2x}{\Lambda(\delta)}\right] + \phi_1\right) \tag{4.19}$$

where Λ is a broadening factor. Λ can be understood as the distance required in the x-axis for the phase jump to become 84% of that attained for a stepped phase jump. This broadening factor depends on the fringing field, the elastic properties, and the thickness of the LC layer. The relationship between Λ and δ is often obtained empirically, with the curve for the liquid crystal mixture BL-037 given by:

$$\Lambda(\hat{\delta}) = \Lambda_{max}\left(1.7273\hat{\delta}^3 - 4.2162\hat{\delta}^2 + 3.4141\hat{\delta} + 0.074\right) \text{ for } 0 \leq \hat{\delta} \leq 1 \tag{4.20}$$

where Λ_{max} is the thickness dependent broadening factor for the maximum phase step shift δ_{max} of the system and $\hat{\delta}$ is a normalised phase shift which is multiplied by δ_{max} when applied to a test device. This expression fits experimental data with an R^2 value of 0.998. Λ_{max} is typically linearly proportional to thickness for a given LC material, and can be found empirically as seen in Figure4.7.

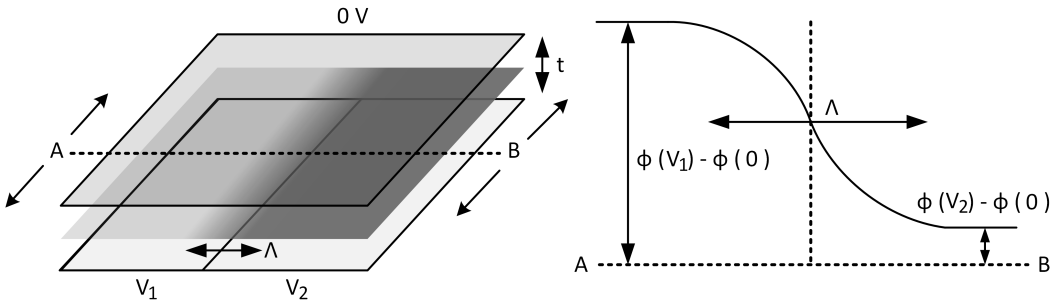

Fig. 4.7 Few pixel cell design and implementation for obtaining an empirical graph describing the key constant for fringing effects, $\Lambda_{max}(t)$.

For a general pixelated phase pattern over N pixels with $N-1$ phase shifts ,such that there is an N-element long phase sequence ϕ_n and an $N-1$-element long phase reset location sequence x_n, the resultant phase pattern is given by:

$$\phi(x) = \sum_{n=1}^{N-1} \frac{\phi_n - \phi_{n+1}}{2}\left(\text{erf}\left[\frac{2(x-x_n)}{\Lambda(|\phi_n - \phi_{n+1}|)}\right] + \phi_n\right) \tag{4.21}$$

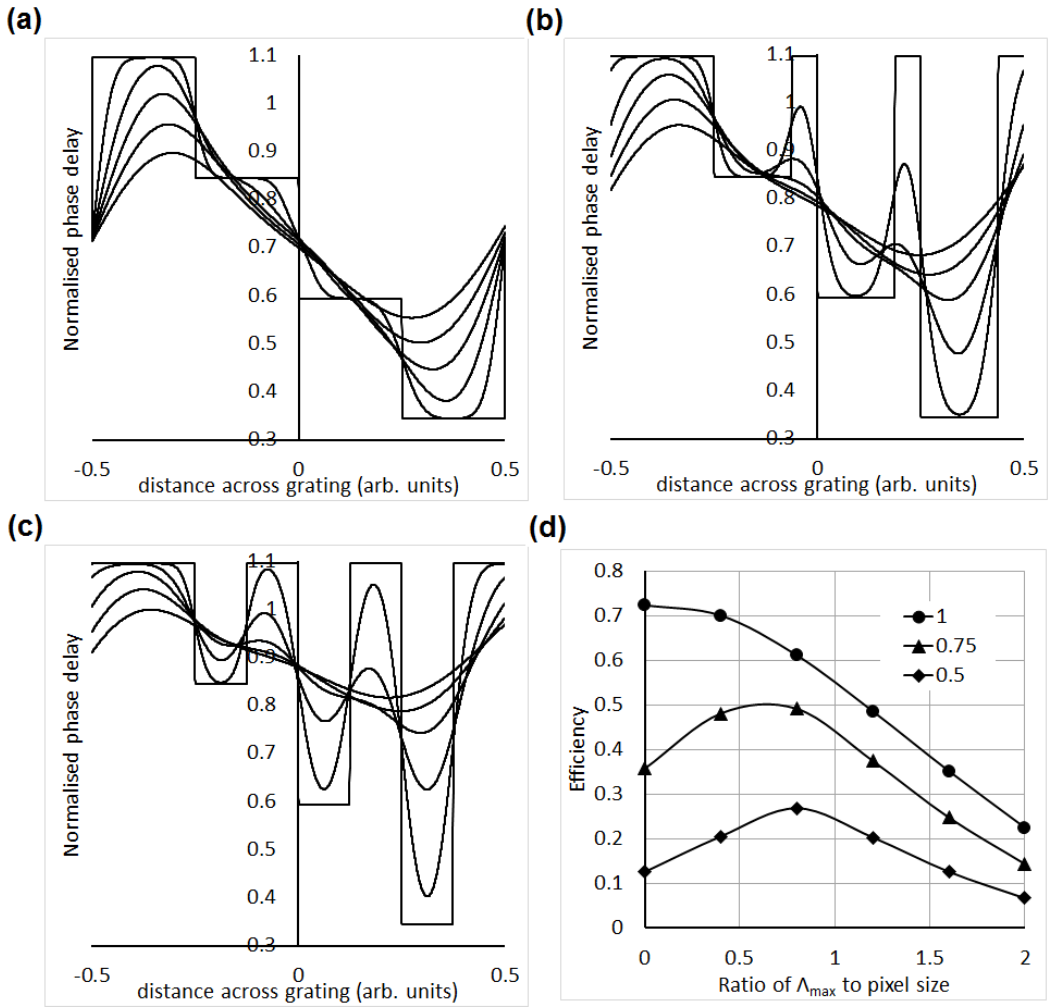

Fig. 4.8 Unit width phase patterns for fill factor f =1(a), 0.75(b) and 0.5(c) along with corresponding target order efficiency for increasing smoothing factor Λ_{max} =0, 0.4, 0.8, 1.2, 1.6 and 2. Note in (a-c) that phase pattern smoothness increases with increasing Λ_{max}.

Note that Λ is equal for a positive or negative phase shift of the same magnitude. Note also that if $\phi(x)$ is a periodic phase pattern, further electrodes need to be added at both edges, representing neighbouring pixels, so as to be able to account for fringing effects at the edges of the periodic phase pattern. The number of additional pixels required depends on Λ, such that the total width of the added pixels is approximately equal to $\Lambda/2$.

Results obtained by applying RCWA via Reticolo for multiple values of Λ are shown in Figure4.8 for a four-level pixelated phased pattern. Values of Λ taken were from 0 to twice the pixel size. The effect for three distinct dead space fractions, 0, 0.25 and 0.5, are also compared. All other parameters were as for the RCWA treatment in Figure4.5. Note that as Λ increases the broadening effects from neighbouring phase jumps start to overlap, such that for $\Lambda >$pixel-size the digitisation of the phase pattern is effectively removed. For no dead-space, however, this does not increase the efficiency. This is due to loss of maximum phase retardation and increase in the width of the fly-back region at the pattern resets. This results in loss of efficiency and accuracy [67], with the effective phase pattern for larger values of Λ being closer to a binary grating with a non-negligible zero-order. While the same holds for phase patterns with dead-space at large values of Λ, in the region where Λ is approximately equal to the dead-space dimension an efficiency improvement is observed.

It is observable in Figure4.8 that the fringing effect could mitigate the degrading effect of pixelation seen in Figure4.5 by removing the step features. The overall loss of phase retardation negates this. However, if the LC layer used is thick enough to allow a phase retardation greater than 2π it is possible to design a phase pattern which compensates for this loss. For the minimum thickness that allows 2π phase shift at a given λ there is a corresponding Λ_{max}. The corresponding stair-stepped steering phase pattern that accounts for fringing effects has a maximum phase delay $2\pi h \leq 2\pi((N-1)/N)\, 0 < h < 1$. Allowing for a greater maximum phase retardation to compensate for this loss requires a larger thickness, which entails a larger Λ_{max}, causing the fringing effect to increase further. However, as seen in Figure4.9, depending on the initial Λ_{max} and, critically, the properties of the positive linear function $\Lambda_{max}(t)$ a cell thickness yielding greater efficiency, alternative to the minimum one, could potentially exist. Cells designed with minimum thickness fall somewhere on the y-axis in Figure4.9. Increasing the thickness for the same system maps out some line that has a gradient determined by the function relating t and Λ_{max}. Steeper lines starting from larger values of $\Lambda_{max}(1)$ are more likely to have their maximum efficiency at the minimum thickness setup. Note that for non-unity fill factors it is far more likely that a better alternative can be found. Note also that as N increases the optimal set-up typically occurs for an equally thick or thicker LC layer.

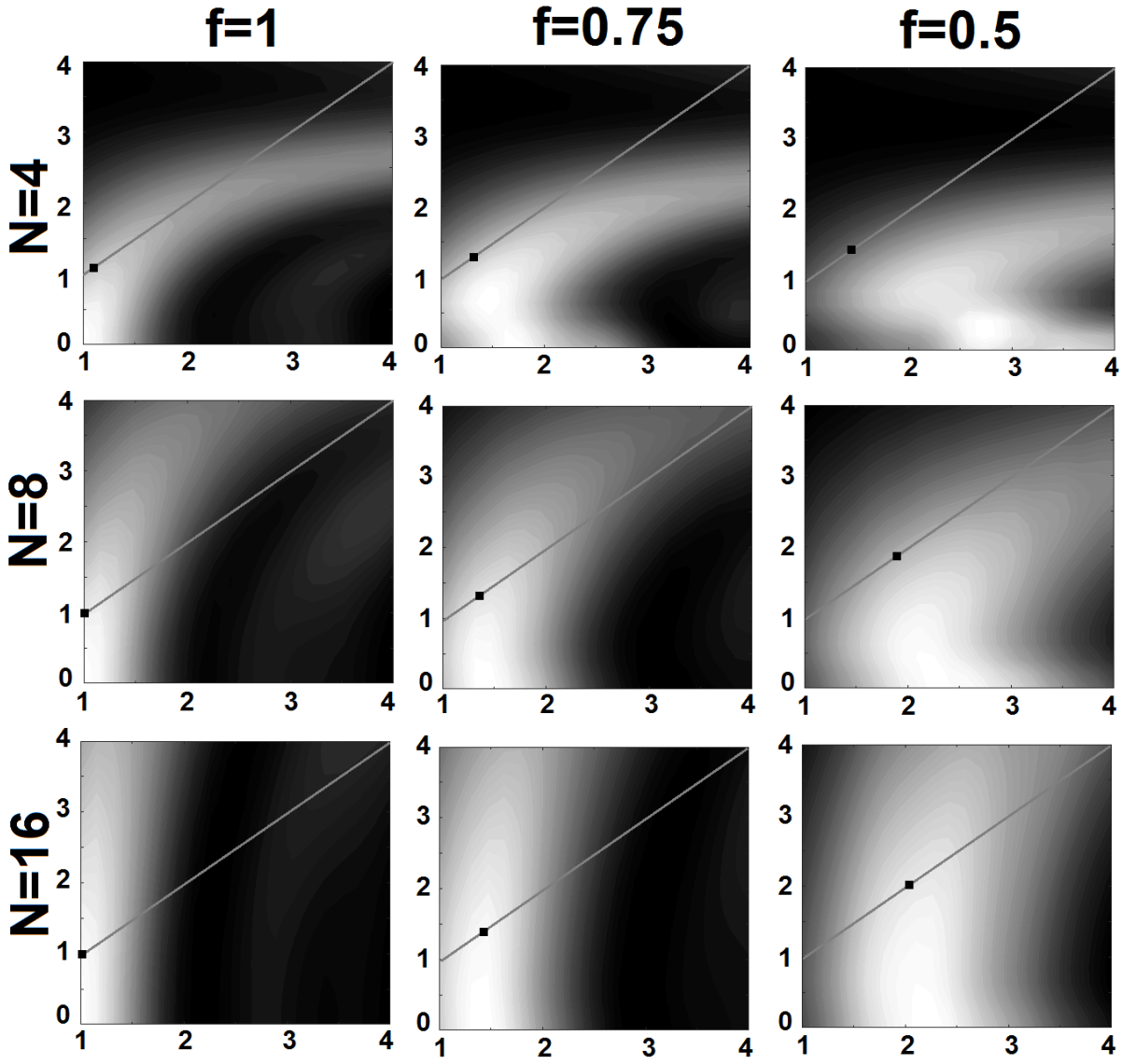

Fig. 4.9 Reticolo extracted target order efficiency plots for selected values of fill f and electrodes per period N. In all cases the x-axis corresponds to the fraction of 2π phase retardation attainable by the LC layer, given by $\phi_{max}(t)/(2\pi)$. The y-axis corresponds to the ratio $\Lambda_{max}(t)/\Lambda_{max}(t_{min})$. The grey line maps out the simple relationship between Λ_{max} and ϕ_{max} given by the function $\Lambda_{max}(t) = (\phi_{max}(t)\Lambda_{max}(t_{min}))/(2\pi)$. The black dot gives the maximum target efficiency along that line, and therefore for a given liquid crystal. Note however that the optimal thickness varies with N and cannot therefore be attained for all phase patterns.

Realising a phase-only LC SLM targeted primarily for beam steering applications requires information on steering range and resolution as dependent on the ratio λ/p, where λ is the operational wavelength and p is the pixel size. This ratio is constant for a given operational set-up, and is a geometrical factor which the rest of the device must account for. The maximum steering angle θ_{max} is given for the smallest period over which 2π phase shift is attained, d_{min}. From Equation4.5 θ_{max} is given by:

$$\sin(\theta_{max}) = \frac{\lambda}{d_{min}} = \frac{\lambda}{p}\frac{1}{q_{min}} \tag{4.22}$$

where $d_{min} = pq_{min}$ and q_{min} is the minimum number of pixels allowable in a period of the grating. So the maximum steering angle is inversely proportional to the number of pixels in the period. From Equation4.15 this corresponds to the minimum efficiency. Figure4.10 shows the steering angles obtained as a function of electrodes per period q for different constants of λ/p along with the target order efficiency. Enabling a viewing angle of 90° requires a maximum steering angle of ±45° which can only be attained for $(\lambda/p) \geq \sqrt{2}$. Furthermore, equality only yields ±45° steering for $N = 2$ which has very low efficiency, so a higher λ/p is typically required to allow this steer to occur for larger values of N and therefore at better efficiency.

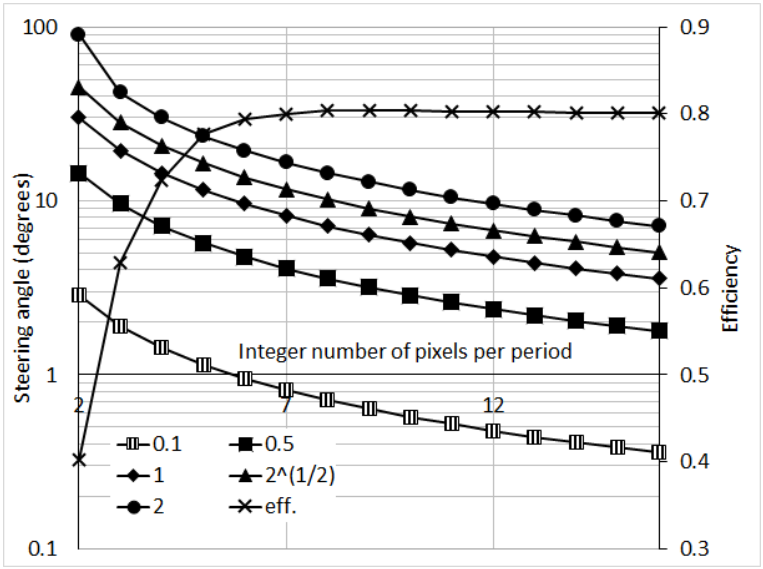

Fig. 4.10 Steering angle variation for increasing integer number of pixels per period for varying geometric constant λ/p values. Efficiency is included for easy comparison.

It is challenging to attain this requirement as it typically requires a sub-micron electronic pixel structure. This not only has high resistances resulting in degrading voltage patterns, as outlined in Equation2.15, but can lead to breakdown even at low voltages [35]. This is due to

the exceedingly small electrode separations required if a good fill-factor is to be maintained. Breakdown voltages for aluminium electrodes in air are given by the modified Paschen's curve, which can be seen in Figure4.11. Breakdown is known to have catastrophic effects on aluminium electrodes, which are normally found to have vaporised [15].

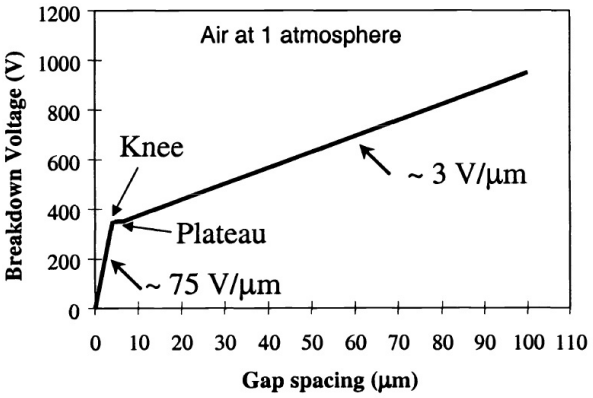

Fig. 4.11 Modified Paschen's breakdown curve for aluminium electrodes separated by air [127].

Additionally, for a given operational wavelength and LC material, the LC layer thickness required to attain the desired maximum phase shift is a constant irrespective of the pixel size. This means that Λ_{max} is also a constant. Decreasing the pixel size, particularly below $\Lambda_{max}/2$, leads to heavy degradation of the phase pattern due to fringing effects, with a corresponding decrease in the steering efficiency and accuracy of the system.

It is possible to increase the steering angle simply by creating an appropriate optical system surrounding the LC SLM. A simple yet effective approach is to set up a lens system which magnifies the steering angle by the factor necessary. An example can be seen in Figure4.12. For such a system the magnified steering angle is given by [71]:

$$\theta_{mag} = \frac{f_1}{f_2}\theta \tag{4.23}$$

where f_1 and f_2 are the focal lengths of the two lenses respectively. Note that this increase in range comes with a corresponding decrease in resolution. The difficulty in realising such a system lies in creating the lens system itself. If the device is to be used in the field it has to be both very compact and durable. Lenses increase in price considerably as their focal length decreases due to the more stringent tolerances of production required. Note that in any and all cases having such an optical system introduces a measure of aberration which can be mitigated by using an ad hoc aberration compensation phase patten, as outlined in Equation4.8.

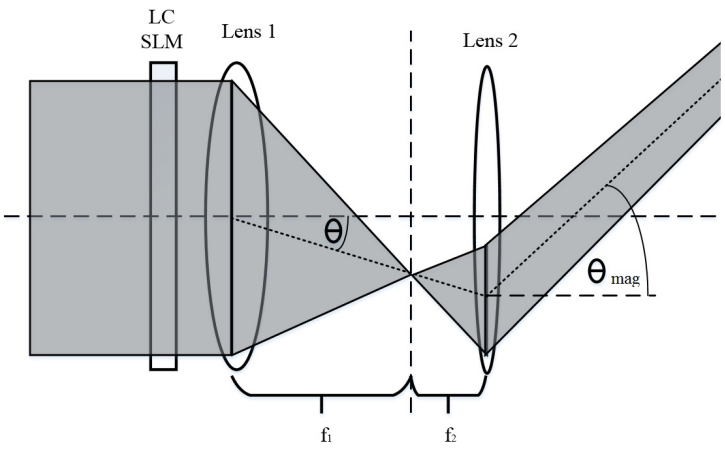

Fig. 4.12 Typical system for the magnification of the steering angle using lenses [71].

Another possible solution uses optical addressing to bypass the electrical challenges in attaining a sub-micron electrode structure. The system, which requires two lasers and two spatial light modulators is seen in Figure4.13. On the left hand side, a 'write' light is incident upon a first SLM which is electrically addressed, transmissive and equipped with crossed polarisers for amplitude modulation. The subsequent Fourier filter is sized so as to remove any high-frequency components, which are associated with the pixel structure of the SLM. The resultant intensity pattern can then be scaled down as required and is incident on the rear side of an optically addressed LC SLM (OASLM). Due to this downscaling, the intensity pattern incident on the OASLM can have periods unattainable with an electronic pixel pattern. This pattern then modulates the conductivity of a photoconductor which in turn varies the voltage across the LC layer of the OASLM [40]. A diagram of an OASLM can be seen in Figure4.13. Note that such a device must necessarily be reflective. Note that this method does not solve the challenges present due to fringing effects.

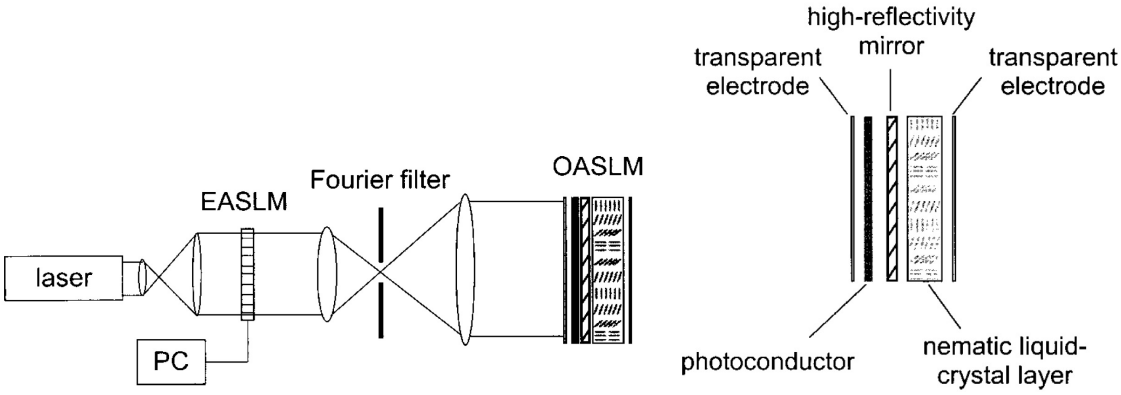

Fig. 4.13 OASLM-based beam steering set-up and primary OASLM components [40].

The resolution of a system depends on the number of addressable angles the system can attain. This is however limited by the beamwidth of the target order. Increasing the electrodes per period from q to $q+1$ and recalling Equation4.22 gives a difference $\Delta\theta(q)$:

$$\Delta\theta(q) = \theta(q) - \theta(q+1) = \sin^{-1}\left(\frac{\lambda}{p \times q}\right) - \sin^{-1}\left(\frac{\lambda}{p \times (q+1)}\right) \tag{4.24}$$

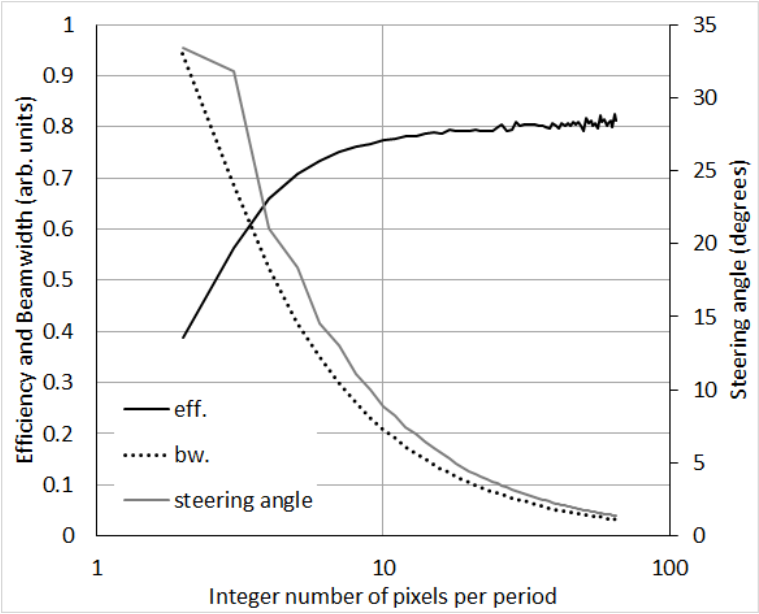

Fig. 4.14 Beamwidth, efficiency and steering angle for a single aperture phase pattern composed of an increasing integer number of constant-width pixels.

Figure4.10 also indicates how $\Delta\theta(q)$ varies for different values of λ/p. As q becomes larger $\Delta\theta(q)$ decreases considerably and is likely to be smaller than the beamwidth. Note that any magnifying optical system will also enlarge the values of $\Delta\theta$ proportionally. Figure4.14 shows the beamwidth of this target order, obtained from Equation4.15, as q is increased above 2. Pixel size is kept constant at 0.5 so as to start from a unit aperture for $q = 2$. This beamwidth decrease effect is compounded with that for a repeated aperture, as outlined in Equation4.9.

For small q values $\Delta\theta(q)$ is large, and it is therefore useful to be able to set up a pixelated phase pattern able to steer light at angles between those for subsequent values of q. For a general steering angle some phase resets will lie within a pixel, such that there is a fractional amount of pixels within each period of the equivalent ideal blazed grating. The phase level within these pixels is given by averaging the phase within the pixel and subsequently applying modulo 2π on the result [120], as seen in Figure4.15. For Reticolo implementation, also

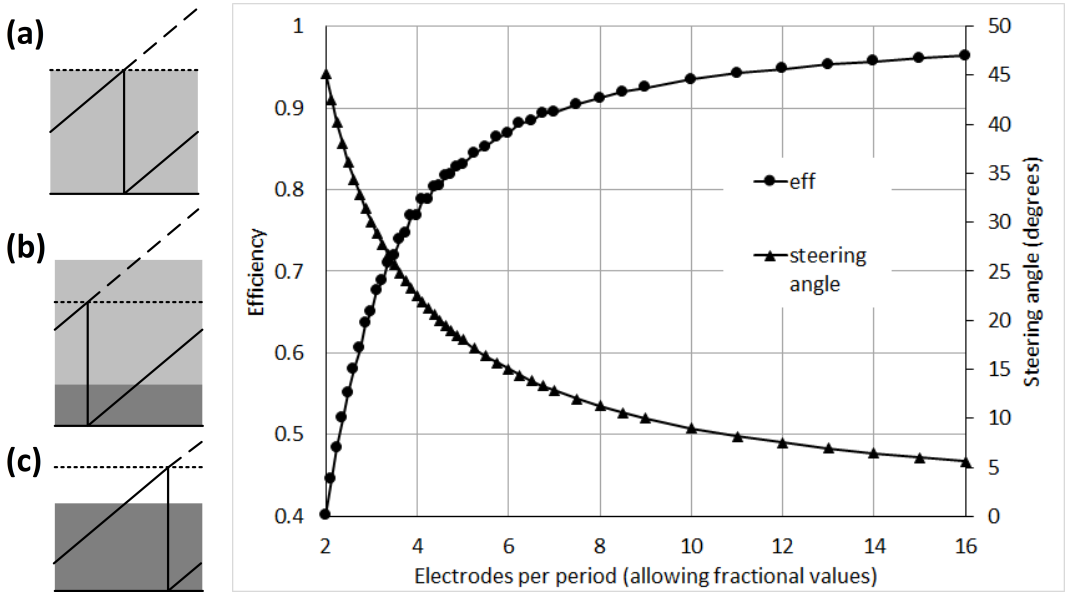

Fig. 4.15 Construction showing the phase approximation process for the pixel containing the phase reset in the case of fractional electrodes per period. The dotted line shows the steering phase pattern without modulo 2π. The solid line shows the phase pattern modulo 2π. The light grey phase level shows the result of averaging the dotted line phase pattern across the electrode. The dark grey phase level shows the value obtained by applying modulo 2π to the light grey phase level. Note that the order of operations is most crucial in (a) where averaging last yields a phase level of π, which is opposite to the intuitive approximation of 0. On the other hand, the order of operations makes no difference in (c). Plot showing efficiency and steering angle for increasing constant-width electrodes per period, allowing fractional values, as implemented in Reticolo.

seen in Figure4.15 for typical demonstration parameters, a periodic structure is required. For a fractional q value the resultant number of pixels within the Reticolo grating period is given by the product qN_{Ret}, where N_{Ret} is the minimum integer such that qN_{Ret} is an integer. Efficiency for the target order with fractional q follows the trend set by results for integer q very well, with steering direction also being as expected.

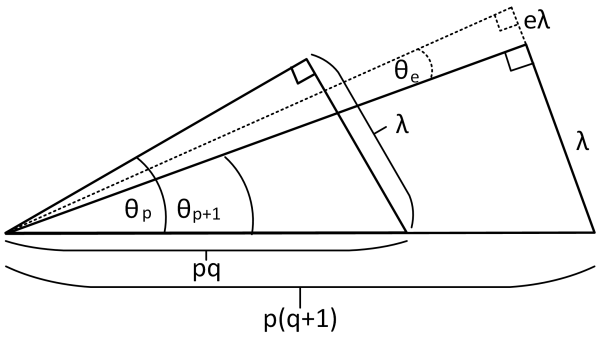

Fig. 4.16 Construction showing the extra angles attainable for an LC layer which can attain $> 2\pi$ phase retardation.

Alternatively, resolution can be increased by increasing the LC layer thickness so as to achieve phase delays of greater than 2π. For an extra amount of phase $2\pi e$, where e is the factor describing the amount of added phase delay attainable, the number of extra angles that can be addressed without changing the value of q becomes:

$$255 \times \frac{e}{1+e} \tag{4.25}$$

for an 8-bit addressing system.

Unfortunately, for a particular value of q, not all of these angles will be new angles lying conveniently between $\theta(q+1)$ and $\theta(q)$. For this to be true, referring to Figure4.16:

$$\theta(q) \geq \theta(q+1) + \theta(e) \quad \Rightarrow \quad \sin^{-1}\left(\frac{\lambda}{pq}\right) \geq \sin^{-1}\left(\frac{\lambda(e+1)}{p(q+1)}\right) \tag{4.26}$$

Which since $\sin^{-1}$ is monotonic reduces to:

$$e \leq \frac{1}{q} \tag{4.27}$$

This implies that the required extra phase is given by $2\pi/q$ and gives floor$(255/(1+q))$ extra addressable angles. This improvement, while marginal, helps to even out the resolution discrepancy between large and small values of q. It also allows larger steering for a given

grating period. The drawback is further loss in operational speed and increase in the fringing effects due to the added LC thickness.

A solution which does not involve the LC SLMs themselves is to cascade two devices, where one is a 'coarse' steerer and the the other is a 'fine' steerer, as seen in Figure4.17. For an LC SLM with a maximum difference between steering directions $\Delta\theta\left(q_{min}\right)$ for a given λ/p_{coarse}, which can be described as the 'coarse' steerer, a 'fine' steerer has a maximum steering direction $\theta_{fine-max}(q_{min}) = (\Delta\theta\left(q_{min}\right))/2$ as set by a constant λ/p_{fine}. Note that $p_{fine} > p_{coarse}$. Note also that in theory, further superfine steering devices may be added having larger pixel size, but in practice this might be prohibitive in terms of efficiency, not only due to material absorption compounding from the many layers, but also due to the large size of the required pixels making it very difficult to have a sufficient amount of pixels illuminated for good steering properties. Note finally that the maximum steering angle θ_r for such a system follows the grating equation such that, for N parallel steering elements having maximum steering angles $\phi_{1...N}$, θ_r is given by:

$$\sin\theta_r = \sin\theta_{inc} + \sum_{n=1}^{N} \sin\phi_n \tag{4.28}$$

where θ_{inc} is the incidence angle on the first steering element. Note that for non-parallel steering elements the expression is more complex as subsequent incident angles cannot easily be decomposed.

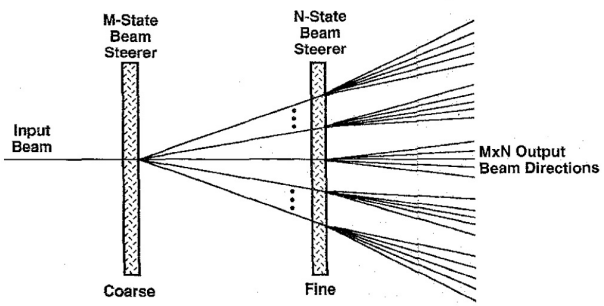

Fig. 4.17 Example of cascaded LC SLMs for resolution increase [76].

4.2 Addressing structures for liquid crystal spatial light modulators

Various addressing structures exist to enable control of the LC layer by applying an electric field. Typically, the more flexibility a technique allows the more complex fabrication and

control will be. It is therefore pivotal to match the address strategy with the application at hand. The most straightforward way of achieving an electrode structure is direct addressing, where each and every single electrode has its own connection and driver, all acting independently. This does give great flexibility but limits the possible size of the device and is only ever used in very simple devices, such as displays for watches and calculators [50]. This method is therefore perfect for proof of concept one-off devices.

For middle infrared beam-steering applications we require electrodes with width comparable to the operational wavelength if we hope to attain high steering angles. For a minimally useful active area of approximately 1 mm^2 this requires between a hundred and a thousand electrodes. Driving so many electrodes independently is prohibitive without ad hoc driving devices which are themselves not trivial to develop. Linking electrodes can dramatically reduce the amount of addressable electrodes. This results in a corresponding reduction in the amount of distinct phase patterns that can be applied to the device, with the simplest case being that of an inter-digitated grating which can only be used as a switchable binary grating of fixed period, as seen in Figure4.18. In this case all the electrodes attached to the same contact pad are effectively connected.

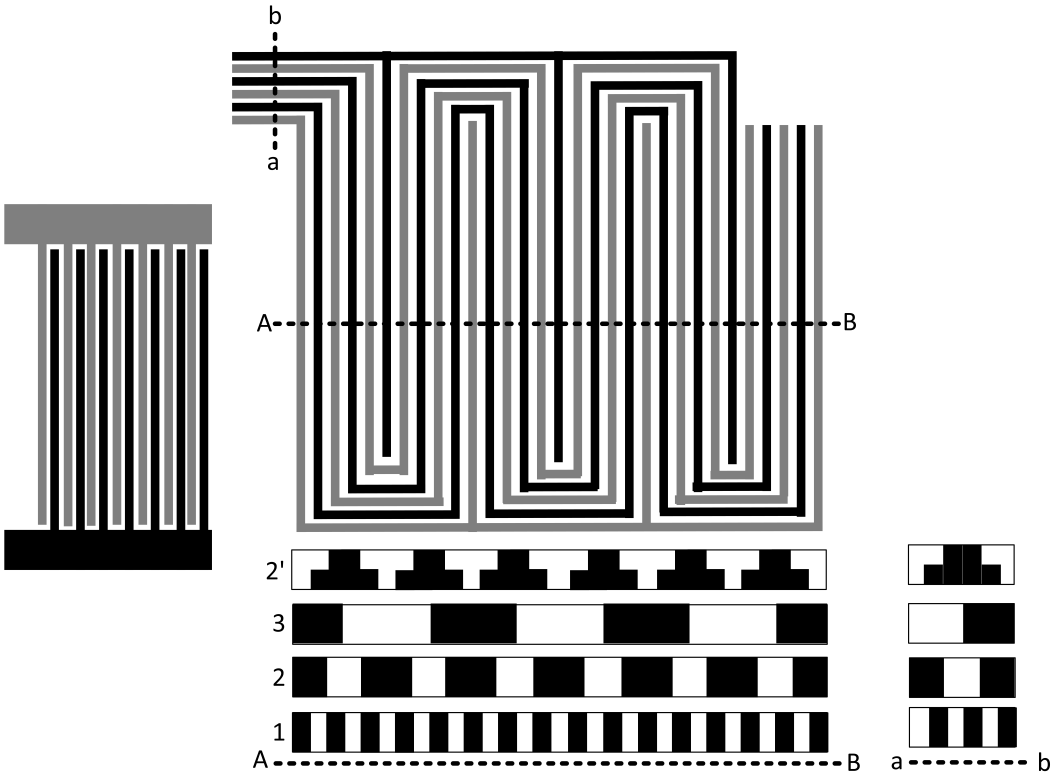

Fig. 4.18 Simple interdigitated switchable binary grating with constant period $2p$ and grating having a 'snake' structure, which allows gratings of different periods to be realised.

A variable period binary grating can be attained by the snaking structure shown in Figure4.18. Depending on the amount of electrodes N_e the amount of distinct binary phase patterns that can be realised is $N_e/2$, with fractions rounded down, having some effective electrode width np depending on the amount of adjacent electrodes n having the same voltage. Note however that at the bends in the electrode structure these effective electrodes might have different widths depending on whether N_e is even or odd and on the value of $(N_e/2)$ mod n . This complication is less critical for larger values of N_e. Constructing the electrode addressing pattern from the centre evens out the effect at the bends. Note also that for large enough values of n a non-binary fan-out pattern can also be realised with such a structure, improving the efficiency when compared to that of the equivalent binary pattern. Note that in this case the maximum attainable phase retardation needs to increase accordingly from the minimum of π required for binary gratings.

The maximum attainable efficiency for a binary grating is 0.4, as seen in Figure4.15. A blazed grating is therefore far more preferable. A very efficient approach is to have a number of address electrodes N_e linked through an insulator to the SLM electrodes. Any amount of SLM electrodes can be addressed in this fashion. Such a system can be seen in Figure4.19. Blazed gratings with electrodes per period $N_e/(2^m)$ where $m \varepsilon \mathbb{Z}$ can be realised, giving $2M+1$ addressable angles with no fractional electrode issues if $N_e = 2^M$ for some $M \varepsilon \mathbb{N}$. It is unfortunately not at all easy to realise such a system. Address electrodes would first have to be deposited and patterned on the substrate. An insulating layer has to be subsequently deposited and patterned so as to yield perforations through to the address electrodes. SLM electrode material needs to be subsequently deposited to fill these holes, allowing electrical contact, and then patterned to generate the SLM electrodes themselves. This process necessarily involves three distinct lithography processes which need to be aligned carefully. Extreme care needs to be also given to the etching processes if electrical contact is to be ensured.

A less lithographically intensive alternative is given in Figure4.20. This method is exactly the same as that in Figure4.19 in terms of the blazed gratings it can realise, but can be attained using only a single lithographic process. The N_e electrodes spiral inward so as to create an active area where the blazed pattern set by the electrodes is repeated for however many revolutions the electrodes undertake within the spiral. For a typical desired active area and electrode widths, along with a moderate $N_e = 16$ which gives 9 addressable angles, between 10 and 100 revolutions *Rev* are required. The area of such a spiral is then given by:

$$Area = (6Rev^2 - 7Rev + 2 + p_{address}/p)(N_e p)^2 \tag{4.29}$$

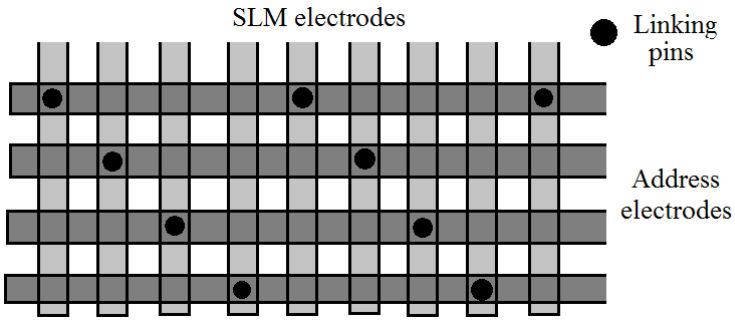

Fig. 4.19 Linked electrode system allowing any number of SLM electrodes to be addressed from a much smaller number of address electrodes. This limits the number of addressable angles greatly but is also much less involved to control.

where $p_{address}$ is the width of each of the N_e address electrodes, which is typically chosen depending on the flex contact to be used. Assuming that the electrodes all have approximately the same length, this length l is given by:

$$l = \left(\frac{Area}{N_e}\right)\left(\frac{fp}{p}\right)\left(\frac{1}{fp}\right) = \frac{Area}{N_e p} = (6Rev^2 - 7Rev + 2 + p_{address}/p)N_e p \qquad (4.30)$$

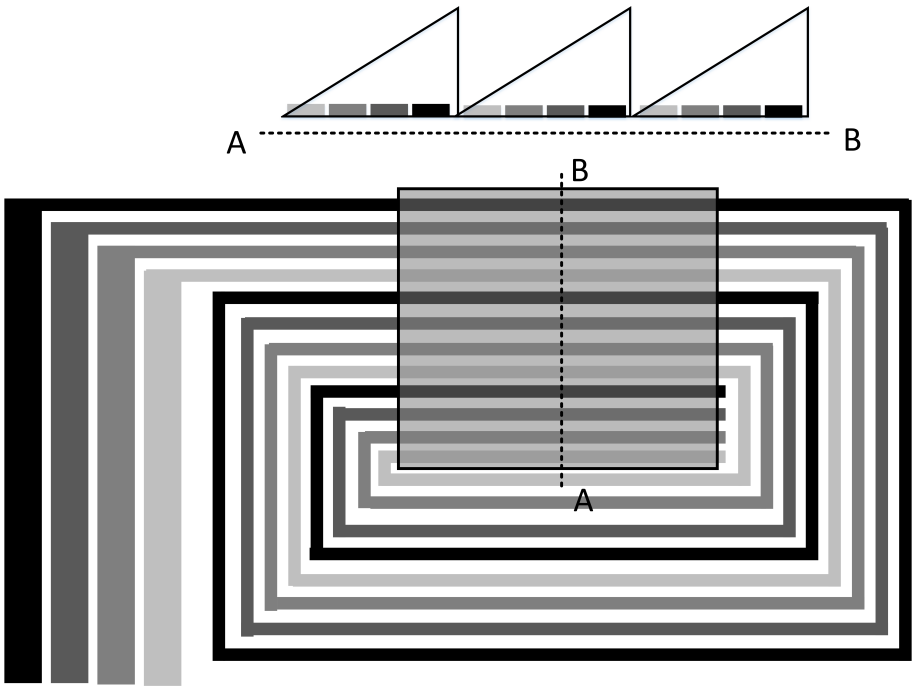

Fig. 4.20 Spiral-enabled blazed grating with limited steering angles.

Ignoring the component related to the address electrodes, the ratio $l/p = 8512$ and 948832 for $Rev = 10$ and 100 respectively. For such a high aspect ratio the voltage loss along the electrode V_{drop-R}, as outlined in Section2.1, could be prohibitive. Assuming uniformity along the electrodes yields a linear voltage drop along its length. We assume further that the normalised voltage drop is equal across the electrodes N_e for one period of the phase pattern and that the voltage drop is negligible along each pass of the active area. The resultant phase pattern across the active area is therefore changed from the ideal blazed grating. Values for every period are divided by a factor determined by the normalised V_{drop-R} and the number of revolutions, which is given for each period n by $1-(V_{drop-R}((n-1)/Rev))$, and can be seen for $Rev = 4$ in Figure4.21.

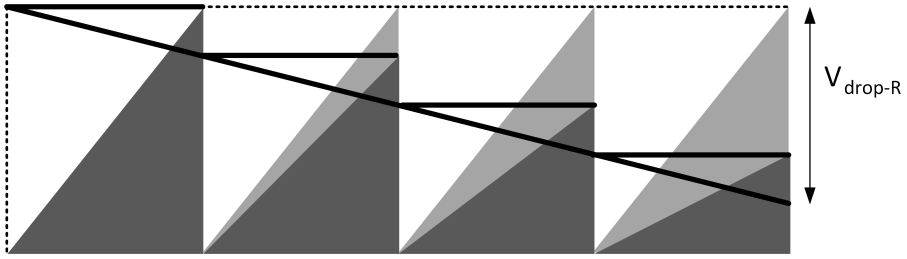

Fig. 4.21 Effect of voltage loss on the addressed phase pattern for a spiral electrode structure with light grey being the original phase pattern and dark grey being the modified phase pattern.

This is implemented in Figure4.22 for $Rev = 10$ and 100. Increasing revolutions results in lower efficiency and greater beamwidth for equal values of fractional voltage drop along patterned electrodes. However, it also results in greater accuracy in the steering angle. In all cases we have a marginal decrease in accuracy, $\approx 20\%$ increase in beamwidth and $\approx 50\%$ decrease in efficiency as $V_{drop-R} \longrightarrow 1$. Calculating V_{drop-R} for a given system using Equation2.12 and subsequent expressions is therefore critical in assessing the performance and viability of a system, particularly for relatively high electrode material sheet resistance, such as that expected for transparent conducting materials.

More complex devices which require a full pixel structure cannot possibly be addressed directly. Passive addressing reduces the electrical connections necessary for an M column by N row device from $M \times N$ to $M+N$. A typical system is given in Figure4.23. The column and row electrodes are on opposite substrates with the LC layer in between. The column electrodes are addressed by a data voltage V_d particular for each pixel in that column. Every pixel that needs to be switched on using V_d is selected by addressing the corresponding row with a select voltage V_s. This is such that $V_d + V_s$ is the voltage necessary to achieve the desired LC molecule re-orientation but both V_d and V_s are smaller than the threshold voltage for the LC material being used V_{th}. Unfortunately this kind of system limits the maximum

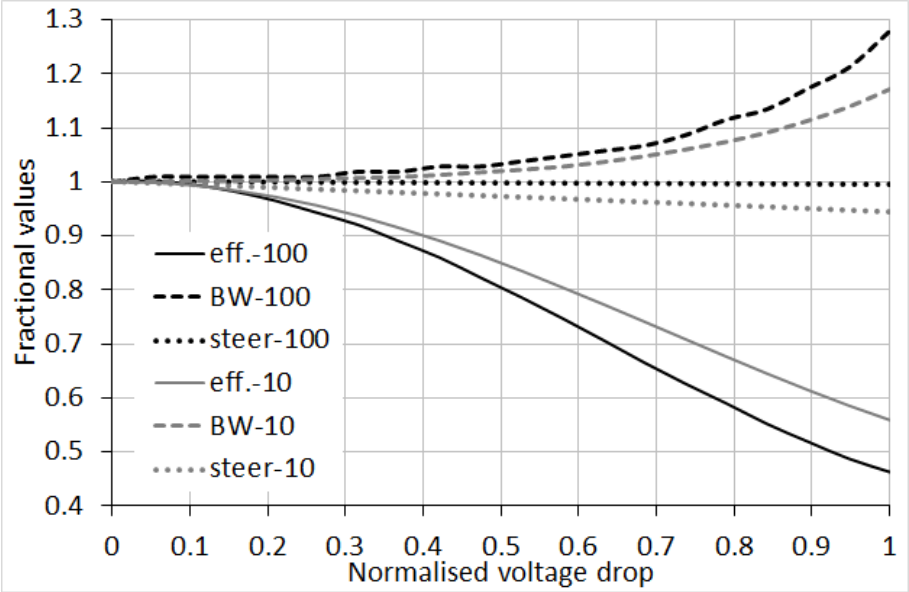

Fig. 4.22 Efficiency, beamwidth and steering angle of the target order for increasing values of normalised V_{drop-R}. Values are given as a ratio to the properties for no voltage drop.

voltage which can be applied across the LC layer to $\approx V_{th}$, such that the higher voltage region of the electro-optic response cannot be made use of. This is typically acceptable for optical devices where the maximum phase retardation extracted from Equation3.2 is typically much larger than for mid-IR wavelengths for comparable LC layer thicknesses due to the much smaller wavelength. These systems are also particularly vulnerable to crosstalk. Since each row is addressed sequentially, successful operation hinges on the fact that a complete frame can be addressed in a time smaller than the decay time of the induced orientation of the LC layer τ_d. It is also therefore non-trivial to construct a driver for such a system.

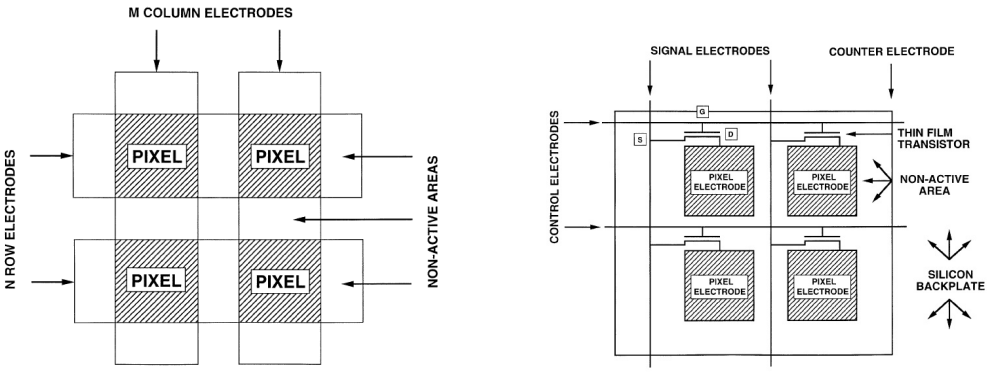

Fig. 4.23 Basic architecture of passive and active addressing systems [50].

Active matrix addressing makes use of a thin film transistor layer to address each pixel separately. This architecture achieves high contrast and greyscale response with sufficient response times and little crosstalk. These devices are expensive to produce and luminosity is an issue, but their high commercial potential powers research and development [50]. Active matrix addressing operates by supplying a pulse to each pixel sequentially with the charge stored in the pixel which acts as a capacitor. Charge leaking to the LC material is in fact a concern in this type of device [104].

4.3 Non-diffractive light steering techniques based on liquid crystals

4.3.1 The liquid crystal active cladding single mode slab optical waveguide

In the above analysis it is seen that it is not trivial to attain a high efficiency with a liquid crystal spatial light modulator. The radiation to be modulated typically passes through all of the components of the device, which puts tight material restrictions. The liquid crystal properties only exacerbate these material hurdles. Fundamental trade-offs mean that it is difficult to improve performance beyond certain limits. Realising a suitable electrode structure is involved. The trade-off between address flexibility and complexity needs to be considered carefully, and the knock-on diffractive effects kept in mind.

Non-diffractive steering techniques allow for beam-steering without any unwanted orders to appear. Two such techniques are described in this section. Both are based on the liquid crystal active cladding optical waveguide as seen in Figure4.24. This is described in the current subsection. Such an optical slab waveguide can be used to achieve in-plane steering by creating prisms of different refractive index in the upper cladding, resulting in steering by Snell's law at each boundary. The steering angle is controlled by varying the refractive index shift at the boundaries. This technique is described in the following subsection. The second technique, described in Subsection 4.3.3, is a complementary technique that achieves out of plane steering by creating a tapering lower cladding. This allows radiation to out-couple at an angle given by, amongst other variables, the upper cladding refractive index. This allows the steering angle to be controlled. The interest in this structure is four-fold. Apart from the possibility of non-diffractive steering, this structure has potential for fast switching devices that can attain large steering angles with low absorption [24].

This structure is formed of a core of thickness t, having refractive index n_1, a lower cladding having refractive index n_2 and a switchable upper cladding formed of an LC layer.

This upper cladding has a refractive index $n_3 + \Delta n_3(V)$, which is a function of the voltage set across the cladding. Note that for typical operational voltages Δn_{3-max} is lower than the LC birefringence since the evanescent wave within the cladding only penetrates a small thickness. Within this thickness the LC molecules are tightly bound to the alignment layer and therefore can only re-orient slightly, even for high voltages. This has the upside of making any re-orientation much faster than for the LC molecules in the bulk of the layer. Note further that the driving voltage is typically set between electrodes on the top of the LC layer and some ground electrode below the lower cladding so as to not interfere with the operation of the optical waveguide.

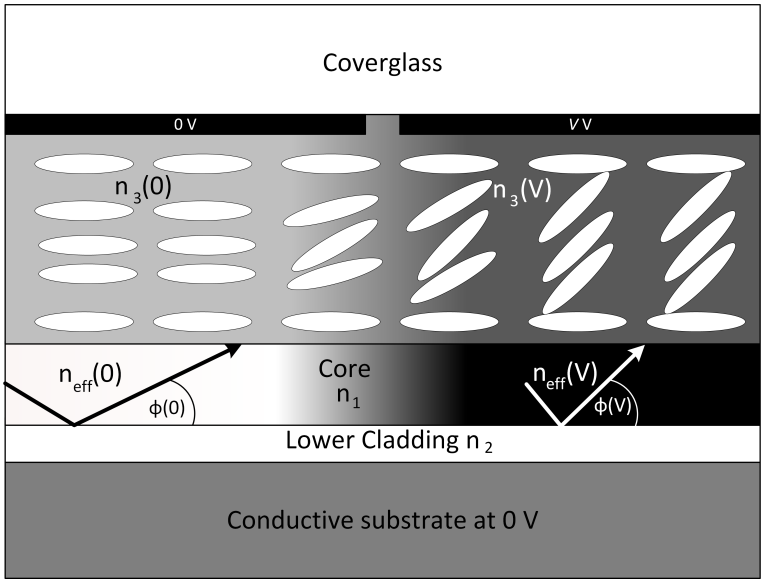

Fig. 4.24 Liquid crystal active cladding optical slab waveguide.

The condition for light propagation in the core arises from total internal reflection, therefore $n_1 > n_2 \geq n_3$ [1]. For some angle ϕ between propagation direction and core boundary, as seen in Figure4.24, applying Snell's law gives the condition $\cos\phi \geq n_2/n_1 \geq n_3/n_1$. Recalling that the propagation constant k for some mono-chromatic radiation becomes nk in a medium of refractive index n, and defining the ϕ-dependent propagation constant within the core as $\beta = n_1 k \cos\phi = n_{eff} k$, the condition for propagation of radiation having propagation constant β becomes $n_1 k > \beta \geq n_2 k \geq n_3 k$. Phase considerations add a quantisation condition by considering that only radiation which has incidence angle ϕ such that constructive interference occurs for subsequent reflections can result in a propagating mode. The phase path difference is given by:

$$2\pi M = 2t \sin\phi - \delta_{12} - \delta_{13} \tag{4.31}$$

where $M \varepsilon \mathbb{Z}^+$ and δ_{12} and δ_{13} are the phase delays at the internal reflections. For a transverse electric polarisation this is given by:

$$2\pi M = 2tq - 2\tan^{-1}(p/q) - 2\tan^{-1}(r/q) \tag{4.32}$$

where $p^2 = \beta^2 - n_2^2k^2$, $q^2 = n_1^2k^2 - \beta^2$ and $r^2 = \beta^2 - n_3^2k^2$. Rearranging yields:

$$\tan(tq - M\pi) = \frac{(p+r)q}{q^2 - pr} \tag{4.33}$$

It is the case that not all modes M are allowed for any thickness t, finding the cut-off thickness t_{c-M} below which mode M cannot propagate allows single mode waveguides to be realised. The cut-off condition arises when total internal reflection becomes disallowed, therefore when $\beta = n_2k$. For this condition $p^2 = 0$, $q_c^2 = k^2(n_1^2 - n_2^2)$ and $r_c^2 = k^2(n_2^2 - n_3^2)$. Substituting this in the above and rearranging for thickness yields:

$$t_{c-M} = \frac{1}{q_c}\left(\tan^{-1}\frac{q_c}{r_c} + M\pi\right) \tag{4.34}$$

Evaluating the above for $M = 0$ and $M = 1$ and subtracting yields the core thickness range for which the waveguide is single moded. Note that due to the active cladding employed both values need to be evaluated at n_3 and $n_3 + \Delta n_3$, with the actual allowable core thickness being that which overlaps for both extremes of cladding refractive index. Note also that if $n_3 < n_2 < n_3 + \Delta n_3$ the cut-off condition changes to comply with the largest cladding refractive index present in the system. For this region it is required to extract $n_{eff} = \beta/k$, which is the effective refractive index of radiation propagating within the core. For a single-moded waveguide from Equation4.35 we have:

$$\tan(tq) = \frac{(p+r)q}{q^2 - pr} \tag{4.35}$$

This equation cannot be solved analytically for β and therefore graphical techniques are used. Finding β, and therefore n_{eff}, as a function of allowable thickness t and n_3 allows the evaluation of Δn_{eff} at a given thickness, such that the ideal thickness is that which results in the greatest value of Δn_{eff}. The usefulness of these structures for beam-steering arises from this voltage controllable n_{eff}.

4.3.2 Patterned electrode enabled steering within the slab waveguide plane

Due to the voltage controllable $n_{eff}(V)$ observed in LC-active cladding waveguides, electrodes which are orders of magnitude greater than the operational wavelength can effectively set up prisms of different refractive indices depending on the voltage applied. Beam-steering can be therefore attained by carefully designed electrodes and the implementation of Snell's Law. Note firstly that in all cases we will consider the active LC cladding as an anti-parallel aligned cell with director in the original propagating direction, typically the x-direction, such that for some driving voltage V, $n_{eff}(V) \leq n_{eff}(0)$, and, crucially, for some beam propagating at an angle $\theta_{beam} > 0$ with respect to the x-axis, $n_{eff-\theta_{beam}}(V) = n_{eff-0}(V)\cos\theta_{beam}$.

Figure4.25 (a) shows a basic implementation with two electrodes forming an array of intersecting prisms. In this case the angle each boundary makes with the x-axis is $\pm\theta_{boundary}$ where $\theta_{boundary}$ is constant. A positive x-axis propagating TE beam with initial $\theta_{beam} = 0$ is steered in the positive or negative y direction depending on which electrode has a voltage $V \neq 0$ applied to it. The steering magnitude is dependent on the difference $n_{eff}(V) - n_{eff}(0)$, with a larger difference corresponding to a larger deflection angle at the prism boundary due to Snell's law. Figure4.25 (b) shows the structure which maximises the number of interactions for a given device length [18].

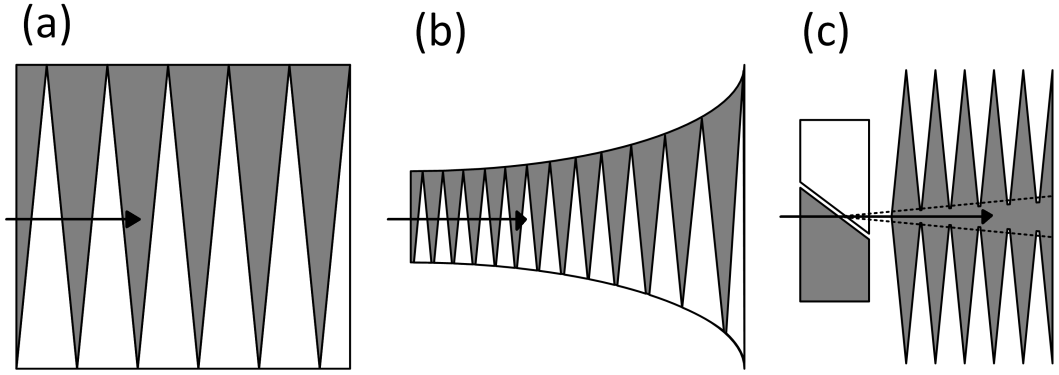

Fig. 4.25 Constant $\theta_{boundary}$ in-plane steering set-up for square and optimised configurations along with set-up involving a direction selector.

In such a system, for a beam propagating upwards at an angle θ_{beam} that hits a positive gradient boundary going from $n_{eff-high} \longrightarrow n_{eff-low}$, the incident angle θ_{inc} is given by $\theta_{inc} = \pi/2 - \theta_{boundary} + \theta_{beam}$. In the same system at the same state, but for a negative gradient boundary, θ_{inc} is given by $\theta_{inc} = \pi/2 - \theta_{boundary} - \theta_{beam}$. Note for the latter that if $\theta_{beam} = \pi/2 - \theta_{boundary}$ then $\theta_{inc} = 0$. The steering limit for such a system is therefore $\theta_{beam-max} = \pi/2 - \theta_{boundary}$. In principle any angle approaching $\pi/2$ can be attained by

choosing a sufficiently low $\theta_{boundary}$. Note however that a limit is still present due to the critical angle for the $n_{eff-high} \longrightarrow n_{eff-low}$ boundary interaction, where the maximum incident angle is $\theta_{crit} = \sin^{-1}(n_{eff-low}/n_{eff-high})$. Note also that as $\theta_{boundary} \longrightarrow 0$ it becomes increasingly difficult to realise such a system. This is because the length of the electrode pattern increases as $(\tan(\theta_{boundary}))^{-1}$. A first improvement can be attained by adding selector electrodes at the start of the electrode pattern. This selects the direction of the steer such that the electrode pattern can be designed individually for each direction. These are typically symmetric about the centre line, as seen in Figure4.25 (c). For a constant $\theta_{boundary}$ system this reduces the length of the equivalent system by a factor of two.

Minimisation of interactions requires maximisation of the refractive effect at each boundary. For given materials this can only be increased by increasing θ_{inc}. Fixing θ_{inc} close to the maximum allowable values enables this. Without loss of generality, for a positive θ_{beam} interacting at a boundary from $n_{eff-high} \longrightarrow n_{eff-low}$ for fixed θ_{inc} results in a $\theta_{boundary}$ given by:

$$\theta_{boundary} = \pi/2 - \theta_{inc} + \theta_{beam}$$

and the resultant $\theta_{beam-new}$ is given by:

$$\theta_{beam-new} = \theta_{beam} + \theta_{ref} - \theta_{inc} \tag{4.36}$$

where:

$$\theta_{ref} = \sin^{-1}\left(\frac{n_{eff-high}}{n_{eff-low}}\sin\theta_{inc}\right)$$

having $\theta_{inc} < \theta_{crit}$ for a critical angle $\theta_{crit} = \sin^{-1}(n_{eff-low}/n_{eff-high})$. For the opposite boundary type:

$$\theta_{boundary} = \theta_{inc} + \theta_{beam} - \pi/2 \quad \text{and} \quad \theta_{beam-new} = \theta_{beam} - \theta_{ref} + \theta_{inc} \tag{4.37}$$

where θ_{ref} is as the previous case but with refractive indices inverted. Note also that unlike the previous case $\theta_{inc} < \pi/2$. Note that in the former case $\theta_{boundary} > 0$ in all cases. Therefore all boundaries have a positive gradient. For the latter case $\theta_{boundary} < 0$ only for $\theta_{beam} < \pi/2 - \theta_{inc}$. Therefore, as seen in Figure4.26(a), a single electrode pattern similar to that in Figure4.25(c) but with the triangle sides having a slope set by $\theta_{boundary}$ can only be realised if the target steering angle is smaller than $\pi/2 - \theta_{inc}$. A first solution, seen in Figure4.26(b), is to only use the former configuration for steering and designing the boundary

corresponding to the latter configuration such that $\theta_{inc} = 0$ for all values of θ_{beam}. This allows designs for a maximum steering angle up to θ_{crit} to be realised.

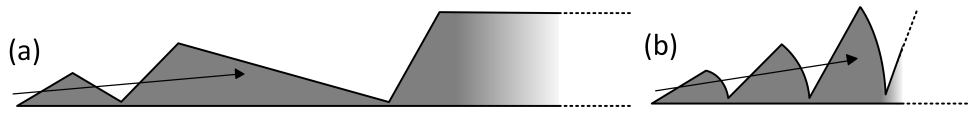

Fig. 4.26 Constant θ_{inc} single electrode patterns for both boundaries (a) and only one boundary (b) being steering enabled.

A key limitation in all the electrode patterns which involve a selector considered up to this point is that enabling full range steering with a single electrode requires each electrode steering element to start and finish at the middle symmetry line, with some tolerance provided by the line making an angle $\theta_{selector}$ to the horizontal symmetry line, as seen in Figure4.25(c). Tackling this problem requires division of the single steering electrode into a number of independently addressed modules. For each such module the steering elements have to be defined to a height determined by $\theta_{beam-max}$ attained by the previous module driven at the highest possible voltage, which is larger than the $\theta_{selector}$ we were restricted to for the case of a single electrode. This shortens the device at the cost of adding more electrodes. Note that for any module to be applied all previous modules need to be maximally applied. A simple graphical representation of this is given in Figure4.27.

An electrode pattern where each steering element is independently addressed is, where the number of electrodes allows, the set-up which minimises device length. All possible configurations are displayed in Figure4.28. All designs can be adapted for a maximum steering angle up to π relatively straightforwardly. Configuration (c) results in the smallest number of interactions required since there is no θ_{crit} restrictions on the θ_{inc} chosen. Configuration (a) uses all boundaries available and therefore designing curved boundaries for $\theta_{inc} = 0$ is not required.

Two fundamental impediments to designing high θ_{inc} systems is increased Fresnel reflections and beam divergence/width effects at the boundary interactions. The former is mitigated by the fringing effect in the LC layer, which causes a graded index at the boundary, thus decreasing reflection considerably, as outlined in Equation2.25. For some divergence ϕ of the incident radiation at a boundary, the divergence of the refracted beam $\phi_{new} = |\Delta\theta_{beam-new}|$ is given by:

$$\phi_{new} = \sin^{-1}\left(\frac{n_{pre}}{n_{post}}\sin(\theta_{inc} + \phi/2)\right) - \sin^{-1}\left(\frac{n_{pre}}{n_{post}}\sin(\theta_{inc} - \phi/2)\right) \tag{4.38}$$

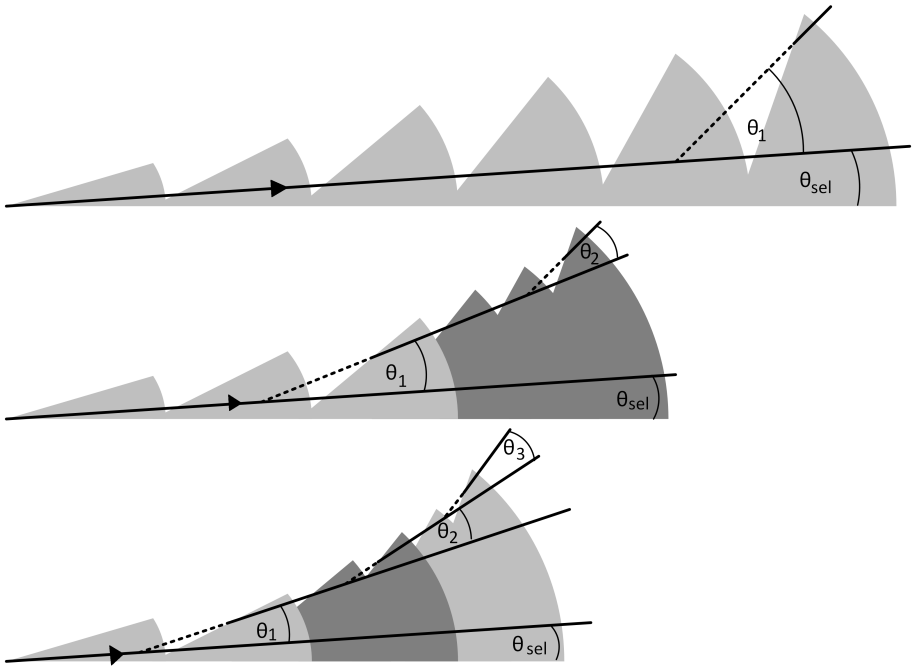

Fig. 4.27 Sample electrode patterns which attain a desires steering angle using 1, 2 and 3 modules respectively, with length decreasing for increasing number of modules.

As seen in Figure4.29, the $\theta_{inc} > \pi/4$ region we are interested in the sin curve becomes flatter as the argument tends to one. Multiplying the sin value of two arguments separated by some angle ϕ by some fixed ratio increases or decreases the sin values accordingly. It also increases or decreases the difference between the two results when compared to the difference between the two original values, labelled $\phi_{\sin}$ for convenience. Note also that for a given ratio which causes an increase when compared to $\phi_{\sin}$, that increase is larger than the decrease to $\phi_{\sin}$ when the reciprocal of that ratio is applied. These intervals correspond to an even larger change when compared to ϕ upon the operation $\sin^{-1}$. This is due to the decrease in gradient of the sin curve in the region of interest. This implies that the divergence is reduced for an electrode set-up resembling that in Figure4.28(c), increased in (b) and modified by some difference between divergent and convergent components in (a). A fuller treatment requires consideration of the effect of those boundaries designed at $\theta_{inc} = 0$, particularly due to their curvature.

Establishing an electrode pattern from the angular description of the system obtained by applying Equations4.36 and 4.37 requires the introduction of the beamwidth parameter. The width of the beam determines the minimum length of each diffractive element required for refraction of the whole beam. For a beam of beamwidth BW propagating at θ_{beam} interacting with a boundary at $\theta_{boundary}$ the length l of the required diffractive element such that all the beam is involved in the interaction is given by:

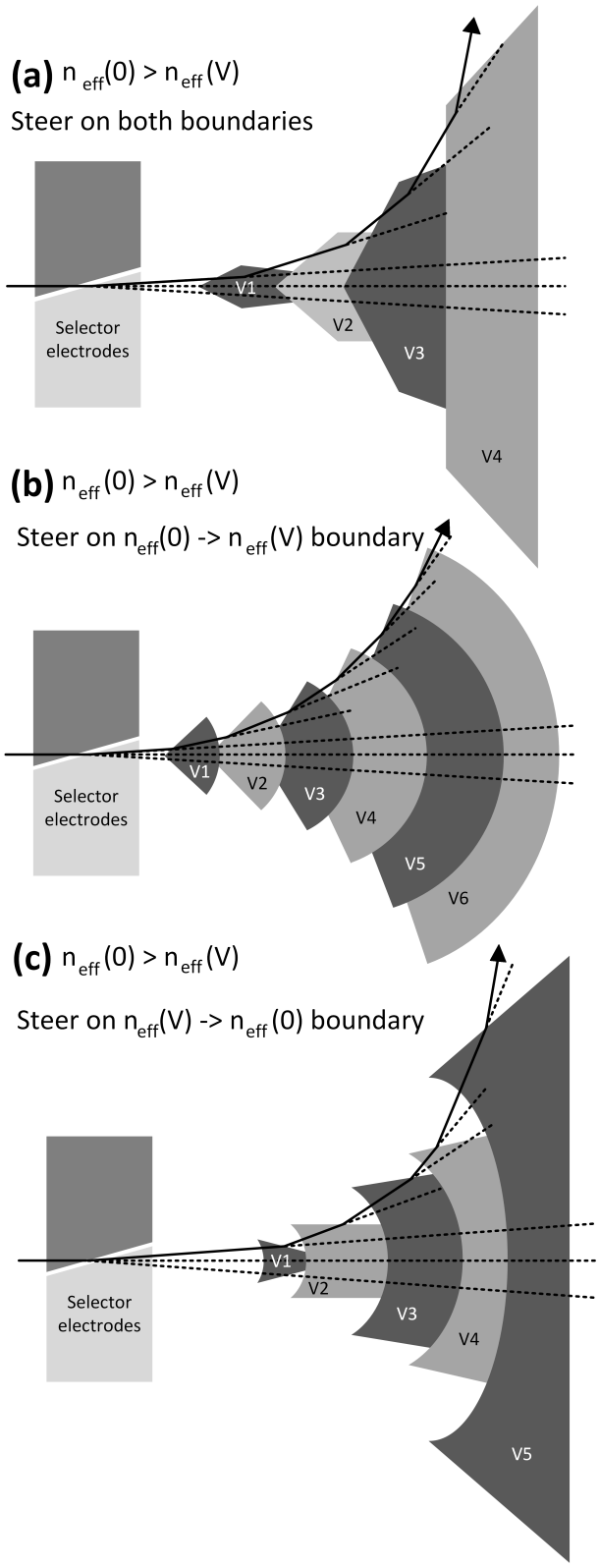

Fig. 4.28 High θ_{inc} electrode patterns for individually addressable electrodes and different types of steering-enabled boundaries.

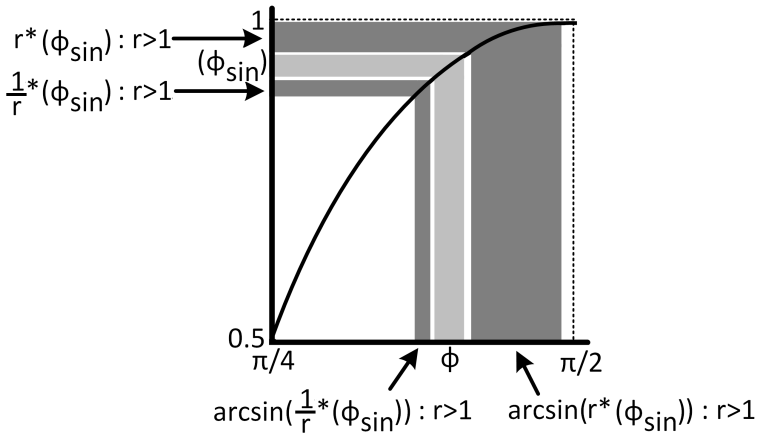

Fig. 4.29 Graphical justification for divergence increase or decrease at a refractive boundary depending on the boundary material properties and direction of incidence.

$$l = \frac{BW}{\sin(\theta_{boundary} - \theta_{beam})} = \frac{BW}{\cos(\theta_{inc})} \tag{4.39}$$

with the x and y components given by $l\cos(\theta_{boundary})$ and $l\sin(\theta_{boundary})$ respectively. Note that depending on angle sign conventions negative values of l can arise, as such the sign of the x and y components is based solely on the sign of $\theta_{boundary}$. Note also that the width of the beam changes after every such interaction, with the new beam width given by:

$$BW_{new} = l\cos(\theta_{ref}) \tag{4.40}$$

Therefore if $\theta_{ref} < \theta_{inc}$ we have a beamwidth increase and a beamwidth decrease when $\theta_{ref} > \theta_{inc}$. These correspond to (c) and (b) respectively in Figure4.28. Note therefore that when choosing between (b) and (c) we have either a divergent system which reduces beamwidth or a convergent system with increases beamwidth. Setup (a) is therefore attractive in mitigating the negative effects of both.

The structure of the electrode pattern given in Figure4.28(a) can be found directly by applying Equation4.39. For (b) and (c) the length of the $\theta_{inc} = 0$ boundaries is given approximately by BW since these will be normal to the direction of propagation. The x and y components are given by $BW\cos(\theta_{beam})$ and $BW\sin(\theta_{beam})$ respectively. The sign of these components depends on the setup with +x and -y for (b) and -x and +y for (c). Note finally that for designs where the refractive elements are not individually addressed the refractive edges need to be extended from the length l to reach a length $l/2$ beyond the line set by the $\theta_{beam-max}$ of the previous module, or $\theta_{selector}$ in the case of a single electrode system. Non-diffractive boundaries can be typically designed as an arc of radius determined

by extending the line of propagation of the beam backwards until the middle symmetry line is intersected. The arc is then large enough such that it goes down to the same length $l/2$ beyond the line set by $\theta_{beam-max}$ of the previous module.

4.3.3 Ulrich out-coupler enabled steering perpendicular to the slab waveguide plane

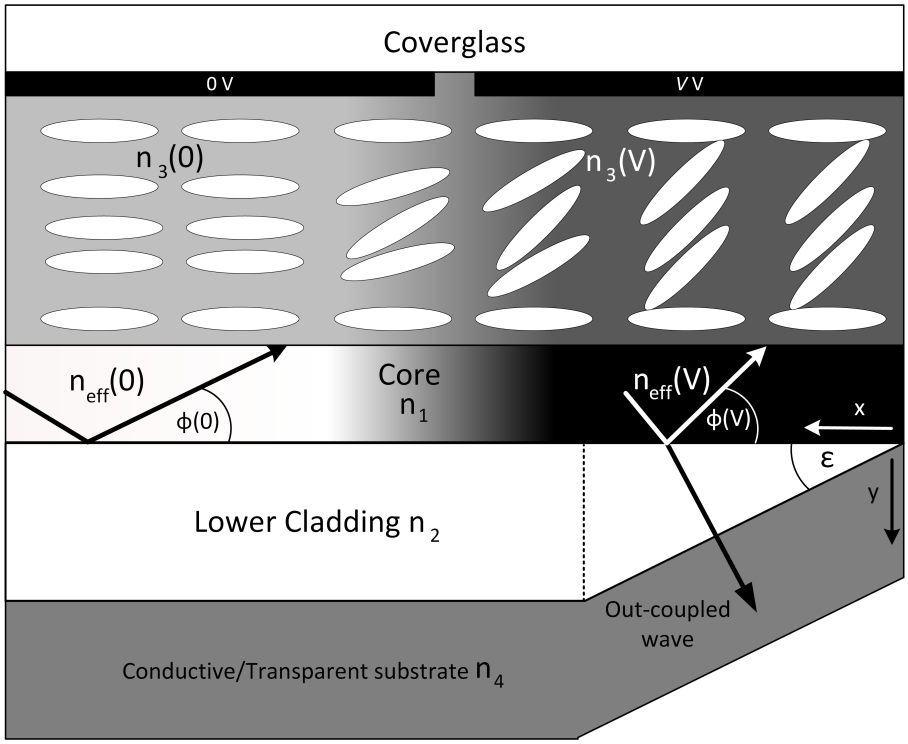

Fig. 4.30 Basic structure of an active LC cladding optical waveguide ending in a linear taper Ulrich in/out coupler.

Consider a wedge at some angle ε cut from the lower cladding of the LC active cladding optical waveguide described in Section4.3. This yields a basic Ulrich out/in coupler [123], [124], as seen in Figure4.30. The decrease of cladding thickness separating the core from some transmissive substrate having refractive index $n_4 > n_{eff-max}$ causes the guided mode to out-couple and propagate within the substrate at some angle $\theta_L = \cos^{-1}(n_{eff}/n_4)$. The maximum steering angle is determined by the ratio $n_{eff-min}/n_4$. For a given range of n_{eff} the steering range increases as $n_{eff-max} \rightarrow n_4$. This is because the cosine curve becomes flatter at an increasingly larger rate as the argument becomes smaller. There is therefore a trade-off between steering range and maximum steering angle.

Extracting the efficiency and width of this out-coupled radiation is more involved. For a taper at some constant ε the coupler has a characteristic electric field function which also depends on the mode being out-coupled. Conversely, in-coupling an electric field corresponding exactly to this function results in the corresponding guided mode, and only that guided mode, occurring in the waveguide. This characteristic out-coupling electric field is given by:

$$\Omega^*(x) = \sqrt{(aDh^2(x))\exp(-aDh^2(x))}\exp(-ikn_{eff}x) \tag{4.41}$$

where $a = (k\varepsilon\sqrt{n_{eff}^2 - n_2^2})^{-1}$ is the characteristic length of the taper coupler, depending on the angle ε and its refractive index n_2. $h(x) = \exp(-x/a)$ is the dimensionless coupling strength. D is a function of n_{eff} and can be described as the specific coupling rate of the guide for the specific mode considered. It is given by:

$$D = 2\frac{k}{\chi}\sin(2\delta_{12})\sin(2\delta_{24}) \tag{4.42}$$

Where χ is the rate of change of phase path difference, as described in Equation4.31, with n_{eff}, and δ_{12} and δ_{24} being the phase delays due to reflection at the core-cladding boundary and at the cladding-substrate boundary respectively. The maximum of this out-coupled electric field occurs at x_m, obtained by $d|\Omega^*(x)|/dx = 0$, and given by $x_m = (a/2)\ln(aD)$. Note that it is critical to be in the weak coupling regime of $h(x) < 0.1$ such that no re-in-coupling occurs. Therefore an upper-bound is set on ε since it is desired that the interaction length is long enough for the whole guided mode to out-couple but a lower bound is set by the fact that re-in-coupling needs to be prevented.

In this regime the full width half maximum(FWHM) allows determination of the beamwidth and efficiency of the emitted radiation. For some $\Omega^*(x)$, once the FWHM is determined, the efficiency is found as the ratio of integrating $|\Omega^*(x)|$ in the region set by the FWHM and the integration over the whole x-axis. Note finally that the structure described, when operated as an in-coupler, has peak performance in setting up the desired guided mode when the impinging radiation is $\Omega(x)$. For a general electric field V, typically a Gaussian beam, the efficiency is given by the normalised overlap integral of the two:

$$eff = \frac{|\langle\Omega|V\rangle|^2}{\langle\Omega|\Omega\rangle\langle V|V\rangle} \quad \text{where:} \quad \langle u|v\rangle = \int u^* v dx \tag{4.43}$$

4.4 Simulation of non-diffractive liquid crystal based beam steering devices

For both parallel-plane and perpendicular-plane steering, as outlined in the previous section, n_{eff} needs to be determined. Silicon was chosen as the core material due to its low absorption in the wavelength range of interest and its high refractive index $n_1 = 3.447$ [64]. SiO_2 was chosen as the lower cladding, again due to its low absorption and $n_2 = 1.433$ [54]. This is a typical silicon-on-insulator(SOI) system [95]. BL-037 was chosen as the upper LC cladding. From Section3.2 for BL-037 the ordinary refractive index is taken to be $n_3 = 1.547$ and the birefringence $\Delta n_3 = 0.23$. Note that the value of Δn_3 used was divided by a factor of ten to account for the small penetration of the evanescent wave within the LC cladding layer, as discussed at the start of the previous section.

Equations4.35-4.31 were used to extract the required waveguide properties. The range of allowable core thickness for a single-moded waveguide was obtained. The corresponding range of n_{eff} as a function of core thickness was then extracted. Sub-micron core thickness is required for a single moded device. This is attainable with standard SOI processes [95]. For both steering methods described it is desirable to maximise the Δn_{eff} attainable. Fixing the core thickness at 100 nm yields $\Delta n_{eff} = 0.011$, the maximum attainable for the materials considered.

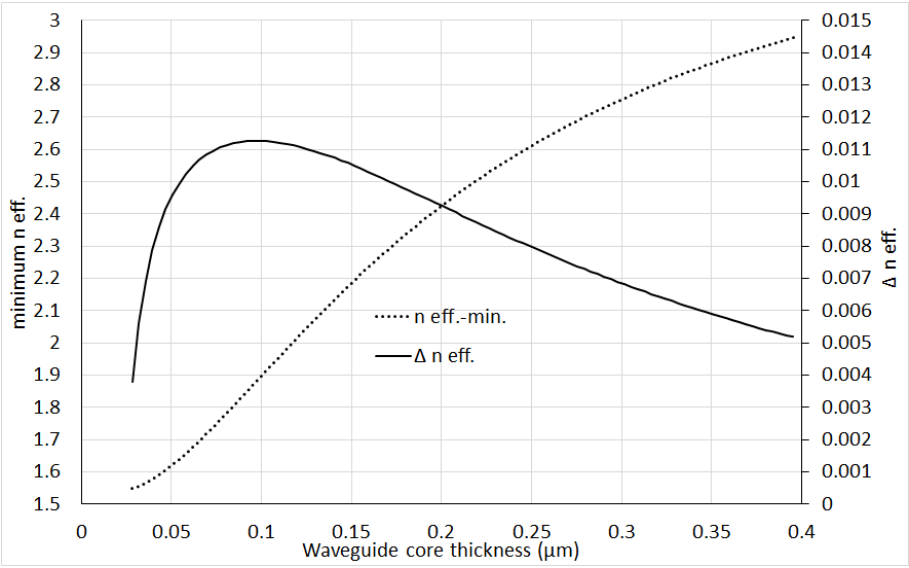

Fig. 4.31 Δn_{eff} and $n_{eff-min}$ for the core thickness range which results in a single mode waveguide.

To attain a viable in-plane steerer as described in the previous section it is important to establish the optimal electrode shape for attaining the desired output beam steering. This involves a multivariate optimisation process where the parameters to be minimised, or upon which we have restrictions, can be divided into two types, optical and practical. The area taken by the required pattern and the number of refractive interactions required, as related to the number of electrodes, are practical limitations. These arise from the increased complexity in designing large size electrode structures to be realised by photolithography and also from the difficulty in creating an active LC cladding optical slab waveguide of large size. The optical parameters to be optimised are not only the steering direction, but also the beamwidth and divergence of the output radiation. Most of these parameters are linked, and trade-offs are therefore inevitable in establishing the best possible device.

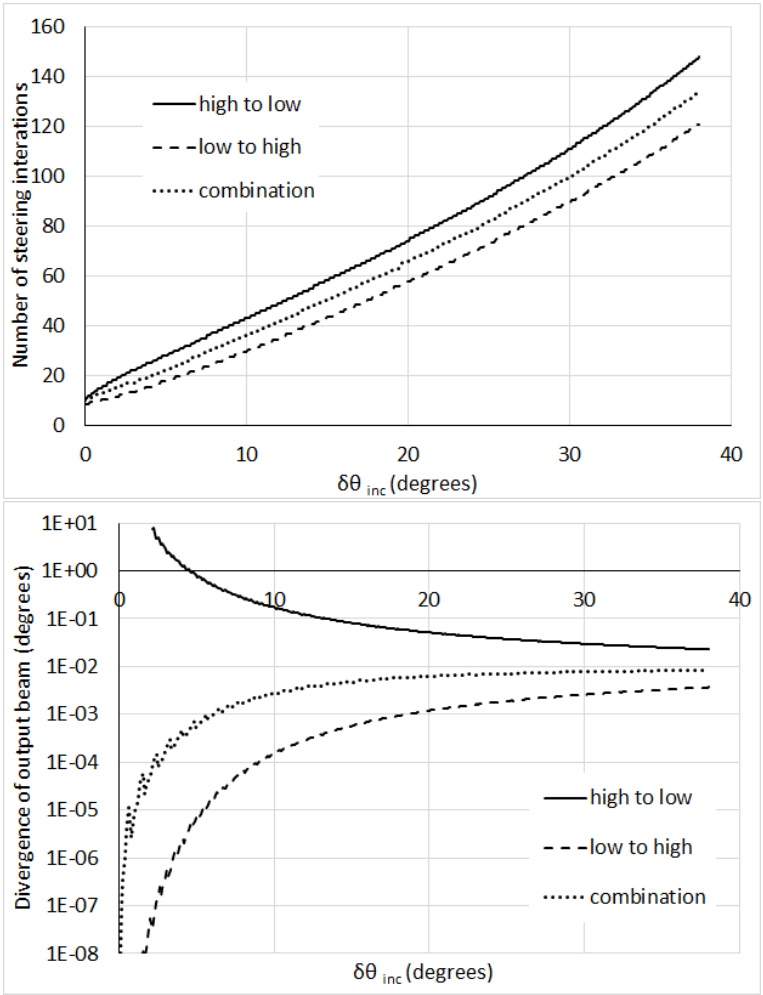

Fig. 4.32 Number of steering interactions required for 45° steering and output beam divergence for increasing values of difference between incident angle and 90° or θ_{crit} depending on refractive index values at boundary.

For a waveguide as described, with an input beam of beam-width 1 mm and divergence of 0.01°, the number of interactions required for a 45° steer and the corresponding output divergence are given in Figure4.32. Note that these are independent of the number of independently addressed electrodes employed. Note also that high-to-low, low-to-high and combine structures correspond to (b), (c) and (a) in Figure4.28 respectively.

The steering boundaries required increase approximately linearly in the range investigated. Note that for non-combined structures the number of interactions involved has been divided in half to account for the non-steering boundaries the beam is subjected to. The difference between the three configurations is due to the larger steering effect that can be attained at a low-to-high boundary since there is no limiting θ_{crit}, as opposed to a high-to-low boundary. For a combined system the requirement lies between the two, as expected.

The divergence of the output beam for different configurations is also seen in Figure4.32. Recall that the divergence is expected to increase at every high-to-low boundary and decrease at every low-to-high boundary when all incidence angles lie above $\pi/4$. The same occurs when the incidence angle is 0. The divergence is therefore always given as a combination of some increasing factor and some decreasing factor which depends on the incident angle and divergence at each boundary. The changes in divergence are also expected to be much larger as $\delta\theta_{inc}$ decreases. It is also the case that for large incidence angles the divergence effect can result in incident angles larger than the critical angle, which for our system is 83.85°. This results in a complex value of divergence as given by Equation4.38, which is interpreted as total internal reflection for part of the incident illumination, adding further complexity. The region where divergence values are not real is ignored.

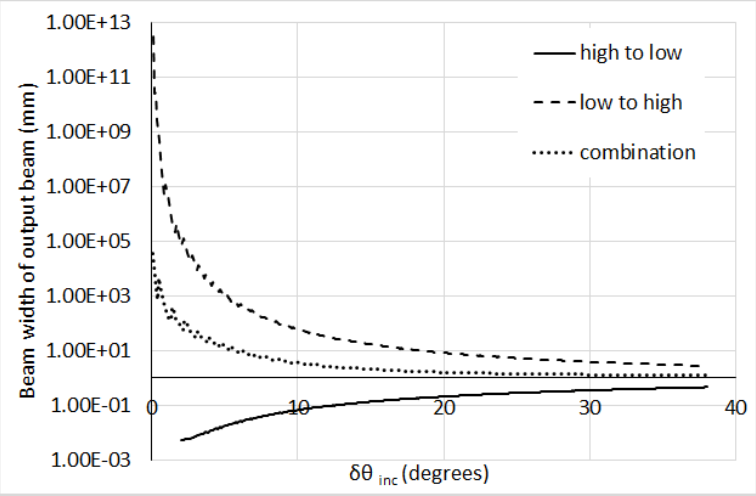

Fig. 4.33 Output beam width for increasing values of difference between incident angle and 90° or θ_{crit} depending on refractive index values at boundary for each boundary being an independently addressed electrode.

Figure4.33 gives the beamwidth of the output beam for varying values of $\delta\theta_{inc}$. As predicted in the previous section the change in beamwidth between the output beam and the input beam is in the opposite direction to the change in divergence. Introducing beamwidth considerations enables the profile of the required steering elements to be simulated. If from this the length and width of the system is extracted then the area of the LC active cladding optical waveguide to be realised is obtained. The minimum area for each configuration that yields 45° steering, which in all cases occurs for individually addressed steering elements, is 139 mm^2, 57481 mm^2 and 20642 mm^2 for high-to-low, low-to-high and combination configurations respectively. The latter two are in excess of the area of a typical wafer and are therefore prohibitive to realise, both in terms of lithogrpahy and LC cell assembly. A target device area < 1000 mm^2 is typically required for a viable device. The high-to-low configuration is geometrically viable, with a length of 21.29 mm and a width of 6.55 mm. The output beam has 0.0055 mm beamwidth and a divergence of 7.35°. This makes such a configuration not viable.

Since the two types of boundary have opposite effects on divergence and beam width, it is possible to design an electrode structure with incident angles such that the output beam properties can be controlled. In general the aim is to minimise both the divergence and the beamwidth. The latter is due to the fact that larger beamwidths require larger electrodes and therefore a larger system. Figure4.34 shows the divergence, beamwidth and surface area for the range of $\delta\theta_{inc}$ investigated. Unless otherwise stated the configuration is similar to a combination one. In each case, however, the incidence angle of the low-to-high boundary is reduced by some factor(0-0.05) when compared to that for the high-to-low boundary. This is so as to approach gradually the high-to-low configuration, which is also included. Figure4.34 shows a dramatic decrease in device area even for configurations where the divergence is $< 0.01°$ for approximately the whole range investigated. Unfortunately configurations within the viable device area region are seen to occur for divergence $\approx 0.1°$ and greater. Note that while minimising the divergence and device area it is also crucial to minimise $\delta\theta_{inc}$, and therefore the number of interactions/electrodes.

Figure4.35 shows the key properties for determining device viability for a combination configuration for selected values of Δn_{eff}. Recall that the value of Δn_{eff} used for all previous considerations was 0.011, which was obtained from Figure4.31 by considering the LC birefringence divided by ten. This basic factor was multiplied by two and five respectively in the analysis so as to account for the possibility of a larger proportion of the LC birefringence being available. Note immediately that even though the effect of increasing Δn_{eff} on the beamwidth and divergence is only pronounced for smaller values of $\delta\theta_{inc}$, the difference in device area and number of interactions is considerable throughout. The number

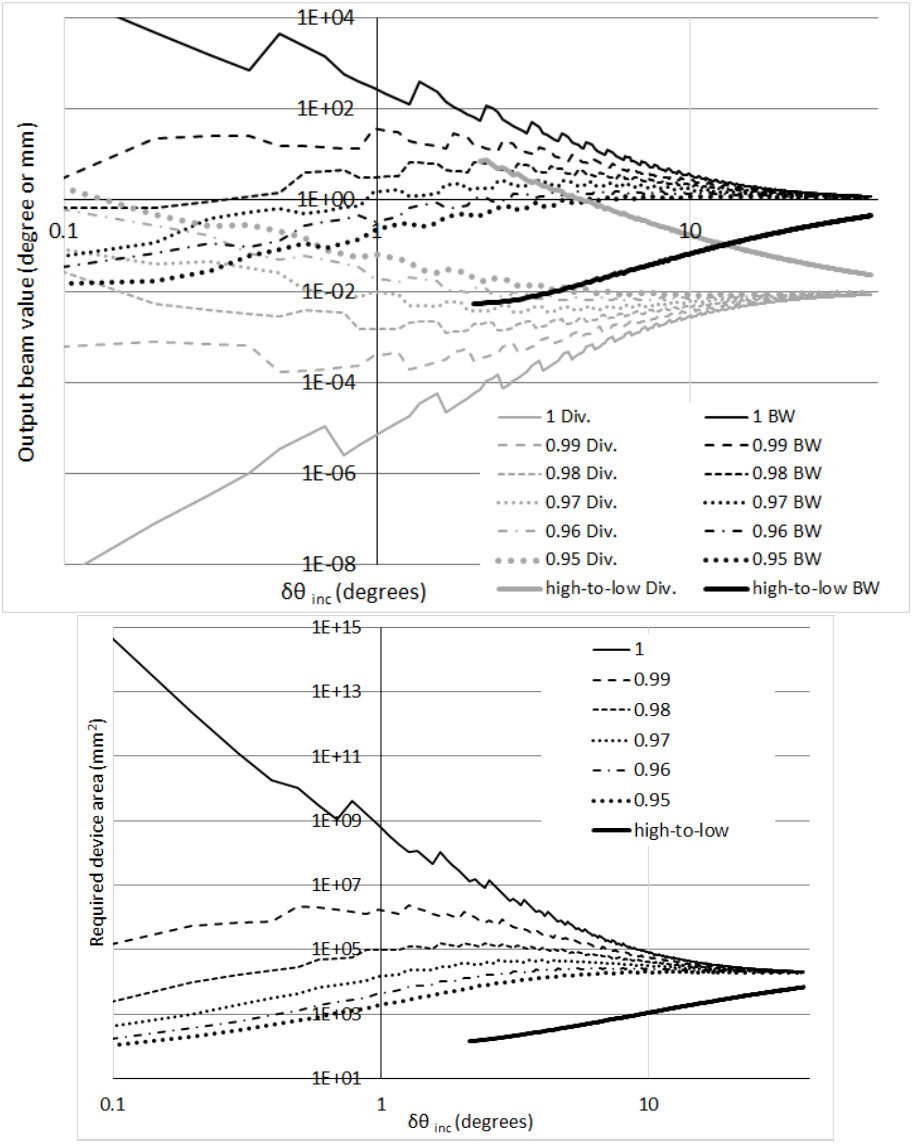

Fig. 4.34 Divergence, beamwidth and device area for the range of $\delta\theta_{inc}$ investigated for a modified combination configuration having the low-to-high boundary θ_{inc} multiplied by some factor (1-0.95). Corresponding values for the high-to-low configuration are also shown.

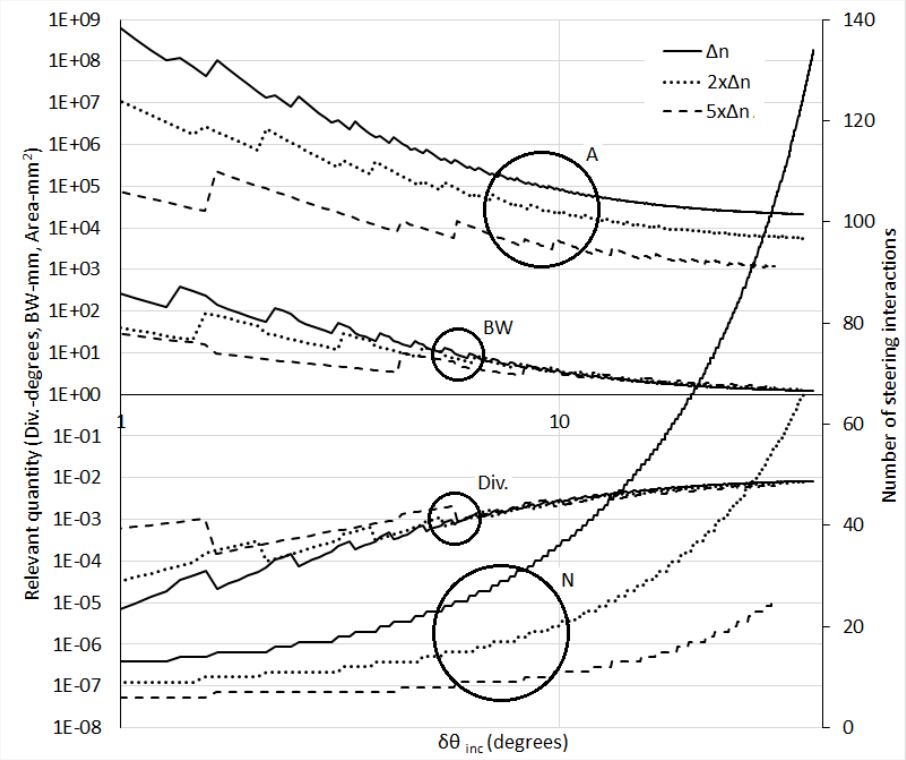

Fig. 4.35 Divergence, beamwidth, device area and number of interactions for the range of $\delta\theta_{inc}$ investigated for a combination configuration for a number of selected values of Δn_{eff}.

of steering interactions drops proportionally with the increase in Δn_{eff}, allowing viability for larger values of $\delta\theta_{inc}$. Device area drops by a factor of ≈ 5 and 20 for $2\times\Delta n_{eff}$ and $5\times\Delta n_{eff}$ respectively for maximal values of $\delta\theta_{inc}$, with the difference increasing dramatically at larger angles of incidence, particularly for $\delta\theta_{inc} < 10$. Tweaking angles of incidence as shown in Figure4.34 allows for fine tuning of device properties.

The importance of establishing an empirically accurate value for the waveguide relevant Δn_{LC}, so as to obtain a correspondingly accurate Δn_{eff}, is therefore of paramount importance. This can be achieved by using a single element steering device with a core thickness which allows single moded operation for the whole range of attainable cladding refractive indices. From the resultant steering angle and known waveguide geometry and materials the fraction of the total Δn_{LC} accessed via the evanescent wave can be determined for the fundamental mode. By employing waveguides with varying LC layer thicknesses, alignment layer types and driving voltages Δn_{eff} can be maximised.

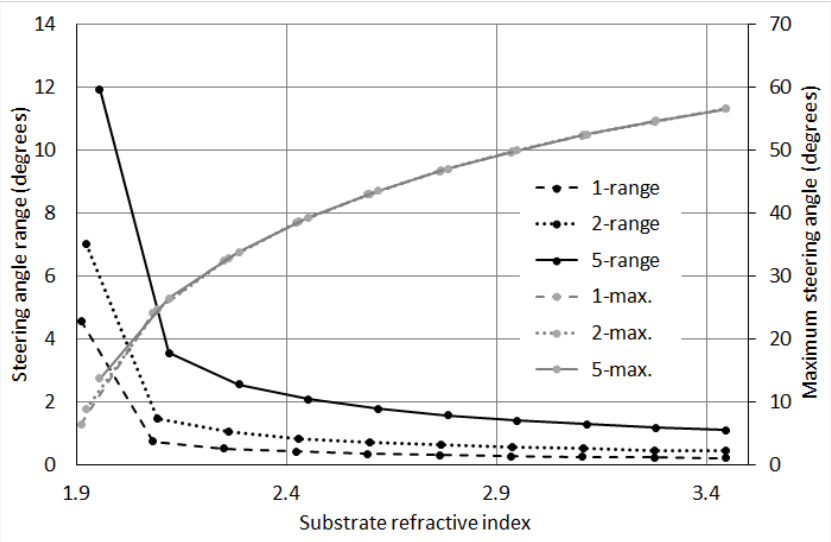

Fig. 4.36 Ulrich out-coupler steering angle maximum and range for increasing substrate refractive index for selected factors applied to $\Delta n_{eff} = 0.011$.

For an Ulrich coupler, the out-coupling angle maximum and range variation with substrate refractive index n_4 for multiple values of Δn_{eff} is given in Figure4.36. A trade-off exists between the maximum steering angle that can be attained and the range of angles obtainable by varying n_{eff}. The maximum angle range is given by $\cos^{-1}(n_{eff-min}/n_{eff-max})$. Attaining a steering range close to this maximum is challenging since it requires a substrate material with very tight refractive index constraints.

Figure4.37 outlines the typical performance of the Ulrich coupler for in-coupling for selected constants ($\varepsilon = 2$ mrad, $n_4 = n_{eff-max}$, $\Delta n_{eff} = 0.011$). In-coupling efficiency for

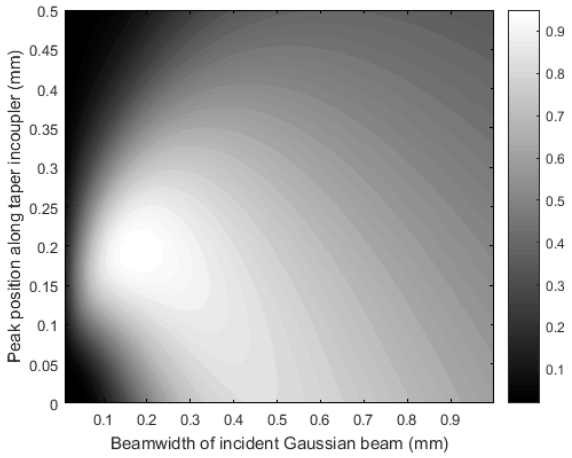

Fig. 4.37 In-coupling efficiency of an Ulrich coupler as it varies with incident Gaussian beam position along taper and Gaussian beamwidth ($\varepsilon = 2$ mrad, $n_4 = n_{eff-max}$, $\Delta n_{eff} = 0.011$).

an incident Gaussian beam depends on the beam width and position along the taper. The peak in-coupling efficiency is ≈ 0.96 which agrees with literature [124]. The peak efficiency position and width increase with increasing n_4 and decreasing taper angle ε respectively.

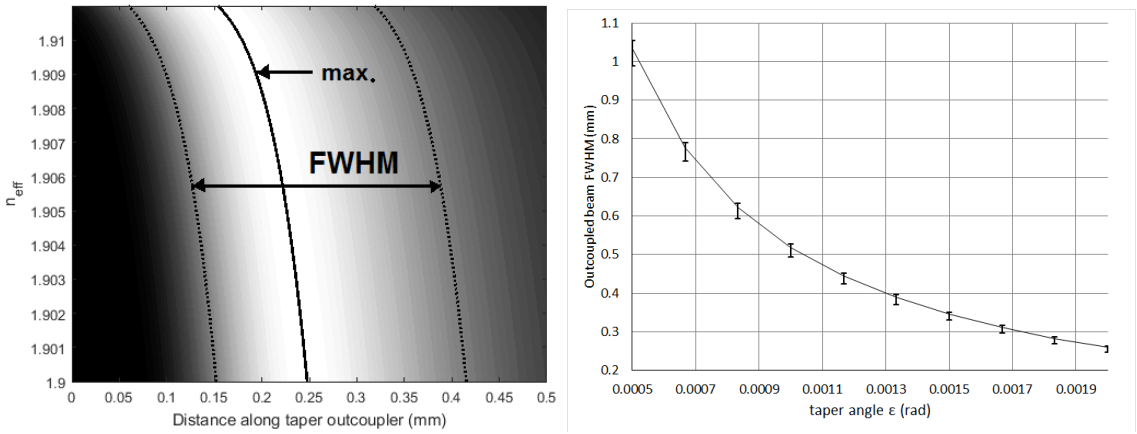

Fig. 4.38 Out-coupled radiation showing maximum and FWHM for selected properties ($\varepsilon = 2$ mrad, $n_4 = n_{eff-max}$, $\Delta n_{eff} = 0.011$) and FWHM variation with ε. Note errorbars showing variation with n_{eff}.

Figure4.38 shows the performance of the Ulrich coupler as an out-coupler for selected constants ($\varepsilon = 2$ mrad, $n_4 = n_{eff-max}$, $\Delta n_{eff} = 0.011$). The efficiency, obtained as described in the previous section, is ≈ 0.88 in all cases. The FWHM of the out-coupled beam decreases with the taper angle ε. Note that the variation of FWHM with n_4 is negligible. However, the maximal position of the out-coupled field does vary. This, combined with the constancy of $h(x)$ with n_4, allows for the determination of the range of values of n_4 which satisfy the weak

coupling condition given some value of ε. Recall that this condition occurs for $h(x) < 0.1$. x_{weak} was defined as the distance along the taper such that $h(x_{weak}) \approx 0.1$. If the difference between this value and x_m, where the maximum of the out-coupled wave occurs, is positive, than $> 50\%$ of the out-coupling does not occur in the weak regime. The process is repeated for $x_m - (FWHM/2)$ such that where this is negative only a negligibly small proportion of the out-coupled wave is not within the weak coupling region. The result of this analysis for a range of values of ε and n_4 can be seen in Figure4.39. As the value of ε increases the minimum value of n_4 which allows operation in the weak coupling region increases. Variation between the results for $n_{eff-max}$ and $n_{eff-min}$ is minimal. Achieving the greatest possible steering range requires operation at low n_4. It is therefore important to minimise the taper angle used. Note that out-coupling can still occur when the weak coupling condition is not fulfilled, but the process is more involved.

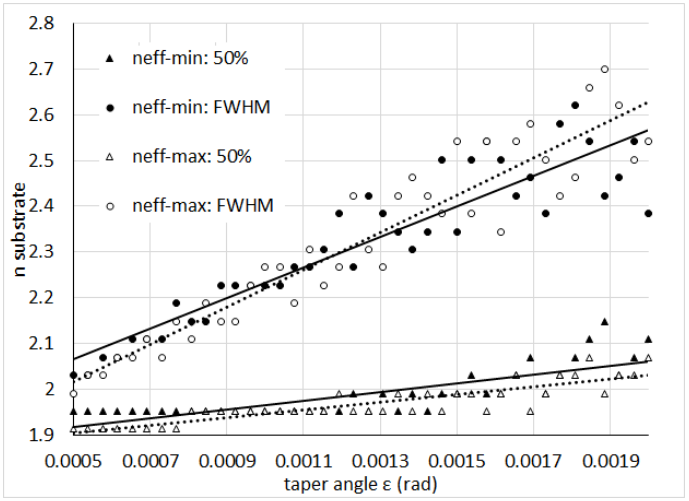

Fig. 4.39 Satisfaction of the weak coupling condition for varying values of ε, n_4 and n_{eff}. The weak coupling condition is effectively satisfied fully in the region above the 'FWHM' lines. Operation under the '50%' lines is highly degraded.

Obtaining a two dimensional steering device requires the two structures outlined above to be combined, as shown in Figure4.40. The whole device is effectively a single active LC cladding optical slab waveguide. The number of electrodes required is the number of electrodes in the in-plane steerer, the two selector electrodes and the single Ulrich electrode. These electrodes are realised using photo-lithography on some coverglass layer. Typical LC cell building processes are followed. For anti-parallel alignment parallel to the original propagation direction we have a reduction in birefringence experienced by the propagating mode as noted earlier. Having an alignment direction which fans out to compensate for this reduction is not trivial to achieve. The opposite substrate is formed of a silicon on insulator

wafer. Realising the taper which allows operation of the Ulrich out-coupler is challenging as it requires bevelling of the thin insulator layer at high precision to an optically smooth grade. The higher refractive index material which allows for the out-coupling and determines the properties of the device is then subsequently deposited. These processes are further complicated by the curved nature of this Ulrich out-coupler, which is required to mantain a high out-plain steering for the whole in-plane steering range.

This device therefore allows for high efficiency, fast, wide-range steering. It is also very challenging to realise, particularly in the case of the Ulrich out-coupler. Obtaining a good out-plane steering range requires a material with precise optical properties that can be also used as the ground plate for the LC layer. There is also no way of incorporating other functionalities within such a device.

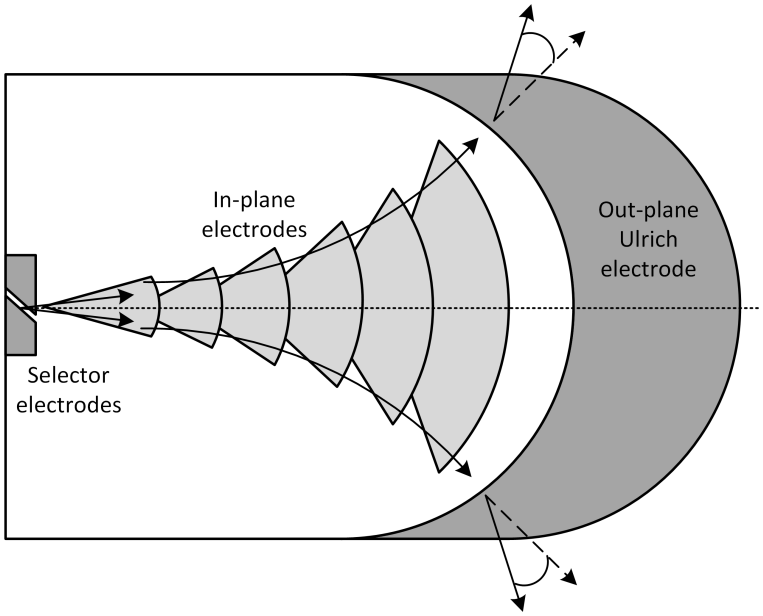

Fig. 4.40 Non-diffractive 2-D steering device combining the structures discussed [24].

4.5 Direct addressing implementation of blazed gratings

Attaining a proof-of-concept spatial light modulator requires the implementation of all the concepts outlined along with the material considerations described in Chapters 2 and 3.

It is evident that the thickness of LC necessary to attain the required phase retardation makes it difficult to achieve the desired response times, particularly for decay, where even for the 7.5μm cell $\tau_d \approx 500$ times the desired response time, as seen in Figure3.11. This LC layer thickness allows $\approx 1.5\pi$ maximum retardation, so that in theory it could be reduced to

5μm and still allow reflective operation. This would shorten response times by a factor of $(2/3)^2 = 4/9$ which would still be over two orders of magnitude too slow.

The desired steering range, in conjunction with the minimum allowable pixels per period, which determines the efficiency loss due to diffraction effects, sets the pixel size required. From Equation4.22, a $\pm 45^\circ$ steering range and a minimum pixel per period count of two, yields a pixel size of 1.63μm for operation at $\lambda = 2.3\mu$m. Achieving a difference $< 10\%$ between pixelated and continuous phase patterns requires $q_{min} > 5$, as seen in Figure4.5. For $q = 6$ we have $p = 0.54\mu$m. These pixel widths are not however the minimum sized feature of the electrode pattern required since space between the electrodes is necessary to prevent shorting. The modified Pachen's curve in Figure4.11 sets the minimum allowable electrode space for our typical operational voltages of < 5 V. This is $5/75 = 0.067\mu$m. This curve is however given for an air separation, which is not the case within an LC SLM. A conservative electrode separation value would be $\geq$ 100nm. This yields a fill factor $f_{N=2} = 0.94$ and $f_{N=6} = 0.81$. From Figure4.6 the former can be seen to yield sufficiently good results, but the latter will be only $\approx 90\%$ accurate in steering direction, efficiency and beamwidth. Fringing field effects, as seen in Figures4.8 and 4.9, might mitigate this effect, but optimisation at a thicker LC layer is not favourable as this would result in slower operation.

Note that realising an electrode structure with these suggested dimensions requires ebeam lithography, which is slow and expensive for our desired active area of ≈ 1mm^2. The in-house photolitography system and standard mask tolerances limit us to a 3μm minimum feature size which translates to a 6μm minimum pixel size having 3μm electrodes separated by 3μm. The maximum steering angle attainable for $\lambda = 2.3\mu$m is therefore 11.05°. Note that this makes breakdown considerations moot. Such a structure has a fill factor of 0.5, which entails considerable inaccuracies. Optimising for a higher thickness might be preferable in this situation. Note also that an active area larger than this minimum results in an improvement of both efficiency and beamwidth of the target order, as per Figure4.3, but this typically makes device design and assembly more challenging.

Realising such a structure as a one dimensional direct address device having an active area of $\approx$1 mm^2 requires $1000/6 \approx 167$ distinct electrodes 1 mm long by 3 μm wide separated by 3 μm spaces. A spiral electrode structure as suggested in Figure4.20 could be used to realise such a setup. For $N_e = 16$, 167 electrodes are approximately attained for $Rev = 10$. Applying Equation4.39 yields $l = 67072\mu$m, such that the electrode aspect ratio is 22357. It is therefore very likely that the V_{drop-R}, as outlined in Section4.2, is not negligible. Figure4.22 shows clearly that this effect could be highly detrimental to the quality of the replay field. Note further that a reasonable minimisation of the degradation due to the Gaussian illumination

requires an active area such that $d \approx 3.25w$, as indicated in Figure4.3. This results in a value for *Rev* of approximately 16 for all other parameters kept constant.

For a transmissive device we have a thickness of 15μm and for BL-037 a ballpark average relative permittivity is $\varepsilon_r = 22$. The length of electrode within the cell is assumed to be the entire length calculated without the factor related to the address electrodes. This enables the capacitative effect between the electrodes across the cell to be calculated. Note also that the leak resistance R_{cap} was set at 20 MΩ, which is the upper limit of resistance which could be detected with the multi-meter available. The sheet resistance for the non-patterned electrode was taken as 360 $\Omega/\square$, corresponding to mono-layer CVD graphene. For the patterned electrode the whole range of $R_\square$ values obtained for Ni UTMFs was considered, namely from 300-1200 $\Omega/\square$ for samples baked according to the alignment layer processing recipe used, as per Figure2.22. Equations2.12-2.15 were used to extract the operational frequency limit for such a system due to capacitative effects and the normalised voltage lost along the patterned electrodes.

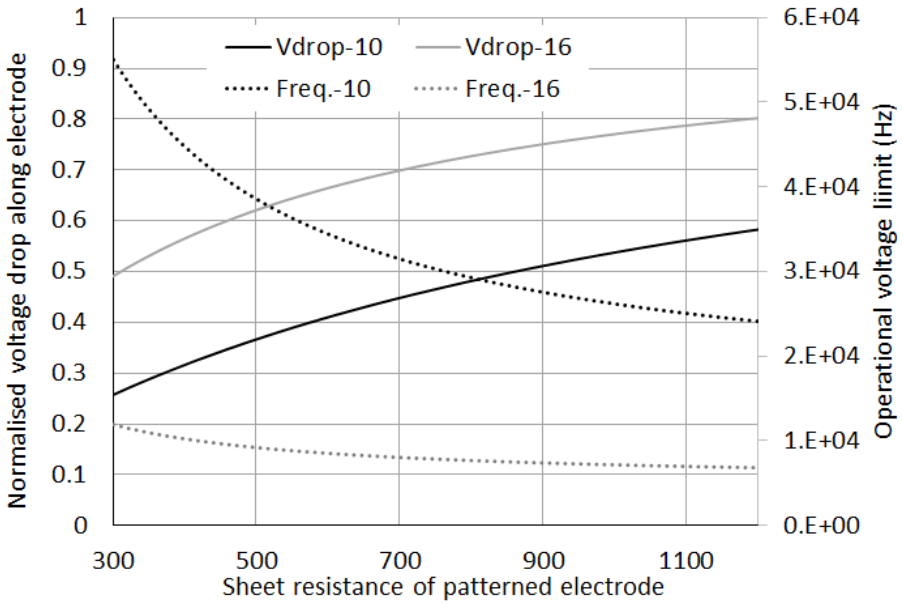

Fig. 4.41 Normalised voltage loss along the patterned electrodes and operational frequency limit for a transmissive cell having a spiral electrode structure as described with $Rev = 10$ for $d \approx 2w$ and $Rev = 16$ for $d \approx 3.25w$.

Figure4.41 shows these values as a function of the sheet resistance of the electrode for $Rev = 10$ and 16. Operation is allowable at the typical 1 kHz driving frequency used for both cases. Note that operation is allowable at frequencies an order of magnitude larger, but this is typically unnecessary unless dual-frequency operation is being investigated. This since it requires operation at high frequency to enable a sign change in the dielectric anisotropy. The

normalised voltage drop goes from $0.25 \rightarrow 0.6$ for $Rev = 10$ and $0.5 \rightarrow 0.8$ for $Rev = 16$ as $R_{\square}$ increases from 300 $\Omega/\square$ to 1200 $\Omega/\square$. From Figure4.22 this corresponds to an efficiency loss of $4\% \rightarrow 20\%$ for $Rev = 10$ and $15\% \rightarrow 33\%$ for $Rev = 16$. When compounded with the low fill factor of 0.5 the quality of such transmissive devices is far from satisfactory. For a comparable reflective device we have half the thickness and reflective electrodes. Typical reflective electrodes are made out of 200 nm thick aluminium. The opposite transmissive electrode is still considered to be CVD graphene. For such a system, assuming perfect reflectivity of the reflective substrate, we have a normalised voltage drop of 0.0005. While such a device is indeed viable, for reflective devices we have the option of using a liquid crystal on silicon backplane (LCOS). This offers a reliable off the shelf alternative with improved performance.

4.6 Preliminary considerations for LCOS simulation and implementation

An LCOS system is an active matrix addressed system which gives a comparable pixel size to that attainable by fabrication in-house. However, it provides a much improved fill factor and two-dimensional implementation with complete control over the address voltage pattern. Furthermore, this is available as an off the shelf system including driving hardware and software.

As outlined in Equations4.19-4.21 the fringing field effect is dependent on some thickness and material dependent factor Λ_{max}. It is of interest to obtain an empirical function $\Lambda_{max}(t)$ for the nematic LC BL-037 used. This requires observation of how the transmissive characteristics of a cell between crossed polarisers vary at the boundary between two electrodes where the voltage applied, and therefore the phase effects due to molecular reorientation, vary [72]. From literature, for a cell thickness of 4μm, Λ_{max} was found to be 5.8μm. Assuming that for no thickness we have no fringing effect, the model $\Lambda_{max} = (5.8/4)t$ was used to determine Λ_{max} for different LC layer thicknesses.

As mentioned in Section4.1 ad-hoc compensation patterns can be applied in conjunction with any modulation pattern so as to mitigate the detrimental effects of optical aberrations and geometrical inaccuracies. Particular to liquid crystal cells are the effects of curvature [117] and warping of the substrates used, as seen in Figure4.42. These are further exacerbated by any inaccuracies in the gluing of the two substrates, meaning that some relative tilting is often also present. For a few-electrode system with addressing restrictions, such as those seen in Section4.2, there is little that can be done to compensate for any such issues, but

for implementation on an LCOS backplane we have full pixel control and therefore it is possible to design a compensation phase pattern which caters even for compounded sources of geometrical inaccuracy.

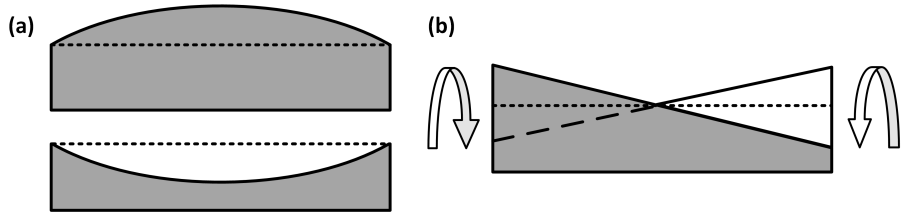

Fig. 4.42 Curving (a) and warping (b) of substrates vary the local LC thickness and therefore the corresponding phase retardation. This has a knock-on effect on the quality of the replay field.

For a device having minimum thickness t_{min} and maximum thickness t_{max} a first compensation caters for the difference in maximum phase retardation between the two. From Equation3.2:

$$\delta_{min} = \frac{2\pi\Delta n t_{min}}{\lambda} \quad \text{and} \quad \delta_{max} = \frac{2\pi\Delta n t_{max}}{\lambda} \tag{4.44}$$

Looking at a device through crossed polarisers with no bias voltage will highlight this effect. Some variable phase retardation function $\delta(x,y)$ can be obtained. A crossed polariser corrective phase function $\delta_{corr-CP}(x,y)$ can then be designed to apply a pre-reorientation so as to reduce the maximum attainable phase retardation to δ_{min} across the device.

For amplitude modulating devices the above is sufficient. On the other hand, for a phase modulating device the absolute phase delay ϕ must also be considered:

$$\phi_{min} = \frac{2\pi n(\theta(V))t_{min}}{\lambda} \quad \text{and} \quad \phi_{max} = \frac{2\pi n(\theta(V))t_{max}}{\lambda} \tag{4.45}$$

The aim is to design some $\delta_{corr-SP}(x,y)$ to limit the effective cell thickness to $t_{min} + N(t_{2\pi})$, where $t_{2\pi}$ is the thickness that yields 2π phase shift and N is some integer greater or equal to zero. The correction function $\delta_{corr-SP}(x,y)$ is therefore obtained as $\phi \bmod 2\pi$, which is then applied as a pre-reorientation, reducing the absolute phase delay ϕ, and therefore its effective thickness as required.

In the previous case it was possible to bypass measuring the thickness directly by observing the device through crossed polarisers, in this case, however, $t(x,y)$ is required to obtain ϕ. For broadband visible radiation the optical retardation varies with wavelength and thickness. The peaks of the electro-optic response for every color will occur at a different thickness. As such, it is possible to obtain a map of the thickness by observing the device

between crossed polarisers when illuminated by a broadband visible source. From Figure3.9 we know that the peak tranmission for a particular wavelength between crossed polarisers is given when the phase retardation is odd multiples of π. From Equation3.2 we therefore obtain the thickness condition for peak transmission:

$$t_{peak-\lambda} = \frac{(2N+1)\lambda}{2\Delta n(\lambda)} \tag{4.46}$$

It is often far more practical, however, to obtain a calibration device by creating a wedge of known start and end thickness [117]. Observing this device through crossed polarisers with a broadband source allows for a calibration graph of $\lambda(t)$ to be extracted. This can then be applied on the test device. Averaging across the calibration cell for equal thickness helps to mitigate any inaccuracies within the calibration device itself.

In conclusion, accounting for these factors enables the user to compensate appropriately when determining the modulating patterns to be applied to the optical phased array. This has the potential to increase the efficiency considerably.

4.7 Middle infrared liquid crystal on silicon SLM simulation

In this section the performance of a device based on an off the shelf LCOS backplane product is simulated. The device was modelled as an assembly of the backplane into an LCOS optical phased array with parameters and materials derived from the investigations conducted in Chapter 2 and Chapter 3. Performance for normal and off-normal operation was simulated along with two-dimensional operation. Integration into a novel multiple interaction device was investigated and simulations were conducted.

4.7.1 Simulation set-up and basic results

Figure4.43 shows the basic LCOS set-up to be simulated. It is based on Jasper Display Corporation LCOS backplane(JD4552), evaluation kit(JD8554) and controller(JD6288). This system is composed of 1920 $\times$ 1080 pixels of pitch 6.4μm with a dead-space of 0.2μm, yielding a fill factor of 0.97. This gives an active area of 12.5mm $\times$ 7.1mm. Pixels are independently addressed with voltages ranging from some $V_{min-RMS} \geq 0$ V to some $V_{max-RMS} \leq 5$ V. $V_{min-RMS}$ and $V_{max-RMS}$ are fully adjustable. This voltage range is divided into 8-bit greyscale levels (0-255). The greyscale voltage pattern is loaded onto the backplane as an 8-bit greyscale bitmap image having 1920 $\times$ 1080 pixels. Note that going from a

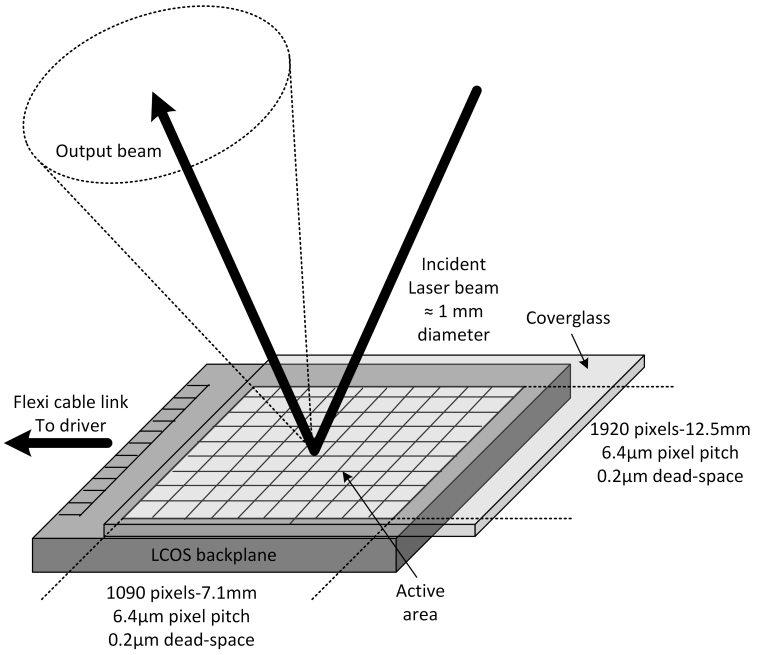

Fig. 4.43 Basic LCOS set-up using available hardware.

voltage pattern to a phase pattern requires some calibration graph based on the electro-optic response.

Simulations were conducted by RCWA as implemented in the Reticolo software. As outlined in Section4.1 this allows simulation of the diffractive characteristics of some periodic stack, accounting also for Fresnel reflections. These stacks are formed of multiple layers which model the various materials the device is made of. The four configurations considered are outlined in Figure4.44. The stack is defined using the thickness and complex refractive index of each layer. For a layer which is not uniform in space the variation in complex refractive index with displacement is accounted for. For all layers, the complex refractive index used was specific to the operational wavelength, with data for CVD graphene and $t_{est} = 3$nm Ni UTMF extracted from results in Chapter2. Note also that the thickness of the anti-reflection coatings employed was extracted by applying the single-layer AR method outlined in Section2.1. Aluminium oxide was employed at the air-Si interface and titanium oxide at the alignment-Si layer.

In all configurations the LC layer is identical. For $\lambda = 2.3\mu$m operation, the BL-037 LC layer thickness was 7.5μm. The variation in refractive index of this layer was computed accounting for fractional electrodes per period, pixelation, dead-space and fringing effects as outlined in Section4.1. Based on this stack, along with some other parameters such as the incident angle and polarisation of impinging radiation, the critical properties of the far-field replay field can be extracted. The efficiencies and propagation angles of the various

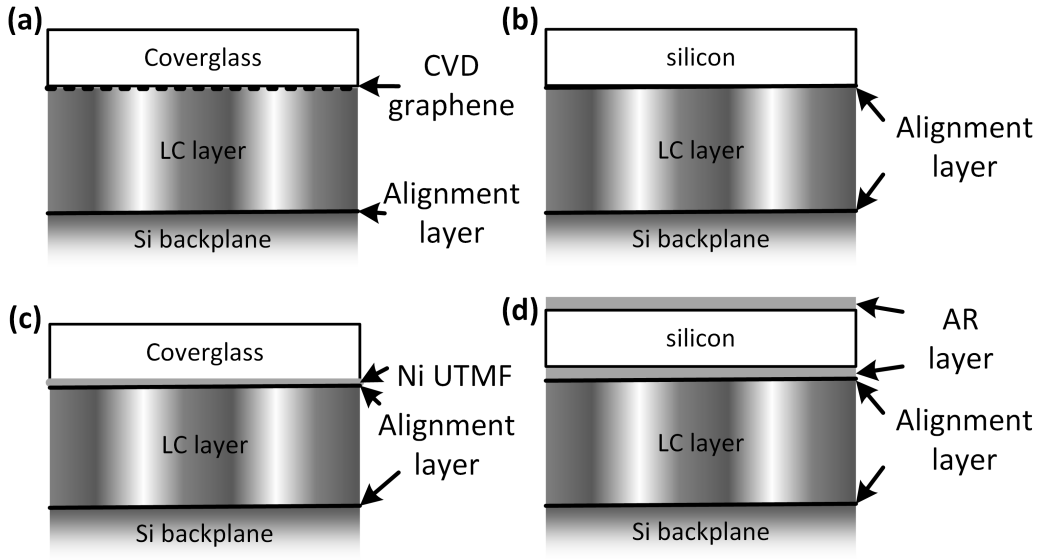

Fig. 4.44 Configurations considered: (a) CVD graphene, (b) bare silicon as electrode and substrate, (c) Ni UTMF, (d) anti-reflection coated silicon as electrode and substrate.

diffraction orders are obtained with an accuracy depending on the the amount of Fourier harmonics accounted for, in this case ten.

Figure4.45 shows the results obtained for all the configurations outlined. In each plot we have the efficiency of the target order, the efficiency of the zero order and the efficiency of the order with the greatest efficiency excluding both the target and the zero order. These are computed for varying values of electrodes per period in one dimension while being constant in the other. Note that for low values of electrodes per period fractional values need to be added between the integer values so as to obtain a more uniform distribution of steering angles. When comparing the different configurations the bare silicon device(b) performs the worst. This is due to the high reflection at the silicon boundaries. When silicon is coated with anti-reflection coatings(d) to account for this it has the best performance of all configurations. Note that CVD graphene(a) only has a marginally weaker performance, while for Ni UTMF(c), unlike bare silicon, the diminished performance is primarily due to absorption. Note that while anti-reflection coated silicon has a better performance it is non-transmissive in the visible spectrum. This makes gauging the quality of the device very complicated and is therefore not ideal for proof-of-concept devices.

It is useful to compare the results in Figure4.45 with the results for direct numerical implementation of the far field diffraction equation. This does not account for the multi-layered structure but gives information regarding the divergence of the target beam. This analysis also accounts for all the LC layer aspects included in the RCWA analysis. As in

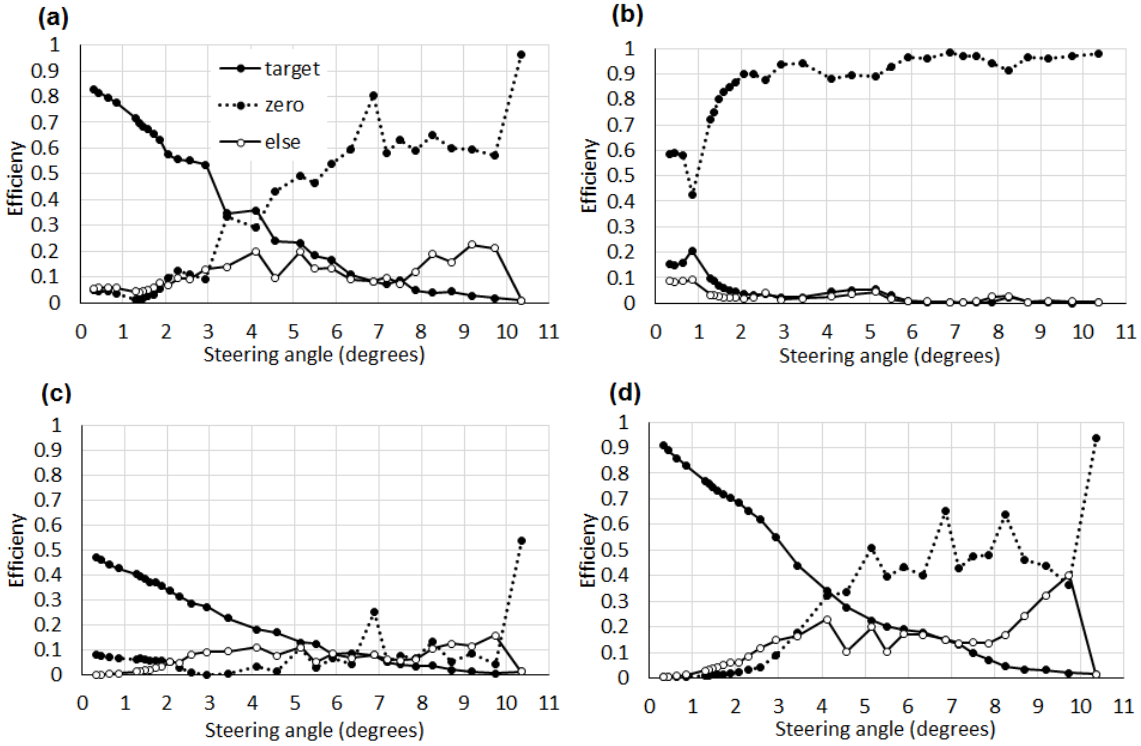

Fig. 4.45 Efficiency of selected orders against steering angle for the four configurations considered: (a) CVD graphene, (b) bare silicon as electrode and substrate, (c) Ni UTMF, (d) anti-reflection coated silicon as electrode and substrate.

Figure4.4 the aperture is determined by multiplying the replay field of the fundamental grating period of length d by a factor determined by the repetition of the basic aperture by M times such that $Md = 2w$, where w is the half width of the incident Gaussian beam. Note that the divergence has been increased by 20% and the efficiency increased by 5% in accordance with observations. Beam divergence is approximately 0.095° for the full range of steering angles apart from the lowest end of the range. Target order efficiency is very similar to that for CVD graphene and Si AR configurations, as expected.

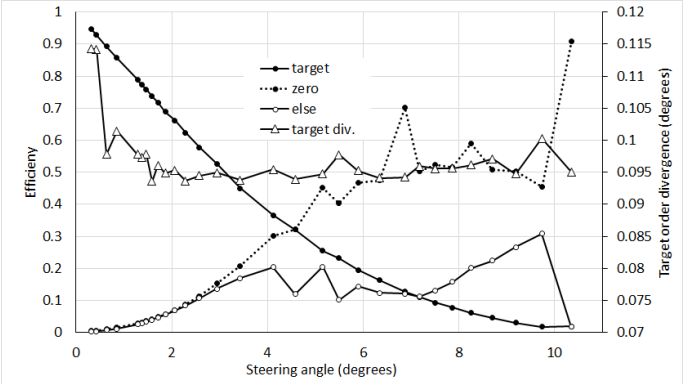

Fig. 4.46 Results for the numerical implementation of the far field diffraction equation on a phase pattern corresponding to that used for RCWA analysis over an aperture representative of the incident laser radiation available.

Results for operation at longer middle infrared wavelengths can be seen in Figure4.47. Due to a larger λ/p factor we have a greater steering capability, as outlined in Figure4.10. For a given steering angle we therefore typically have a higher efficiency. For a given thickness there is a maximum wavelength which can be suitably steered. This is not only limited by the maximum optical birefringence, in this case ≈ 0.23, but the fraction of this birefringence that can be harnessed is limited by the maximum RMS voltage that can be applied, in this case 5 V. For an increased wavelength which requires a thicker LC layer the increase in efficiency is somewhat mitigated by the higher Λ_{max}.

4.7.2 Off-normal incident light

Typical LCOS operation involves off-normal incidence. In this case reflection, including internal reflections, and transmission characteristics will change. Furthermore, the path of the radiation within the phase modulating layer not only increases, but is also not perpendicular to the layer plane. Figure4.48 shows the off-normal LCOS performance for CVD graphene(a) and AR Si(b). Efficiency data is presented as a ratio with respect to performance for normal operation. In all cases bright and dark fringes are observable as the incident angle increases.

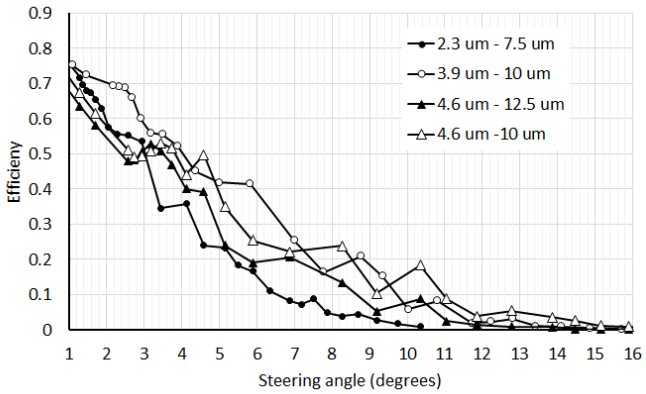

Fig. 4.47 CVD graphene configuration target order efficiency for LCOS operation at longer middle infrared wavelengths. Note that this involves a thicker LC layer and sapphire as cover glass.

For each layer in the stack we expect a distinct pattern with amplitude depending on the reflectivity and period depending on the thickness and refractive index of the material. These variations in efficiency are most pronounced in the zero-order data since there is no steering involved. In both cases the effect due to the cover layer is most pronounced, with the low frequency component due to the liquid crystal layer itself only visible for the AR Si configuration. Note that as the steering angle varies there is a similar effect, but this is only visible for small steering angles, where there is higher angle data density for a given range of values of electrodes per period, and for small incidence angles, where the path difference between adjacent values is smaller.

4.7.3 Two-dimensional operation

Two dimensional implementation requires a two dimensional phase pattern accounting for pixelation, dead-space and fringing effects. Figure4.50 shows the pattern for two representative configurations. In this case fringing effects cannot be accounted for by summating the necessary error functions, as we did in Equation4.21, in both directions. Note that the convolution:

$$\mathrm{conv}\left[step, \exp\left(-\left(\frac{2x}{\Lambda}\right)^2\right)\right] \propto \mathrm{erf}\left(\frac{2x}{\Lambda}\right) + 1 \tag{4.47}$$

where $step$ is the step function going from 0 to 1 at the origin. The pixelated pattern was therefore convoluted with the two dimensional equivalent of the exponential expression in Equation4.47 to obtain a pattern that can be implemented in Reticolo.

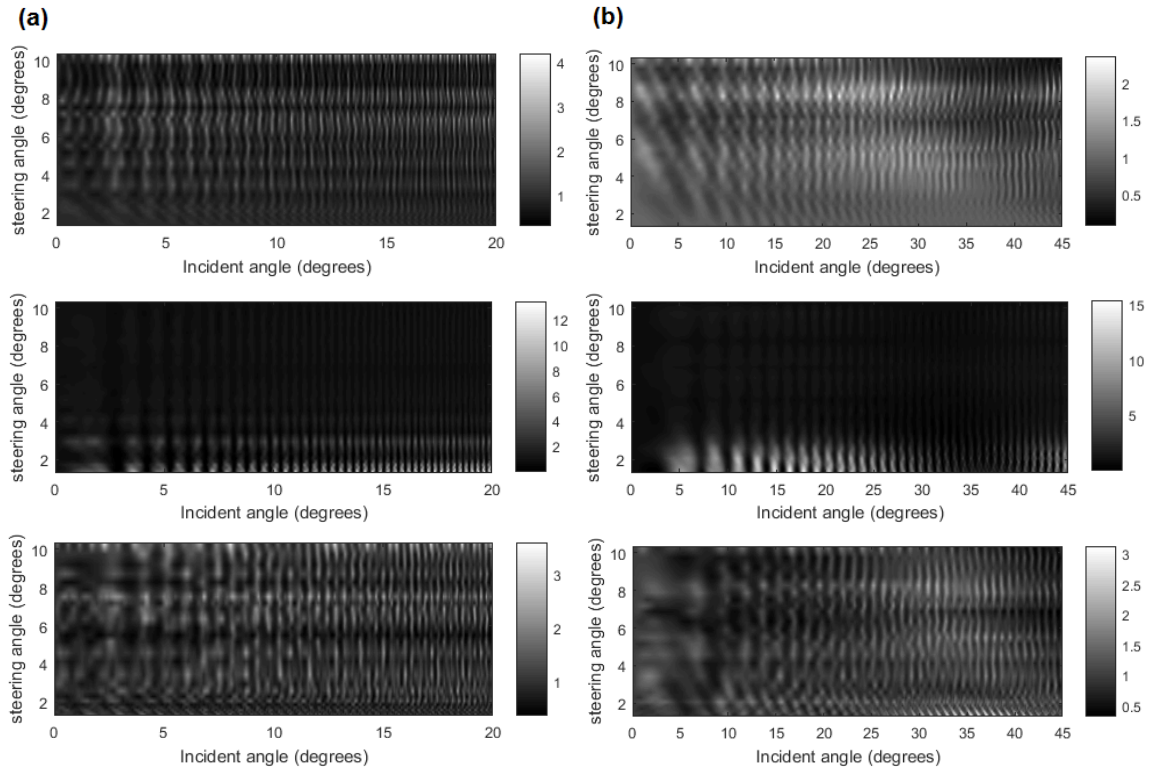

Fig. 4.48 Off-normal LCOS performance for CVD graphene(a) and AR Si(b). Efficiency data is presented as a ratio with respect to performance for normal operation. Note that the first row shows the target efficiency, the second row shows the zero-order efficiency and the third row shows the greatest efficiency amongst the remaining orders.

Two dimensional results for the CVD graphene device as described in Figure4.44(a) are given in Figure4.51. Figure4.51(a), (c) and (d) are obtained using a two dimensional phase pattern as described. Figure4.51(b) is obtained by extracting the equivalent electrodes per period value perpendicular to the phase pattern reset lines. This is obtained by:

$$elp_{\perp} = elp_y \sin(\tan^{-1}(elp_x/elp_y)) \tag{4.48}$$

where elp_x, elp_y and $elp_{\perp}$ are the potentially fractional electrodes per period in the x-direction, the y-direction and the perpendicular direction. This is displayed in Figure4.49.

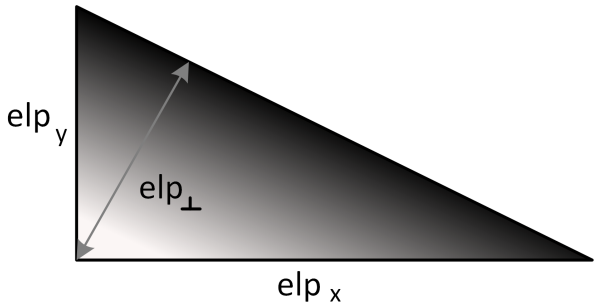

Fig. 4.49 Diagram for the extraction of $elp_{\perp}$ from elp_x and elp_y.

Comparing the target order efficiency data in Figure4.44(a) and (b) it can be observed that the pixelation issue discussed degrades efficiency at the high electrode per period limit for two dimensional implementation. The opposite holds true at the other end of the electrode per period range investigated. Note that the data in Figure4.45 corresponds to the $elp_x = \infty$ or $elp_y = \infty$ case. As such a higher efficiency in these cases is expected. From these results the operation of a CVD graphene based device seems attractive, with an efficiency greater than 10% for steering under 8° in the whole azimuth range.

4.7.4 Multiple interaction devices

As outlined in Section4.1 it is challenging to attain high steering angles using a single LCOS device. Magnification using lens pairs reduces resolution proportionally and optically addressed LC SLMs are non-trivial to implement. Multiple interaction devices are an attractive option for increasing the steering range. The most straightforward implementation of this is to use distinct devices. Allowing for the effects of off-normal incidence, for such a set-up the final target steering angle is well approximated by the summation of the target steering angle of each device and the final target efficiency by the product of the target efficiency of each device. Note that a particular target steering angle can be attained via many different combinations of individual device values. Figure4.52 compares the performance of

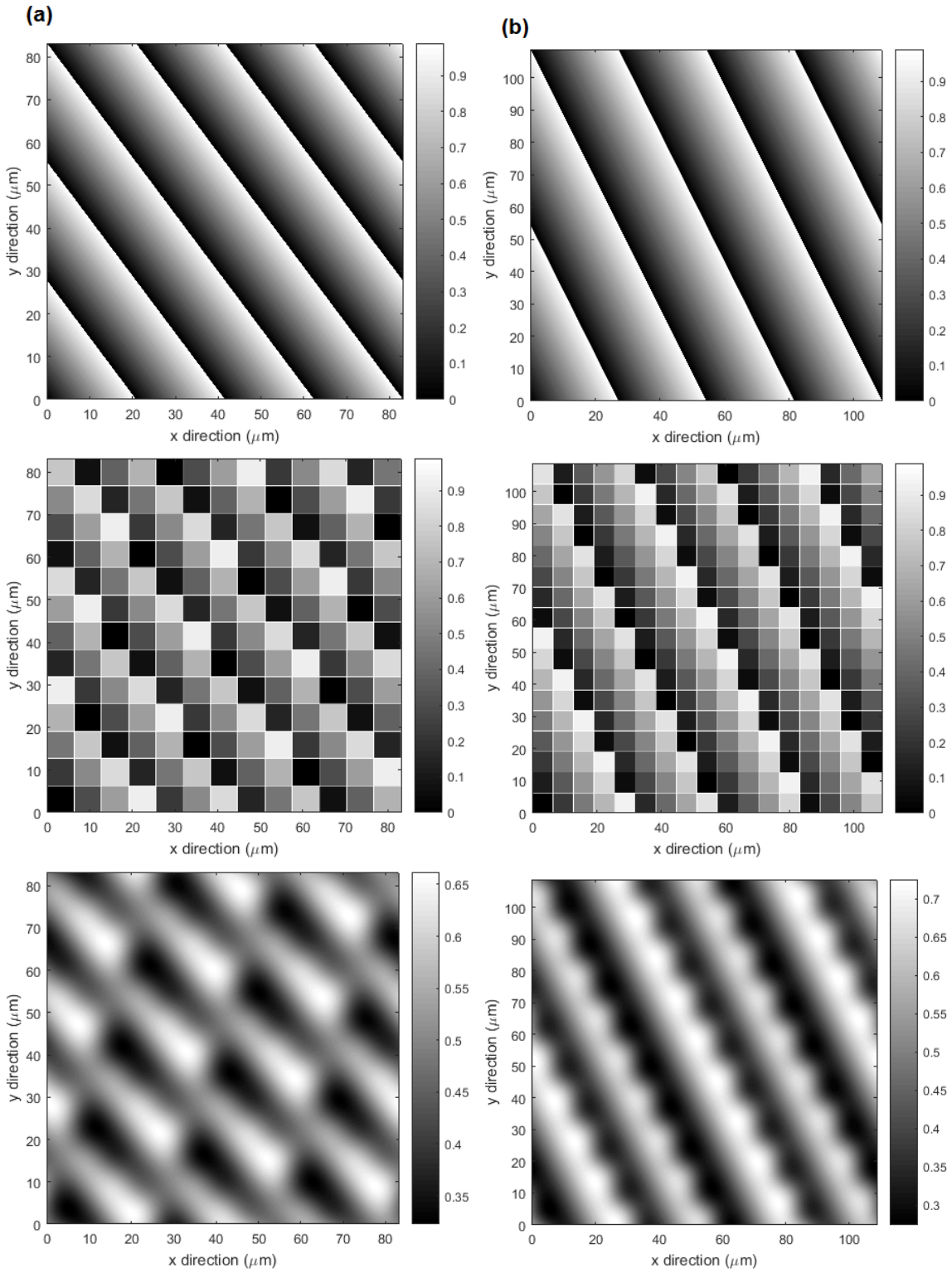

Fig. 4.50 Theoretical, pixelated and fringing-modified normalised refractive index pattern for 3.25×4.33(a) and 4.25×8.5(b) electrode per period patterns.

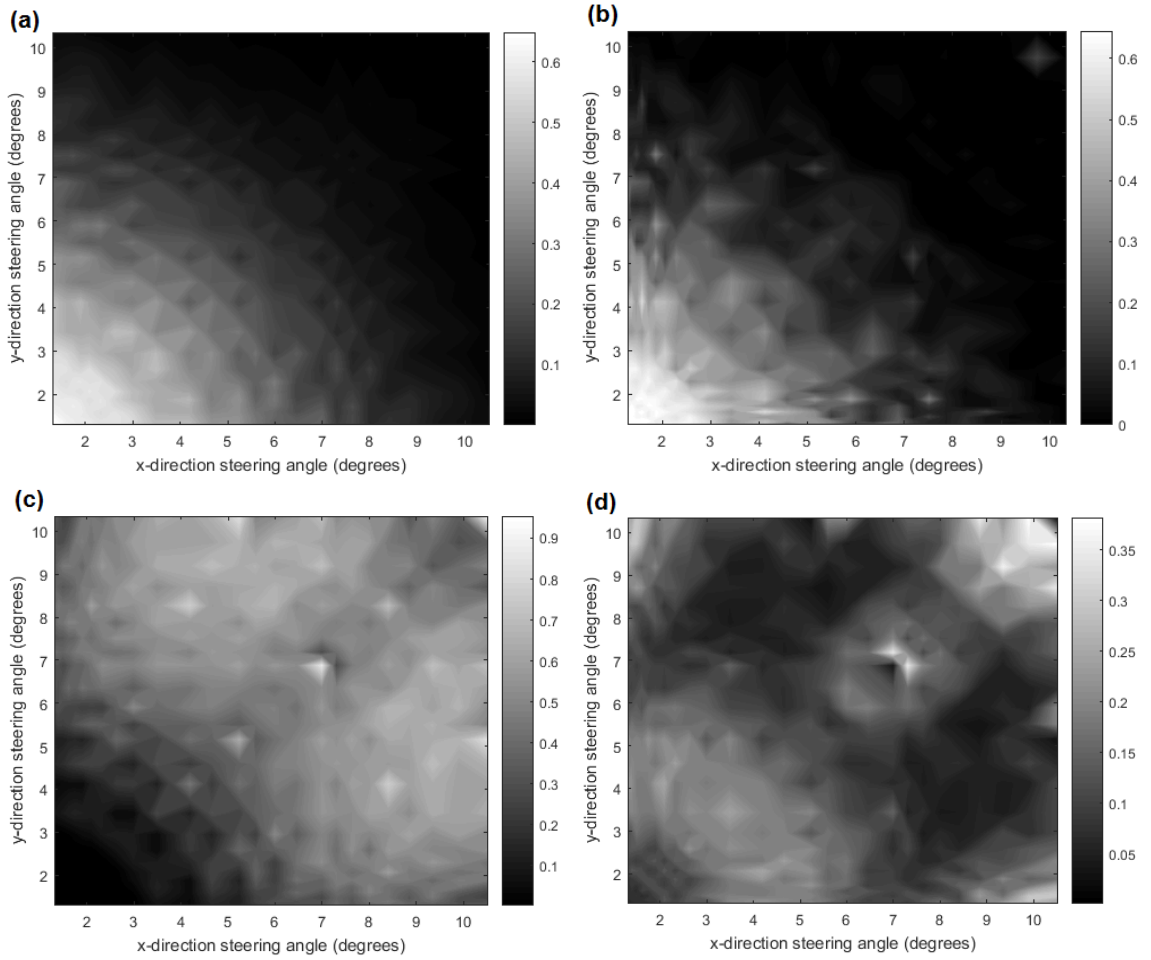

Fig. 4.51 Target order(a), zero order(c) and other maximum order(d) efficiency for two dimensional implementation of a CVD graphene device. (b) is the target order efficiency of a comparable one dimensional implementation obtained by finding $elp_{\perp}$ from elp_x and elp_y.

a single device set-up with a two device set-up with half of the steer attained by each device. Note that for small target angles the multi-device set-up is out-performed by the single device set-up. An improvement of 5% to 10% is observed for steering angles in the second half of the single device steering range, with an improvement of 5% at 10°. This is hardly enough to justify the employment of a second independent device.

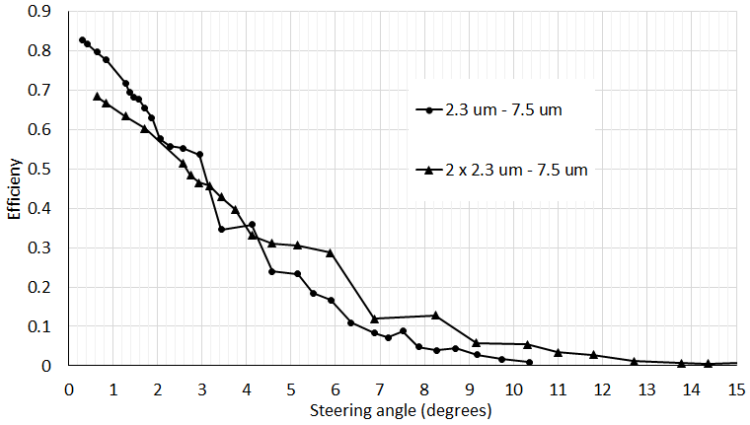

Fig. 4.52 Target order efficiency for a single and double LCOS device with final steering angle attained with half of it applied by each device.

A further complication arises from the fact that radiation must be incident on the active area of the second device for the whole steering range of the first device. This limits their maximum possible separation. For $\lambda = 2.3\mu$m and the Jasper LCOS microdisplay available this maximum distance is given by $(7.1-1)/(2*(\tan(10.35°))) \approx 17$mm, where 10.35° is the maximum steering angle for a single device. Note that 1mm has been reduced from the active area width to account for the beamwidth of the steered radiation. It is not only challenging to realise a system with multiple LCOS devices due to the presence of multiple drivers and controllers in close proximity, but the return is minimal at best.

Note that such a system can be simplified by replacing the second LCOS device with some coarse steerer, as outlined in Figure4.17. This coarse steerer is used to tile the steering range of the fine steerer across a larger area. For some fine steering range $\pm\theta_{fine-max}$, the maximum angle required by the coarse steerer for 45° total steering range is $\theta_{coarse-max} = 45 - \theta_{fine-max}$. Note further that this coarse steerer does not require continuous steering, but discrete steering at $\pm(45-((2N-1)\times\theta_{fine-max}))$ where $N\,\varepsilon\,\mathbb{N}$. A reflective spiral electrode enabled few-angle direct address device, as outlined in Figure4.20 holds some potential as a coarse steerer. For a $\theta_{fine-max} = 5°$, so as to have a minimum efficiency above 20%, the required coarse steering angles are ±40°, ±30°, ±20° and ±10°. For the maximum coarse steering angle being attained by a binary pixelated pattern the pixel pitch required is 1.8μm. The

required number of angles can be obtained by a system with $N_e = 16$. Note that such a coarse steerer is one dimensional, and two would therefore be required for complete coverage.

For e-beam lithography a good fill factor can be attained and for a reflective device we do not expect the voltage drop to be crucially debilitating. On the other hand, for such a system the ratio of Λ_{max} to pixel pitch is approximately six, such that any few electrode per period phase pattern will be degraded beyond use. This is a limitation rooted in the LC layer thickness which is itself determined by the birefringence. For a nematic liquid crystal based coarse steerer in the middle infrared an LC material with considerably higher birefringence is required.

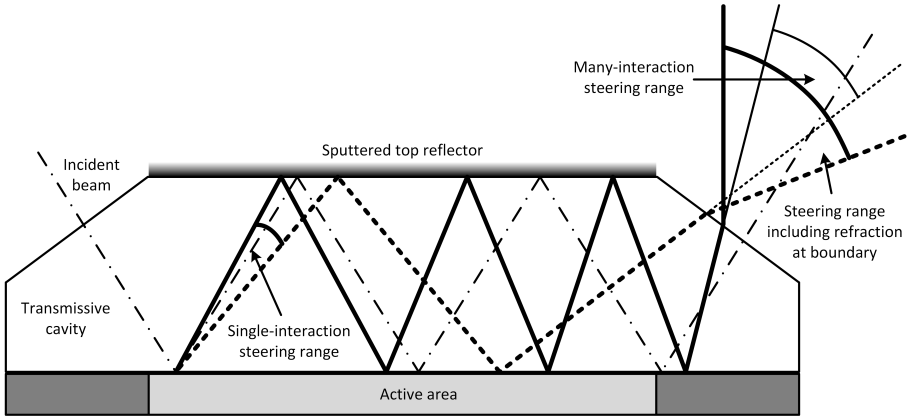

Fig. 4.53 Basic operational principle of a few-interaction, cavity-based, LCOS device.

Up to this point the problem of attaining a steering range larger than that possible via a single LCOS device has been approached by adding further devices. Figure4.53 outlines a potential strategy for attaining multiple diffractive interactions off of a single device. The covering substrate, typically used solely for the structural support of the top electrode and alignment layers, is here used as a high thickness cavity. To this end the cover glass layer, which must be chosen to have exceedingly low absorption in the operational wavelength, is thicker and has some reflective layer deposited on top. Ad hoc structures at the ends of the device are required for favourable input and output interactions.

For such a set-up RCWA implementation has to account for the fact that the background medium is soda lime glass. The effective wavelength is therefore $\lambda/1.4334$, where 1.4334 is the refractive index of soda lime glass. The target order efficiency of such a set-up is compared to that of the single interaction LCOS device in Figure4.54. The maximum steering angle for efficiency $> 10\%$ is 5°. Note that since for our geometry the Fraunhofer diffraction condition is given by $500^2/2.3 \approx 11$cm, the far-field approximations cannot be implemented and therefore the general diffraction equation, given in Equation4.1, has to be numerically implemented. This equation was implemented accounting for Gaussian illumination, off-

normal incidence and an LC layer induced phase pattern involving fractional electrodes per period, pixelation, dead-space and fringing effects.

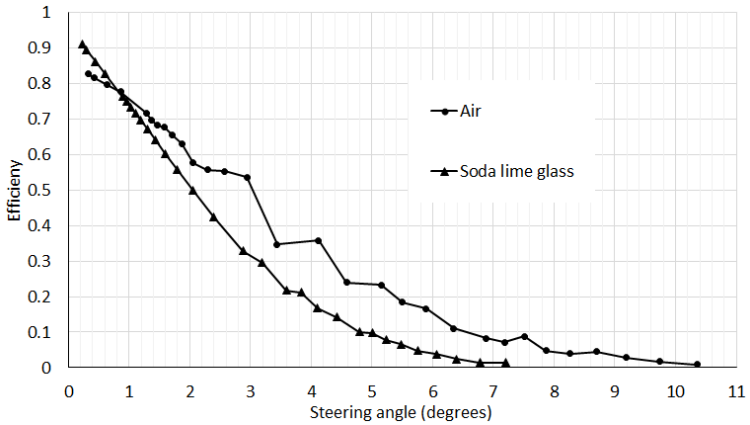

Fig. 4.54 One dimensional RCWA Reticolo implementation for $\lambda = 2.3\mu$m in a system having an air background medium and a soda lime glass background medium.

The grating equation as expressed in Equation4.28 is still useful in obtaining the constant steering angle θ_{int} for each interaction since this is not correct solely for far-field operation. Given the incident angle θ_{inc} for the first interaction, the target final angle θ_{tar-N} and the number of interactions N, θ_{int} is given by:

$$\theta_{int} = \sin^{-1}\left(\frac{1}{N}\left(\sin\theta_{tar-N} - \sin\theta_{inc}\right)\right) \tag{4.49}$$

Note that all of the parameters in the above equation are within the soda lime layer. θ_{int} is used to determine the properties of the phase pattern required, namely the amount of electrodes per period. Note that the largest θ_{int} attainable, or desirable based on expected efficiency, sets the lower bound limitation on N for a given range of angles to be steered. θ_{int} is also necessary, in conjunction with the cavity thickness t, in determining the length of active area required to achieve the required number of interactions. This length L is given by:

$$L = 2t\sum_{n=1}^{N}\tan\theta_{tar-n} = 2t\sum_{n=1}^{N}\tan\left(\sin^{-1}\left(\sin\theta_{inc} + n\sin\theta_{int}\right)\right) =$$

$$2t\sum_{n=1}^{N}\frac{\sin\theta_{inc} + n\sin\theta_{int}}{\sqrt{1-(\sin\theta_{inc} + n\sin\theta_{int})^2}} \tag{4.50}$$

Therefore $L \propto t$ and this expression gives the upper bound on N or t if the other is fixed since L needs to be smaller than the active area of the LCOS microdisplay.

For each diffractive interaction, the image plane is set a distance $2t$ away to account for the double pass in the cavity required to reach the LC layer phase pattern again. The field at this image plane is then set as the field at the object plane for the next interaction. The field at the first object plane is a Gaussian beam at the incidence angle and the final image plane is set in the far-field. Note further that while far-field operation cannot be assumed, for increase in t in the few millimetre range we expect the efficiency increases dramatically as the thickness increases, as seen in Figure4.55. This sets a lower bound on the cavity thickness. Fresnel equations were used to account for non-perfect reflection at the top of the cavity.

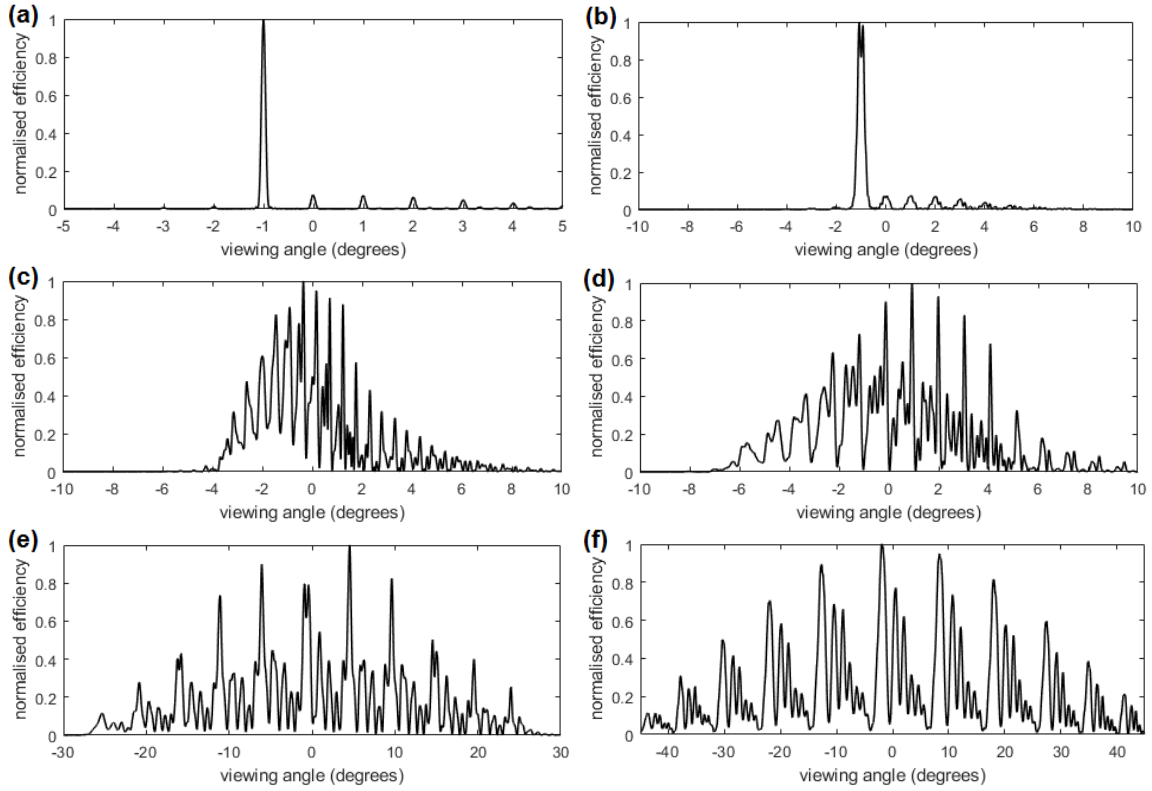

Fig. 4.55 Variation of intensity with viewing angle on an image plane (a)1m. (b)10cm, (c)1cm, (d)5mm ,(e)1mm and (f)0.5mm away. Note that the limits on the x-axis are not constant.

The target steering range within the soda lime layer is obtained from that within air by using Snell's law. For a 90° viewing range with resolution loss minimised the non-steered beam must correspond to the normal. The steering range in air is therefore ±45° so that in soda lime it is $\sin^{-1}((\sin(\pm 45))/1.4334) = \pm 29.6°$. On the other hand, the minimum steering range within the soda lime layer is attained when the 90° steering range goes from the normal to the boundary. In this case the soda lime steering range is equal to the critical

angle, 44.2°. This does not only result in loss of resolution, but also high loss of efficiency due to reflection arising from the high incidence angle Fresnel interactions at the boundary.

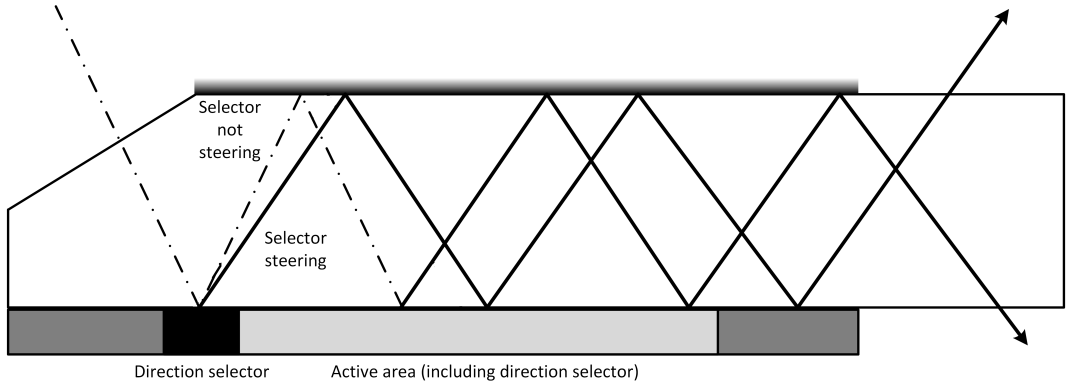

Fig. 4.56 Schematic for the use of a portion of the active area as an ad hoc direction selector. Using this technique, for a given steering angle, its reflection in the device plane can be obtained.

Figure4.56 outlines a method for doubling the steering range of such a cavity enabled multi-interaction LCOS device. For a given set-up and target steering angle we have some interaction length L, as determined by Equation4.49, smaller than the length of the active area. For this length L at different positions along the active area the resultant beam is at the same angle, reflecting repeatedly between two non-diffractive boundaries and shifted by some distance with respect to each other. If this shift is such that the last reflection is at the top boundary for one and at the bottom boundary for the other, then the angle steered is equal in both cases but reflected in the LCOS plane in one case.

In this case the final boundary is parallel to the LCOS plane for simplicity and symmetry. For angles measured with respect to the perpendicular to the LCOS parallel plane, for large angles only few interactions can be conducted even for very thin cavities and for very small angles an excessively large cavity would be necessary to have the correct amount of interactions. For a 45° viewing range attained between 22.5° and 67.5°, for $\lambda = 2.3\mu$m operation with a soda lime cavity, the angle range in the cavity is given by $27.8° \pm 12.3°$. For the same range but for $\lambda = 3.9\mu$m operation with a sapphire cavity, the angle range in the cavity is given by $23.8° \pm 10.4°$.

Results for $\lambda = 2.3\mu$m and $\lambda = 3.9\mu$m are given if Figure4.57. In all cases results are given for three to eight steering interactions. Note that the cavity thickness increases with lower diffractive interactions. Note that for a negative steering angle we have a larger number of non-diffractive interactions since L is considerably smaller than the active area length if L needs to also be smaller than the active area length for the maximum positive steered angle. Efficiency is approximately 0.4 for no steering in both cases, increasing marginally

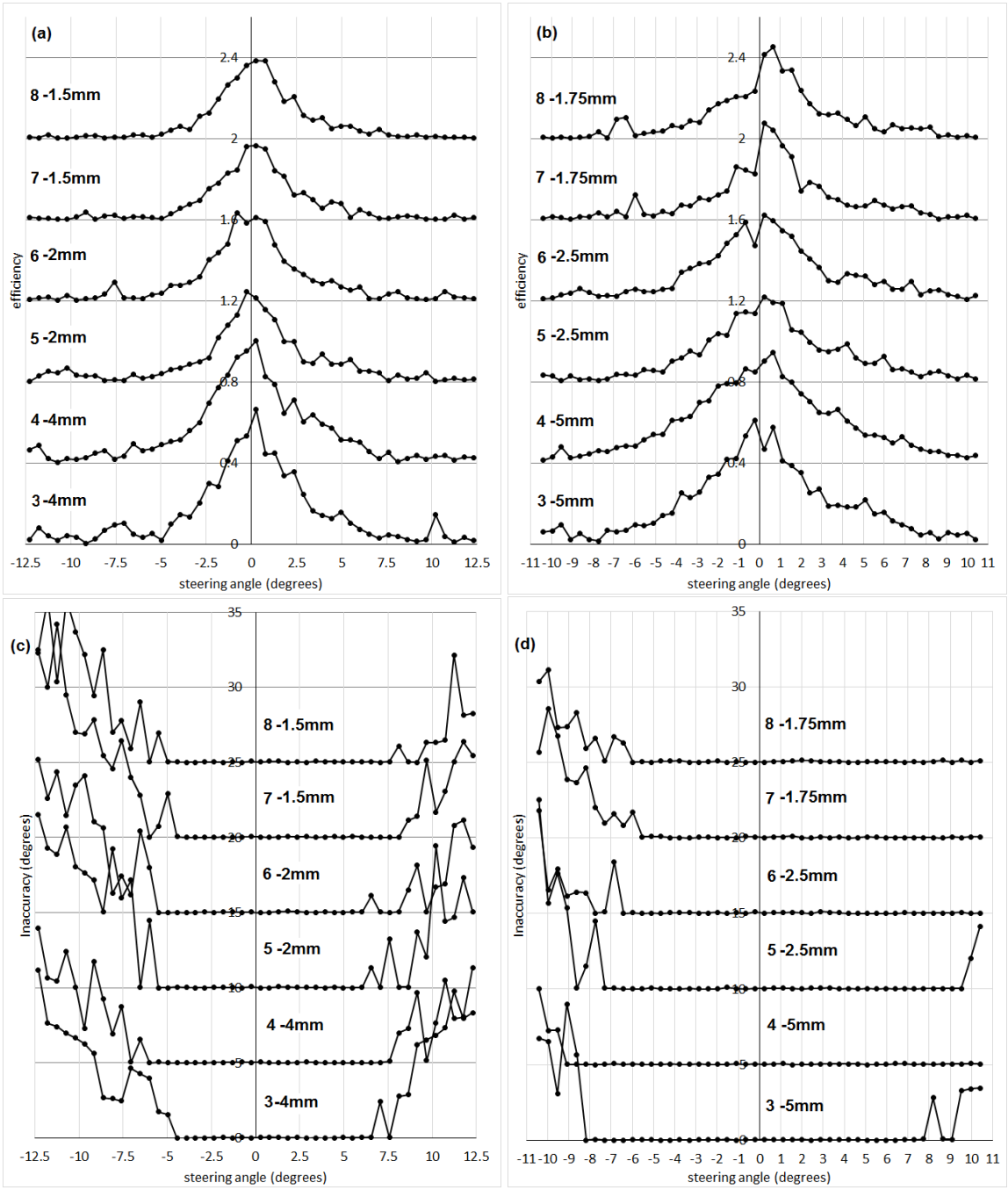

Fig. 4.57 Efficiency (a-b) and inaccuracy (degrees) (c-d) against steered angle (degrees) for $\lambda = 2.3\mu$m (a-c) and $\lambda = 3.9\mu$m (b-d). The number of diffractive interactions and the cavity thickness are given near each plot. Note the shift along the y-axis for readability.

for less diffractive interactions. Within the required steering range efficiency is higher for larger angles for the $\lambda = 3.9\mu$m case. The range where inaccuracy is negligible is also higher for this case. For negative steering angles inaccuracy is more debilitating than for positive steering angles, again due to added non-diffractive interactions. Note that beamwidth increases for increasing diffractive interactions, but is typically smaller than 0.6°.

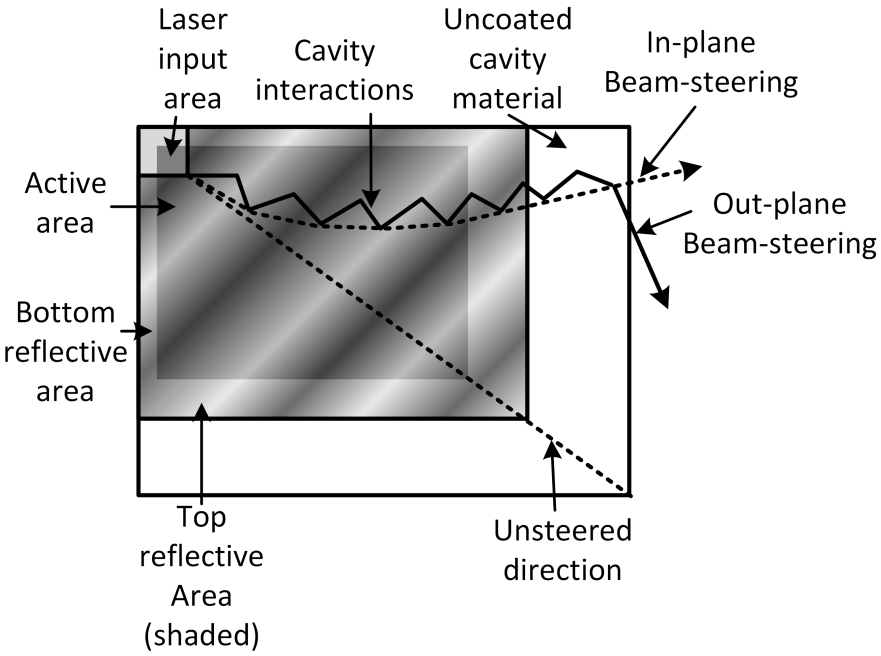

Fig. 4.58 Outline of a two dimensional cavity-enabled multi-interaction LCOS-based beam-steerer.

Operation at $\lambda = 3.9\mu$m is superior due to the larger range in which we have non-negligible efficiency and negligible inaccuracy. Note that one-dimensional operation was assumed. Two dimensional operation is possible by considering the active area length and the path the radiation follows within the cavity. Figure4.58 shows a possible realisation of a two dimensional cavity-enabled multi-interaction LCOS device. Note that doubling the steering range by employing a shift of the diffraction pattern cannot be employed for steering within the LCOS plane, only perpendicular to it.

Chapter 5

Conclusions and future work

Material and geometric considerations for the realisation of a middle infrared beam-steering device by liquid crystal spatial light modulation were considered. Various materials were proposed as potential candidates for use as a transparent conductor in such devices. For thin metallic films the granularity was a crucial factor, with less granularity leading to better properties. Beyond the electrical and optical properties both the durability of the films and their potential to be patterned was investigated. From this study CVD graphene emerged as the best option, with a sheet resistance of a few hundred ohms per square, an optical transmission better than 97% for the whole middle infrared range, good thermal stability and potential for lithography. CVD graphene is expensive, slow to produce and challenging to manufacture for areas above approximately 1cm^2 , but barring these considerations it is excellent for the application at hand.

Choosing an appropriate liquid crystal for the required application is a problem involving multiple variables, trade-offs and optical, electrical, elastic and fluid considerations. The LC optical birefringence and absorption spectrum are the paramount optical properties. For BL-037 we extracted a middle infrared birefringence of approximately 0.23 and the absorption peaks are well defined and can be avoided with ease. Implementation into an anti-parallel LC cell of thickness appropriate for middle infrared operation introduced further considerations. Typical equations could not be employed successfully since the amount of reorientation required is much larger than for operation in the visible spectrum. This introduces backflow which increases operation times dramatically. Even for a minimally thin cell thickness of 7.5μm, rise and decay times with respect to 0V are longer than the millisecond target. Operational times could be marginally improved by rising and decaying with respect to 10V, but this was still not comparable to the target response times.

Aperture shape, illumination type, pixelation, dead-space and fringing effects were all considered with respect to their influence on the performance of a liquid crystal spatial light

modulator. Different configurations were considered with graphene and Si AR based devices having the best performance. Graphene was preferable because it enabled observation in the visible spectrum. For our increased LC layer thickness fringing effects were the primary concern. Performance improved marginally at longer middle infrared wavelengths due to a reduced ratio between the fringing effect characteristic width Λ_{max} and the wavelength. Multiple interactions can increase the steering range. Multiple LCOS devices are not only financially prohibitive and operationally cumbersome, but result in redundancy since the same angle can be addressed in many different ways. Furthermore, the efficiency of the extended range is poor. Using a coarse steerer has the potential to achieve a larger steering range without redundancy and with greater efficiency. Configurations with cavity-enabled multiple-interactions using a single LCOS microdisplay hold some promise, particularly for larger middle infrared wavelengths. This is particularly true for shift-enabled doubling of the steering range. Non-diffractive steering techniques based on active LC cladding single-mode optical waveguides also have some potential, particularly for patterned electrode steering in-plane, but realising such a device has considerable fabrication hurdles.

In the immediate future work will focus upon the realisation of a middle infrared single interaction LCOS device. However, for progress to be made it is crucial that a liquid crystal material with higher birefringence can be found such that a thinner LC layer can be used. This allows for faster operation with higher efficiency due to reduced fringing effect. A smaller fringing effect also allows for smaller pixel sizes to be implemented successfully, which helps in achieving a coarse steerer. Steering with better efficiency would also allow better performance of cavity-based devices, which are an elegant, compact solution to the problem at hand. Realisation of a cavity-based device would allow for better investigation of the factors involved.

References

[1] Adams, M. (1982). An introduction to optical waveguides. *IEEE Journal of Quantum Electronics*, 18(11):1984. cited By 2.

[2] Al-Mumen, H., Rao, F., Li, W., and Dong, L. (2014). Singular sheet etching of graphene with oxygen plasma. *Nano-Micro Letters*, 6(2):116–124.

[3] Angadi, M. and Udachan, L. (1981). Electrical properties of thin nickel films. *Thin Solid Films*, 79(2):149 – 153.

[4] Basu, R. and Shalov, S. (2017). Graphene as transmissive electrodes and aligning layers for liquid-crystal-based electro-optic devices. *Physical Review E*, 96(1). cited By 2.

[5] Battaglin, G., Bello, V., Cattaruzza, E., Gonella, F., Mattei, G., Mazzoldi, P., Polloni, R., Sada, C., and Scremin, B. F. (2004). RF magnetron co-sputtering deposition of Cu-based nanocomposite silica films for optical applications. *Journal of Non-Crystalline Solids*, 345-346:689–693.

[6] Bianco, G. V., Losurdo, M., Giangregorio, M. M., Capezzuto, P., and Bruno, G. (2014). Exploring and rationalising effective n-doping of large area cvd-graphene by nh3. *Phys. Chem. Chem. Phys.*, 16:3632–3639.

[7] Bingel, A., Füchsel, K., Kaiser, N., and Tünnermann, A. (2011). Tailored tcos. volume 8168. cited By 1.

[8] Blake, P., Brimicombe, P. D., Nair, R. R., Booth, T. J., Jiang, D., Schedin, F., Ponomarenko, L. A., Morozov, S. V., Gleeson, H. F., Hill, E. W., Geim, A. K., and Novoselov, K. S. (2008). Graphene-based liquid crystal device. *Nano Lett.*, 8(6):1704–8.

[9] Bolotin, K., Sikes, K., Jiang, Z., Klima, M., Fudenberg, G., Hone, J., Kim, P., and Stormer, H. (2008). Ultrahigh electron mobility in suspended graphene. *Solid State Communications*, 146(9-10):351–355. cited By 4080.

[10] Born, M. and Wolf, E. (1970). *Principles of Optics: Electromagnetic Theory of Propagation, Interference and Diffraction of Light*. Pergamon.

[11] Brandli, G. and Olsen, J. (1969). Size effects in electron transport in metals. *Materials Science and Engineering*, 4(2):61 – 83.

[12] Camacho, J. M. and Oliva, A. I. (2006). Surface and grain boundary contributions in the electrical resistivity of metallic nanofilms. *Thin Solid Films*, 515(4):1881–1885.

[13] Chan, T. K., Megens, M., Yoo, B.-W., Wyras, J., Chang-Hasnain, C. J., Wu, M. C., and Horsley, D. a. (2013). Optical beamsteering using an 8 × 8 MEMS phased array with closed-loop interferometric phase control. *Opt. Express*, 21(3):2807–15.

[14] Charlet, E. and Grelet, E. (2008). Anisotropic light absorption, refractive indices, and orientational order parameter of unidirectionally aligned columnar liquid crystal films. *Phys. Rev. E*, 78:041707.

[15] Chen, C.-H., Yeh, J. A., and Wang, P.-J. (2006). Electrical breakdown phenomena for devices with micron separations. *J. Micromechanics Microengineering*, 16(7):1366–1373.

[16] Chen, X., Zhang, L., and Chen, S. (2015). Large area cvd growth of graphene. *Synthetic Metals*, 210:95–108. cited By 38.

[17] Chen, Y., Xianyu, H., Sun, J., Kula, P., Dabrowski, R., Tripathi, S., Twieg, R. J., and Wu, S.-T. (2011). Low absorption liquid crystals for mid-wave infrared applications. *Opt. Express*, 19(11):10843–10848.

[18] Chiu, Y., Zou, J., Stancil, D., and Schlesinger, T. (1999). Shape-optimized electrooptic beam scanners: Analysis, design, and simulation. *Journal of Lightwave Technology*, 17(1):108–113. cited By 40.

[19] Choy, K. (2003). Chemical vapour deposition of coatings. *Prog. Mater. Sci.*, 48(2):57–170.

[20] Chu, C.-L., Lu, H.-C., Lo, C.-Y., Lai, C.-Y., and Wang, Y.-H. (2009). Physical properties of copper oxide thin films prepared by dc reactive magnetron sputtering under different oxygen partial pressures. *Phys. B Condens. Matter*, 404(23-24):4831–4834.

[21] Clapham, P. and Hutley, M. (1973). Reduction of lens reflexion by the "moth eye" principle. *Nature*, 244(5414):281–282. cited By 561.

[22] Cohen, R., Cody, G., Coutts, M., and Abeles, B. (1973). Optical Properties of Granular Silver and Gold Films. *Phys. Rev. B*, 8(8):3689–3701.

[23] Conway, D. J. (2013). *Short-Range, Wide Field-of-View Extremely agile, Electronically Steered Photonic Emitter (SWEEPER)*. Darpa. http://www.darpa.mil/program/short-range-wide-field-of-view-extremely-agile-electronically-steered-photonic-emitter, Date accessed, 17th August 2015.

[24] Davis, S., Farca, G., Rommel, S., Johnson, S., and Anderson, M. (2010). Liquid crystal waveguides: New devices enabled by >1000 waves of optical phase control. volume 7618. cited By 19.

[25] Dayton, D., Browne, S., Gonglewski, J., and Restaino, S. (2001). Characterization and control of a multielement dual-frequency liquid-crystal device for high-speed adaptive optical wave-front correction. *Appl. Opt.*, 40(15):2345–2355.

[26] Dimaki, M., Vergani, M., Heiskanen, A., Kwasny, D., Sasso, L., Carminati, M., Gerrard, J. A., Emneus, J., and Svendsen, W. E. (2014). A compact microelectrode array chip with multiple measuring sites for electrochemical applications. *Sensors*, 14(6):9505–9521.

[27] Ding, F., Pors, A., and Bozhevolnyi, S. (2018). Gradient metasurfaces: A review of fundamentals and applications. *Reports on Progress in Physics*, 81(2). cited By 28.

[28] Ebbesen, T., Lezec, H., Ghaemi, H., Thio, T., and Wolff, P. (1998). Extraordinary optical transmission through sub-wavelenght hole arrays. *Nature*, 391(6668):667–669. cited By 6166.

[29] Ewing, T. K. and Folks, W. R. (2005). Liquid crystal on silicon infrared scene projectors. *Technol. Synth. Environ. Hardware-in-the-Loop Test. X*, 5785(1):36–45.

[30] Fan, J., Michalik, J., Casado, L., Roddaro, S., Ibarra, M., and De Teresa, J. (2011). Investigation of the influence on graphene by using electron-beam and photo-lithography. *Solid State Communications*, 151(21):1574–1578.

[31] Franssila, S. (2010). *Introduction to Microfabrication*. cited By 297.

[32] Gall, D. (2016). Electron mean free path in elemental metals. *Journal of Applied Physics*, 119(8):085101.

[33] Garcia-Vidal, F., Martin-Moreno, L., Ebbesen, T., and Kuipers, L. (2010). Light passing through subwavelength apertures. *Reviews of Modern Physics*, 82(1):729–787. cited By 798.

[34] Gates, B., Xu, Q., Stewart, M., Ryan, D., Willson, C., and Whitesides, G. (2005). New approaches to nanofabrication: Molding, printing, and other techniques. *Chemical Reviews*, 105(4):1171–1196. cited By 1434.

[35] Go, D. B. and Pohlman, D. a. (2010). A mathematical model of the modified Paschen's curve for breakdown in microscale gaps. *J. Appl. Phys.*, 107(10).

[36] Gonçalves, D. and Irene, E. (2002). Fundamentals and applications of spectroscopic ellipsometry. *Quimica Nova*, 25(5):794–800. cited By 27.

[37] Gou, F., Peng, F., Ru, Q., Lee, Y.-H., Chen, H., He, Z., Zhan, T., Vodopyanov, K., and Wu, S.-T. (2017). Mid-wave infrared beam steering based on high-efficiency liquid crystal diffractive waveplates. *Optics Express*, 25(19):22404–22410. cited By 0.

[38] Grundmann, M. (2010). *The Physics of Semiconductors: An Introduction Including Nanophysics and Applications*. Springer, U.S.A, second edition.

[39] Gruneisen, M., Martinez, T., and Lubin, D. (2002). Dynamic holography for high-dynamic-range two-dimensional laser wavefront control. volume 4493, pages 224–238. cited By 29.

[40] Gruneisen, M. T., DeSandre, L. F., Rotge, J. R., Dymale, R. C., and Lubin, D. L. (2004). Programmable diffractive optics for wide-dynamic-range wavefront control using liquid-crystal spatial light modulators. *Opt. Eng.*, 43(6):1387.

[41] Gupta, A., Sakthivel, T., and Seal, S. (2015). Recent development in 2d materials beyond graphene. *Progress in Materials Science*, 73:44–126. cited By 237.

[42] Hecht, J. (2011). *PHOTONIC FRONTIERS: DARPA PROJECTS: DARPA's photonics projects - At the edge of possibility*. Laser Focus World. http://www.laserfocusworld.com/articles/print/volume-47/issue-9/features/photonic-frontiers-darpa-projects-darpas-photonics-projects-at-the-edge-of-possibility.html, Date accessed, 17th August 2015.

[43] Heck, M. (2017). Highly integrated optical phased arrays: Photonic integrated circuits for optical beam shaping and beam steering. *Nanophotonics*, 6(1):93–107. cited By 15.

[44] Herman, R., Pardo, J., and Wiggins, T. (1985). Diffraction and focusing of gaussian beams. *Applied Optics*, 24(9):1346–1354. cited By 18.

[45] Hsin-Chun Lu, Chun-Lung Chu, C.-Y. L. Y.-H. W. (2009). Property variations of direct-current reactive magnetron sputtered copper oxide thin films deposited at different oxygen partial pressures. *Thin Solid Films*, 517:4408–4412.

[46] Hu, L., Xuan, L., Liu, Y., Cao, Z., Li, D., and Mu, Q. (2004). Phase-only liquid-crystal spatial light modulator for wave-front correction with high precision. *Optics Express*, 12(26):6403–6409. cited By 112.

[47] Hugonin, J. and Lalanne, P. (2005). *Reticolo software for grating analysis*. Orsay, France.

[48] Johnson L.F., M. M. B. (2001). Infrared transparent conductive oxides. *Proc. SPIE - Int. Soc. Opt. Eng.*, 4375:289–299.

[49] Kahn, J. (1997). Wireless infrared communications. *Proceedings of the IEEE*, 85(2):265–298. cited By 1662.

[50] Kelly, S. M. and Neill, M. O. (2000). *Handb. Adv. Electron. Photonic Mater. Devices, Vol. 7 Liq. Crystals, Disp. Laser Mater.*, volume 7.

[51] Khoo, I. C. (2009). Nonlinear optics of liquid crystalline materials. *Phys. Rep.*, 471(5-6):221–267.

[52] Kim, J., Oh, C., Escuti, M., Hosting, L., and Serati, S. (2008). Wide-angle nonmechanical beam steering using thin liquid crystal polarization gratings. volume 7093. cited By 53.

[53] Kim, K., Reina, A., Shi, Y., Park, H., Li, L.-J., Lee, Y., and Kong, J. (2010). Enhancing the conductivity of transparent graphene films via doping. *Nanotechnology*, 21(28):285205.

[54] Kitamura, R., Pilon, L., and Jonasz, M. (2007). Optical constants of silica glass from extreme ultraviolet to far infrared at near room temperature. *Applied Optics*, 46(33):8118–8133. cited By 376.

[55] Klapetek, P., Necas, D., and Anderson, C. (2009). Gwyddion user guide. (accessed 06.11.17).

[56] Kleine-Ostmann, T. and Nagatsuma, T. (2011). A review on terahertz communications research. *Journal of Infrared, Millimeter, and Terahertz Waves*, 32(2):143–171. cited By 432.

[57] Kumar, S., Murthy, J., and Alam, M. (2005). Percolating conduction in finite nanotube networks. *Physical Review Letters*, 95(6). cited By 193.

[58] Lantagne, S., Prel, F., Moreau, L., Roy, C., and Willers, C. (2015). Ircm spectral signature measurements instrumentation featuring enhanced radiometric accuracy. volume 9650. cited By 0.

[59] Lapanik, V., Sasnouski, G., Timofeev, S., Shepeleva, E., Evtyushkin, G., and Haase, W. (2018). New highly anisotropic liquid crystal materials for high-frequency applications. *Liquid Crystals*, pages 1–8. cited By 0; Article in Press.

[60] Lawes, R. (1989). Sub-micron lithography techniques. *Applied Surface Science*, 36(1-4):485–499. cited By 3.

[61] Lee, H. S. and Yoon, J.-B. (2005). A simple and effective lift-off with positive photoresist. *Journal of Micromechanics and Microengineering*, 15(11):2136–2140.

[62] Lee, J.-Y., Connor, S., Cui, Y., and Peumans, P. (2008). Solution-processed metal nanowire mesh transparent electrodes. *Nano Letters*, 8(2):689–692. cited By 1253.

[63] Lee, S.-K., Hsu, H.-C., and Tuan, W.-H. (2016). Oxidation Behavior of Copper at a Temperature below 300 °C and the Methodology for Passivation. *Mater. Res.*, 19(1):51–56.

[64] Li, H. (1980). Refractive index of silicon and germanium and its wavelength and temperature derivatives. *Journal of Physical and Chemical Reference Data*, 9(3):561–658. cited By 353.

[65] Li, Y., Wang, W., Zhang, J., and Wang, R. (2012). Preparation and properties of tungsten-doped indium oxide thin films. *Rare Metals*, 31(2):158–163. cited By 8.

[66] LIANG, Y. (2012). Liquid crystal alignment agent, and liquid crystal alignment film and liquid crystal display element formed from the liquid crystal alignment agent. us patent app. 13/467,811.

[67] Lin, Z., Kong, L., and Yang, X. (2011). The influence factors analysis on the steering performances of liquid crystal optical phased array. volume 2, pages 1131–1134. cited By 3.

[68] Lipiansky, E. (2013). *Electrical, Electronics, and Digital Hardware Essentials for Scientists and Engineers*. cited By 0.

[69] Liu, L., Tian, S., Long, Y., Li, W., Yang, H., Li, J., and Gu, C. (2014). Tunable periodic graphene antidot lattices fabricated by e-beam lithography and oxygen ion etching. *Vacuum*, 105(Supplement C):21 – 25.

[70] Liu, Z., Yu, F., Zhang, Q., Zeng, Y., and Wang, Y. (2008). Preparation and characterization of a novel polyimide liquid crystal vertical alignment layer. *Eur. Polym. J.*, 44(8):2718–2727.

[71] Lofving, B. and Hard, S. (1999). Beam steering with two ferroelectric liquid-crystal spatial light modulators. *Doktorsavhandlingar vid Chalmers Tek. Hogsk.*, 23(1560):1541–1543.

[72] Lu, T., Pivnenko, M., Robertson, B., and Chu, D. (2015). Pixel-level fringing-effect model to describe the phase profile and diffraction efficiency of a liquid crystal on silicon device. *Applied Optics*, 54(19):5903–5910. cited By 7.

[73] Mahulikar, S., Sonawane, H., and Arvind Rao, G. (2007). Infrared signature studies of aerospace vehicles. *Progress in Aerospace Sciences*, 43(7-8):218–245. cited By 157.

[74] Mattox, D. (1985). Substrate preparation for thin film deposition—a survey. *Thin Solid Films*, 124(1):3 – 10.

[75] Mayadas, A. F. and Shatzkes, M. (1970). Electrical-resistivity model for polycrystalline films: The case of arbitrary reflection at external surfaces. *Phys. Rev. B*, 1(4):1382–1389.

[76] McManamon, P. F., Dorschner, T. A., Corkum, D., Friedman, L., Hobbs, D., Holz, M., Liberman, S., Nguyen, H., Resler, D., Sharp, R., and Watson (1996). Optical phased array technology. *Proc. IEEE*, 84(2):268–298.

[77] Megens, M., Yoo, B.-W., Chan, T., Yang, W., Sun, T., Chang-Hasnain, C. J., Wu, M. C., and Horsley, D. a. (2014). High-speed 32×32 MEMS optical phased array. 8977:89770H.

[78] Meinel, H. (1995). Commercial applications of millimeterwaves history, present status, and future trends. *IEEE Transactions on Microwave Theory and Techniques*, 43(7):1639–1653. cited By 186.

[79] Meng, Y., Yang, X.-l., Chen, H.-x., Shen, J., Jiang, Y.-m., Zhang, Z.-j., and Hua, Z.-y. (2002). Molybdenum-doped indium oxide transparent conductive thin films. *Journal of Vacuum Science & Technology A*, 20(1):288–290.

[80] Meyerhofer, D. (1978). Characteristics of resist films produced by spinning. *Journal of Applied Physics*, 49(7):3993–3997. cited By 482.

[81] Miccoli, I., Edler, F., Pfnür, H., and Tegenkamp, C. (2015). The 100th anniversary of the four-point probe technique: The role of probe geometries in isotropic and anisotropic systems. *Journal of Physics Condensed Matter*, 27(22). cited By 39.

[82] Miedzinska, K., Hollebone, B., and Cook, J. (1988). Optical properties and assignment of the absorption spectra of sputtered mixed valence nickel oxide films. *Journal of Physics and Chemistry of Solids*, 49(11):1355 – 1362.

[83] Miller, R., Mooty, G., and Hilkert, J. (2013). Gimbal system configurations and line-of-sight control techniques for small uav applications. volume 8713. cited By 7.

[84] Mishra, S. and Yadava, V. (2015). Laser beam micromachining (lbmm) - a review. *Optics and Lasers in Engineering*, 73:89–122. cited By 32.

[85] Moharam, M., Grann, E., Pommet, D., and Gaylord, T. (1995). Formulation for stable and efficient implementation of the rigorous coupled-wave analysis of binary gratings. *Journal of the Optical Society of America A: Optics and Image Science, and Vision*, 12(5):1068–1076. cited By 1961.

[86] Moon, S., Lee, J., Yun, J., Lim, J., Gwak, M.-J., Kim, K.-S., and Lee, J.-H. (2016). Two-axis electrostatic gimbaled mirror scanner with self-aligned tilted stationary combs. *IEEE Photonics Technology Letters*, 28(5):557–560. cited By 12.

[87] Murty, M. and Shukla, R. (1980). Liquid crystal wedge as a polarizing element and its use in shearing inteferometry. *Optical Engineering*, 19(1):113–115. cited By 6.

[88] Nan, H. Y., Ni, Z. H., Wang, J., Zafar, Z., Shi, Z. X., and Wang, Y. Y. (2013). The thermal stability of graphene in air investigated by Raman spectroscopy. *J. Raman Spectrosc.*, 44(7):1018–1021.

[89] Nanda, S., Kim, M., Yeom, K., An, S., Ju, H., and Yi, D. (2016). Raman spectrum of graphene with its versatile future perspectives. *TrAC - Trends in Analytical Chemistry*, 80:125–131. cited By 21.

[90] Pal, R. (2007). On the Electrical Conductivity of Particulate Composites. *J. Compos. Mater.*, 41(20):2499–2511.

[91] Park, H., Parrott, E., Fan, F., Lim, M., Han, H., Chigrinov, V., and Pickwell-Macpherson, E. (2012). Evaluating liquid crystal properties for use in terahertz devices. *Optics Express*, 20(11):11899–11905. cited By 50.

[92] Peng, F., Chen, Y., Wu, S.-T., Tripathi, S., and Twieg, R. (2014). Low loss liquid crystals for infrared applications. *Liquid Crystals*, 41(11):1545–1552.

[93] Pierson, H. O. (1999). *Handbook of Chemical Vapor Deposition (CVD) (Second Edition)-Principles, Technology, and Applications*. William Andrew Inc., 2nd edition.

[94] Pinnel, M. R. (1979). Oxidation of Nickel and Nickel-Gold Alloys in Air at 50°–150°C. *J. Electrochem. Soc.*, 126(7):1274–1281.

[95] Plößl, A. and Kräuter, G. (2000). Silicon-on-insulator: Materials aspects and applications. *Solid-State Electronics*, 44(5):775–782. cited By 30.

[96] Querry, M. R. (1985). Optical constants. Defence technical information centre. (accessed 06.11.17).

[97] Reddy, A. S., Park, H. H., Reddy, V. S., Reddy, K. V. S., Sarma, N. S., Kaleemulla, S., Uthanna, S., and Reddy, P. S. (2008). Effect of sputtering power on the physical properties of dc magnetron sputtered copper oxide thin films. *Mater. Chem. Phys.*, 110(2-3):397–401.

[98] Rieck, U., Sweeny, C., and Norian, K. (1988). Reflectivity of sputtered aluminum alloy films. *Thin Solid Films*, 167(1):L35 – L38.

[99] Rothschild, M. (2005). Projection optical lithography. *Materials Today*, 8(2):18–24. cited By 32.

[100] Sahin, R., Simsek, E., and Akturk, S. (2014). Nanoscale patterning of graphene through femtosecond laser ablation. *Applied Physics Letters*, 104(5):053118.

[101] Saleh, B. E. A. and Teich, M. C. (2007). *Fundamentals of Photonics*. Wiley-Interscience.

[102] Schadt, M. (1997). Liquid crystal materials and liquid crystal displays. *Annual Review of Materials Science*, 27(1):305–379. cited By 224.

[103] Seki, T., Nagano, S., and Hara, M. (2013). Versatility of photoalignment techniques: From nematics to a wide range of functional materials. *Polymer (United Kingdom)*, 54(22):6053–6072. cited By 79.

[104] Serati, S., Stockley, J., and Way, C. (2002). Advanced Liquid Crystal on Silicon Optical Phased Arrays '. pages 1395–1402.

[105] Seshan, K. (2012). *Handbook of Thin Film Deposition: Techniques, Processes, and Technologies: Third Edition*. cited By 6.

[106] Shannon, R. D., Shannon, R. C., Medenbach, O., and Fischer, R. X. (2002). Refractive index and dispersion of fluorides and oxides. *J. Phys. Chem. Ref. Data*, 31(4):931–970.

[107] Shi, R., Xu, H., Chen, B., Zhang, Z., and Peng, L.-M. (2013). Scalable fabrication of graphene devices through photolithography. *Applied Physics Letters*, 102(11):113102.

[108] Sikder, U. and Zaman, M. (2016). Optimization of multilayer antireflection coating for photovoltaic applications. *Optics and Laser Technology*, 79:88–94. cited By 9.

[109] Skolnik, M. I. (2002). *Introduction to Radar Systems*. McGraw-Hill Education - Europe, 3 edition.

[110] Smith, H. (1974). Fabrication techniques for surface-acoustic-wave and thin-film optical devices. *Proceedings of the IEEE*, 62(10):1361–1387. cited By 115.

[111] Song, M., Park, E., Hyun, M. S., Kim, T. H., Kim, H. Y., and Lee, G. (2012). Studies on transmittance of silicon with ar coating films for ir transparent window.

[112] Stailey, J. (1981). Some uses of infrared (ir) sensors in meteorology. *Proceedings of the Society of Photo-Optical Instrumentation Engineers*, 253:222–236. cited By 0.

[113] Steven Serati, J. S. (2005). Advances in liquid crystal based devices for wavefront control and beamsteering.

[114] Stöhr, J. and Samant, M. (1999). Liquid crystal alignment by rubbed polymer surfaces: A microscopic bond orientation model. *Journal of Electron Spectroscopy and Related Phenomena*, 98-99:189–207. cited By 133.

[115] Stuart, B. (2005). *Infrared Spectroscopy: Fundamentals and Applications*. cited By 1320.

[116] Sun, Z. and Wang, Y. (2013). Hyperbranched polyimide application in liquid crystal alignment layers. *Polym. Adv. Technol.*, 24(1):126–129.

[117] Teng, L., Pivnenko, M., Robertson, B., Zhang, R., and Chu, D. (2014). A compensation method for the full phase retardance nonuniformity in phase-only liquid crystal on silicon spatial light modulators. *Optics Express*, 22(21):26392–26402. cited By 5.

[118] Timoshevskii, V., Ke, Y., Guo, H., and Gall, D. (2008). The influence of surface roughness on electrical conductance of thin Cu films: An ab initio study. *J. Appl. Phys.*, 103(11):9–12.

[119] Tinin, M., Afanasyev, N., Mikheev, S., Pobedina, A., and Fridman, O. (1992). On some problems of the theory of radio wave propagation in a randomly inhomogeneous ionosphere. *Radio Science*, 27(2):245–255. cited By 18.

[120] Titus, C. M., Pouch, J., Nguyen, H., and Bos, F. M. P. J. (2002). Diffraction efficiency of thin film holographic beam steering devices. *High-Resolution Wavefront Control: Methods, Devices, and Applications IV*, 4825.

[121] Torrisi, F., Hasan, T., Wu, W., Sun, Z., Lombardo, A., Kulmala, T., Hsieh, G.-W., Jung, S., Bonaccorso, F., Paul, P., Chu, D., and Ferrari, A. (2012). Inkjet-printed graphene electronics. *ACS Nano*, 6(4):2992–3006. cited By 424.

[122] Tsuchiyama, Y. and Matsushima, K. (2017). Full-color large-scaled computer-generated holograms using rgb color filters. *Optics Express*, 25(3):2016–2030. cited By 14.

[123] Ulrich, R. (1970). Theory of the prism–film coupler by plane-wave analysis. *J. Opt. Soc. Am.*, 60(10):1337–1350.

[124] Ulrich, R. (1971). Optimum excitation of optical surface waves. *J. Opt. Soc. Am.*, 61(11):1467–1477.

[125] Venediktov, V., Venediktov, V., Berenberg, V., Berenberg, V., Danilov, V., Danilov, V., Freygang, N., Freygang, N., Leshchev, A., Leshchev, A., Semenov, P., Semenov, P., Vasil, M., Vasil, M., Gruneisen, M., and Gruneisen, M. (2000). Holographic correction in mid-IR using OA LC SLM elements. *Methods*, 4124:257–264.

[126] Vieweg, N., Shakfa, M. K., and Koch, M. (2011). BL037: A nematic mixture with high terahertz birefringence. *Opt. Commun.*, 284(7):1887–1889.

[127] Wallash, A. J. and Levit, L. (2003). Electrical breakdown and ESD phenomena for devices with nanometer-to-micron gaps. *Proc. SPIE - Int. Soc. Opt. Eng.*, 4980:87–96.

[128] Wang, X., Wang, B., Pouch, J., Miranda, F., Anderson, J. E., and Bos, P. J. (2004). Performance evaluation of a liquid-crystal-on-silicon spatial light modulator. *Optical Engineering*, 43:2769–2774.

[129] Wang, Y. and Wu, M. (2017). Micromirror based optical phased array for wide-angle beamsteering. pages 897–900. cited By 7.

[130] Weber, M. (2002). *Handbook of Optical Materials*. Laser & Optical Science & Technology. Taylor & Francis.

[131] Weichelt, T., Bourgin, Y., and Zeitner, U. (2017). Mask aligner lithography using laser illumination for versatile pattern generation. *Optics Express*, 25(18):20983–20992. cited By 1.

[132] Wilson, J. and Hawkes, J. (1989). *Optoelectroncis: An Introduction*. Prentice Hall, UK, second edition.

[133] Wilson, K. and Enoch, M. (2000). Optical communications for deep space missions. *IEEE Communications Magazine*, 38(8):134–139. cited By 23.

[134] Wu, Y., Ruan, X., Chen, C.-H., Shin, Y. J., Lee, Y., Niu, J., Liu, J., Chen, Y., Yang, K.-L., Zhang, X., Ahn, J.-H., and Yang, H. (2013). Graphene/liquid crystal based terahertz phase shifters. *Opt. Express*, 21(18):21395–402.

[135] Wu, Z., Chen, Z., Du, X., Logan, J., Sippel, J., Nikolou, M., Kamaras, K., Reynolds, J., Tanner, D., Hebard, A., and Rinzler, A. (2004). Transparent, conductive carbon nanotube films. *Science*, 305(5688):1273–1276. cited By 2168.

[136] Yang, D.-K. and Wu, S.-T. (2006). *Fundamentals of Liquid Crystal Devices*. cited By 599.

[137] Yun, Z. and Iskander, M. (2015). Ray tracing for radio propagation modeling: Principles and applications. *IEEE Access*, 3:1089–1100. cited By 33.

[138] Zhang, H., Huang, J., Wang, Y., Liu, R., Huai, X., Jiang, J., and Anfuso, C. (2018). Atomic force microscopy for two-dimensional materials: A tutorial review. *Optics Communications*, 406:3–17. cited By 0.

[139] Zhong, Z.-X., Li, X., Lee, S., and Lee, M.-H. (2004). Liquid crystal photoalignment material based on chloromethylated polyimide. *Applied Physics Letters*, 85(13):2520–2522. cited By 28.

[140] Zhu, X., Sun, W., Tao, F., Cao, X., and Zhang, X. (2013). Infrared transmission characteristic of indium-tin-oxide thin films prepared by femtosecond pulsed laser deposition. volume 8907. cited By 1.